R-13-10

Thermal and thermo-mechanical evolution of the Äspö Prototype Repository rock mass

Modelling and assessment of sensors data undertaken in connection with the dismantling of the outer section

Margareta Lönnqvist, Harald Hökmark
Clay Technology AB

January 2015

Svensk Kärnbränslehantering AB
Swedish Nuclear Fuel
and Waste Management Co

Box 250, SE-101 24 Stockholm
Phone +46 8 459 84 00

ISSN 1402-3091
SKB R-13-10
ID 1391844

January 2015

Thermal and thermo-mechanical evolution of the Äspö Prototype Repository rock mass

Modelling and assessment of sensors data undertaken in connection with the dismantling of the outer section

Margareta Lönnqvist, Harald Hökmark
Clay Technology AB

Summary

The Prototype Repository is a large-scale field experiment conducted at 450 m depth in crystalline rock with a layout that, although on a much smaller scale, very closely resembles that of the KBS-3 repository projected for the Forsmark site. This unique experiment consists of a 5 m-diameter TBM tunnel and six full-scale deposition holes, each equipped with an electrically heated canister with heat generation that is on level with a real KBS-3 canister. At the time of the dismantling of the outer section, the Prototype Repository has been in operation for sufficiently long time that considerable volumes of rock have been heated. At the hottest points close to the deposition holes, measurements indicate that the temperature increase is just 5–10°C lower than the maximum rock temperature increase predicted for the Forsmark repository. Therefore, the extensively instrumented Prototype Repository is a suitable testing ground for the modelling approach, based on the distinct element code 3DEC, used for assessing the thermo-mechanical evolution of the near-field rock at Forsmark. The present report describes the rock mechanics modelling undertaken, using that approach, in connection with the dismantling of the outer section of the Prototype Repository.

As a first measure, a uniform, constant and isotropic thermal conductivity effectively valid for the entire Prototype Repository rock mass is determined by comparing measured temperatures with temperatures calculated using the FEM program Code_Bright. As for the thermal analyses conducted for the Forsmark repository, heat transport is assumed to take place by means of conduction only, i.e., without explicit account of any convection. The models account for the thermal properties of the tunnel backfill, the tunnel plugs and the interior of the deposition holes. Figure S-1 shows result examples for the outer section. At positions within the rock mass where the temperatures can be assumed to be determined by heat transport properties averaged over large volumes, the models appear to reproduce the measurements better for thermal conductivity values picked from the higher end of the tested range (2.52–2.72 W/(m·K)) than the lower end. Therefore, in all following analyses rock thermal properties corresponding to the CB2 model (2.72 W/(m·K)) are assumed for the entire Prototype Repository rock mass. In the inner section, the temperatures are concluded to be affected by the significant outflow of water. The approximation of heat transport exclusively by means of thermal conduction is, therefore, not fully adequate for the inner section.

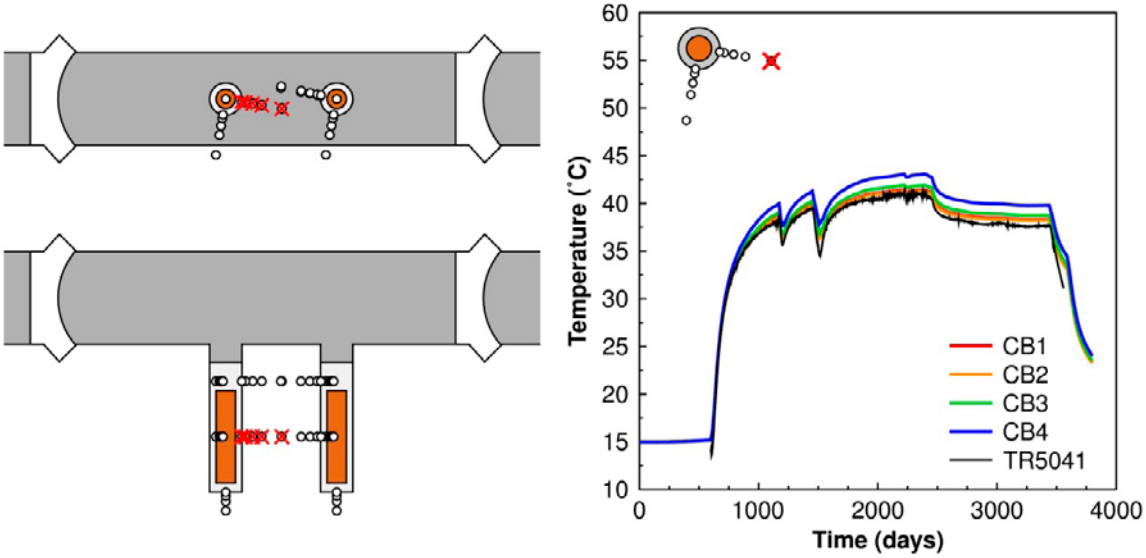

Figure S-1. *Temperatures in the pillar between the two deposition holes in the outer, dismantled, section of the Prototype Repository.*

Next, it is verified that the analytically-based 3DEC thermal logic and the representation of the heat-generating canisters by so-called compound line sources reproduce the Code_Bright temperatures with very good accuracy. Assuming uniform linear elastic and thermo-elastic properties of the rock mass, it is then verified by comparison with corresponding Code_Bright results that the 3DEC thermal stresses are correct, or rather, consistent with the input assumptions.

Having established that the 3DEC thermal and thermo-mechanical modelling approach is adequate for the purpose, a number of issues are addressed: comparison between calculated and monitored stresses and deformations, potential for spalling in the walls of the deposition holes, stability of wedges and scope and impact of fracture shear displacements. Several models with different sizes, mesh densities and material properties are analysed in which the details of the model depend on the different particular issues under consideration. To improve computational efficiency, a method to specify boundary conditions that allows for the model boundaries to be located arbitrarily close to the region of interest is developed. The method is based on the built-in programming language FISH and includes procedures that transfer and interpolate data from the interior of large models to the boundaries of smaller, more detailed models.

The following conclusions can be drawn from the modelling work:

- Modelled stress changes and deformations at points close to the deposition holes in the outer section are compared with corresponding measurements. Comparisons are made for a number of assumptions regarding *in situ* stresses, elastic properties, impact of fractures etc. A few mechanical measurements can be reproduced reasonably well and some disagreements can be explained by intersecting fractures or other inhomogeneities in the rock. The majority of the mechanical instruments are, however, judged to be unsuitable for the types of measurements attempted in the Prototype Repository. The inadequate performance of some instruments is particularly evident during the heated phase.
- Patterns of acoustic emissions registered around the two deposition holes in the outer section during the construction phase are compared with major principal stress contours obtained from calculations. Regions of stress concentrations appear to coincide with regions of acoustic emissions. This verifies that the assumed *in situ* major horizontal stress orientation is in the correct azimuth range.
- Calculated major principal stresses around the peripheries of the deposition holes are below the nominal spalling strength at all times (except for positions in the uppermost parts of the holes), which is in agreement with the observation that no spalling had occurred in the walls of the deposition holes. It should be noted, however, that the support pressure provided by the pellets filling out the slot between the bentonite blocks and the rock wall may be sufficient to suppress initiation of spalling should the stresses exceed the nominal spalling strength. Not observing spalling does, therefore, not necessarily mean that the tangential stresses could not be underpredicted by some amount during the heated phase.
- The dense network of intersecting circular fractures does not appear to have generated any serious instability in the tunnel floor. Even for a fracture pore pressure of 4.4 MPa just below the tunnel floor no blocks are detached, although rock displacements in excess of 15 mm occur locally. In reality, the pore pressure in the floor region is much lower.
- Additional stability analyses of wedges formed in the walls of the deposition holes are assessed by use of models with explicitly modelled wedges and by use of semi-analytical expressions. Results from the two methods are consistent. Wedges that are stable after the drilling of the deposition holes appear to be stable also throughout the heated phase.
- Shear displacements along the modelled fractures occur mainly in the most stress-disturbed regions around the repository openings. Results from all models suggest that most of the displacements take place during the construction phase with very little additional movements during the heated phase. Displacements exceeding a few millimetres over any significant area are found only along fractures within the fracture network just below the tunnel floor and only if the fracture pore pressure is high. Reducing the pore pressure suppresses the maximum shear displacements very efficiently. Some distance away from the openings, the shear displacements are small for all considered combinations of pore pressure and friction angles.

It is concluded that the response of a moderately fractured rock mass in reasonable initial compression with modest deviatoric stresses to excavation of repository-scale openings and to modest, local heating, can be reasonably well approximated with the corresponding response of an elastic continuum. Stress disturbances caused by fractures are significant only close to the openings for fractures that tend to be oriented tangentially relative to the opening peripheries.

It is also noted that the idealized geometry of the individual fractures, with perfectly planar fracture surfaces, and the idealized fracture material model may have contributed to exaggerate the stress disturbance caused by fractures. The local stress concentrations found in the walls of the deposition holes in models with explicitly modelled fractures, for instance, would be sufficient to initiate spalling already after excavation. Not observing any indications of spalling at any position in the walls, therefore, could mean that the stress redistribution effects of the fracture network in reality are less important.

Contents

1 Introduction

The Prototype Repository is a unique large-scale field experiment aimed at assessing the response of the rock mass and engineered barriers in a nuclear waste repository to changes in thermal, mechanical and hydraulic conditions. The experiment is conducted at the –450 m-level in the inner end of the TBM tunnel at the Äspö Hard Rock Laboratory (see Figure 1-1).

The Prototype Repository comprises two virtually independent sections separated by a concrete plug (see Figure 1-2): an inner section with four vertical, full-scale deposition holes drilled from the floor of the tunnel and an outer section with two deposition holes. Each deposition hole contains a buffer consisting of bentonite blocks and a copper canister with built-in electrical heaters to simulate the heat generated by the decaying nuclear waste. The tunnel is backfilled with a mixture of crushed rock and bentonite (Börgesson et al. 2002, Johannesson et al. 2004) and is sealed at the outer end by a second concrete plug. Geometric data for the different components in the Prototype Repository are listed in Table 1-1.

In 2010, after more than seven years of operation, work began to dismantle the outer section. This work was completed during 2011. The inner section continues to be in operation. At the time of the opening and retrieval of the outer section, the Prototype Repository had been in operation for a sufficiently long time that considerable volumes of rock had been heated. Therefore, the extensively instrumented Prototype Repository is also a suitable testing ground for the modelling approach used for assessing the thermo-mechanical evolution of the near-field rock at Forsmark (cf. Hökmark et al. 2010). The present report describes the three-dimensional rock mechanics modelling undertaken in connection with the opening and retrieval of the outer section.

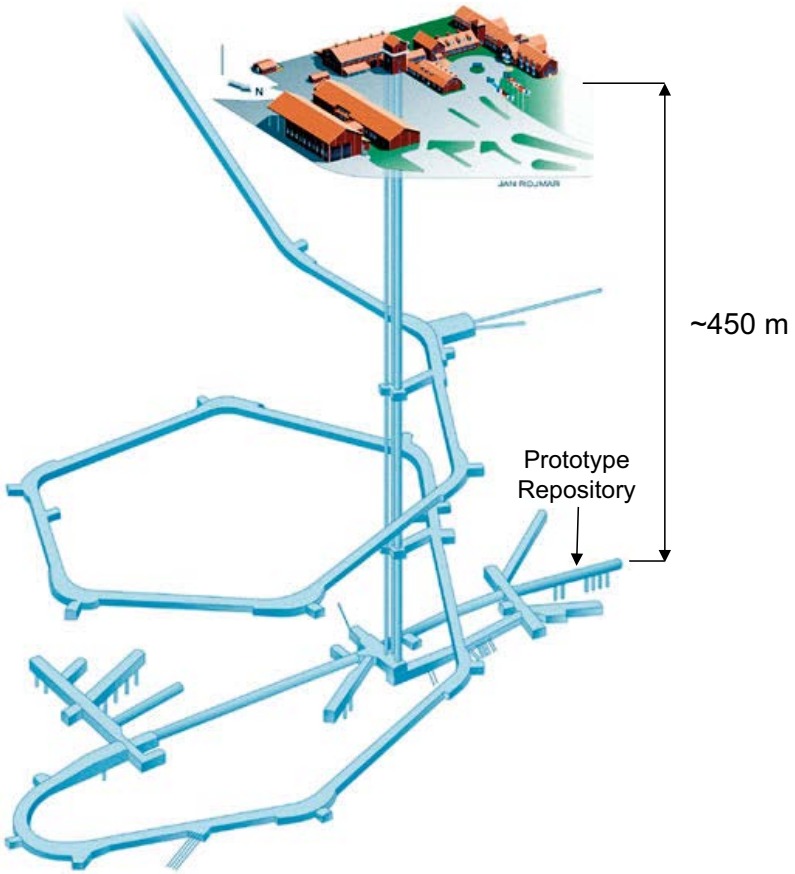

Figure 1-1. *Location of the Prototype Repository at Äspö HRL (figure modified after Fransson et al. 2012).*

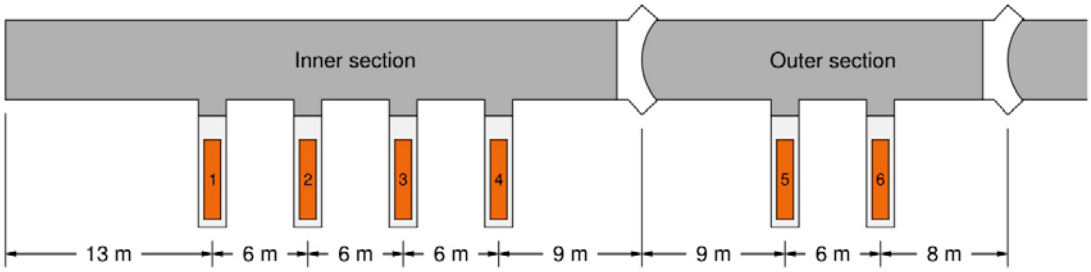

Figure 1-2. *Schematic view of the Prototype Repository.*

Table 1-1. Geometric data of the Prototype Repository, after Kristensson and Hökmark (2007).

Deposition hole depth	~8 m	Bentonite thickness above the canister	1.5 m
Deposition hole diameter	1.75 m	Total tunnel length	63 m
Canister height	~5 m	Length of inner section	40 m
Canister diameter	1.05 m	Length of outer section	23 m
Bentonite thickness below the canister	0.5 m	Tunnel diameter	5 m

2 Objectives

The objectives of the present study are to

- Describe the thermal evolution within the rock mass surrounding the Prototype Repository with the aim to obtain best-estimate global values for the heat transport properties and to demonstrate the capabilities of the model to reproduce measurement data in a long time-perspective.
- Describe the mechanical and thermo-mechanical evolution in the outer section of the Prototype Repository using the best-estimate thermal model as input for the heated phase.
  - Compare model results with mechanical measurements made in the rock and assess the relevance of these measurements.
  - Assess the potential for spalling and identify regions with spalling along the deposition hole walls.
- Assess the impact of a simplistic fracture network on stresses around the deposition holes.
- Assess the stability and normal stress variations of selected fracture planes intersecting the repository openings.

3 Overview of site conditions and input data to models

3.1 General

In this chapter, a brief summary is given of the site conditions in the Prototype Repository and an overview of the sources for information on the state of stress and the properties of the rock mass and fractures. Since part of the work is to assess the relevance of assumed input data, the actual parameter values used in the modelling work are given in the modelling chapters (see Chapters 4-8).

3.2 Overview of rock types and fractures

Geological mapping of the TBM tunnel prior to the drilling of the deposition holes in the Prototype Repository is described by Patel et al. (1997). The rock mass consists mainly of Äspö diorite (Patel et al. 1997), cf. Figure 3-1. Additional rock types observed in the tunnel are pegmatite, fine grained granite and greenstone of which the latter two rock types occur as inclusions, bands or veins (Patel et al. 1997).

Fracture mappings of the tunnel and the deposition holes are presented by Patel et al. (1997) and e.g. Rhén and Forsmark (2001), respectively. For modelling purposes, a simplistic deterministic fracture model for the outer section of the Prototype Repository based on the fracture mappings of the tunnel and deposition holes has been developed[1]. The model, denoted "the Prototype Fracture model" in the following, is "limited to major fractures with a focus on water bearing fractures" and contains 19 fractures in a 30 m × 30 m × 30 m box approximately centred on Holes 5 and 6 as shown in Figure 3-2. The Prototype Fracture model is used as a basis for the fracture network implemented in the numerical models presented in Chapter 8.

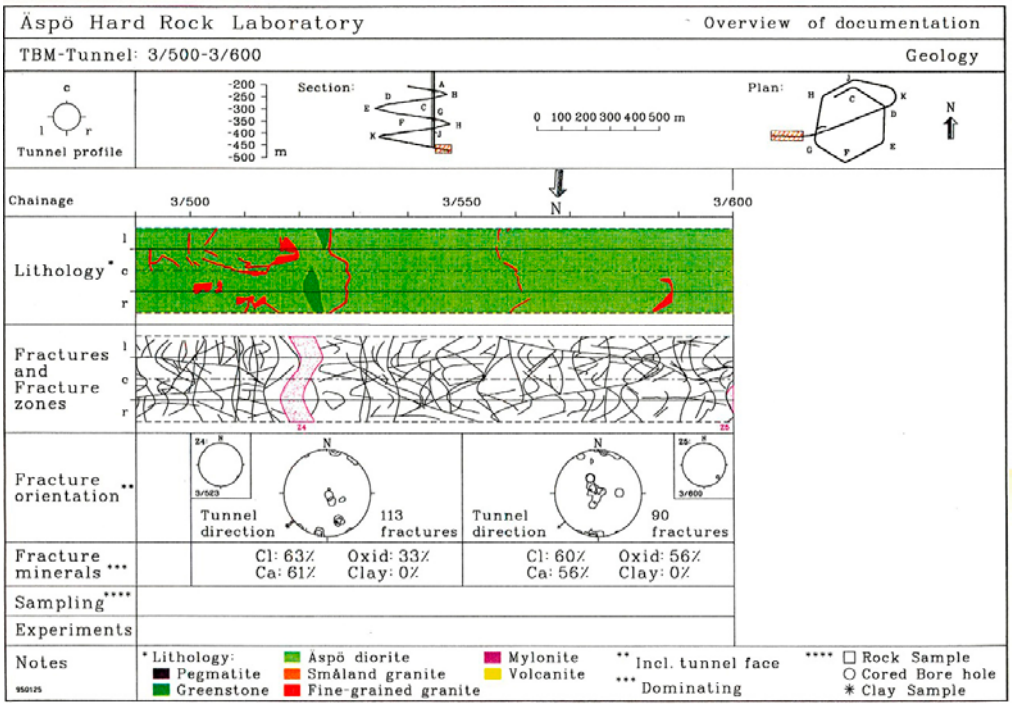

Figure 3-1. *Overview of geological mapping of the TBM tunnel, from Sundberg et al. (2005).*

[1] P. Curtis, 2011. Deterministic fracture model surrounding Deposition holes five and six in the TBM PROTOTYPE tunnel, https://service.projectplace.com/pp/pp.cgi/0/663761558

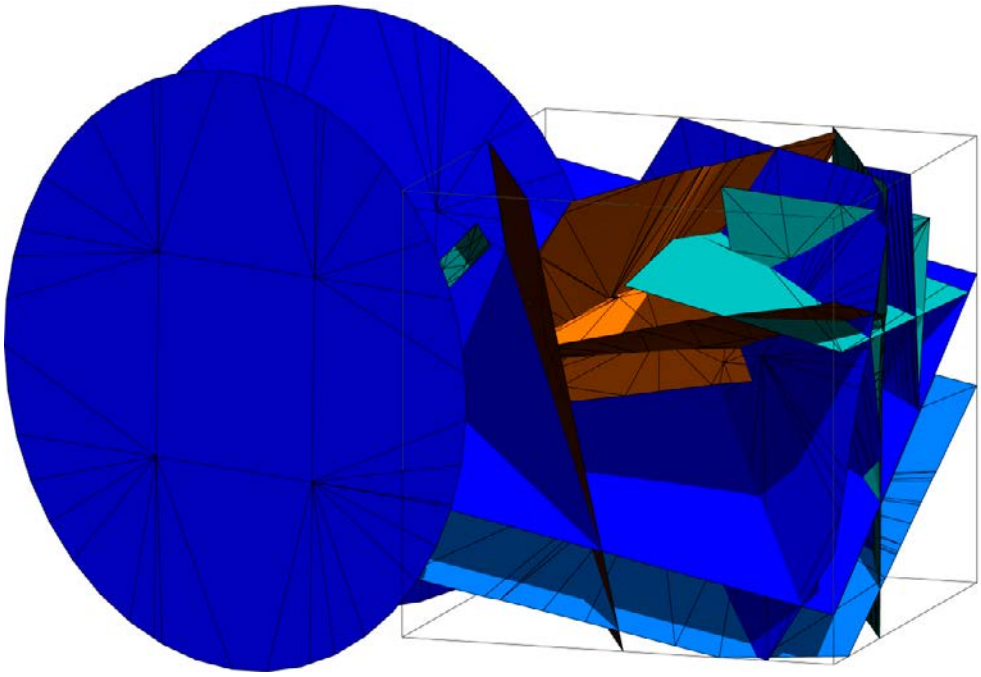

Figure 3-2. *Illustration of the Prototype Fracture model. The cube is approximately centred on Holes 5 and 6 with the inner section to the left in the figure.*

3.3 State of stress

In this study, the principal *in situ* stress components are assumed to lie in the horizontal-vertical planes with the major principal stress ($\sigma_1 = \sigma_H$) equal to 26–30 MPa and oriented 304° ± 10°, the intermediate principal stress ($\sigma_2 = \sigma_h$) equal to 13–15 MPa and the minor principal (vertical) stress ($\sigma_3 = \sigma_v$) equal to 12.5–13 MPa. This stress model has been used to set up five different modelling cases, which are further described in Chapters 6-8. The background and justification for the stress model is provided in Appendix I. In some analyses, the best estimate stress model for the Äspö Pillar Stability Experiment (APSE) test site (Andersson 2007) is used as an alternative (see Chapter 6 for details).

3.4 Thermal, thermo-mechanical and mechanical properties of the rock mass and fractures

Thermal properties of the Prototype Repository host rock have previously been assessed in laboratory tests (Sundberg et al. 2005) and by use of temperature measurements in the rock surrounding the deposition holes in combination with numerical modelling (Sundberg et al. 2005, Kristensson and Hökmark 2007). Results from both studies suggest that the effective large-scale thermal conductivity is higher than that obtained in the laboratory tests. Some measurements conducted close to the floor in the inner section were found to be significantly influenced by water movements (Sundberg et al. 2005). In this study, four different thermal conductivity models are tested (see Chapter 4). These are based on the best-estimate values obtained in the studies by Sundberg et al. (2005) and by Kristensson and Hökmark (2007) and include values from the laboratory tests. Reference values for the density and specific heat are as reported by Kristensson and Hökmark (2007). However, alternative values for the heat capacity based on the ranges of variations reported for the APSE test site and for Äspö in general (Sundberg 2003, Andersson 2007) are also tested (see Appendix A). The best-estimate heat transport properties obtained in the thermal analyses presented in Chapter 4 are subsequently propagated into the thermo-mechanical models analyzed in Chapters 6–8.

Mechanical and thermo-mechanical properties of the intact rock are assumed to be as determined for the APSE test site (Staub et al. 2004, Andersson 2007). The value of Young's modulus presented by Staub et al. (2004) for Äspö diorite (76 GPa) is in close agreement with the ones presented by Patel et al. (1997) for Äspö diorite, fine grained granite and greenstone (73–78 GPa). Staub et al. (2004) also present back-calculated effective rock-mass-scale elastic properties that may be more appropriate for the large-scale modelling of the Prototype Repository. In the analyses, values relevant for each scale are tested (see Chapters 6 and 7).

The elastic properties and Mohr-Coulomb shear strength properties of the fractures are based on average laboratory-scale values obtained in the Laxemar site investigation (Hakami et al. 2008). A general parameter study of the impact of increasing or decreasing the fracture shear strength is provided in Appendix G.

4 Thermal evolution

In a previous thermal assessment of the Prototype Repository host comprising the first 1,400 days of heating, Kristensson and Hökmark (2007) showed that measured temperatures close to the deposition holes could be reproduced very well using homogeneous, isotropic and globally valid thermal properties of the rock mass. Here, the first 3,800 days of heating are analyzed and the results are compared with data collected from all installed sensors. For the analyses, the finite-element code Code_Bright, version 2.3beta (CIMNE 2004) is used. Results for the outer section are given in this chapter, whereas results for the remaining sensors and some complementary analyses for the outer section are provided in Appendix A.

4.1 Overview of instruments

There are, in total, 85 sensors that specifically measure the temperature in the rock (Figure 4-1). These sensors are identified by a label (TROA*x* or TR*x*) and position relative to a given deposition hole ($z\backslash\alpha\backslash r$), where z (m) is vertical position measured upwards from the concrete casting (in the present analyses equal to the bottom of the hole), α (°) is angular position measured anti-clockwise from the tunnel axis and r (m) is radial position measured from the centre of the hole (Goudarzi 2012).

4.2 Description of Code_Bright models

4.2.1 Model geometry

The geometry is based on the description given by Goudarzi (2012, Figures 1-1 and 4-3) and is the same as in the study by Kristensson and Hökmark (2007). The depth of all deposition holes is schematically set at 8 m. In order to reduce the size of the model, advantage is taken of the vertical symmetry plane through the tunnel axis as shown in Figure 4-2.

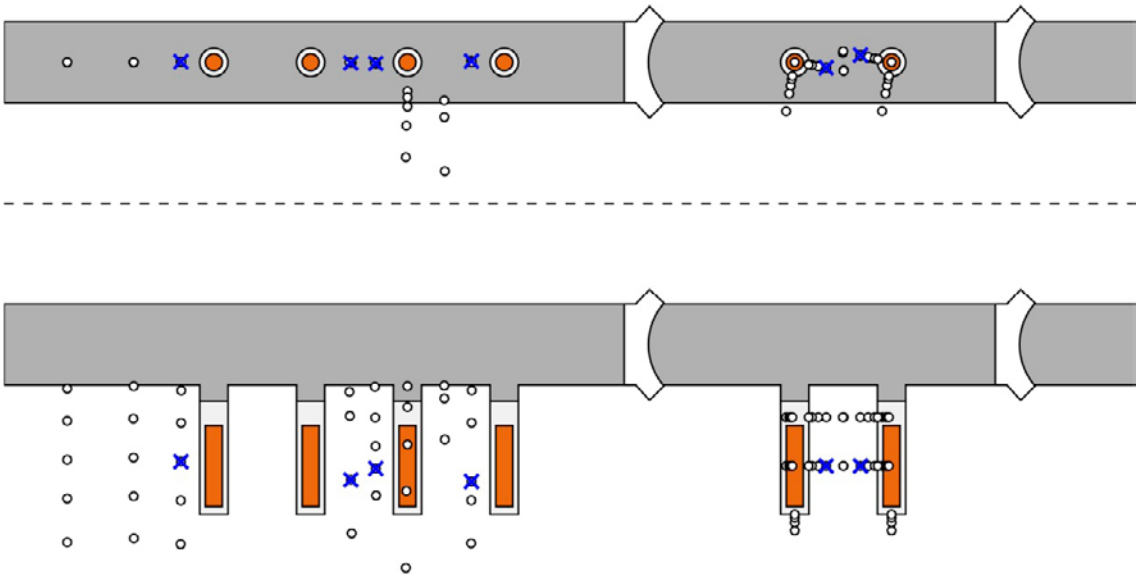

Figure 4-1. *Locations of temperature gauges around the deposition holes. Sensors considered by Kristensson and Hökmark (2007) are marked in blue.*

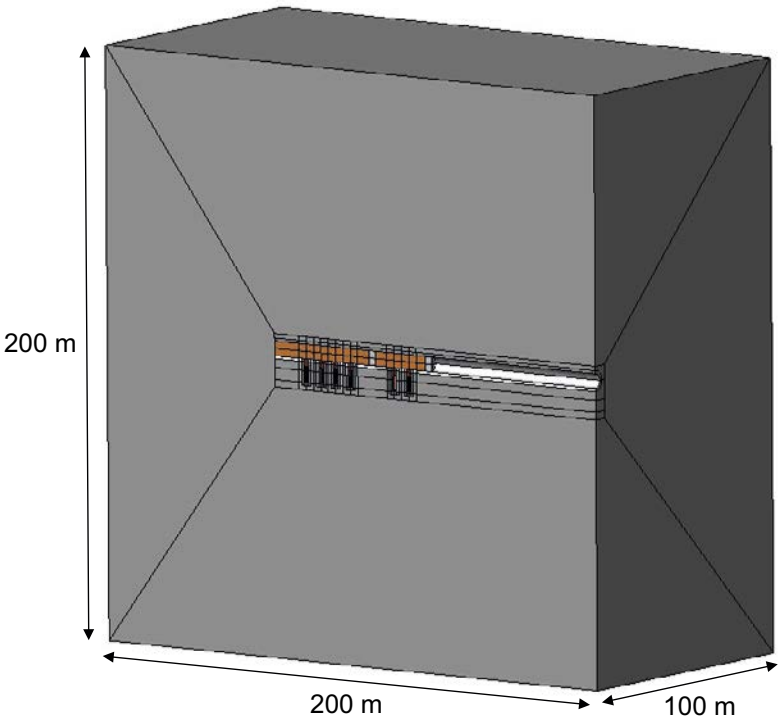

Figure 4-2. *Outline of Code_Bright model.*

4.2.2 Boundary conditions

All external boundaries are adiabatic.

4.2.3 Initial conditions

The background temperature is set at 15°C.

4.2.4 Canister power

Figure 4-3 shows a comparison between the measured heat output from all electrical heaters in the experiment and the power evolution applied in the Code_Bright model. The power is presented in the range 1–2.2 kW. Where it dips below 1 kW, it is in fact zero.

4.2.5 Material properties

The thermal properties of rock mass, plugs and other system components are listed in Table 4-1. The tunnel plugs are assumed to have the same thermal properties as the surrounding rock.

Four different sets of rock thermal properties are tested (labelled CB 1 to CB 4). Model CB 1 uses the best-estimate thermal conductivity values in the study by Kristensson and Hökmark (2007). This model has a higher thermal conductivity in the floor of the tunnel to reflect the influence of water movements (Sundberg et al. 2005). Since the intention is to use the distinct element code 3DEC for the subsequent thermo-mechanical modelling of the Prototype Repository, global, homogeneous values of the rock thermal conductivity are also tested. Models CB 2–3 and CB 4 are based on inverse modelling and laboratory measurements, respectively (Sundberg et al. 2005). The value of the specific heat is consistent with that obtained for the APSE test site (Staub et al. 2004). The influence of variations in specific heat is provided in Appendix A.

Parameter values for the backfill, buffer and canister are the same as in the study by Kristensson and Hökmark (2007).

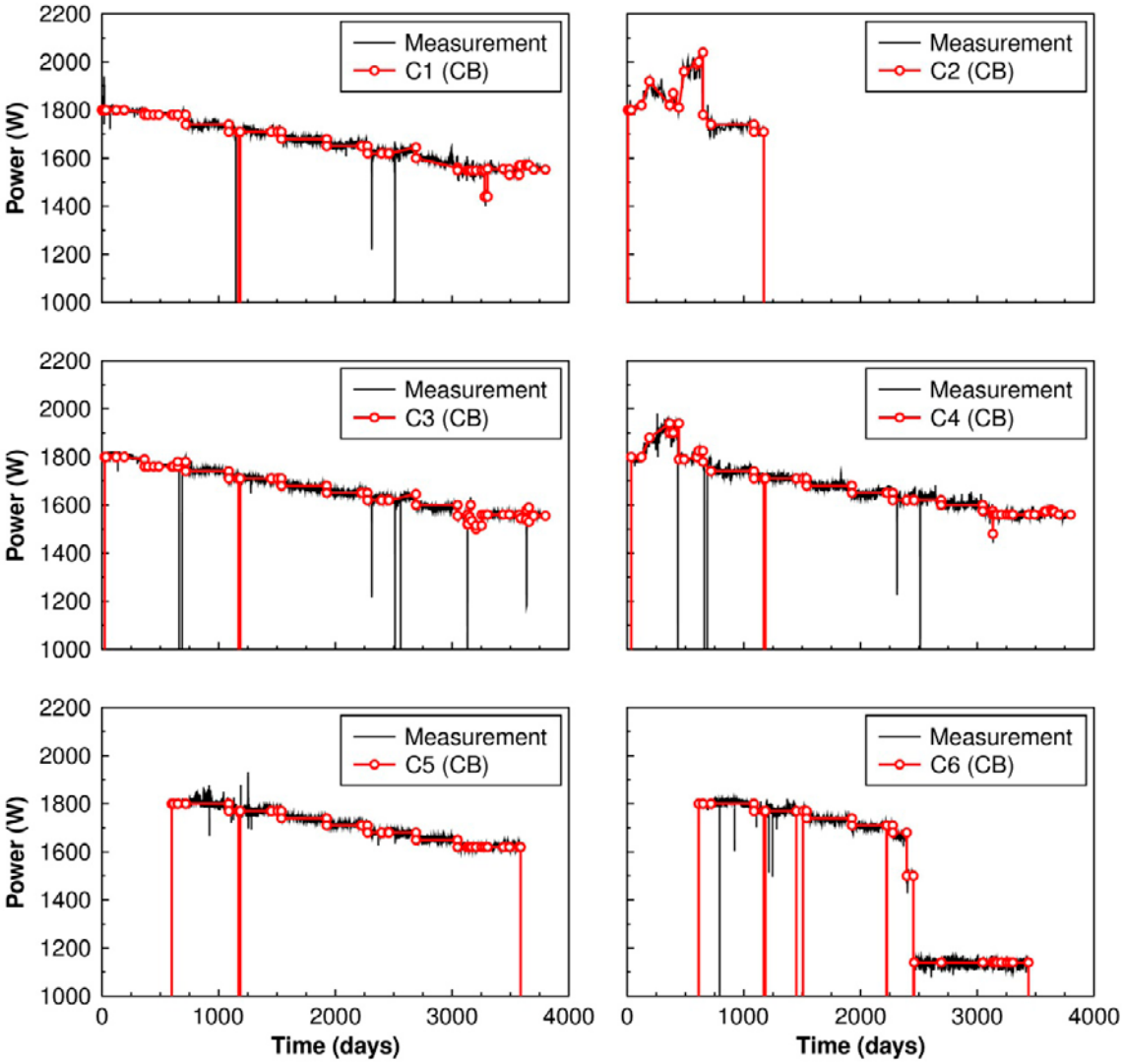

Figure 4-3. *Power evolution used in Code_Bright model (same as in Kristensson and Hökmark (2007) for the first 1,400 days) (red) and measured power (Goudarzi 2012) (black). Note that where the graphs indicate values below 1 kW, the power is, in fact, zero.*

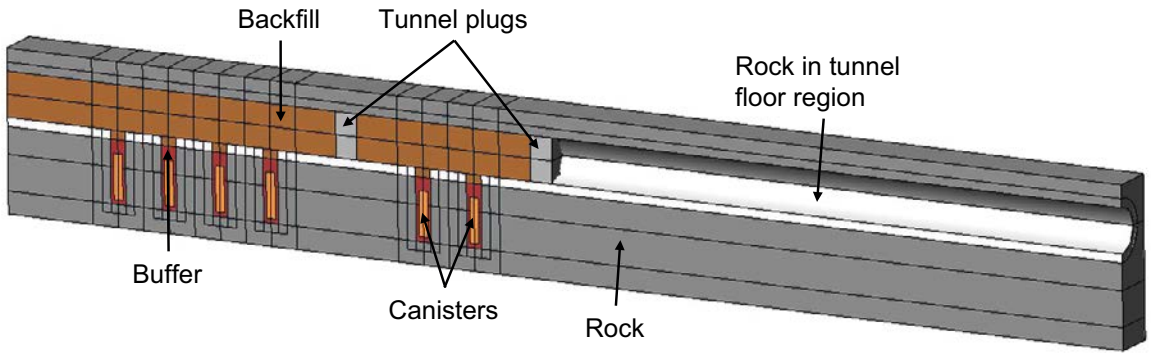

Figure 4-4. *Close-up of Code_Bright model.*

Table 4-1. Model map and data used in the thermal assessment (data marked '*' represent thermal conductivity in the floor region, see Figure 4-4).

Parameter	Unit	Rock mass and plugs				Backfill	Buffer	Canister
		CB1	CB2	CB3	CB4			
Thermal conductivity	W/(m·K)	2.685 (3.5*)	2.72	2.65	2.52	1.5	1.0	390
Specific heat	J/(kg·K)	770	770	770	770	780	800	390
Solid phase density	kg/m^3	2,770	2,770	2,770	2,770	2,500	2,780	8,930

4.3 Results

4.3.1 Sensors around Holes 5 and 6

The following general observations can be made regarding the comparison of model results to measurements:

- For sensors located 2 m below the floor (see Figure 4-5 and Figure 4-6 for Hole 5 and Figure 4-10 and Figure 4-11 for Hole 6), there is a good fit of models to measurements for the lowest value of the thermal conductivity (2.52 W/(m·K)) during the beginning of the measurement period. At the end of the measurement period, there is a better fit of models to measurements for higher thermal conductivity values. The maximum difference between measured and calculated temperatures is in the order of two degrees.
- For sensors located 5 m below the floor, i.e. at canister mid-height (see Figure 4-7 and Figure 4-8 for Hole 5 and Figure 4-12 and Figure 4-13 for Hole 6), the best fit of models to measurements was found for low values of the thermal conductivity close to the deposition hole and for higher values of the thermal conductivity at larger distances. Again, the maximum difference between measured and calculated temperatures is about two degrees.
- All models overestimate the temperature beneath the holes (see Figure 4-9 for Hole 5 and Figure 4-14 for Hole 6), in particular at the smallest distances from the bottom of the holes.
- Sensors TR6054 and TR6055 (see Figure 4-13) display a more rapid increase in temperature than the predictions by the models after the power to all canisters was switched on in December 2004 (day 1,185). The rapid increase is observed only for the array of sensors shown in Figure 4-13 and cannot be attributed to errors in the power input. Possibly these sensors overestimate the temperature slightly after day 1,185.
- Results calculated for sensors TR5021 (Figure 4-5) and TR6031 (Figure 4-11) are identical because these sensors are located symmetrically between the two holes with almost exactly the same distance to the two both heaters. The sensor readings are not identical, however: the TR6031 reading is slightly higher than the TR5021 reading after a little more than 1,000 days. The difference is small but may point to a variability in the accuracy of the measured results.

4.3.2 Sensors in the inner section

Comparisons between calculated and measured inner section results are provided in Appendix A. The calculated temperatures are generally greater than the measured temperatures, even for the highest thermal conductivity values tried here. The temperature overestimate is, however, significant only after a little more than 1,000 days, i.e., the overestimate appears to coincide with changes to the draining of the inner section that started at about that time. Typically, the outflow amounted to 10 kg of water per minute (cf. Goudarzi 2012), which corresponds to 700 W of power loss per degree of water temperature increase. There are no records of the actual temperature of the water extracted from the inner section, but even a modest increase in water temperature would obviously explain very significant differences between measured and calculated temperatures. A power loss of 700 W, for instance, corresponds to about 15% of the heat generated after a little more than 1,000 days in the inner section (cf. Figure 4-3) and would explain a corresponding average reduction of the temperature increase. Positions close to the tunnel would be more affected than sensors a distance away from tunnel in agreement with the overall appearance of the set of graphs in Appendix A.

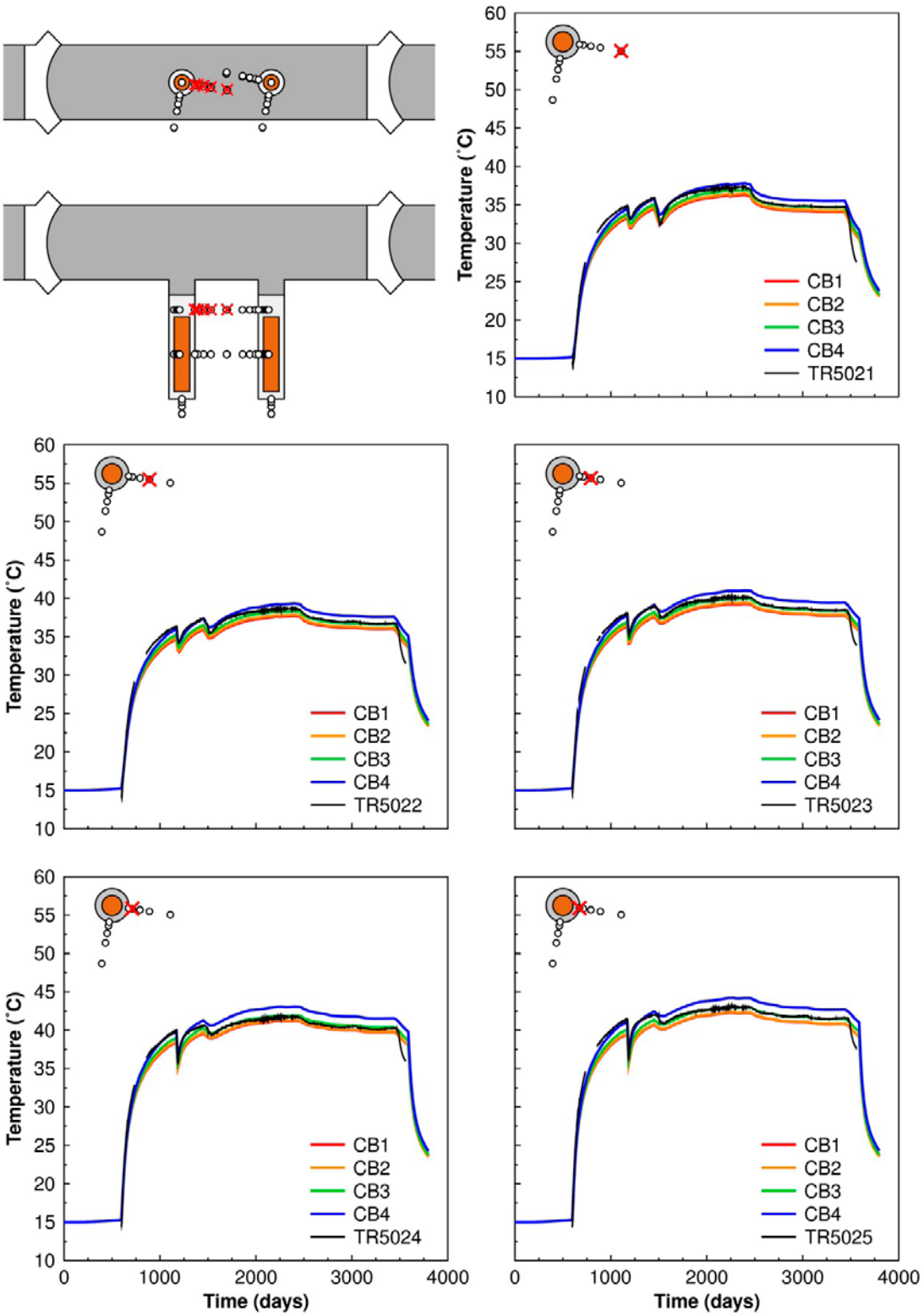

Figure 4-5. *Sensors located in the pillar between Holes 5 and 6 at 2 m below the tunnel floor. Comparison between measurements (black curves) and models.*

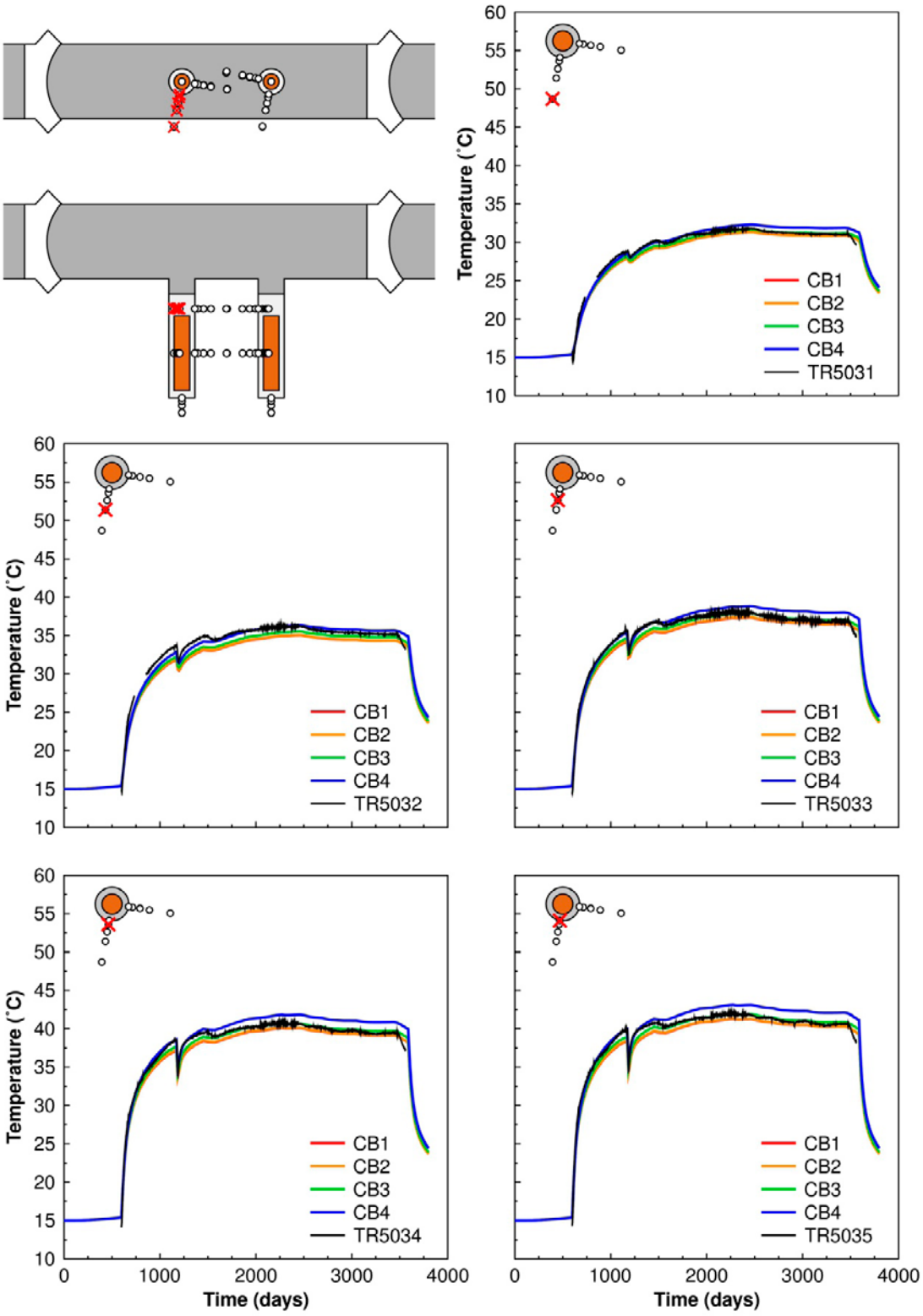

Figure 4-6. *Sensors located approximately perpendicular to the tunnel axis at 2 m below the tunnel floor. Comparison between measurements (black curves) and models.*

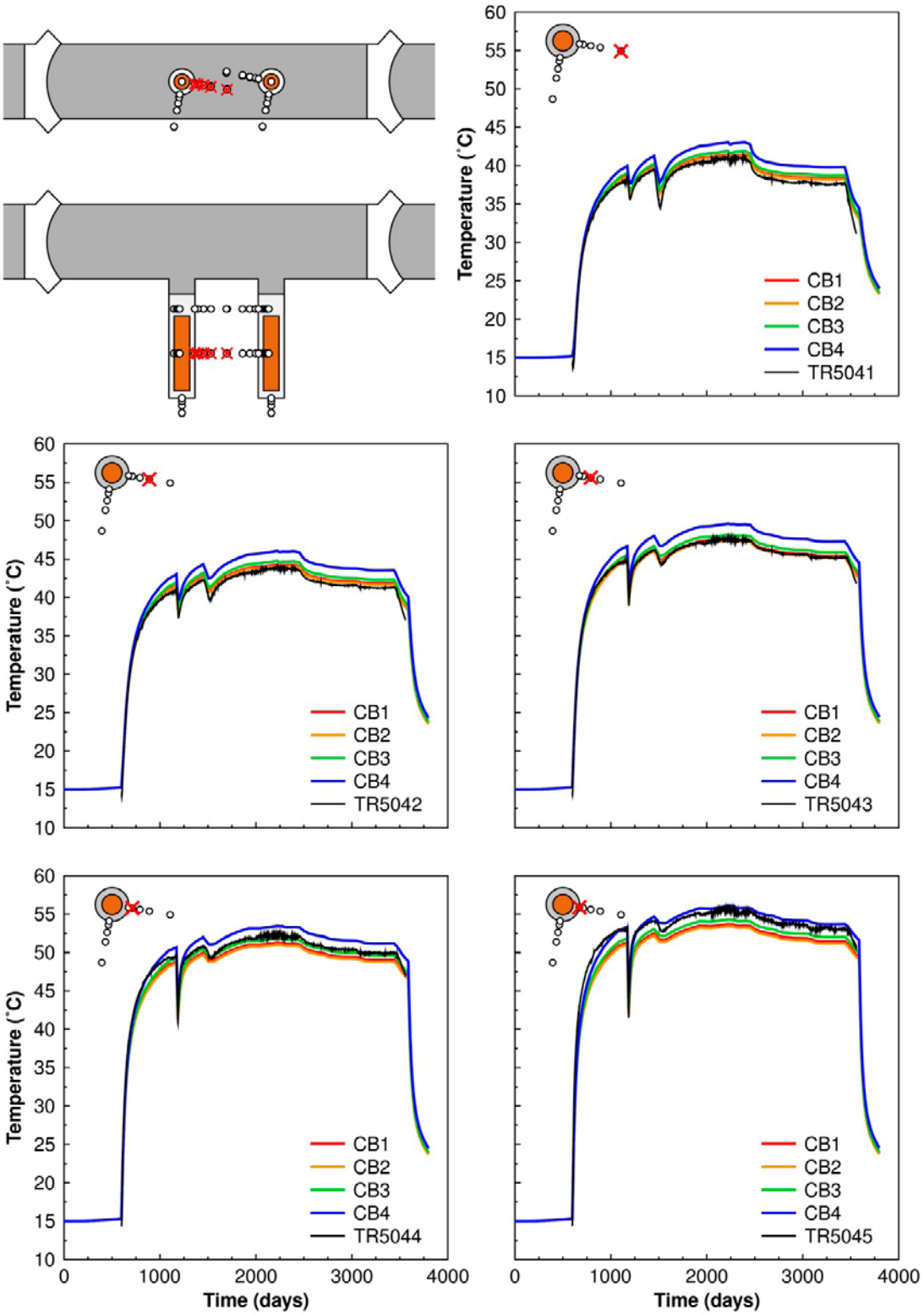

Figure 4-7. *Sensors located in the pillar between Holes 5 and 6 at 5 m below the tunnel floor. Comparison between measurements (black curves) and models.*

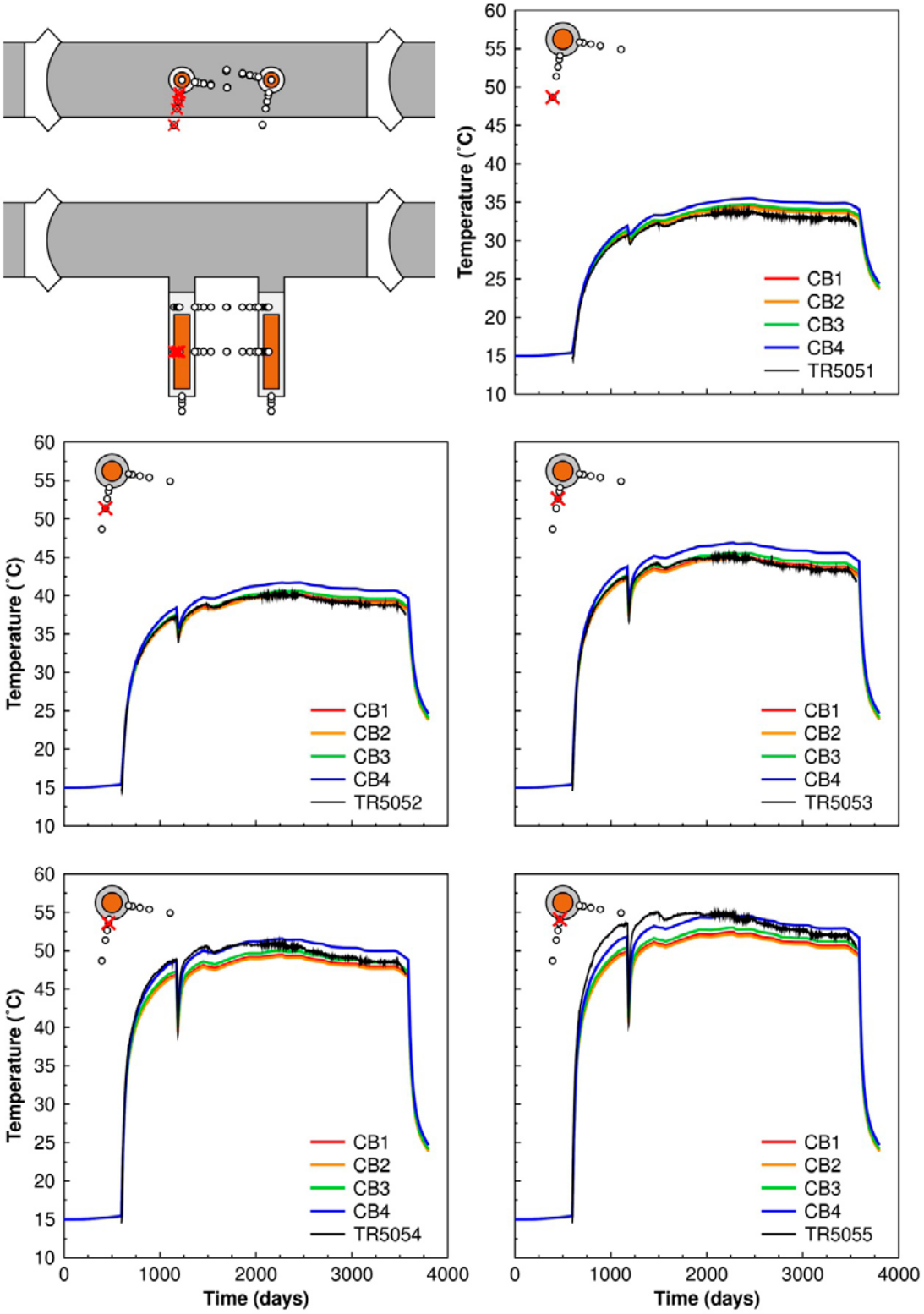

Figure 4-8. *Sensors located approximately perpendicular to the tunnel axis at 5 m below the tunnel floor. Comparison between measurements (black curves) and models.*

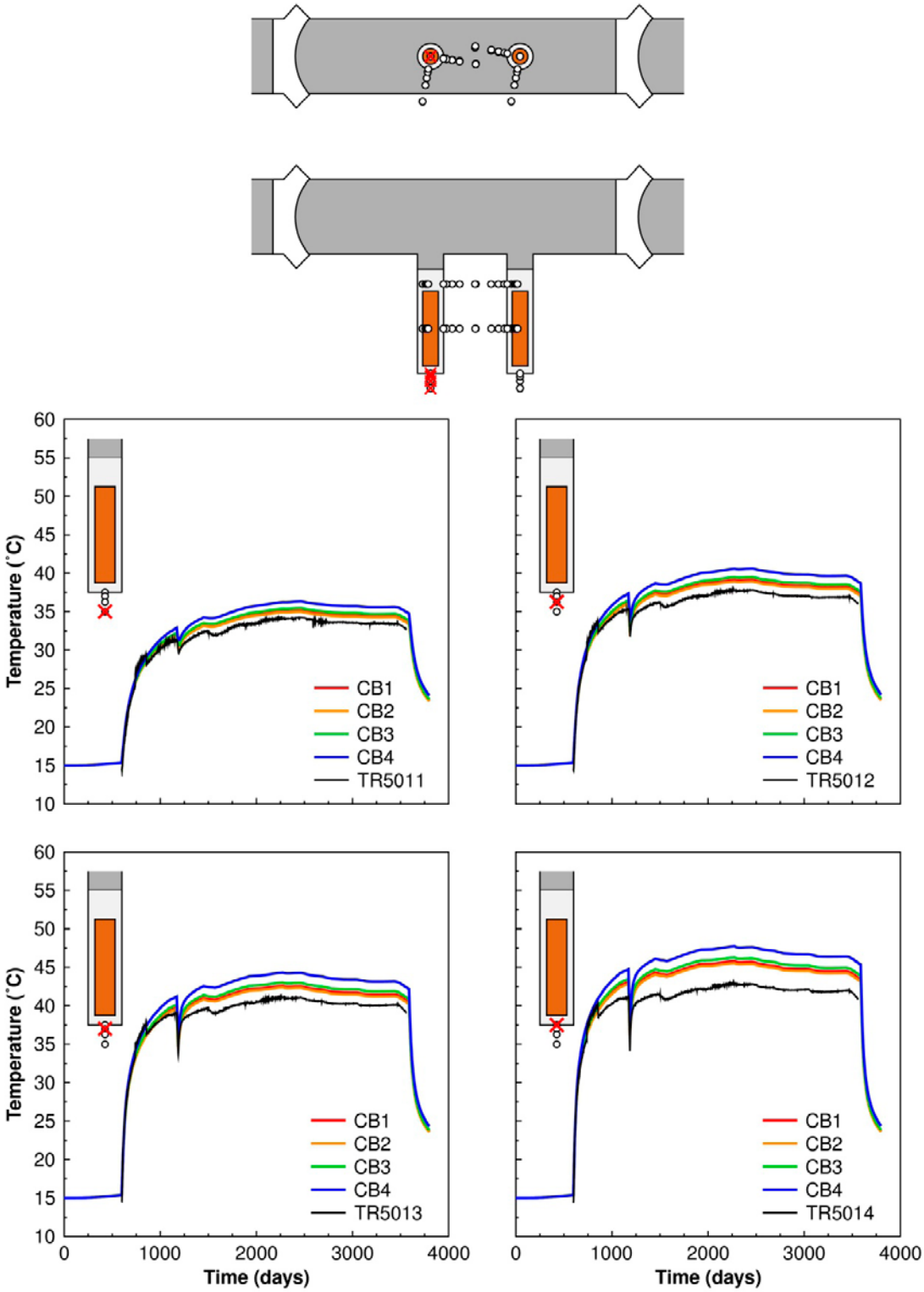

Figure 4-9. *Sensors located below the bottom of Hole 5. Comparison between measurements (black curves) and models.*

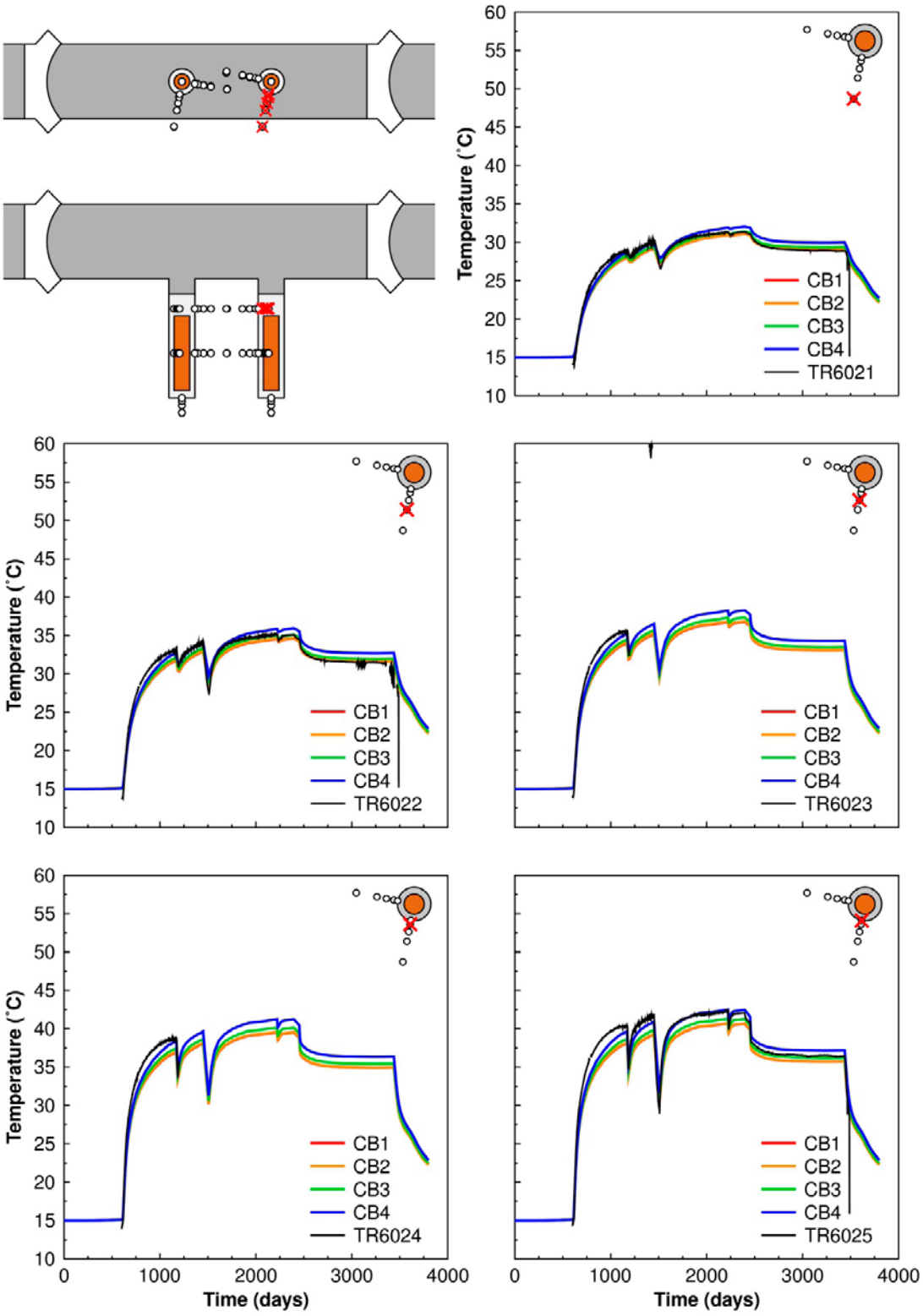

Figure 4-10. *Sensors located approximately perpendicular to the tunnel axis at 2 m below the tunnel floor. Comparison between measurements (black curves) and models.*

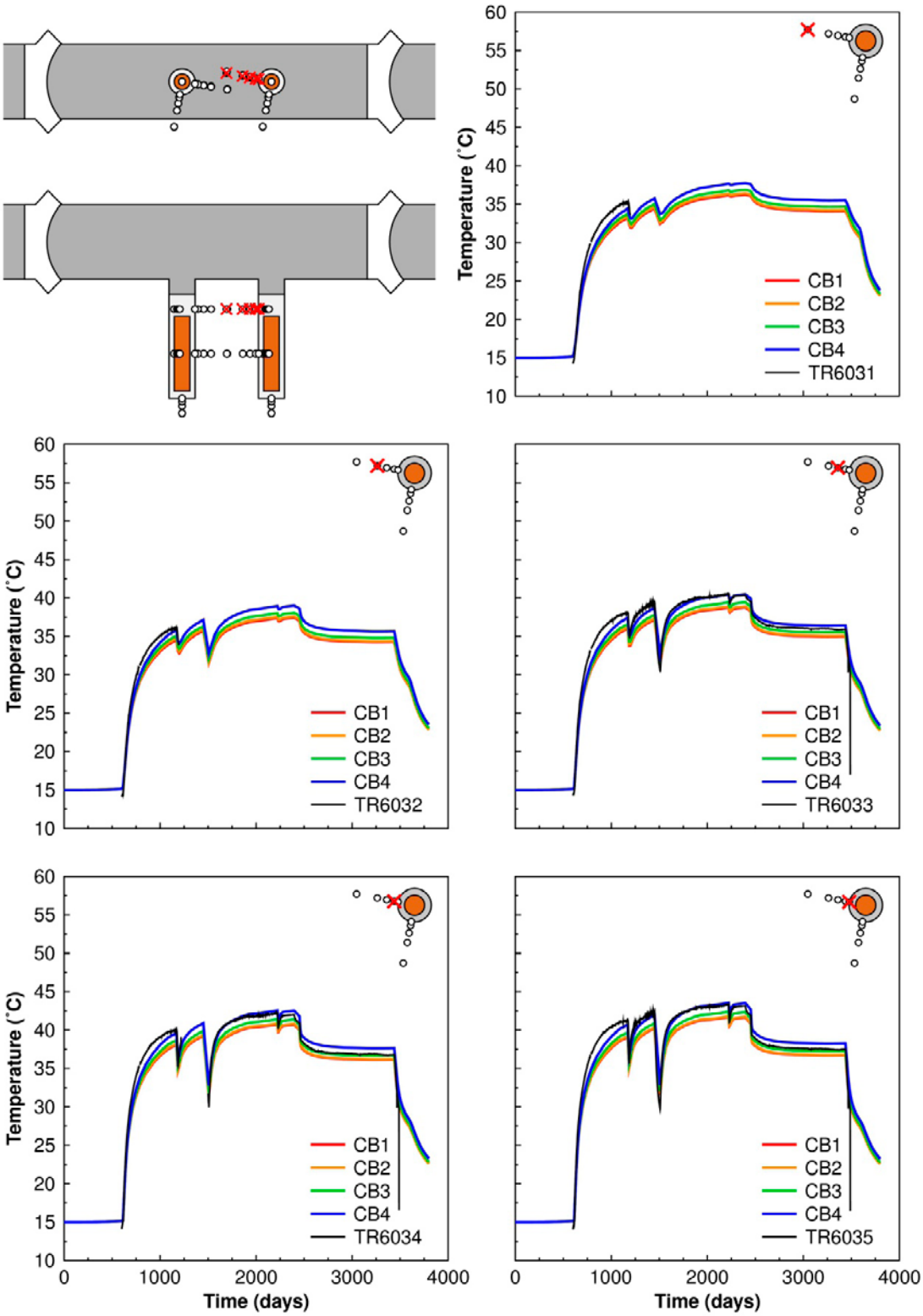

Figure 4-11. *Sensors located in the pillar between Holes 5 and 6 at 2 m below the tunnel floor. Comparison between measurements (black curves) and models.*

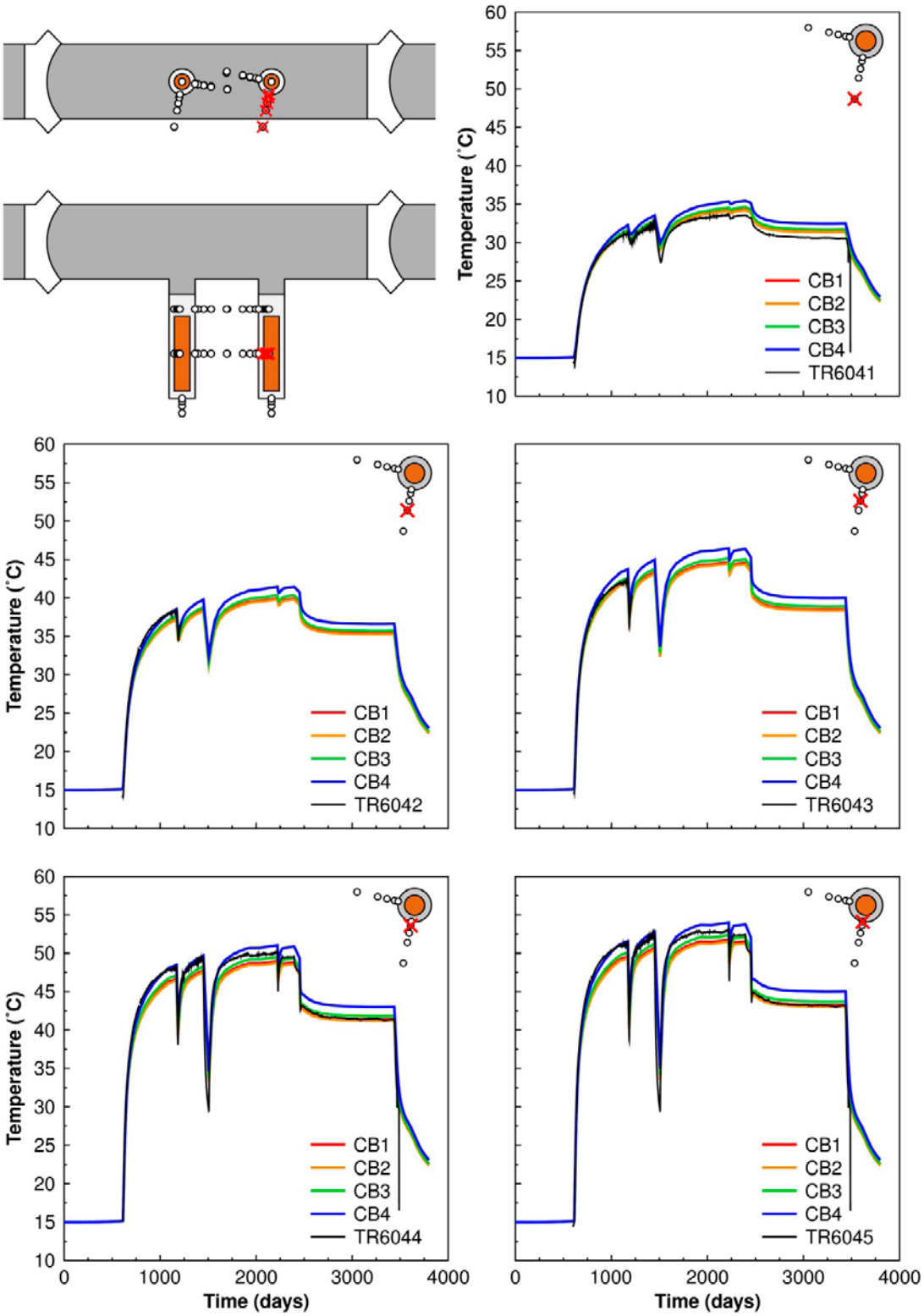

Figure 4-12. *Sensors located approximately perpendicular to the tunnel axis at 5 m below the tunnel floor. Comparison between measurements (black curves) and models.*

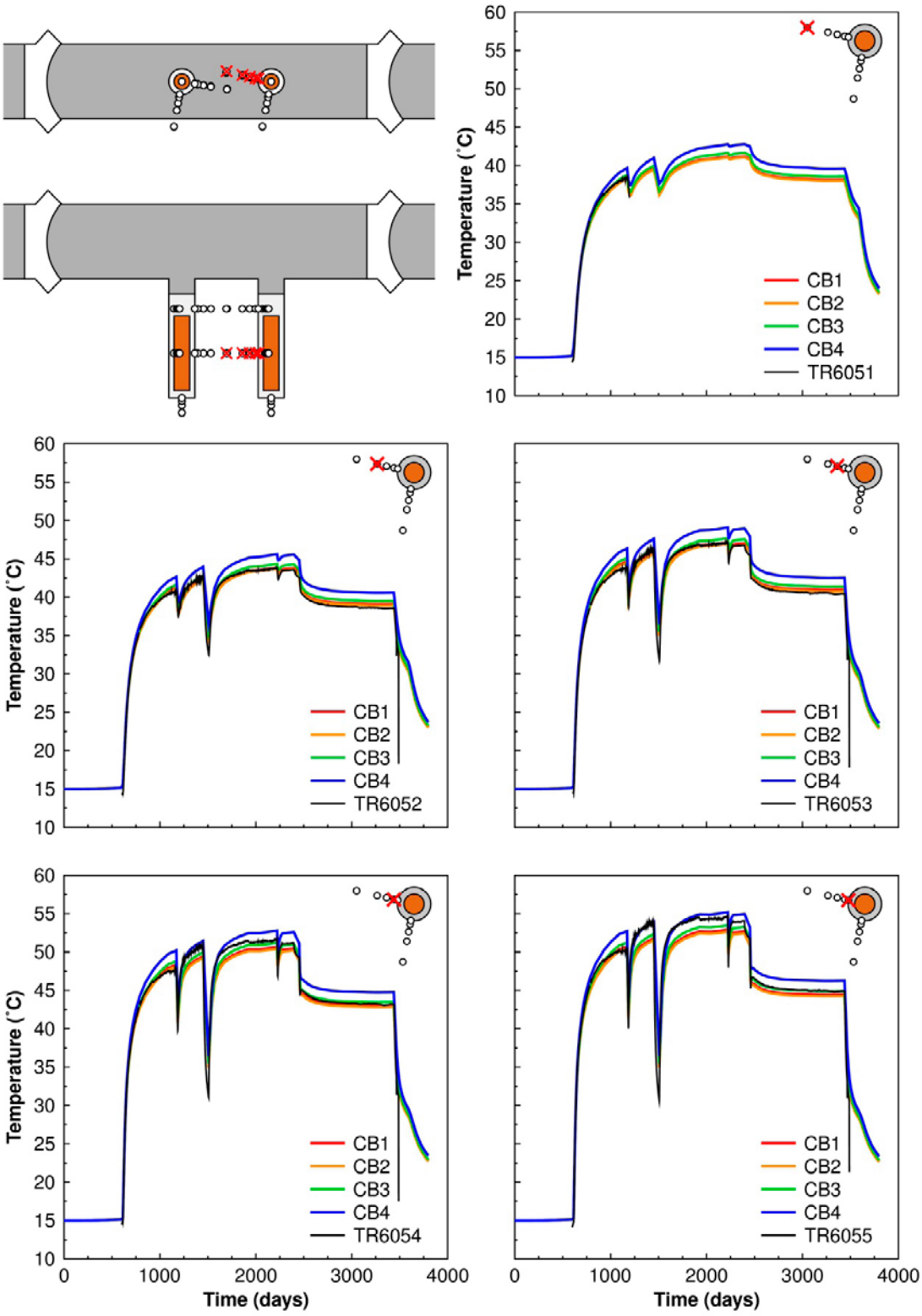

Figure 4-13. *Sensors located in the pillar between Holes 5 and 6 at 5 m below the tunnel floor. Comparison between measurements (black curves) and models.*

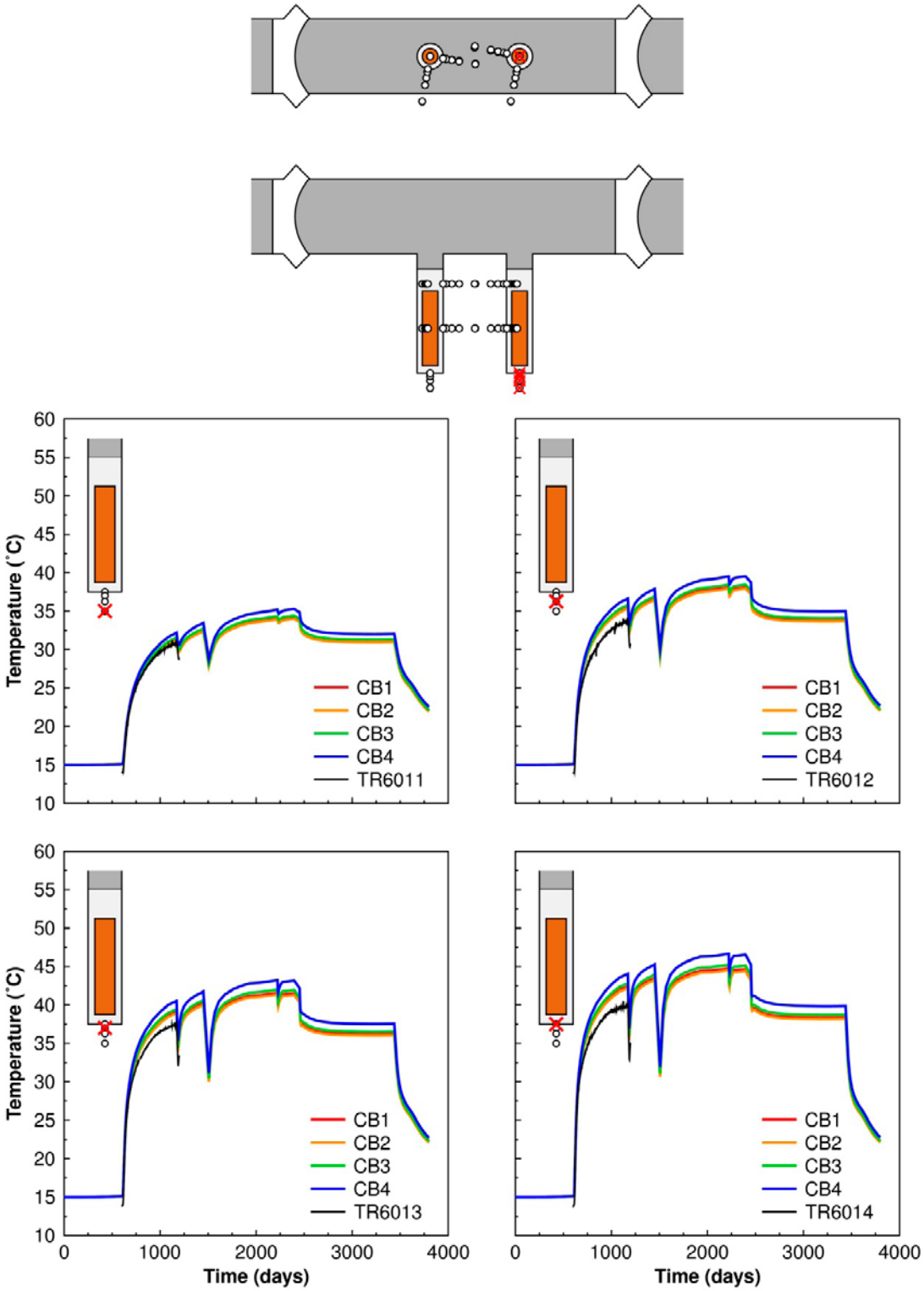

Figure 4-14. *Sensors located below the bottom of Hole 6. Comparison between measurements (black curves) and models.*

4.4 Summary

The measured temperatures around Holes 5 and 6 in the outer section can be reproduced well using homogeneous, isotropic and global rock thermal conductivities in the range 2.52–2.72 W/(m·K). The small differences found between measured and calculated results can be attributed to a number of factors:

- Variations in rock thermal properties. In reality there is a variability in rock thermal properties, i.e., in thermal conductivity and in heat capacity. As demonstrated in Appendix A, reasonably realistic errors, or variations, in heat capacity do not produce more than insignificant disturbances. Thermal conductivity variations within the range tried here (2.52–2.72 W/(m·K)) result in maximum temperature differences of about 2°C.
- Effects of water movement. Here it is assumed that heat transport in the Prototype Repository rock mass is a question of heat conduction only. In reality, there are contributions also from water movement around the unsaturated tunnel. The changes to the drainage of the tunnel during 2004 and the subsequent breakage of a packer in the rock in 2006 (see Goudarzi 2014) appear to have significant effects only in the inner section (cf. Appendix A).
- Temperature dependence. There is a small temperature dependence in the heat conductivity of most rock types. Typically, the conductivity could decrease by about 10% per 100ºC (Hökmark et al. 2009).
- Conditions in the interior of the deposition holes. At some distance from a deposition hole, the total heater power and the rock heat transport properties determine the temperature contribution from that heater. Close to the deposition holes, the rock temperatures will depend also on details of the heat flux distribution. This distribution will, in turn, depend on details of the heater geometry, water uptake in the buffer etc.
- There may be a slow temperature reduction associated with restoration of the true background temperature after backfilling and closure.

In the inner section the calculated temperatures are, in general, significantly overestimated at late times for all conductivity assumptions. No accurate quantitative assessment of the cooling effect of the draining of the inner section that started about 1,000 days after test start in, but the order of magnitude of the estimated power loss caused by the water movement is sufficient to explain the difference between measurements and calculations.

In the following 3DEC analyses the value 2.72 W/(m·K) is used as a global value for the thermal conductivity of the Prototype Repository rock mass. At some distance from the heaters, where the temperatures are controlled by heat transport properties averaged over large volumes, the value 2.72 W/(m·K) appears to reproduce the measured temperatures slightly better than the lower values tried here.

5 Thermal and thermo-mechanical modelling approach: Comparison between Code_Bright and 3DEC

5.1 General

The distinct element code 3DEC (Itasca 2007) has been used extensively to analyze the response of the rock mass within and around a nuclear waste repository to changes in thermal and mechanical conditions (e.g. Hökmark et al. 2006, 2010, Fälth and Hökmark 2007, Fälth et al. 2010). This is done on different scales and, when appropriate, with due account of the rock fractures. However, the built-in thermal logic in 3DEC is based on an analytical solution of the temperature evolution in an infinite medium with homogeneous and isotropic thermal properties (Itasca 2007), meaning that the thermal properties of heaters, deposition holes, backfilled tunnels cannot be accounted for. 3DEC is therefore not suitable for very detailed thermal calculations such as those made with Code_Bright in Chapter 4.

As seen in Chapter 4, the temperature field within the rock mass can be described well using a uniform value of the rock thermal conductivity. The best agreement between measurements and model results was found for values of the rock thermal conductivity in the range 2.65–2.72 W/(m·K). In the following, the value 2.72 W/(m·K) is used. Kristensson and Hökmark (2007) have shown that if the thermal conductivity of the back-fill is varied in the range 1.0–2.72 W/(m·K), i.e. between the values assumed for bentonite buffer and rock, respectively, the resulting variations in temperature at positions a few metres below the tunnel floor are negligible.

The primary objective in this chapter is to investigate to what extent the back-filled tunnel, the plugs, the deposition holes and the details of the geometry of the heaters influence the rock temperatures and the thermally induced stresses in the rock surrounding the tunnel. This is done by direct comparison between Code_Bright results and corresponding 3DEC results. If there are significant differences in the thermal stresses as calculated by the two codes, there would be a need to devise a strategy to import temperatures into 3DEC from Code_Bright. In the present study, 3DEC version 5.00 is used.

5.2 Thermal analyses using 3DEC

5.2.1 Calibration of heat sources

The built-in thermal logic in 3DEC is based on an analytical solution of the temperature evolution due to a point source in an infinite medium with uniform properties (Itasca 2007). Heat sources are represented either by individual point sources or by grids of point sources that can be "switched on" at arbitrary points in time to represent e.g. deposition of a canister. The thermal logic supports either constant power or exponentially decaying power (Itasca 2007). In order to obtain other temporal power variations, heat sources with a suitable power increment/decrement need to be added to the model at suitable points in time. In the present modelling work, a step-function approximation of the actual, documented, power evolution (see Figure 5-1) is used.

Real canisters have a non-uniform heat flux distribution with higher surface heat flux at the top and bottom, see e.g. Kristensson and Hökmark (2007). Hökmark and Fälth (2003) showed that a good representation of a KBS-3V canister could be obtained by a superposition of two line sources with uniform power distributions (Figure 5-2). This approach was used in SKB's safety analyses SR-Can and SR-Site (Hökmark et al. 2006, 2010, Fälth and Hökmark 2007).

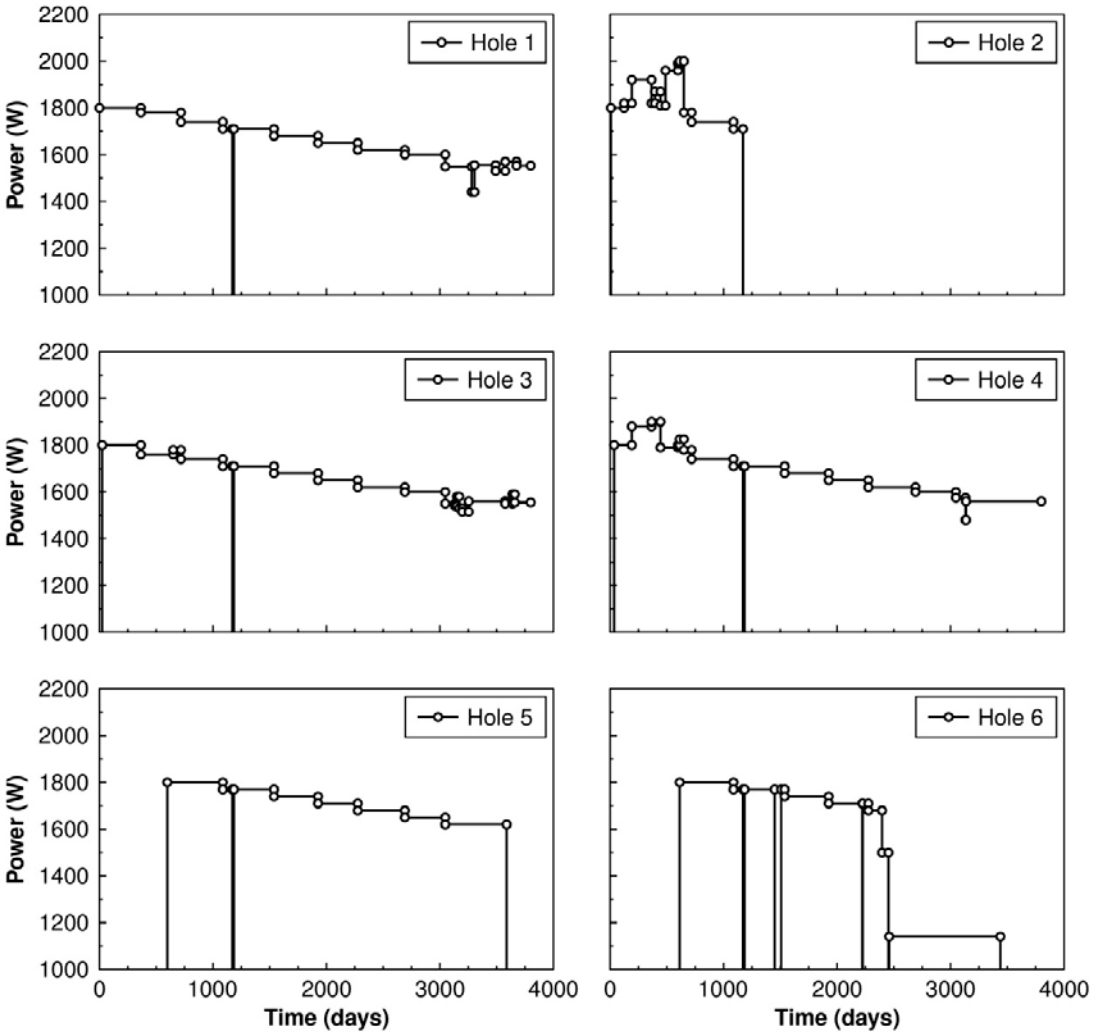

Figure 5-1. *Power evolution used in 3DEC. Note that where the graphs indicate values below 1 kW, the power is, in fact, zero.*

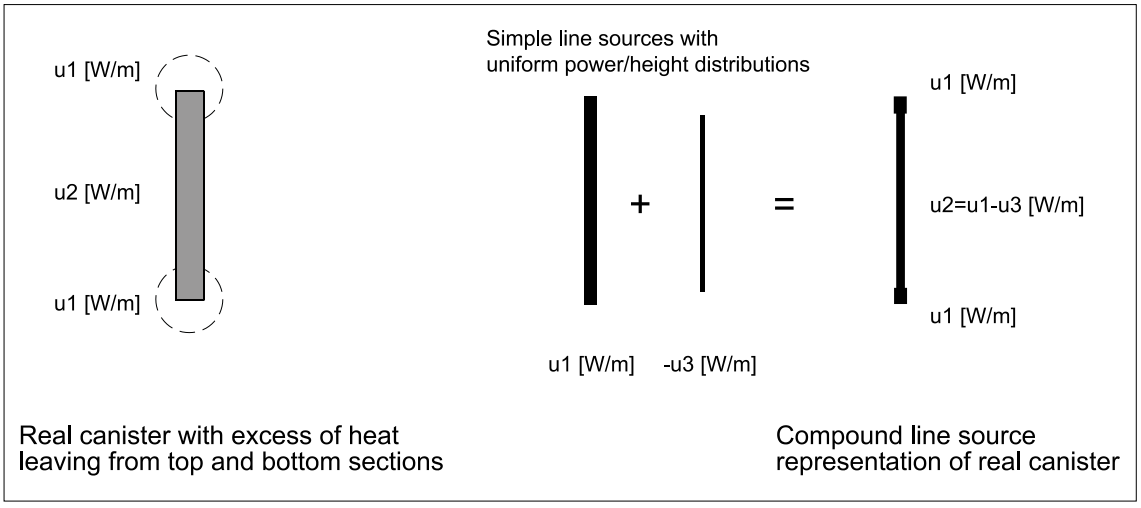

Figure 5-2. *Description of compound line sources, from Hökmark and Fälth (2003).*

5.2.2 Results

A good agreement of the temperature along the deposition hole walls in the outer section was found between 3DEC and Code_Bright for compound-line source representations consisting of a superposition of one 5 m-long line source composed out of 51 uniformly distributed point sources and one 4.6 m-long line source with 47 uniformly distributed point sources, see Figure 5-3. The power (p_1) of each point source in the longer line source is given by $p_1 = p/15$, where p is the total canister power. For the shorter line source, the power (p_2) of each point source is given by $p_2 = -(51\ p_1 - p)/47$. As a detailed representation of the temperature field in the immediate vicinity of the deposition holes in the inner section (Holes 1-4) is not the main purpose of the present modelling work, the heat sources in these holes are represented by simple 5 m long line sources composed out of five evenly distributed point sources each with one fifth of the total canister power.

Figure 5-4 shows a comparison at nine additional points surrounding the tunnel and the deposition holes in the outer section. As seen in the figure, not taking the low-conductivity backfill into account gives an insignificant temperature underestimate just below the tunnel floor (see Pt. 2) and a corresponding small overestimate just above the tunnel roof (see Pt. 1) compared with Code_Bright. At the remaining points, the agreement between 3DEC and Code_Bright is very good.

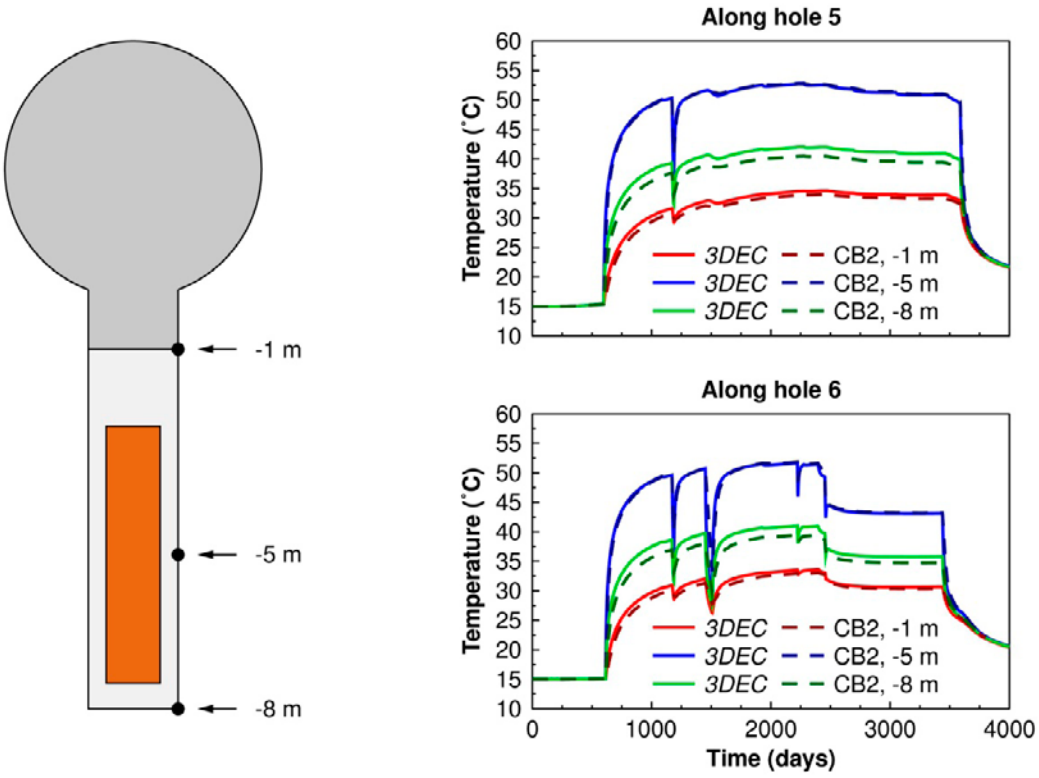

Figure 5-3. *Comparison between 3DEC and Code_Bright (CB2) at points along the deposition hole wall.*

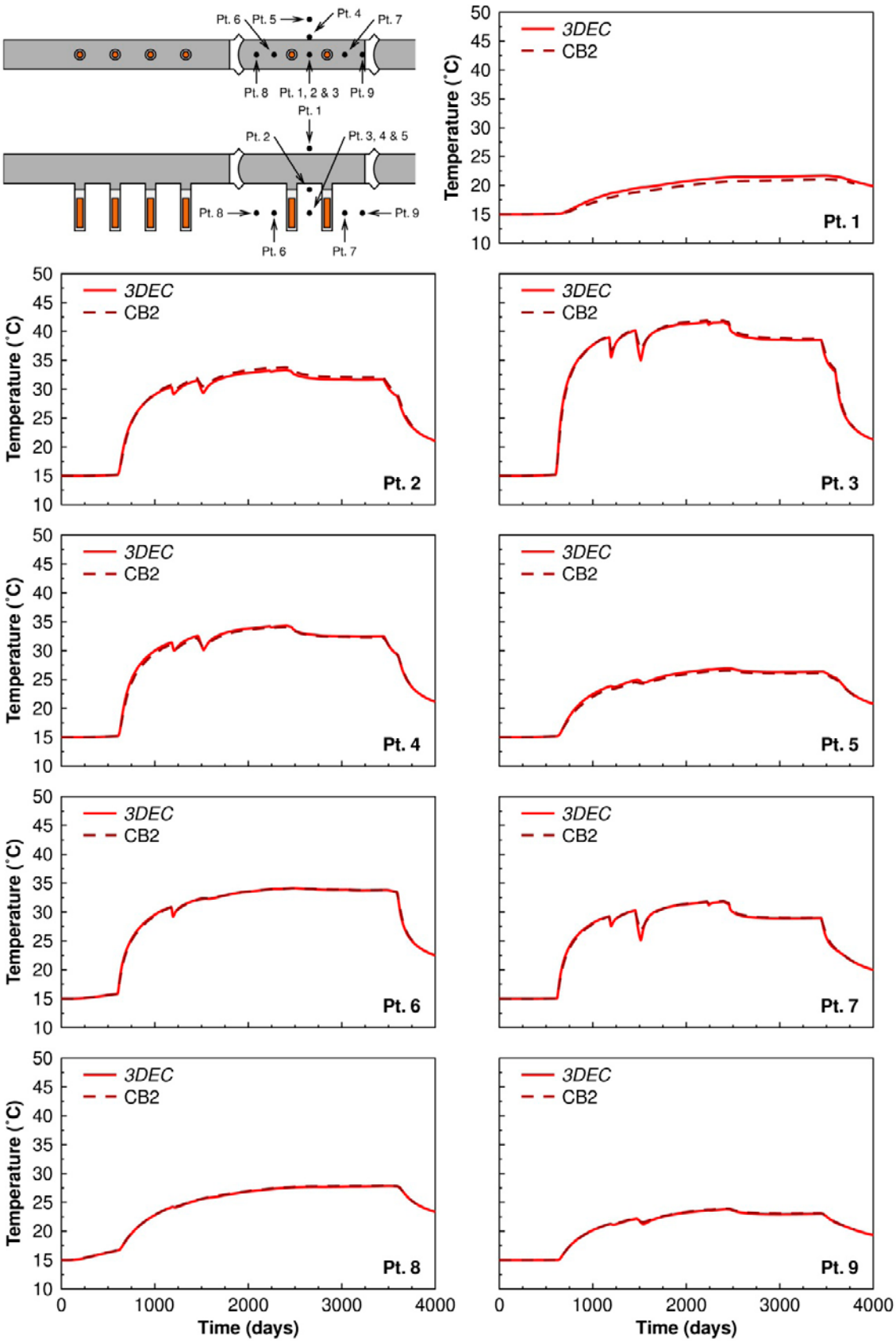

Figure 5-4. *Comparison between 3DEC and Code_Bright (CB2).*

5.3 Thermo-mechanical analyses

5.3.1 Input data

In the comparison with 3DEC, the thermal Code_Bright model CB 2 (cf. Table 4-1) is used. Values for the mechanical and thermo-mechanical properties of the rock are taken to be those of intact rock in the APSE (Staub et al. 2004).

As the canister, buffer, backfill and plugs are explicitly modelled in Code_Bright, the code requires mechanical and thermo-mechanical properties for these materials as well. However, it is not the purpose of the modelling to describe the mechanical interaction between different system components. The water uptake, the swelling of the bentonite buffer and the associated evolution of the pressure on the walls of the deposition holes are complicated processes with different effects in the two holes considered in the following (cf. Goudarzi 2014). The effects will also vary along the height and around the perimeter of the holes. Ignoring the uncertain effects of the buffer and the backfill mechanical behaviour will give only local errors in the rock thermal stress calculations: close to the walls of the deposition holes the tangential stresses will be overestimated by, at maximum about 10 MPa (maximum total pressure that is reported for either of the two holes (cf. Goudarzi 2014)). On average, the overestimate is significantly smaller. To avoid any not-verified stabilization of the deposition hole walls, the value of Young's modulus for the canister, buffer, backfill and plugs is set at 1 kPa (the other thermo-mechanical and mechanical properties are the same as for the rock). A summary of the material properties is given in Table 5-1.

5.3.2 Description of thermo-mechanical Code_Bright model

The thermo-mechanical Code_Bright model is identical to the corresponding thermal model (see Chapter 4) with regards to model geometry, heat load and thermal boundary conditions. Mechanical boundary conditions are given as roller boundaries.

In the thermo-mechanical calculations, the coarse mesh density at the interface between the bentonite buffer and the rock used in the thermal models was found to influence stress magnitudes not only around the deposition holes but also at positions a few metres away from the holes (Figure 5-5). Increasing the mesh density at the interface between the rock and the bentonite was found to reduce the error (Figure 5-5, right). The temperatures were not influenced by the change in mesh density. Ideally, the model should have an even higher mesh density than the one given in Figure 5-5 (right) in order to produce correct results. However, there is a limitation to the number of nodes and elements than can be included in a model. Therefore, in order to ensure that any discrepancy in results between Code_Bright and 3DEC is due to the inadequate mesh density in Code_Bright and not because of variations in temperature, a second Code_Bright model with thermal properties of the backfill set at that of the rock mass is also analyzed. As seen in Figure 5-6, the differences in stresses and temperatures are very small.

Table 5-1. Input data to thermo-mechanical Code_Bright and 3DEC models. Note that material properties given for the canister, buffer, backfill and plugs are only used in the Code_Bright model.

Material property	Unit	Rock	Canister	Buffer	Backfill	Plugs
Thermal conductivity	W/(m·K)	2.72	390	1.0	1.5	2.72
Heat capacity	MJ/(m^3·K)	2.13	3.48	2.22	1.95	2.13
Solid phase density	kg/m^3	2,770	8,930	2,780	2,500	2,770
Young's modulus	GPa	76	$1\cdot10^{-6}$	$1\cdot10^{-6}$	$1\cdot10^{-6}$	$1\cdot10^{-6}$
Poisson's ratio	–	0.25	0.25	0.25	0.25	0.25
Coefficient of linear thermal expansion	K^{-1}	$7\cdot10^{-6}$	$7\cdot10^{-6}$	$7\cdot10^{-6}$	$7\cdot10^{-6}$	$7\cdot10^{-6}$

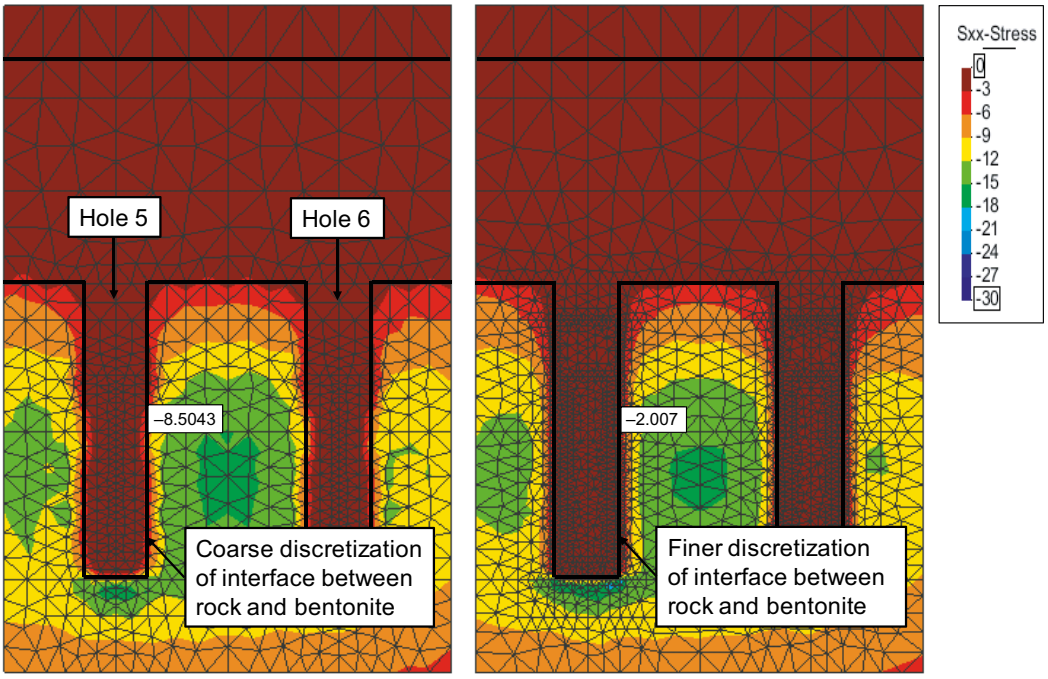

Figure 5-5. *Contours of thermally induced stress along the tunnel (Sxx) after approximately 2,042 days for a coarse discretization of the interface between the rock and bentonite buffer (left) and a corresponding finer discretization (right).*

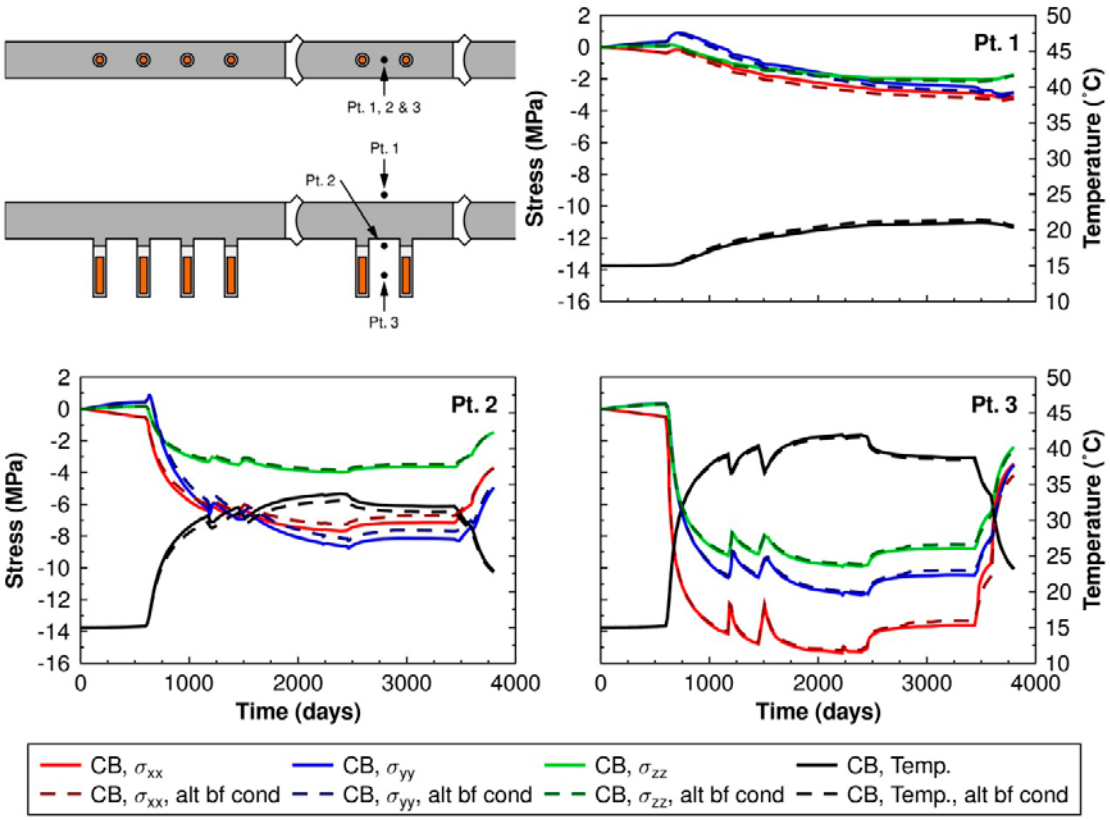

Figure 5-6. *Comparison of thermally induced stress additions and temperature for base-case values for the thermal conductivity of the backfill and using the same thermal properties as for the rock (alt bf cond).*

5.3.3 Description of thermo-mechanical 3DEC model

The rock mass in 3DEC is assumed to be linear elastic and consists of a 400 m × 400 m × 400 m block of rock in which the tunnel, plug slots and all six deposition holes are explicitly represented (see Figure 5-7). Since the focus is on the outer section, the tunnel and deposition holes in these parts of the model have a finer discretization (see the figure inset). Roller boundaries are applied on the top and bottom boundaries whereas all vertical boundaries are locked in all directions.

5.3.4 Results

Figure 5-8 shows a comparison of the thermally induced stress additions in the directions parallel to the tunnel (σ_{xx}), perpendicular to the tunnel (σ_{yy}) and in the vertical direction (σ_{zz}) at nine different points in the outer section. These points are located at approximately the same positions as in the thermal analysis (cf. Figure 5-4).

There is generally a good agreement between the two codes. The difference in results for the σ_{xx} stress-component at Pts. 3, 6 and 7 is due to the inadequate mesh density at the buffer/rock interface in Code_Bright. A similar error, but not as pronounced, can be seen in the σ_{yy} stress component at Pt. 4.

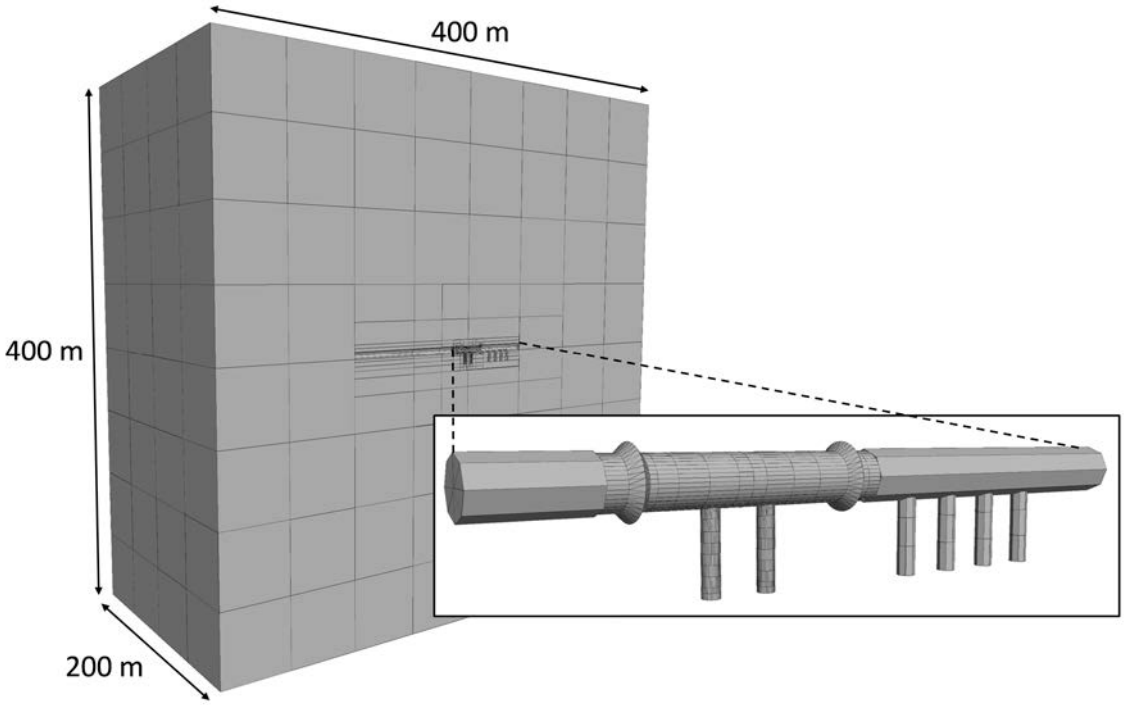

Figure 5-7. *3DEC model geometry. Note that parts of the model are hidden in order to expose the tunnel and deposition holes.*

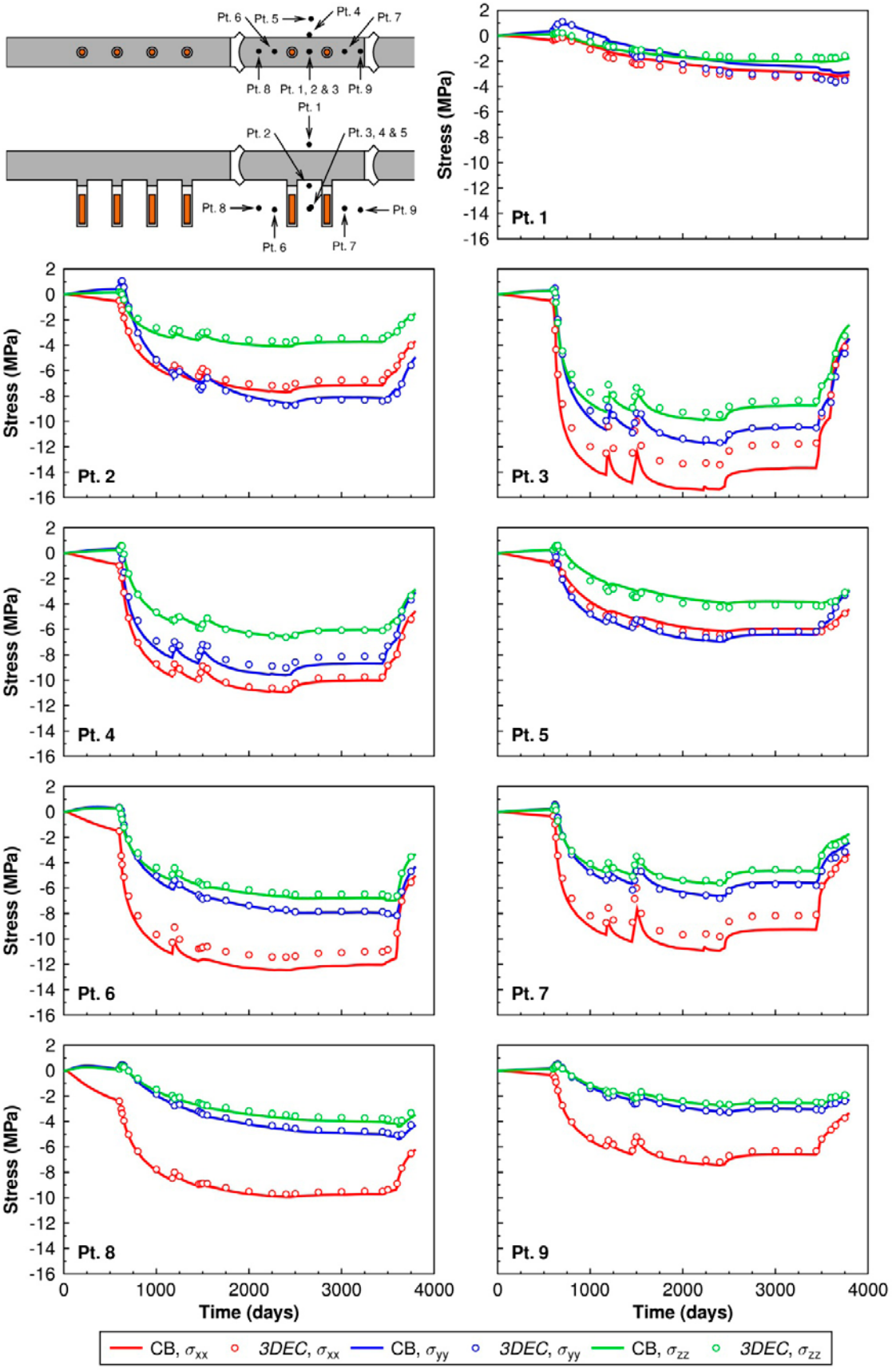

Figure 5-8. *Comparison of thermally induced stress additions as calculated by 3DEC and Code_Bright.*

5.4 Summary

The following is concluded:

- There is good agreement between the rock temperatures as calculated by the two codes. For the present study, in which rock thermal stress is the main issue, this is sufficient. Temperatures in the interior of the deposition holes, which depend also on buffer and heater heat transport properties and on details of the heater geometry, are not considered here. To determine these temperatures it would not be possible to use the analytically-based 3DEC thermal logic.
- Ignoring the difference between backfill and rock thermal conductivity, as in the 3DEC models, appears to have little influence on rock temperatures (Figure 5-3 and Figure 5-4) and, consequently, also little influence on rock thermal stresses (Figure 5-6).
- There is good agreement between Code_Bright and 3DEC rock thermal stresses at all points except those at heater mid-height close to the deposition holes (pts 3, 6 and 7 in Figure 5-8). At these points the Code_Bright results are influenced by the coarse discretization of the interior of the deposition holes, which appears to cause an overestimation of the radial stress at the buffer-rock interface (Figure 5-5). The Code_Bright rock stress overestimate at these points is at maximum about 15%. The 3DEC results, which agree with the Code_Bright results at all other points, are judged to be correct and consistent with the input assumption at all points.

The 3DEC thermal logic and the compound line source representation of the heat output from the Prototype Repository heaters is concluded to be adequate for the purpose of the modelling undertaken in this report, i.e., there is no need to device a scheme to import temperatures and temperature increments into the 3DEC models from the Code_Bright models or from any other calculations.

6 Evaluation of rock mechanical measurements

Since the start of the experiment, the mechanical response of the rock mass to changes in temperature and loading conditions has been extensively monitored by use of stress meters, deformation meters, strain gauges and instruments recording acoustic emissions. In this Chapter, an attempt is made at reproducing these measurements using linear elastic thermo-mechanical 3DEC models with heat load as described in Chapter 5.

6.1 Description of instruments

6.1.1 Locations

Instruments were installed in twelve vertical boreholes (see Figure 6-1) located 0.3 m from the hole periphery of Holes 5 and 6 to monitor changes in stress, deformation and strain in the rock during the drilling of the holes and during the subsequent heated phase (Bono and Röshoff 2003). Additional deformation meters and strain gauges specifically aimed at monitoring the response of the rock during the heated phase were installed in horizontal boreholes drilled from inside the deposition holes (see Figure 6-2) and in vertical boreholes drilled from the bottom of the holes, respectively (Bono and Röshoff 2003). The number and types of instruments are presented in Table 6-1. Detailed information regarding the position of each instrument is provided in Appendix B.

6.1.2 Sources of measurement data

The sources of measurement data used in the comparison with modelling results are presented in Table 6-2. Results from measurements during the excavation phase have been evaluated using raw data from each instrument. With the exception of measurements by the biaxial stress meters, which have been re-evaluated from raw data using different properties for the rock mass (see below), the results from the heated phase are as presented in the sensors data reports.

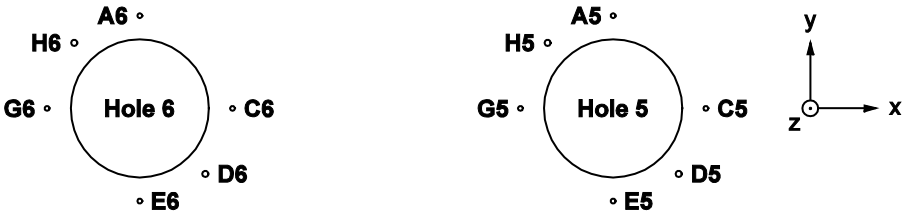

Figure 6-1. *Plan view of primary (vertical) boreholes (after Bono and Röshoff 2003). Each primary borehole is located 0.3 m from the deposition hole perimeter.*

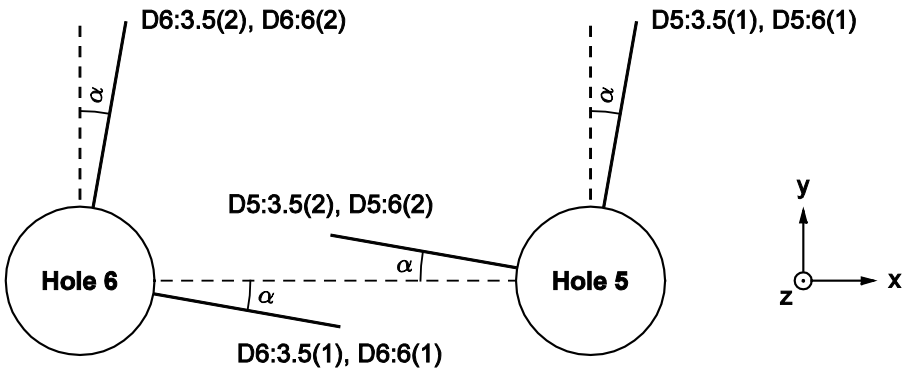

Figure 6-2. *Plan view of complementary (horizontal) boreholes (after Bono and Röshoff 2003). The angle α is equal to 10°. The depths of the boreholes below the tunnel floor are 2.46 m for D5:3.5(1) and D5:3.5(2), 4.96 m for D5:6(1) and D5:6(2), 2.73 m for D6:3.5(1) and D6:3.5(2), and 5.23 m for D6:6(1) and D6:6(2).*

Table 6-1. Overview of sensors in bore holes.

Type	Number	Quantity	Period
Biaxial stress meter, Model 4350	8	Change in horizontal stresses	Excavation Heated phase
Soft inclusion stress cells, Model 4360-1	8	Change in borehole diameter	Excavation Heated phase
Deformation meter, Model 4430	17	Vertical deformation	Excavation Heated phase
Strain gage*, Model 4200	7	Vertical strain	Excavation Heated phase
Deformation meter, Model 4430	32	Horizontal deformation	Heated phase
Strain gage*, Model 4200	8	Vertical strain below dep hole	Heated phase

*Measurements by the strain gauges are judged to be too uncertain for a comparison with modelling results to be meaningful (cf. Chapter 9).

Table 6-2. Sources of measurement data.

Measurement		Source	Comment
AE data	Excavation	Sicada_13_046_02	As in Pettitt et al. (1999)
Biaxial stress meters	Excavation	Sicada_12_104_1	Evaluated from raw data
	Heated phase	Sicada_11_074	Evaluated from raw data
Soft inclusion stress cells	Excavation	Sicada_12_104_1	Evaluated from raw data
	Heated phase	Sicada_11_066	As in sensors data reports*
Deformation meters (vertical)	Excavation	Sicada_12_104_1	Evaluated from raw data
	Heated phase	Sicada_11_066	As in sensors data reports*
Deformation meters (horizontal)	Heated phase	Sicada_11_066	As in sensors data reports*

*Goudarzi and Johannesson (2003, 2004a, b, c, d, e, 2005a, b, 2006a, b, 2007a, b, 2008, 2009a, b, c, 2010), Goudarzi (2012, 2014).

6.1.3 Evaluation of measurement data

Biaxial stress meters

Each biaxial stress meter contains two sets of three vibrating wires at 60° intervals labelled 1, 2 and 3 and 4, 5 and 6 (Geokon 2010a). The wires are oriented such that wires 1 and 4 have the same orientation (Geokon 2010a) (similarly, wires 2 and 5 are aligned and 3 and 6 are aligned). In the Prototype Repository, the sensors have been oriented such that wires V_{r1} and V_{r4} are tangential to the deposition hole (Bono and Röshoff 2003). The deformation of each vibrating wire (V_{ri}, i = 1, 2 and 3; 4, 5 and 6) is calculated using the formula (Geokon 2010a)

$$V_{ri} = G\left(R_0 - R\right) \tag{6-1}$$

where G is a calibration factor supplied with the sensor and R_0 and R are initial and current readings, respectively. The change in principal stresses perpendicular to the borehole axis is subsequently calculated from the deformations of the vibrating wires (compressive stresses are positive) by the following expressions (Geokon 2010a)

$$\begin{aligned}
\sigma_H &= \frac{1}{2}\left[\frac{1}{3B}\left(\left(2V_{r1(4)} - V_{r2(5)} - V_{r3(6)}\right)^2 + 3\left(V_{r2(5)} - V_{r3(6)}\right)^2\right)^{1/2}\right. \\
&\quad \left. + \frac{1}{3A}\left(V_{r1(4)} + V_{r2(5)} + V_{r3(6)}\right)\right] \\
\sigma_h &= \frac{1}{3A}\left(V_{r1(4)} + V_{r2(5)} + V_{r3(6)}\right) - \sigma_H \\
\theta &= \frac{1}{2}\cos^{-1}\left(\frac{V_{r1(4)} - A\left(\sigma_H + \sigma_h\right)}{B\left(\sigma_H - \sigma_h\right)}\right)
\end{aligned} \tag{6-2}$$

Equivalent expressions for wires 4-6 are obtained by using the subscripts within brackets. The coefficients A and B depend on the geometry and properties of the sensor and on the properties of the surrounding rock mass (Geokon 2010a), see Figure 6-3. In the sensors data reports (Goudarzi 2012), the values E = 69 GPa and ν = 0.25 for the rock mass have been used. In the present analyses, the raw data from the stress monitoring have been re-evaluated using values of the rock Young's modulus corresponding to "rock mass" and "intact rock" (see Figure 6-3 and Table 6-4), respectively.

Soft inclusion stress cells

The change in borehole diameter (u) is calculated using the formula (Geokon 2009)

$$u = G\left(R - R_0\right) \tag{6-3}$$

where G is a calibration factor supplied with the sensor and R and R_0 are current and initial readings, respectively. An increase in reading digits corresponds to a reduction in borehole diameter (Goudarzi 2012).

Deformation meters

Axial deformations along the borehole (d_A) are calculated using the formula (Geokon 2010b)

$$d_A = G\left(R - R_0\right) \tag{6-4}$$

where G is a calibration factor supplied with the sensor and R and R_0 are current and initial readings, respectively. For sensors measuring axial deformations in the boreholes, a thermal correction factor is applied to account for the thermal expansion of the instrument (Bono and Röshoff 2003, Geokon 2010b). The deformations have been temperature corrected by addition of the expression (Geokon 2010b)

$$\left(R \cdot M + B\right)\left(T - T_0\right) + 17.3 \cdot 10^{-6} L\left(T - T_0\right) \tag{6-5}$$

where R is the current reading, M = 0.000295 is a multiplier, B = 1.724 is a constant, L is the difference in length between the deformation meter and the length of the transducer (267 mm), T and T_0 are current and initial temperatures, respectively. However, for deformations resulting mainly from thermal expansion of the rock, the correction seems to invalidate the measurement, see Figure 6-4. In some cases, the measured thermally induced rock deformations are much greater than corresponding deformations of unconfined rock.

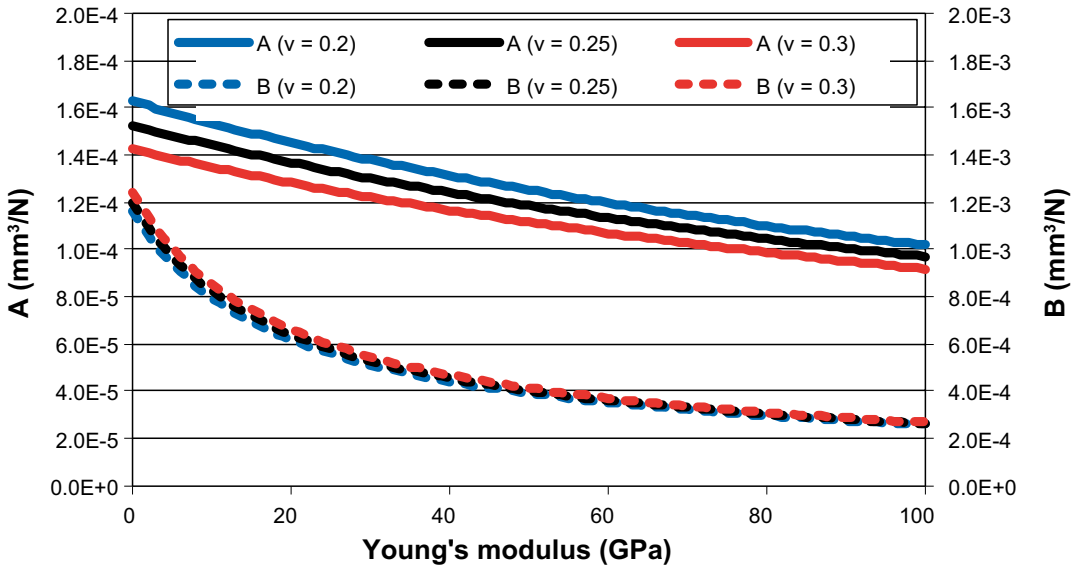

Figure 6-3. *Variation in coefficients A and B with rock properties (Geokon 2010a).*

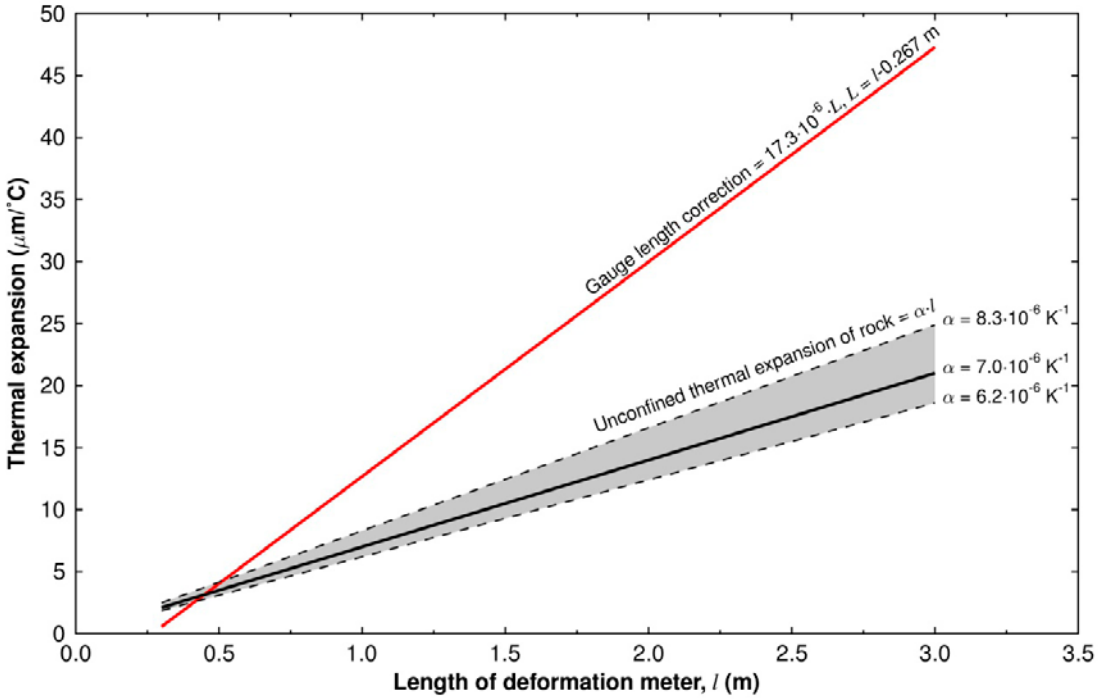

Figure 6-4. *Comparison between gauge length correction (Geokon 2010b) and unconfined thermal expansion of rock.*

6.2 Description of 3DEC models

6.2.1 Geometry

Two model sizes are considered: a small model for the excavation phase and a large model for the subsequent heated phase.

Excavation

The rock mass in 3DEC is assumed to be linear elastic and consists of a 66 m × 60 m × 60 m block of rock in which the tunnel and the two holes in the outer section are explicitly modelled (see Figure 6-5). Both deposition holes are 8.4 m deep.

Heated phase

For the heated phase, the model size is increased. Here, the rock mass consists of a 400 m × 400 m × 400 m block of rock in which the tunnel, plug slots and all six deposition holes are explicitly represented (see Figure 6-6). Since the focus is on the outer section, the tunnel and deposition holes in these parts of the model have a finer discretization (see the figure inset).

Before installation of the buffer and canister system, concrete was cast at the bottom of the holes to create a horizontal base (e.g. Pusch and Andersson 2004). In the present modelling work, it is assumed that the top of the concrete casting corresponds to the bottom of the hole, i.e. no distinction is made between the material properties of the concrete and that of the surrounding rock. The depth of all deposition holes is schematically set at 8.1 m.

6.2.2 Input data

Thermal properties

Thermal input parameters to the 3DEC models are listed in Table 6-3. These are the same as in the Code_Bright model CB 2 (cf. Table 4-1).

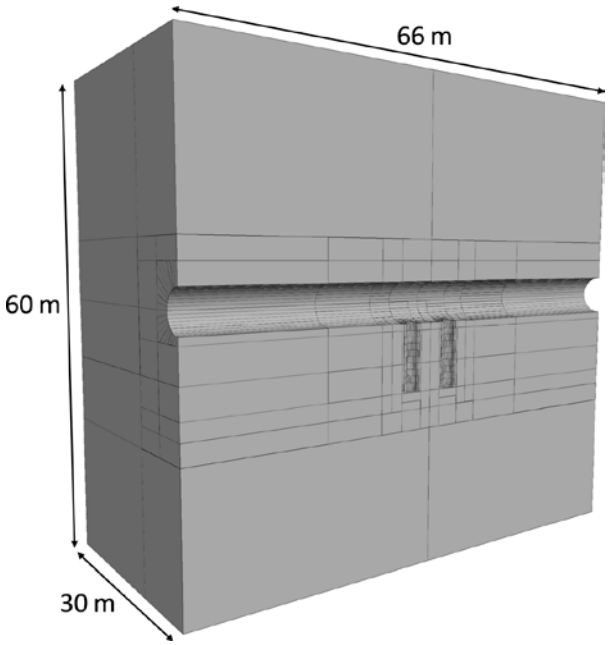

Figure 6-5. *Model geometry for the excavation phase. Note that parts of the model are hidden to expose the tunnel and deposition holes.*

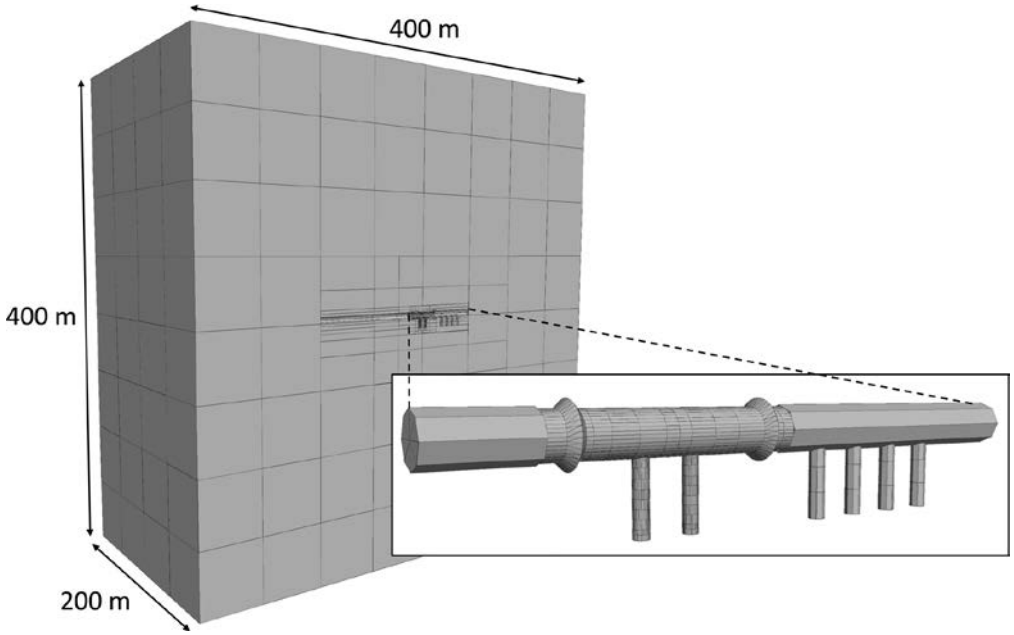

Figure 6-6. *Model geometry for the heated phase. Note that parts of the model are hidden to expose the tunnel and deposition holes.*

Table 6-3. Thermal properties of the rock, cf. Table 4-1.

Parameter	Unit	Value
Thermal conductivity	W/(m·K)	2.72
Thermal diffusivity	m^2/s	$1.275 \cdot 10^{-6}$
Density	kg/m^3	2,770

Mechanical and thermo-mechanical properties

Input mechanical and thermo-mechanical parameter values to the 3DEC models are listed in Table 6-4. The mechanical and thermo-mechanical rock property parameters are those established by Staub et al. (2004) for the rock in the APSE.

In situ stresses

The Prototype Repository stress model described in Section 3.3 has been used to set up modelling cases 1-5 presented in Table 6-5. The best estimate of the state of stress for the APSE test site (Andersson 2007) (case 8) is also considered. The six stress models are also shown graphically in Figure 6-7.

Table 6-4. Mechanical and thermo-mechanical properties of the rock.

Parameter	Unit	Value
Young's modulus	GPa	
Intact rock		76
Rock mass		55
Poisson's ratio	–	0.25
Coefficient of thermal expansion	K^{-1}	$7 \cdot 10^{-6}$

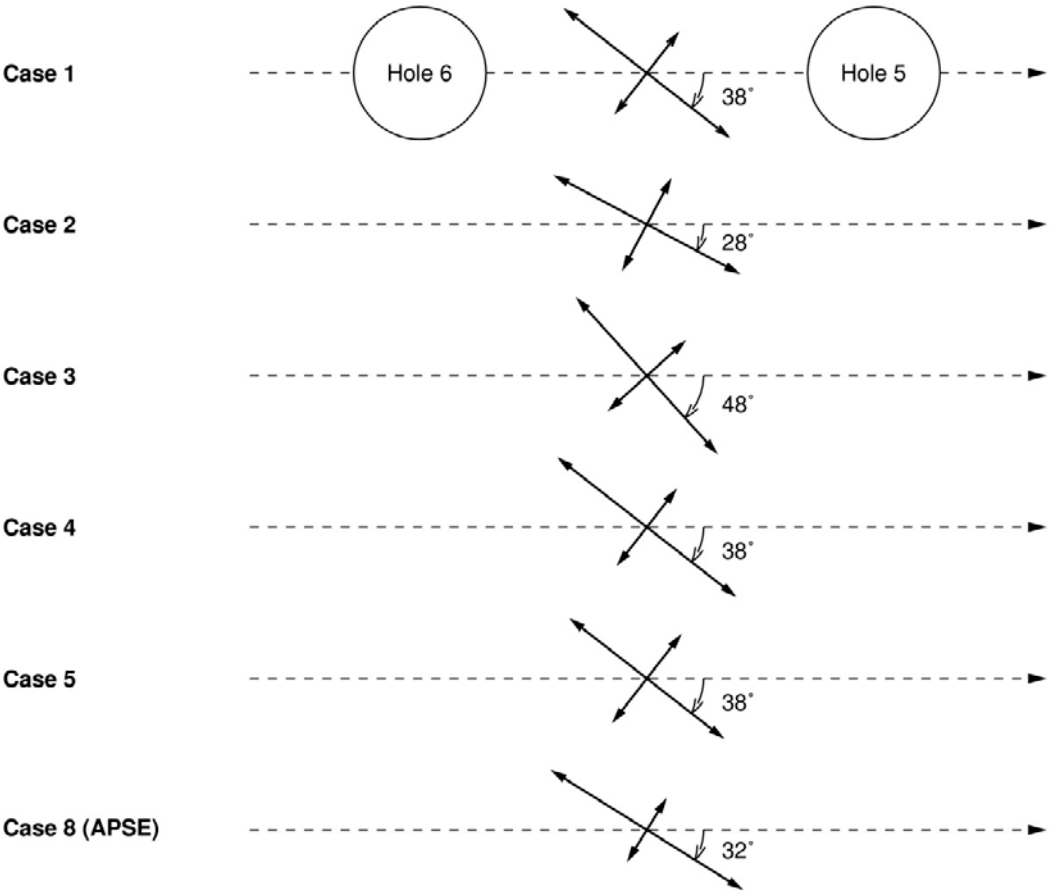

Figure 6-7. *Orientations of the horizontal in situ stresses for the six different stress models described in Table 6-5.*

Table 6-5. Tested *in situ* stress models. Magnitudes in MPa; Trend in degrees in the Swedish national RT90 system; Plunge in degrees from horizontal.

Model name	σ1			σ2			σ3		
	Magnitude	Trend	Plunge	Magnitude	Trend	Plunge	Magnitude	Trend	Plunge
Case 1	28	304	0	14	214	0	12.8	–	90
Case 2	28	294	0	14	204	0	12.8	–	90
Case 3	28	314	0	14	224	0	12.8	–	90
Case 4	30	304	0	13	214	0	12.8	–	90
Case 5	26	304	0	15	214	0	12.8	–	90
Case 8	30	298	0	15	–	90	10	208	0

1. Base case. Mean stress magnitudes and orientations in the stress model given in Section 3.3.
2. Base case stress magnitudes. Minimum deviation of σ_H from tunnel axis.
3. Base case stress magnitudes. Maximum deviation of σ_H from tunnel axis.
4. Maximum horizontal stress anisotropy. Base case orientations.
5. Minimum horizontal stress anisotropy. Base case orientations.
8. Best estimate of state of stress for the APSE test site (Andersson 2007).

6.2.3 Modelling sequence

The response of the rock mass to changes in mechanical conditions during the excavation is assessed in three steps:

1. A primary equilibrium is established,
2. the tunnel is excavated and,
3. the deposition holes are excavated.

All results are evaluated using the change in stress from step 2 to step 3. For the heated phase, only the thermal impact is determined, i.e., the *in situ* stresses are set at zero. The concrete plugs create a small local disturbance around the plug slots (cf. Appendix C). This is judged to have an insignificant influence on the stresses and deformations around the deposition holes. The plugs are therefore not included in the models.

6.2.4 Evaluation of measurements using 3DEC

None of the 3DEC models includes the small boreholes in which the instruments were installed. Instead, changes in stress and deformations are estimated from stresses and deformations of the intact rock at the measurement positions.

Biaxial stress meters

The change in principal horizontal stresses is evaluated as (e.g. Brady and Brown 1993)

$$\sigma_H = \frac{1}{2}\left(\sigma_{xx} + \sigma_{yy}\right) + \left[\frac{1}{4}\left(\sigma_{xx} - \sigma_{yy}\right)^2 + \sigma_{xy}{}^2\right]^{1/2}$$

$$\sigma_h = \frac{1}{2}\left(\sigma_{xx} + \sigma_{yy}\right) - \left[\frac{1}{4}\left(\sigma_{xx} - \sigma_{yy}\right)^2 + \sigma_{xy}{}^2\right]^{1/2} \qquad (6\text{-}6)$$

$$\theta = \tan^{-1}\left(\frac{\sigma_H - \sigma_{xx}}{\sigma_{xy}}\right)$$

where σ_{xx} is the stress component along the tunnel axis, σ_{yy} is the stress component across the tunnel and σ_{xy} is the shear stress component.

Soft inclusion stress cells

The change in borehole diameter (u) is evaluated for both plane stress conditions and for plain strain conditions. For plane stress conditions the expression for the borehole diameter is given by (Geokon 2009)

$$u = \left[(\sigma_H + \sigma_h) + 2(\sigma_H - \sigma_h)\cos(2\theta) \right] d / E \tag{6-7a}$$

and for plane strain conditions by (Brady and Brown 1993)

$$u = \left[(\sigma_H + \sigma_h) + (\sigma_H - \sigma_h)(3 - 4\nu)\cos(2\theta) \right] d / 4G \tag{6-7b}$$

where σ_H and σ_h are the (change in) horizontal principal stresses, d = 76 mm is the borehole diameter, E is Young's modulus of the rock, G is the shear modulus of the rock and θ is the anti-clockwise angle measured from the major horizontal principal stress.

Deformation meters

The axial deformation along the borehole (d_A) is estimated by

$$d_A = u_1 - u_2 \tag{6-8}$$

where u_1 and u_2 are the calculated deformations at the positions corresponding to each end point of the deformation meter.

6.3 Acoustic emission data: Evaluation of *in situ* stress orientations

According to the Kirsch solution (e.g. Brady and Brown 1993) for the stress distribution around an infinitely long circular excavation subjected to a biaxial stress-field, the maximum tangential stress on the boundary is located at an azimuth perpendicular to the major principal stress and has a magnitude of $3 \cdot \sigma_1 - \sigma_3$. There is typically a clear correlation between acoustic emission (AE) events and regions of high compressive stress (e.g. Pettitt et al. 2000).

Figure 6-8 shows the cumulative number of AE events around Holes 5 and 6 during the excavation of these holes. As seen in the plan view of the AE events (inset to Figure 6-9), there are significantly fewer events around Hole 5 than around Hole 6. Therefore, only the events located around the latter hole are used to assess the orientations of the *in situ* stresses. However, for completeness, the orientations of the AE events around both holes are assessed. The reasons for the qualitatively and quantitatively different patterns of AE events are unknown, but could possibly be related to stress redistribution effects due to shear displacements along fractures intersecting the deposition holes (cf. Chapter 8 and Appendix G).

Figure 6-9 shows the orientations of all AE events located within 0.5 m of the hole perimeter of Hole 5 (left) and Hole 6 (right). Note that AE events seemingly located inside the deposition holes (see inset to Figure 6-9) are in fact located below the bottom of the hole during the drilling and have been removed in all analyses presented here. The AE events around Hole 6 have maxima at around 40°N and at 220°N, which corresponds to the upper limit of the uncertainty span of the orientations of the horizontal *in situ* stresses.

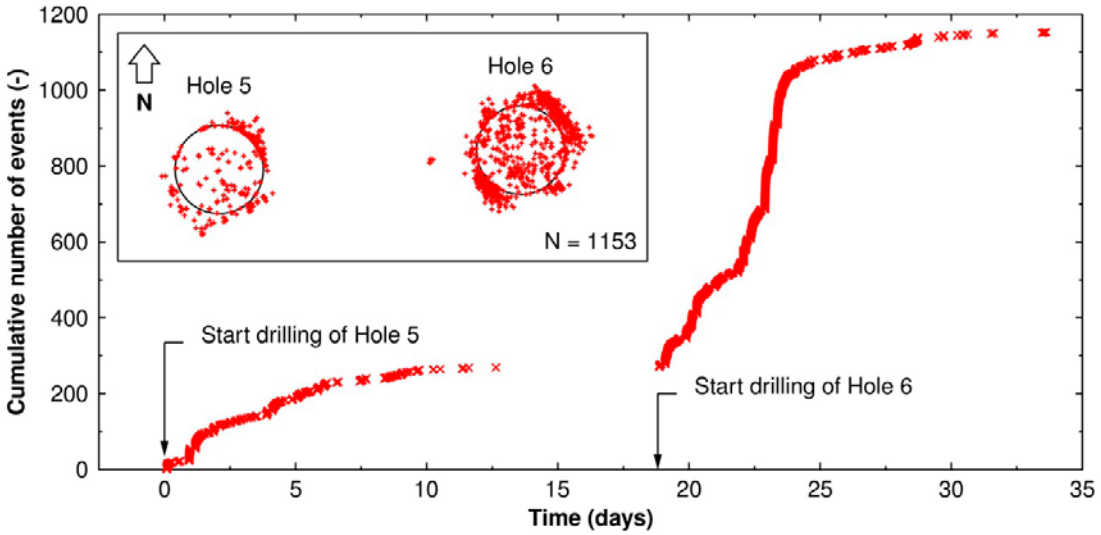

Figure 6-8. *Cumulative number of acoustic emission (AE) events during the excavation of Holes 5 and 6. Inset shows a plan view of all AE events around these holes after the excavation. North is given in the coordinate system RT90.*

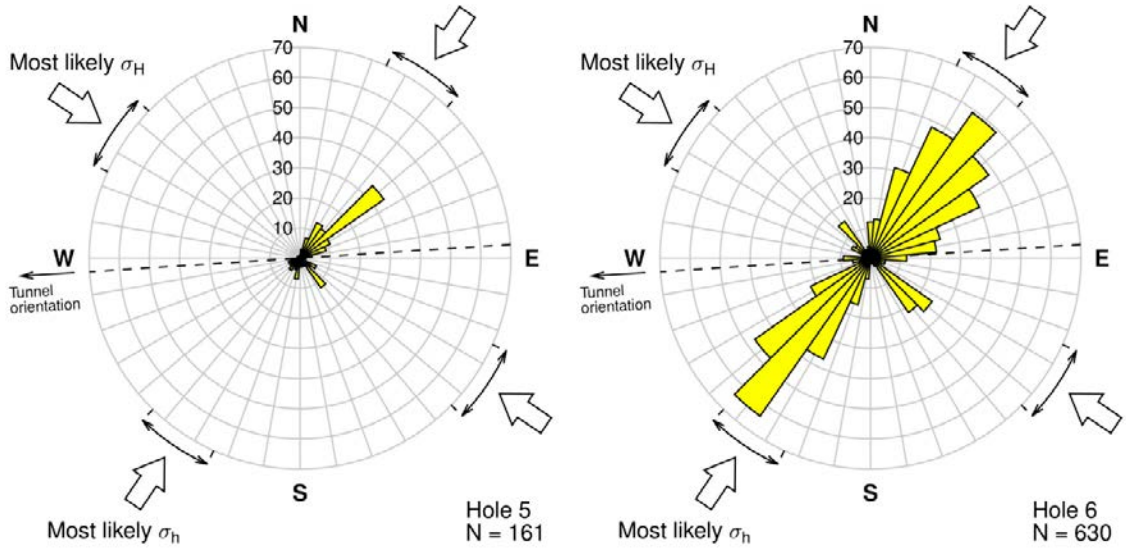

Figure 6-9. *Orientations of AE events around Hole 5 (left) and around Hole 6 (right) together with the orientations of the major and minor horizontal stress components. North is given in the coordinate system RT90.*

Figure 6-10 to Figure 6-15 show all AE events located within 0.5 m of the perimeter of Hole 6 superimposed on the numerically calculated major principal stress as function of depth and azimuth and in two horizontal planes after excavation. For all six *in situ* stress models, the majority of the AE events coincide with the calculated tangential stress maxima.

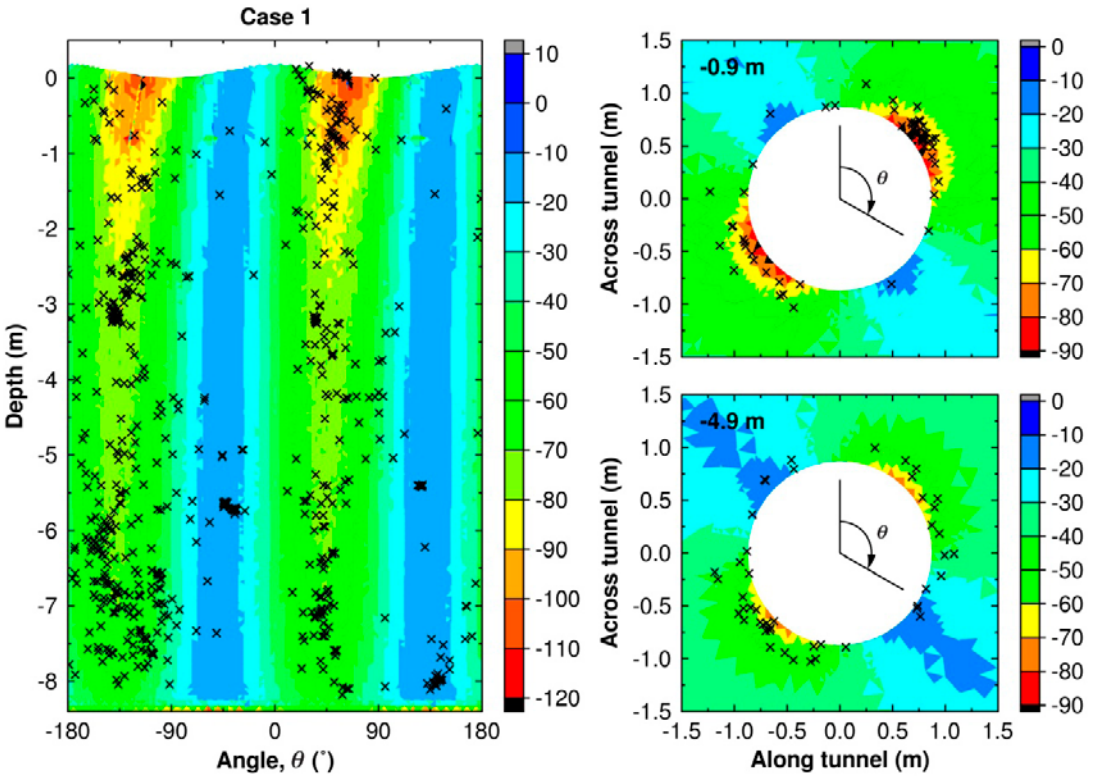

Figure 6-10. *Left: Contour plot of the major principal stress as function of azimuth and depth around Hole 6 (contours in MPa) for the stress model Case 1 (cf. Table 6-5). Right: Corresponding contour plots in two horizontal planes at 0.9 m depth (top) and 4.9 m depth (bottom).*

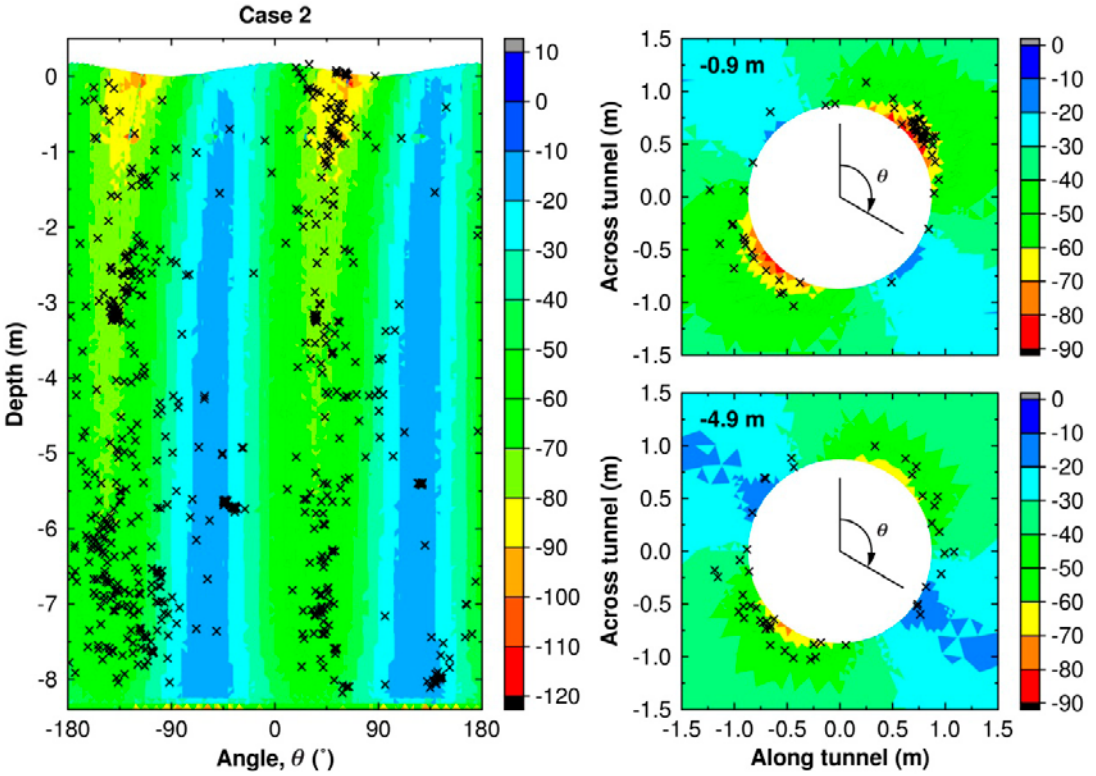

Figure 6-11. *Left: Contour plot of the major principal stress as function of azimuth and depth around Hole 6 (contours in MPa) for the stress model Case 2 (cf. Table 6-5). Right: Corresponding contour plots in two horizontal planes at 0.9 m depth (top) and 4.9 m depth (bottom).*

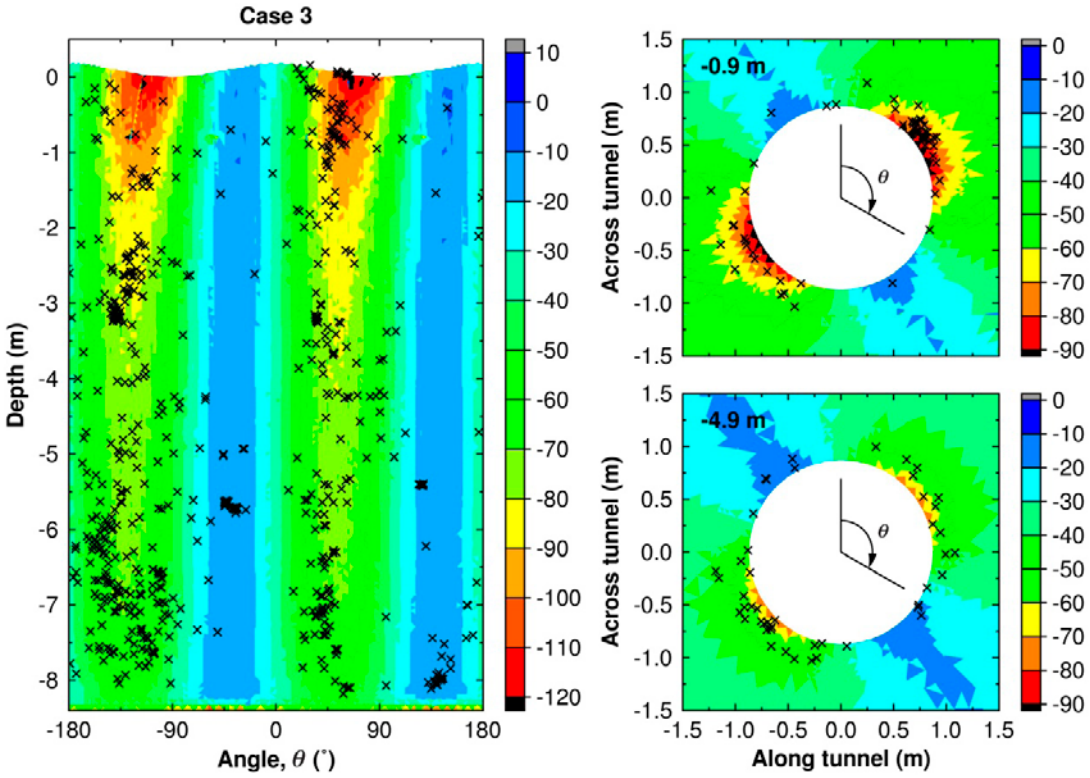

Figure 6-12. *Left: Contour plot of the major principal stress as function of azimuth and depth around Hole 6 (contours in MPa) for the stress model Case 3 (cf. Table 6-5). Right: Corresponding contour plots in two horizontal planes at 0.9 m depth (top) and 4.9 m depth (bottom).*

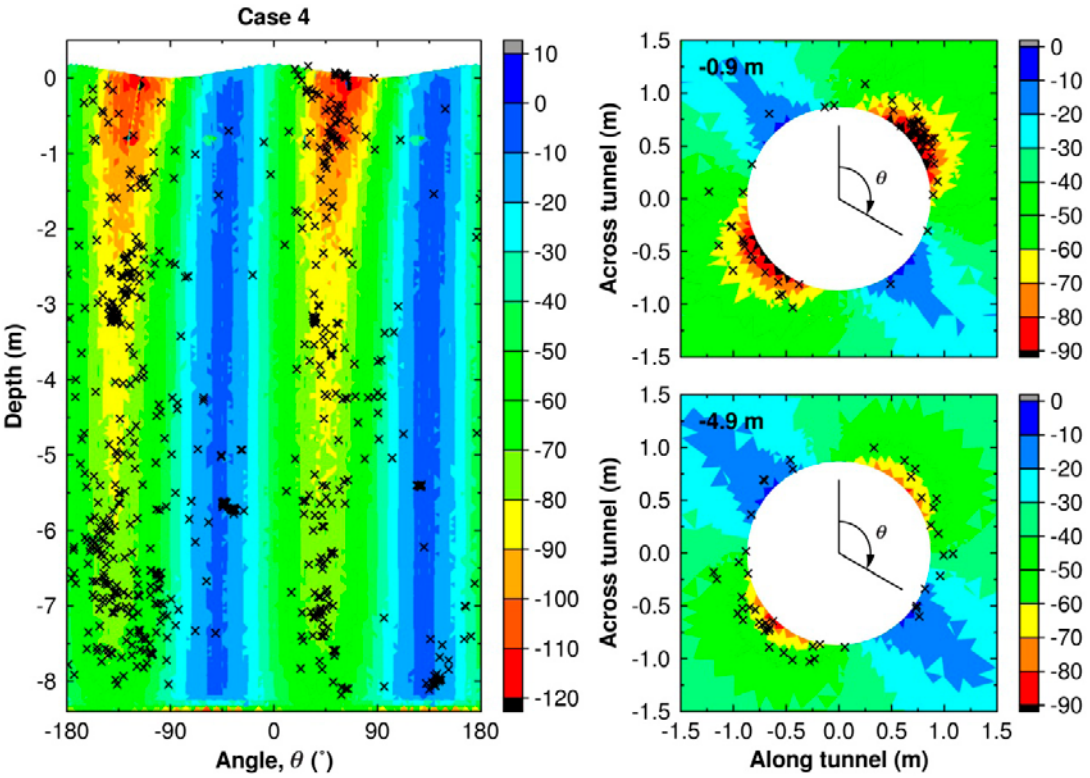

Figure 6-13. *Left: Contour plot of the major principal stress as function of azimuth and depth around Hole 6 (contours in MPa) for the stress model Case 4 (cf. Table 6-5). Right: Corresponding contour plots in two horizontal planes at 0.9 m depth (top) and 4.9 m depth (bottom).*

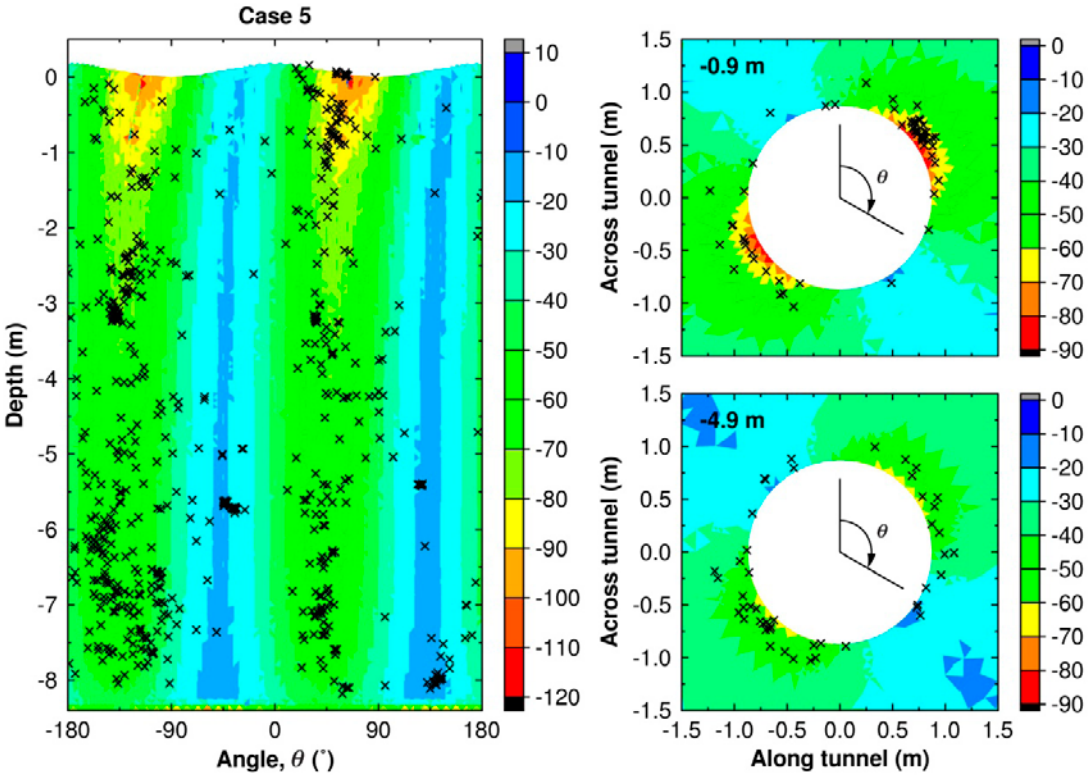

Figure 6-14. *Left: Contour plot of the major principal stress as function of azimuth and depth around Hole 6 (contours in MPa) for the stress model Case 5 (cf. Table 6-5). Right: Corresponding contour plots in two horizontal planes at 0.9 m depth (top) and 4.9 m depth (bottom).*

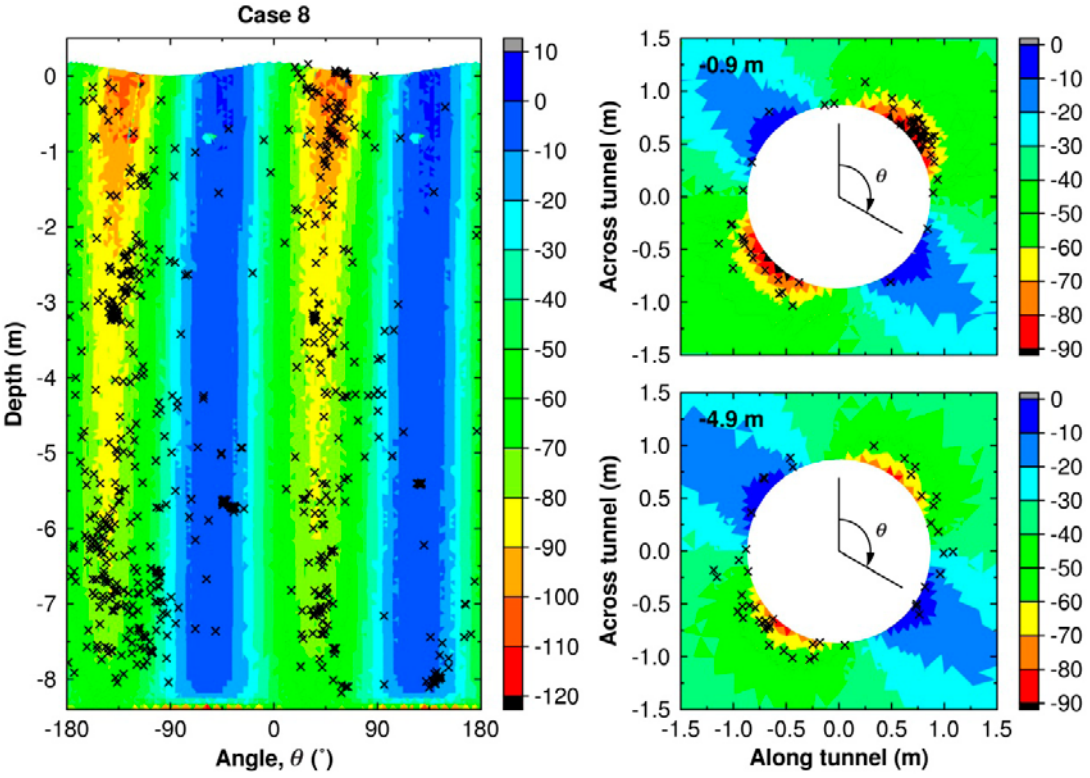

Figure 6-15. *Left: Contour plot of the major principal stress as function of azimuth and depth around Hole 6 (contours in MPa) for the stress model Case 8 (cf. Table 6-5). Right: Corresponding contour plots in two horizontal planes at 0.9 m depth (top) and 4.9 m depth (bottom).*

6.4 Biaxial stress meters

6.4.1 Locations of sensors

Stress monitoring was conducted in four vertical boreholes around each deposition hole with one instrument in each hole. Stressmeters are labelled according to borehole (Bono and Röshoff 2003), e.g. A5:Bi is the biaxial stressmeter located in borehole A5. Figure 6-16 shows the locations of the instruments.

6.4.2 Excavation

Figure 6-17 and Figure 6-18 show the change in horizontal principal stresses around Hole 5 and around Hole 6, respectively, as the two holes were excavated. The final state of stress after excavation is evaluated as the mean stress from day 50 to the end of the measurement period. As seen in the two figures, the drilling of one deposition hole does not affect the state of stress in the neighbouring deposition hole. Thus, the state of stress at equivalent positions around both holes should be the same if the rock can be approximated to be a linear elastic isotropic continuum. Therefore, measurements from stressmeters A5:Bi, E5:Bi, A6:Bi and E6:Bi are presented together in the same graph (see Figure 6-19, left) as functions of depth. Corresponding results from C5:Bi, G5:Bi, C6:Bi and G6:Bi are presented together in Figure 6-19 (right). All numerically obtained results are evaluated around Hole 5. The measured orientations of the major principal stress are presented in Figure 6-20. Two, or possibly three, measurements (A5:Bi, E6:Bi and G5:Bi) deviate from the rest in both magnitude and orientation. This could, possibly, be due to a combination of elastic and plastic shear displacements along intersecting fractures or that the instruments are located within inclusions of rock with different mechanical properties.

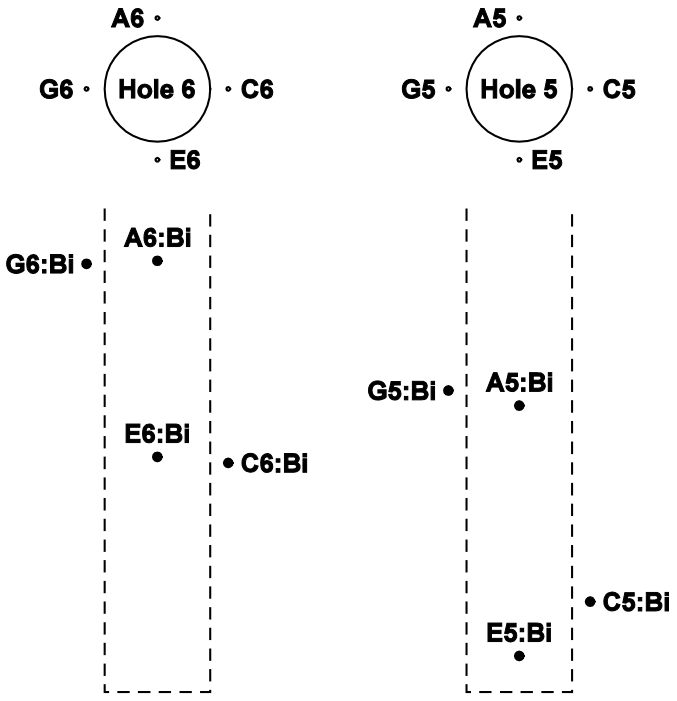

Figure 6-16. *Locations of biaxial stressmeters.*

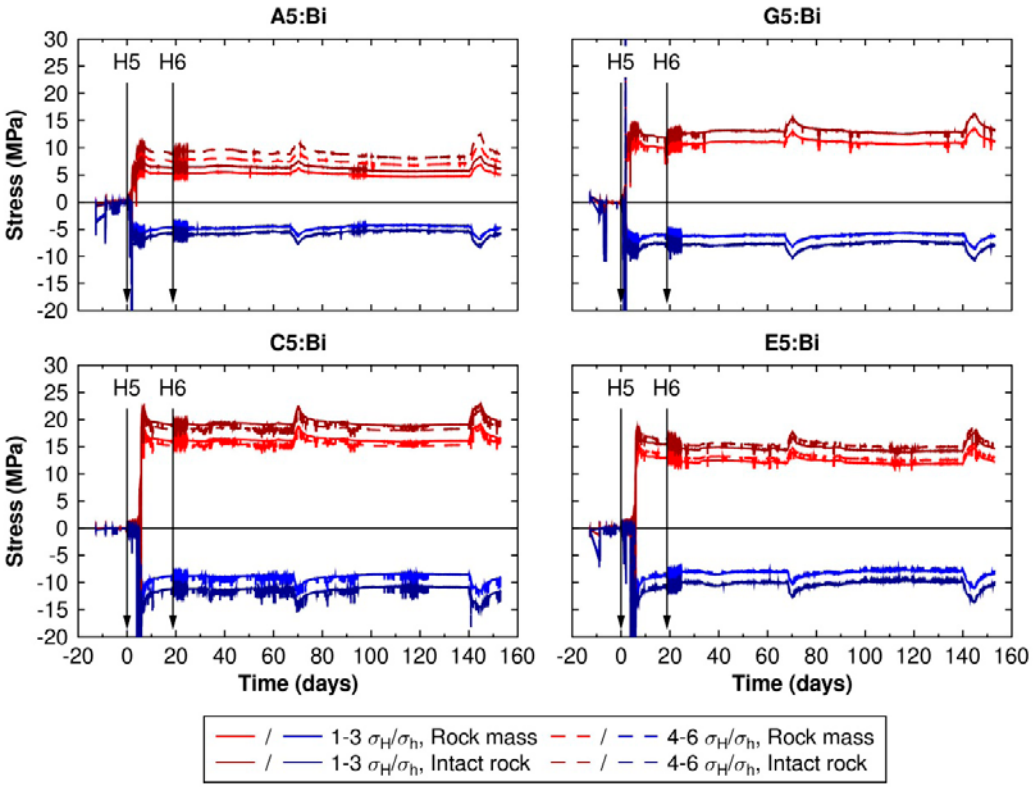

Figure 6-17. *Monitored changes in stress around Hole 5. Each measurement is evaluated for both "rock mass" and "intact rock" properties, cf. Table 6-4. The start of the drilling of each deposition hole is marked with an arrow.*

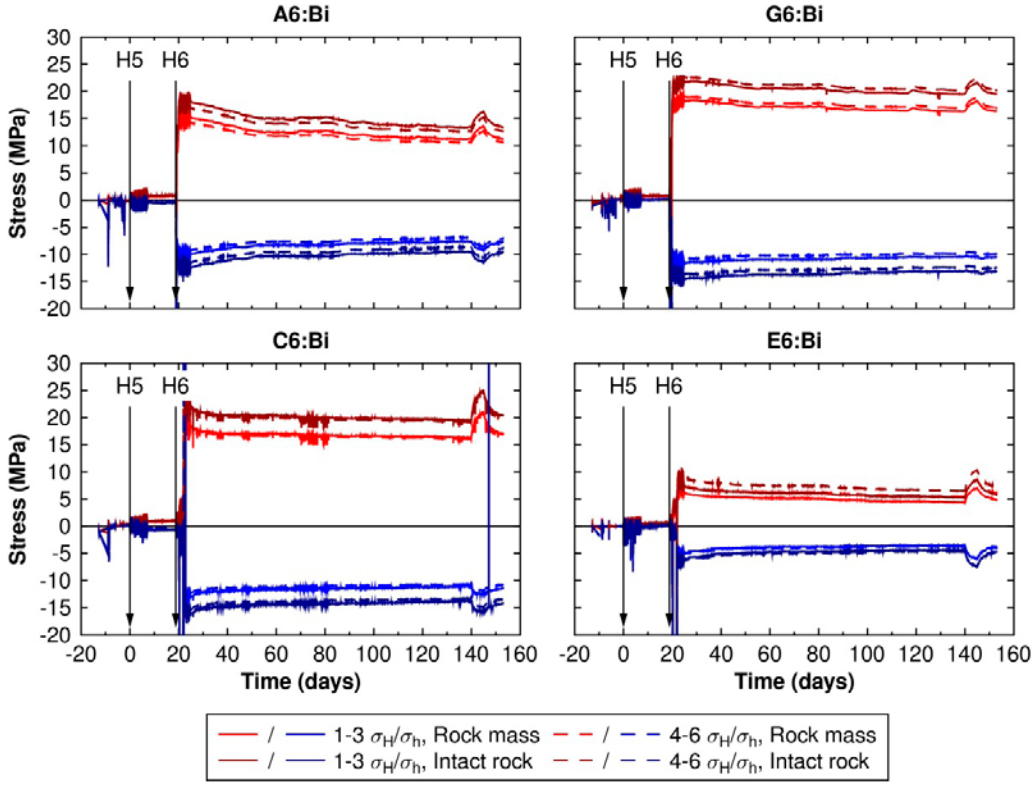

Figure 6-18. *Monitored changes in stress around Hole 6. Each measurement is evaluated for both "rock mass" and "intact rock" properties, cf. Table 6-4. The start of the drilling of each deposition hole is marked with an arrow.*

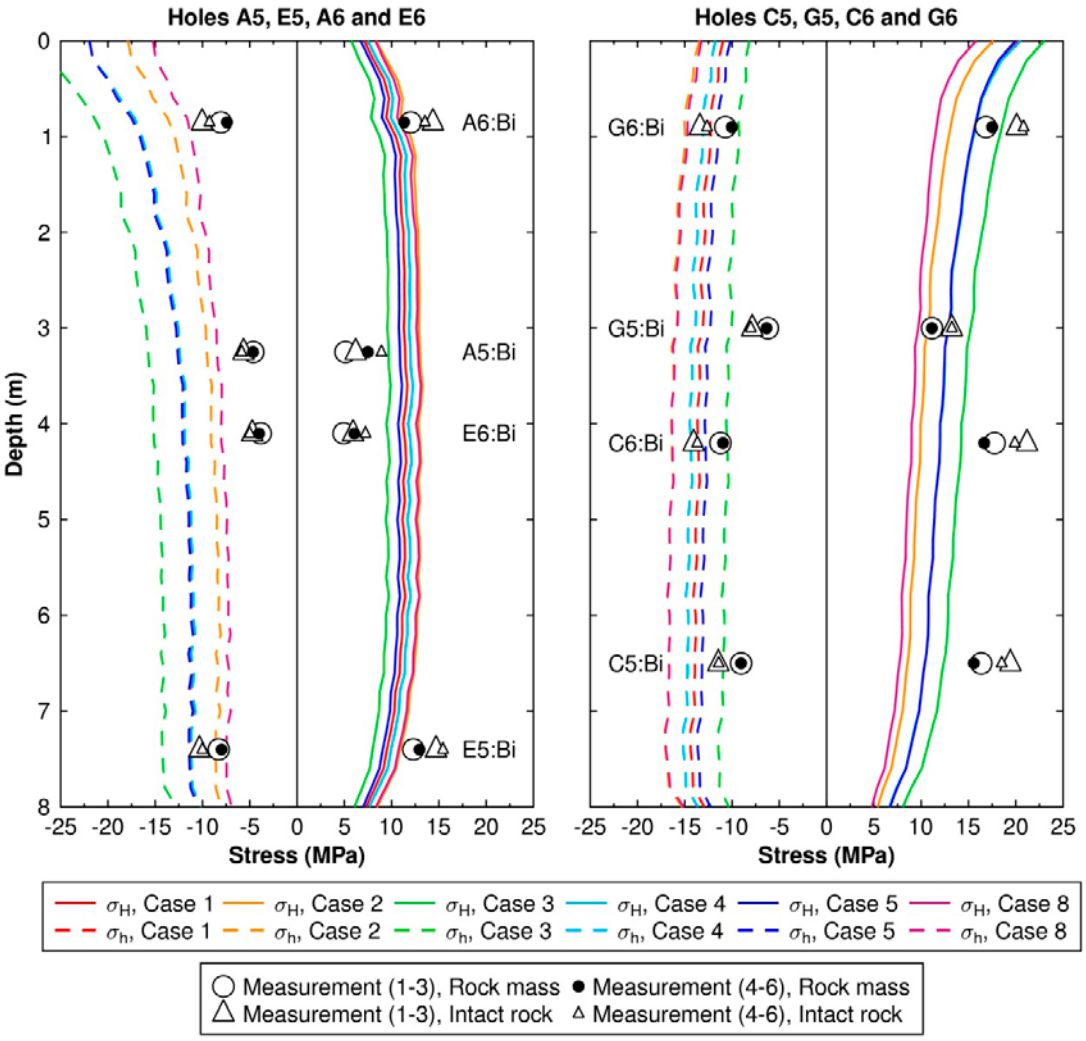

Figure 6-19. *Comparison between measurements (plot symbols) and numerically obtained stresses around Hole 5 (lines).*

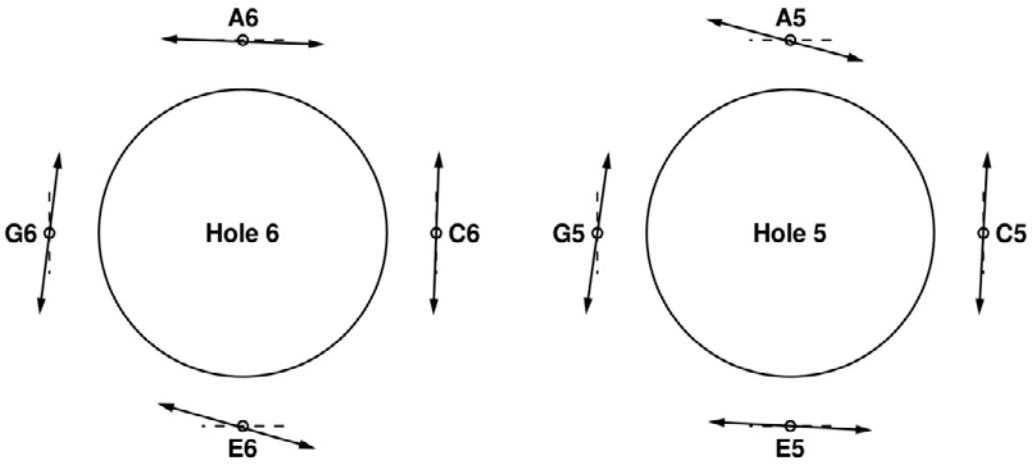

Figure 6-20. *Measured orientations of σ_H.*

6.4.3 Heated phase

Figure 6-21 to Figure 6-28 show stress monitoring conducted during the heated phase. There is significant scattering of data at the beginning of the measurement series and many of the sensors started malfunctioning when the power to all canisters was switched off in December 2004 (day 1,172). Therefore, the results are only presented until day 1,500.

As seen in the figures, the change in σ_H can be reasonably well predicted in magnitude by the models with a somewhat better fit of models to measurement using rock properties corresponding to "intact rock", cf. Table 6-4. However, the measurements show consistently a reduction in the minor horizontal stress something that is not seen in the linear elastic models. The corresponding measured orientations during the first 1,200 days of heating vary between the instruments: some measurements are in reasonable agreement with the models whereas others disagree by rather a large amount.

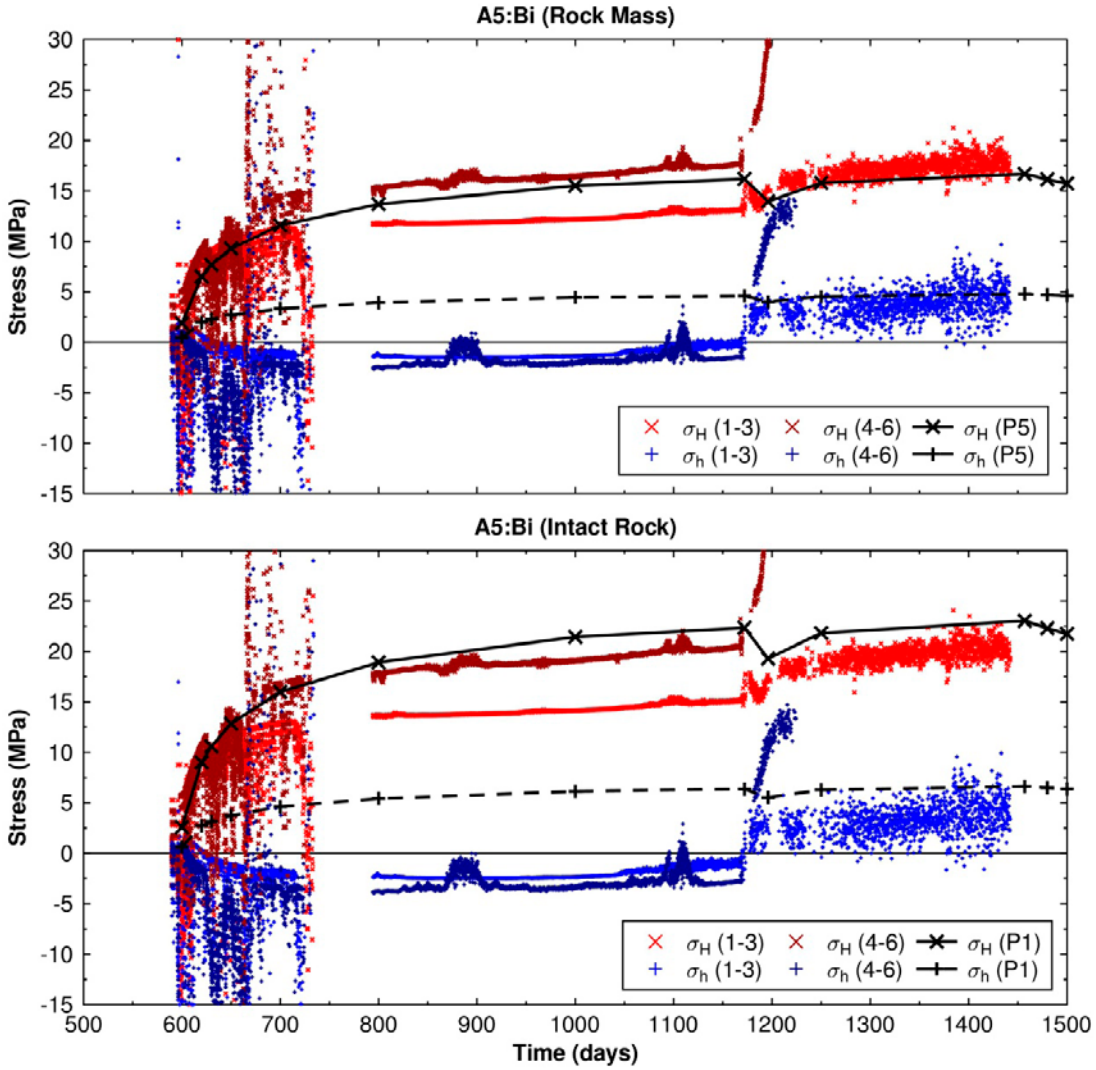

Figure 6-21. *Biaxial stress monitoring by A5:Bi. Comparison between measurements and modelling results for "rock mass" properties (top) and "intact rock" properties (bottom), respectively. '1-3' represents measurements evaluated using vibrating wires 1, 2 and 3. '4-6' represents corresponding measurements evaluated using vibrating wires 4, 5 and 6. P5 and P1 are 3DEC models with "rock mass" and "intact rock" properties, respectively.*

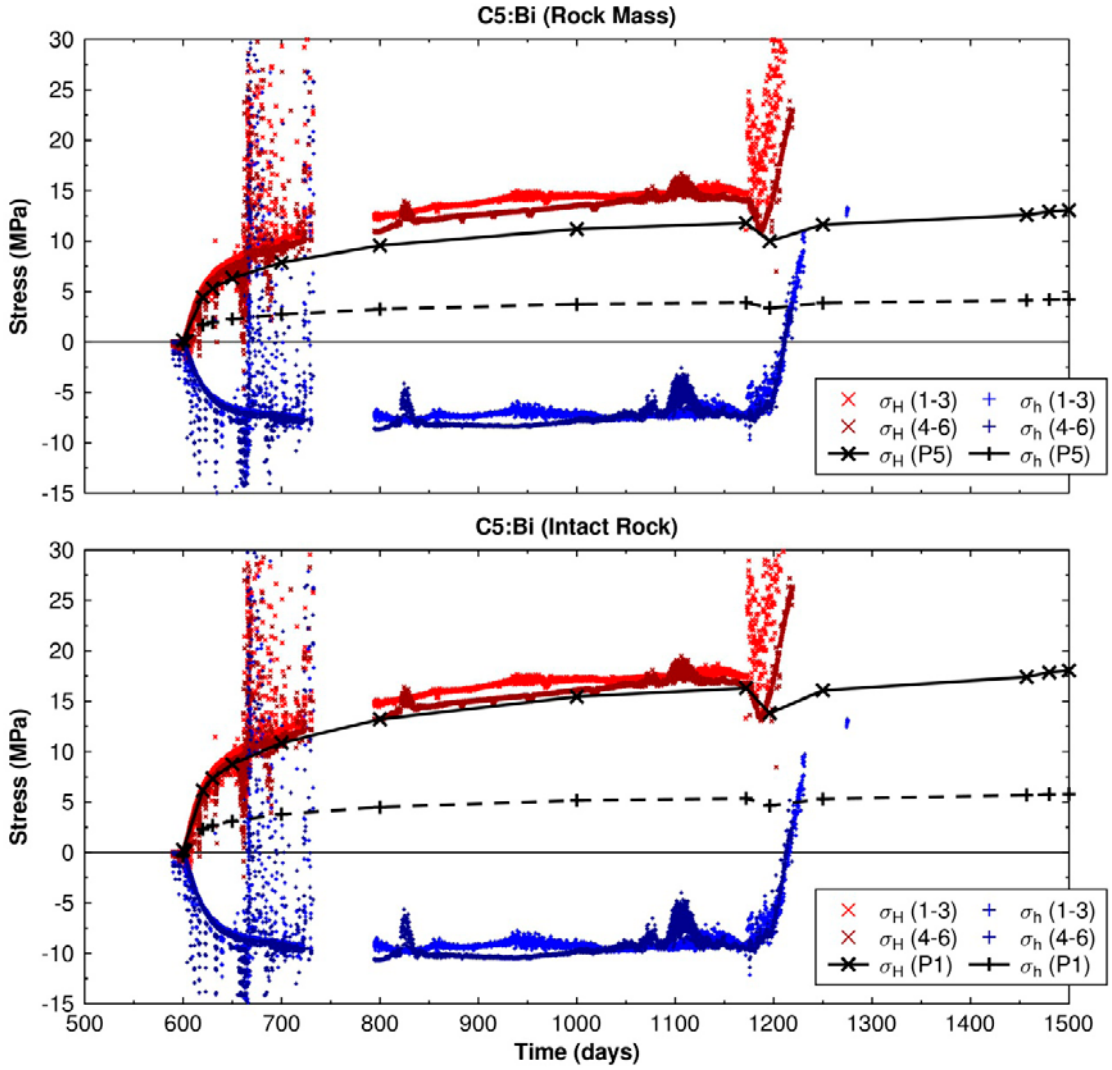

Figure 6-22. *Biaxial stress monitoring by C5:Bi. Comparison between measurements and modelling results for "rock mass" properties (top) and "intact rock" properties (bottom), respectively. '1-3' represents measurements evaluated using vibrating wires 1, 2 and 3. '4-6' represents corresponding measurements evaluated using vibrating wires 4, 5 and 6. P5 and P1 are 3DEC models with "rock mass" and "intact rock" properties, respectively.*

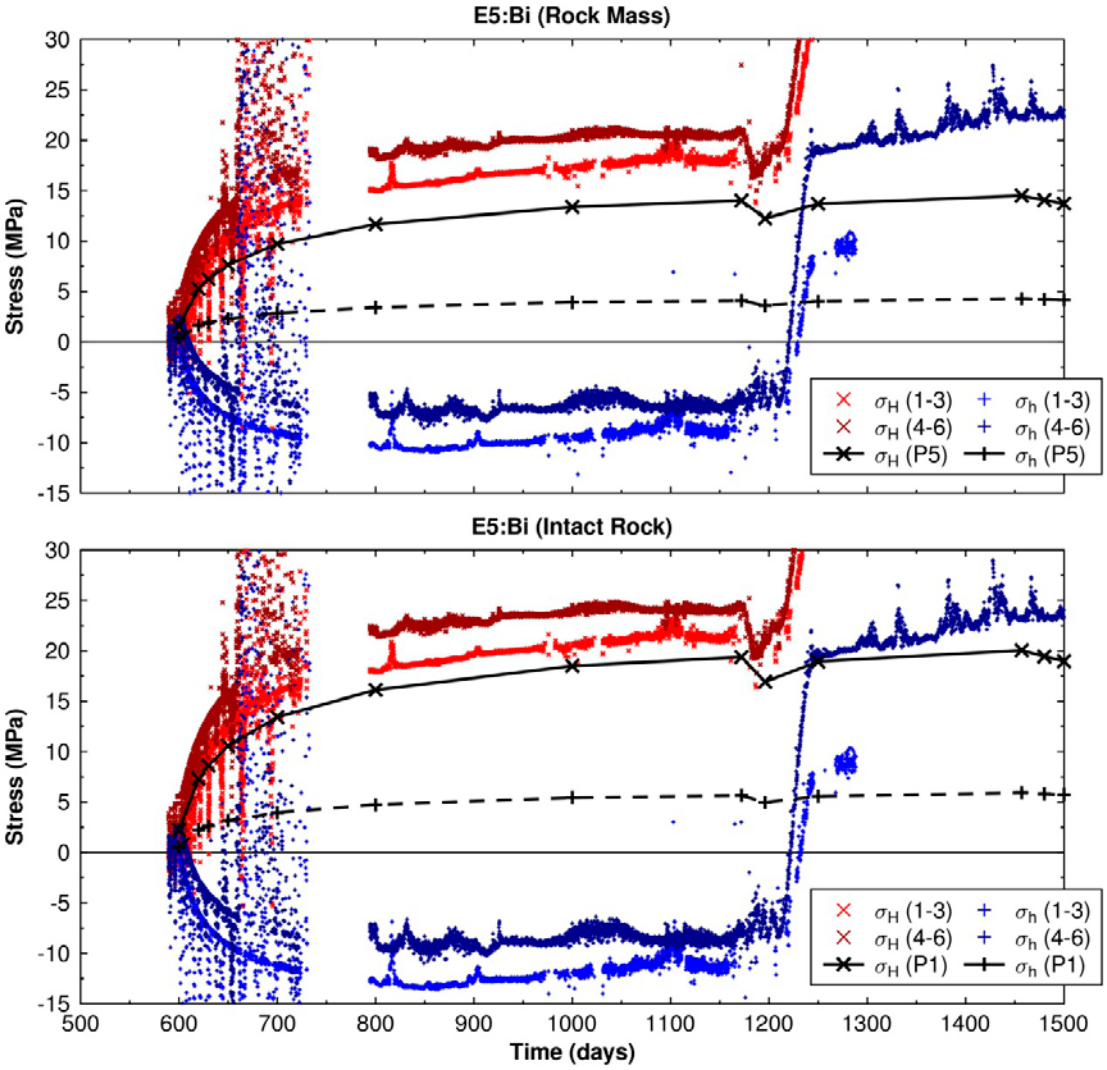

Figure 6-23. *Biaxial stress monitoring by E5:Bi. Comparison between measurements and modelling results for "rock mass" properties (top) and "intact rock" properties (bottom), respectively. '1-3' represents measurements evaluated using vibrating wires 1, 2 and 3. '4-6' represents corresponding measurements evaluated using vibrating wires 4, 5 and 6. P5 and P1 are 3DEC models with "rock mass" and "intact rock" properties, respectively.*

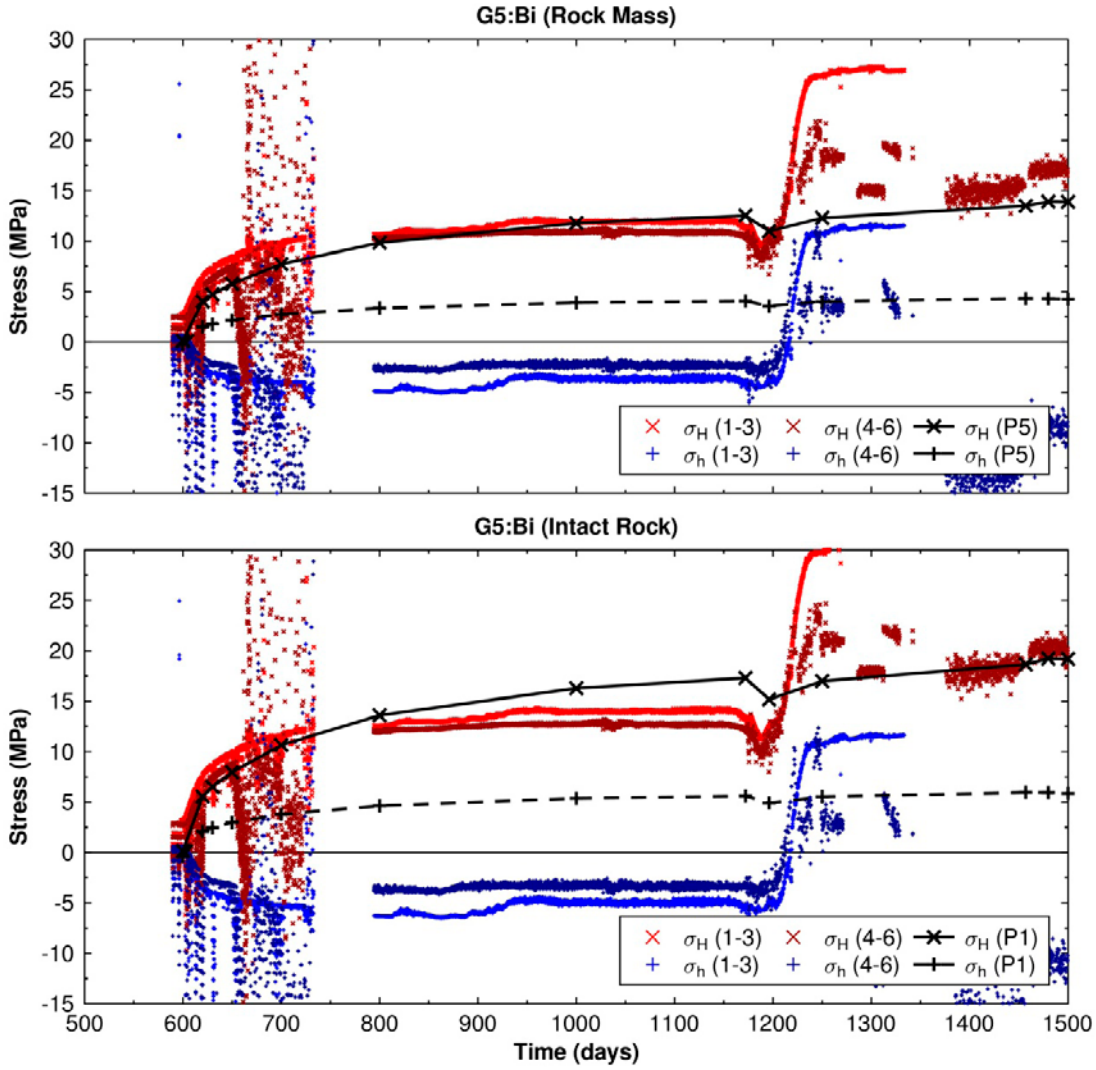

Figure 6-24. *Biaxial stress monitoring by G5:Bi. Comparison between measurements and modelling results for "rock mass" properties (top) and "intact rock" properties (bottom), respectively. '1-3' represents measurements evaluated using vibrating wires 1, 2 and 3. '4-6' represents corresponding measurements evaluated using vibrating wires 4, 5 and 6. P5 and P1 are 3DEC models with "rock mass" and "intact rock" properties, respectively.*

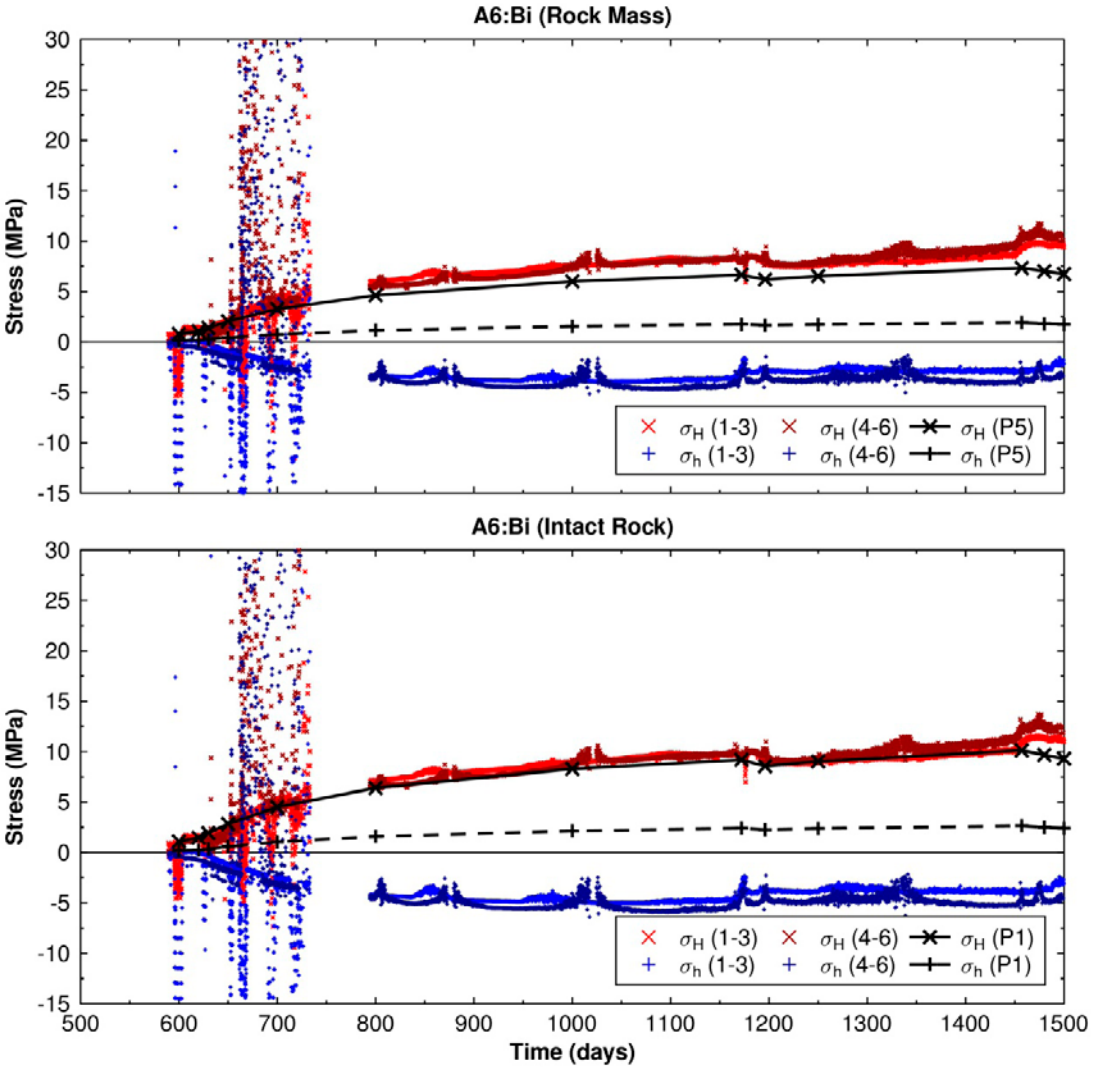

Figure 6-25. *Biaxial stress measurements by A6:Bi. Comparison between measurements and modelling results for "rock mass" properties (top) and "intact rock" properties (bottom), respectively. '1-3' represents measurements evaluated using vibrating wires 1, 2 and 3. '4-6' represents corresponding measurements evaluated using vibrating wires 4, 5 and 6. P5 and P1 are 3DEC models with "rock mass" and "intact rock" properties, respectively.*

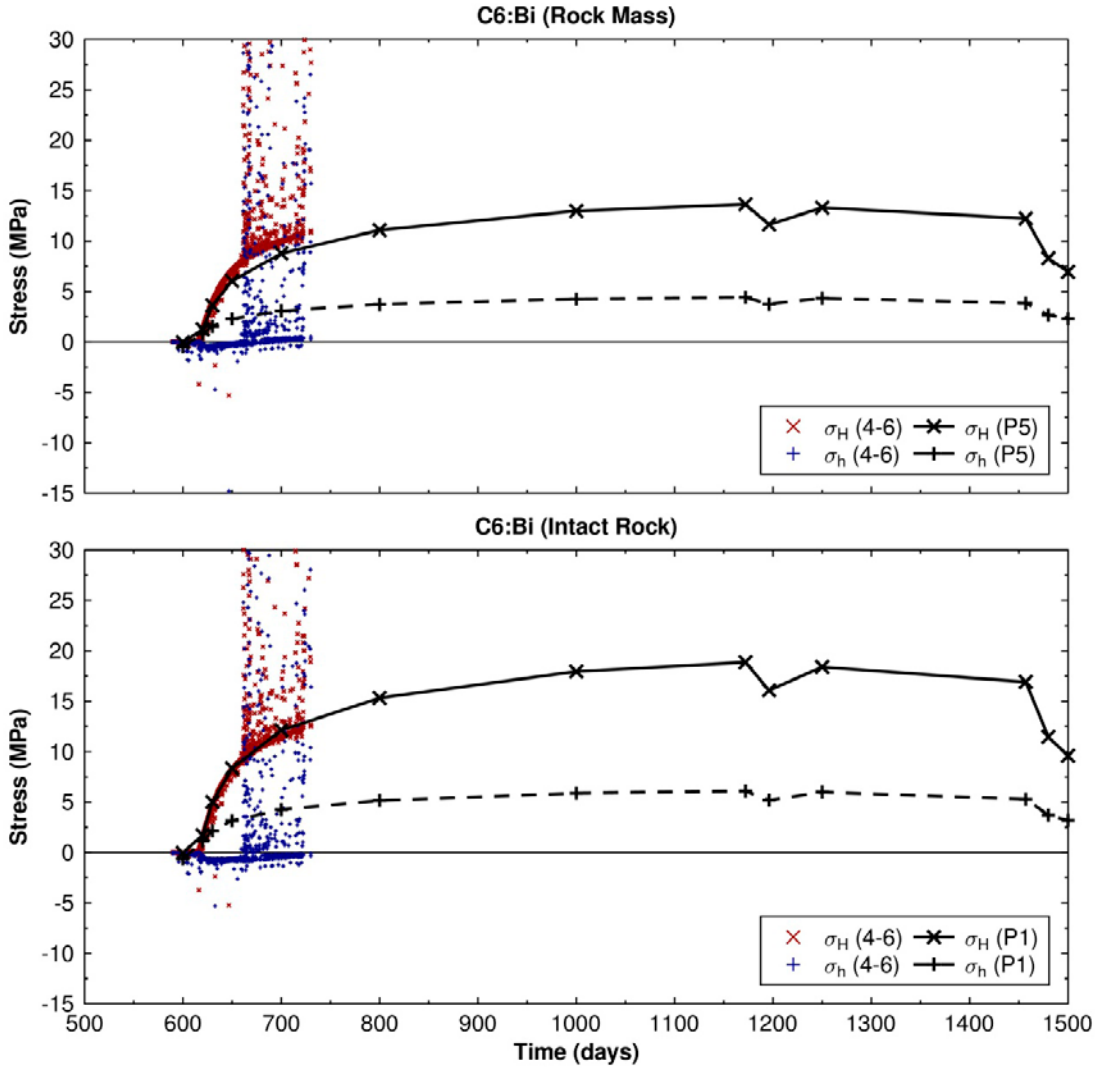

Figure 6-26. *Biaxial stress monitoring by C6:Bi. Comparison between measurements and modelling results for "rock mass" properties (top) and "intact rock" properties (bottom), respectively. '1-3' represents measurements evaluated using vibrating wires 1, 2 and 3. '4-6' represents corresponding measurements evaluated using vibrating wires 4, 5 and 6. P5 and P1 are 3DEC models with "rock mass" and "intact rock" properties, respectively.*

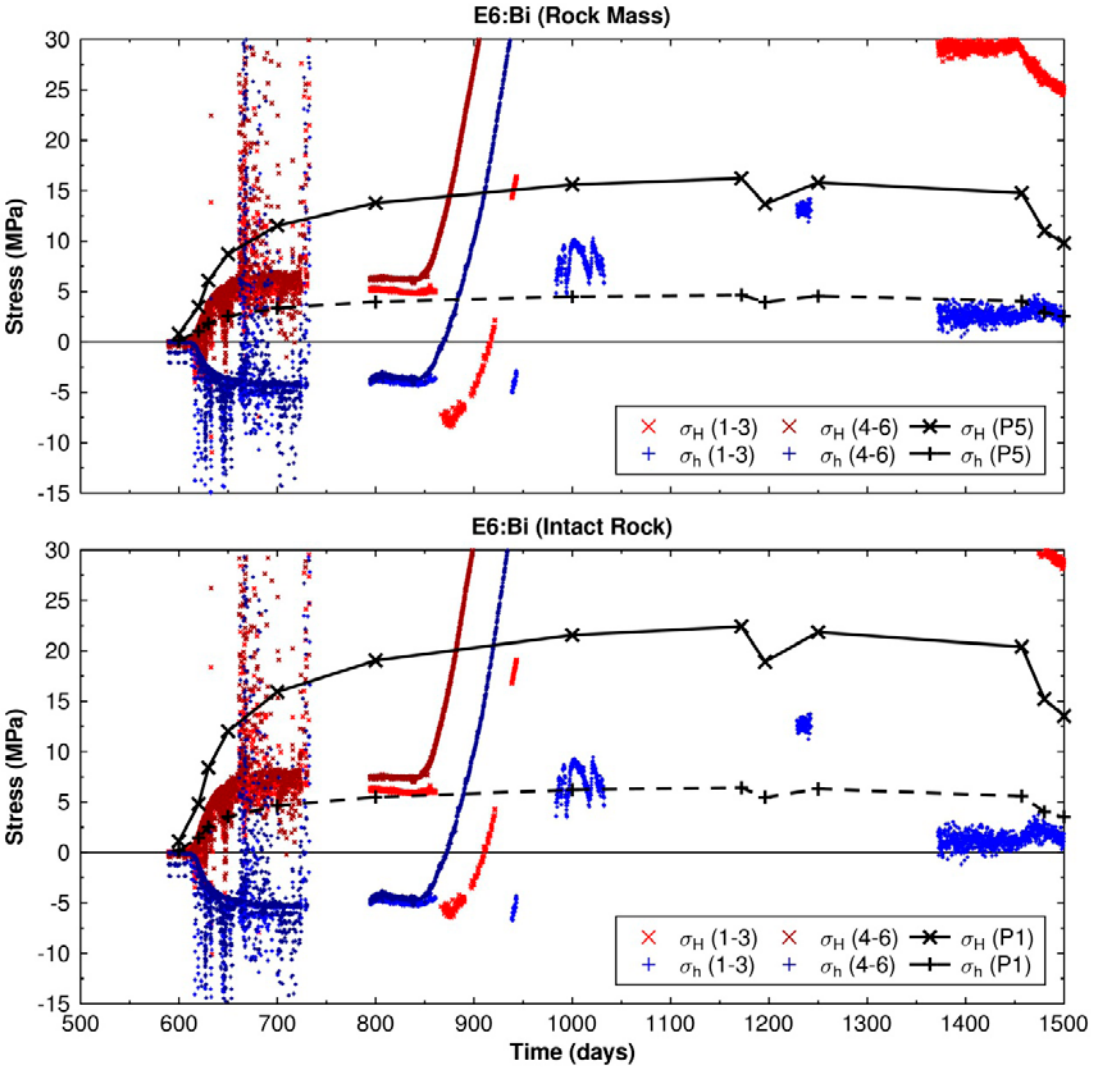

Figure 6-27. *Biaxial stress monitoring by E6:Bi. Comparison between measurements and modelling results for "rock mass" properties (top) and "intact rock" properties (bottom), respectively. '1-3' represents measurements evaluated using vibrating wires 1, 2 and 3. '4-6' represents corresponding measurements evaluated using vibrating wires 4, 5 and 6. P5 and P1 are 3DEC models with "rock mass" and "intact rock" properties, respectively.*

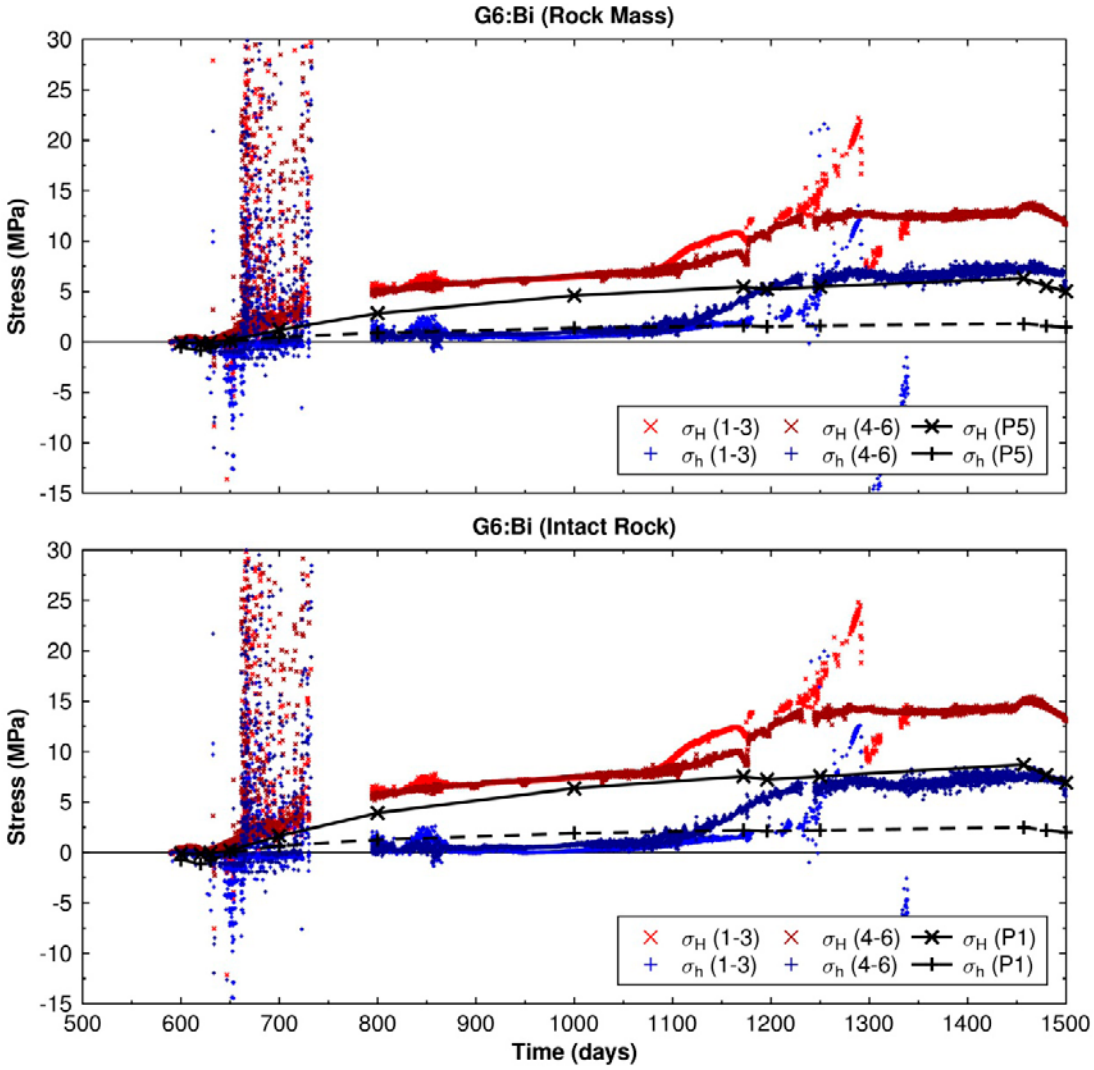

Figure 6-28. *Biaxial stress monitoring by G6:Bi. Comparison between measurements and modelling results for "rock mass" properties (top) and "intact rock" properties (bottom), respectively. '1-3' represents measurements evaluated using vibrating wires 1, 2 and 3. '4-6' represents corresponding measurements evaluated using vibrating wires 4, 5 and 6. P5 and P1 are 3DEC models with "rock mass" and "intact rock" properties, respectively.*

6.5 Soft inclusion stress cells

6.5.1 Locations of sensors

Measurements of the change in borehole diameter were made in two vertical boreholes located at a 45° angle off the tunnel axis around each deposition hole with two instruments in each hole: one instrument measuring the change in radial stress and one instrument measuring the change in tangential stress. The instruments were labelled according to borehole (Bono and Röshoff 2003), e.g. D5 represent the instruments located in borehole D5. Figure 6-29 shows the locations of the instruments. However, there is no clear description of the orientations of the vibrating wires was given by Bono and Röshoff (2003). Based on comparison of measurements to modelling results from the excavation phase (see below), it is judged that a) instruments labelled 'SSR' measure the change in radial stress (the wire is oriented tangential to the deposition hole) and b) instruments labelled 'SST' measure the change in tangential stress (the wire is oriented radial to the deposition hole), see Figure 6-29.

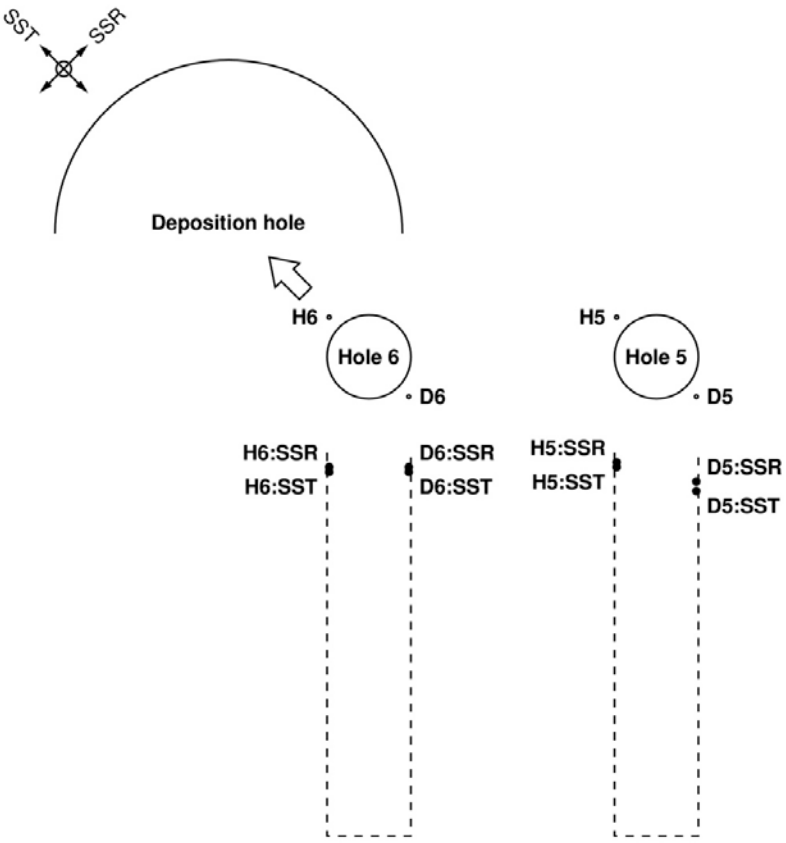

Figure 6-29. *Locations of soft inclusion stress cells and orientations of vibrating wires.*

6.5.2 Excavation

Figure 6-30 and Figure 6-31 show the change in borehole diameter as Holes 5 and 6 were excavated. The final change in diameter after excavation is evaluated as the mean diameter from day 50 to the end of the measurement period.

Here, the measurements are compared with model results for intact rock properties only, see Figure 6-32 to Figure 6-35. There is an insignificant variation in the change in borehole diameter depending on the chosen stress model. A better fit of models to measurements was found for the plane stress approximation. This is consistent since the soft stress cells are located on average about 0.5 m from a constant stress boundary, i.e., the tunnel floor.

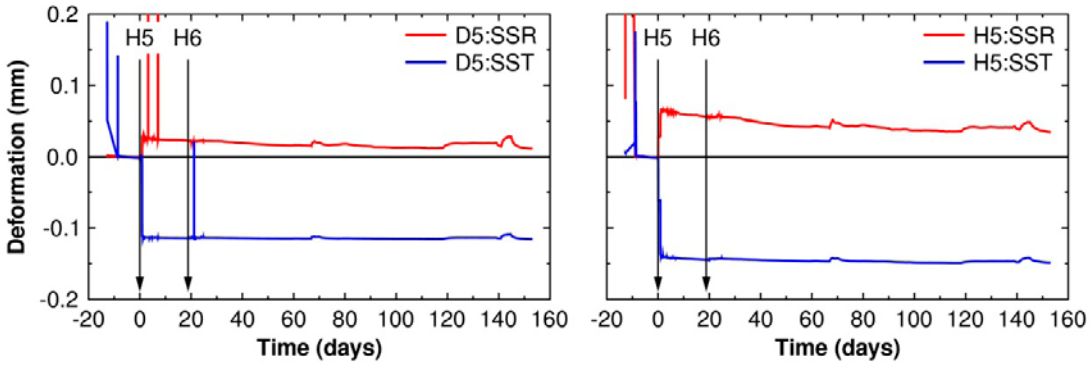

Figure 6-30. *Measured changes in borehole diameter around Hole 5. The start of the drilling of each deposition hole is marked with an arrow.*

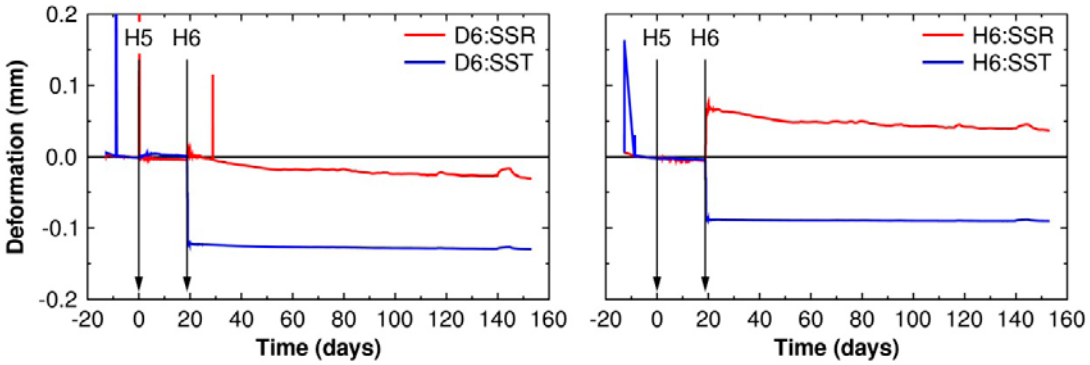

Figure 6-31. *Measured changes in borehole diameter around Hole 6. The start of the drilling of each deposition hole is marked with an arrow.*

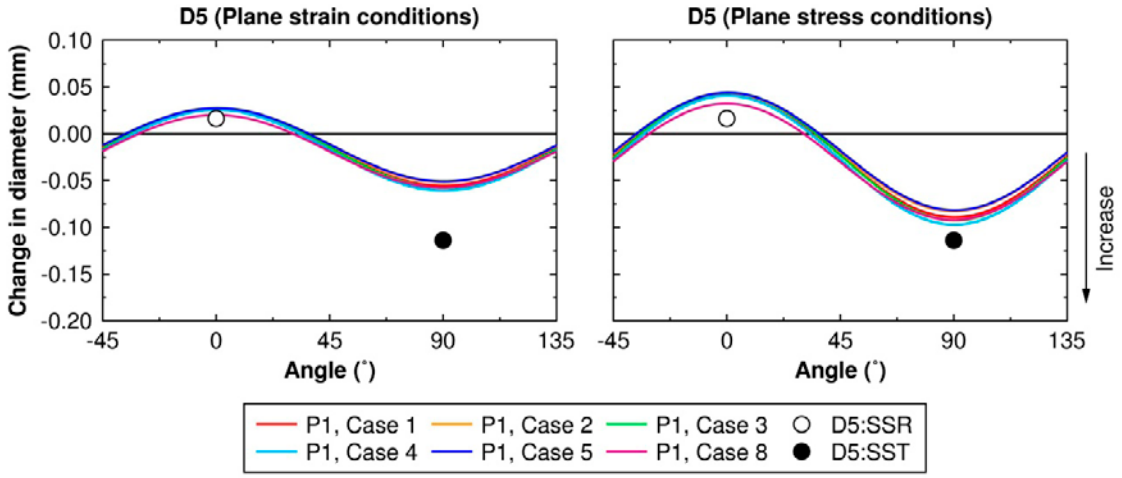

Figure 6-32. *Measured changes in borehole diameter by D5:SSR and D5:SST. Comparison between measurements and modelling results for plane strain conditions (left) and plane stress conditions (right). P1, Case 1 to Case 8 are 3DEC models with different in situ stress models, cf. Table 6-5.*

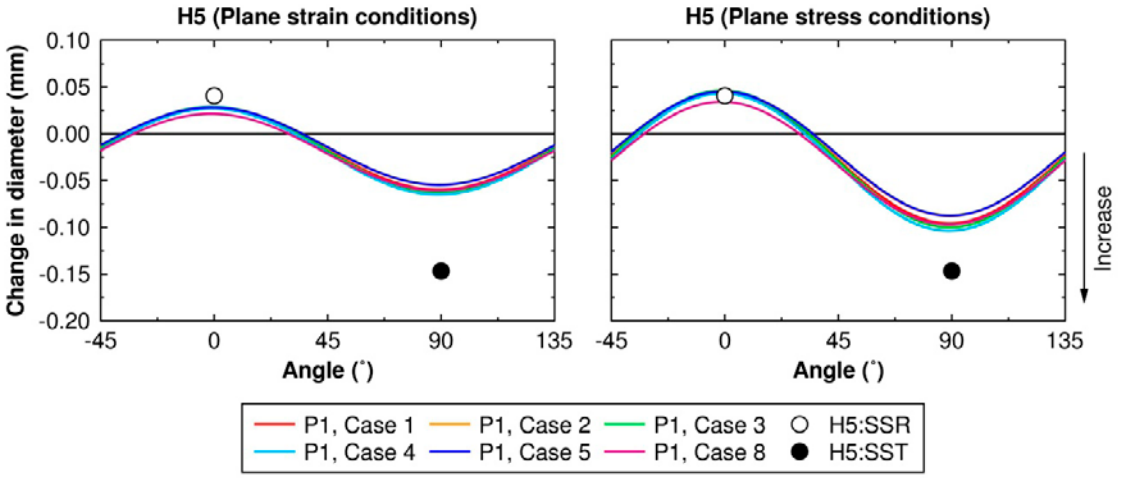

Figure 6-33. *Measured changes in borehole diameter by H5:SSR and H5:SST. Comparison between measurements and modelling results for plane strain conditions (left) and plane stress conditions (right). P1, Case 1 to Case 8 are 3DEC models with different in situ stress models, cf. Table 6-5.*

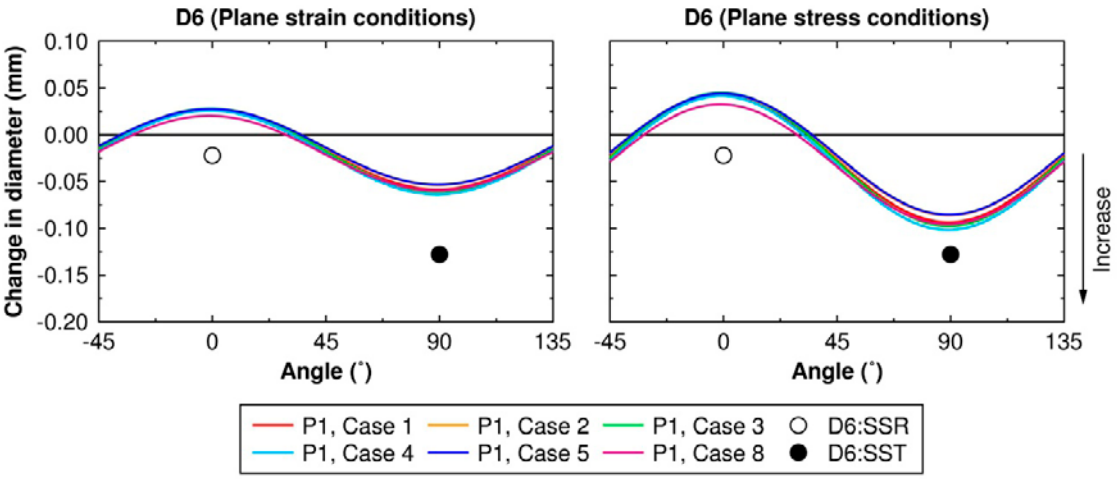

Figure 6-34. *Measured changes in borehole diameter by D6:SSR and D6:SST. Comparison between measurements and modelling results for plane strain conditions (left) and plane stress conditions (right). P1, Case 1 to Case 8 are 3DEC models with different in situ stress models, cf. Table 6-5.*

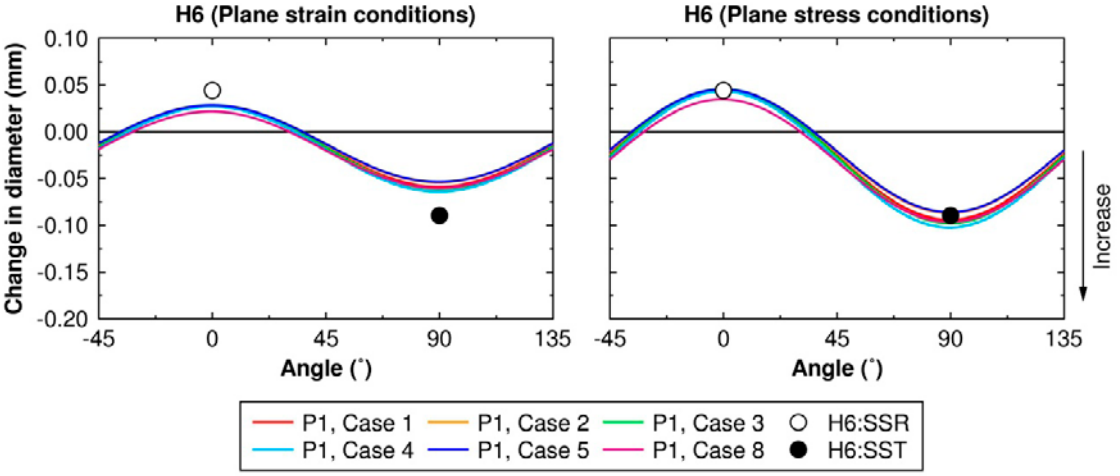

Figure 6-35. *Measured changes in borehole diameter by H6:SSR and H6:SST. Comparison between measurements and modelling results for plane strain conditions (left) and plane stress conditions (right). P1, Case 1 to Case 8 are 3DEC models with different in situ stress models, cf. Table 6-5.*

6.5.3 Heated phase

Figure 6-36 to Figure 6-39 show comparisons of the change in borehole diameter during the heated phase. Data points marked as unreliable in Sicada have been removed in the comparison with 3DEC. There are no reliable measurement data from soft stress cells D6:SSR and H6:SSR.

The measurements show a reduction of similar magnitude in both radial and tangential directions. As evaluated from the model results, there is an insignificant change in borehole diameter in the radial direction (SST) at all measurement positions. The measured reduction in borehole diameter in the tangential direction (SSR) is more rapid than predicted by the models.

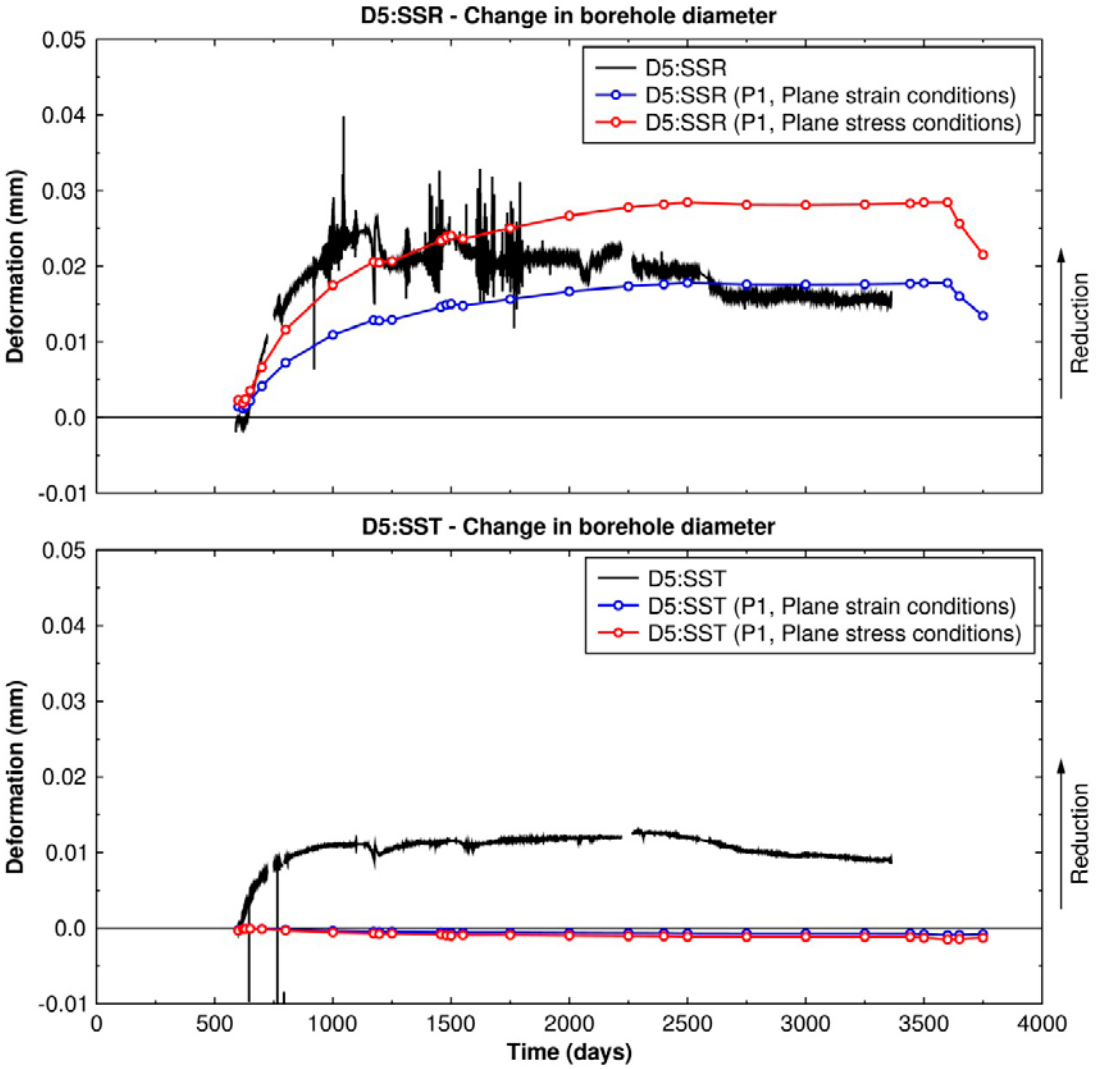

Figure 6-36. *Measured changes in borehole diameter by D5:SSR (top) and D5:SST (bottom). Comparison between measurements and modelling results for plane strain conditions and plane stress conditions. P1 is a 3DEC models with "intact rock" properties.*

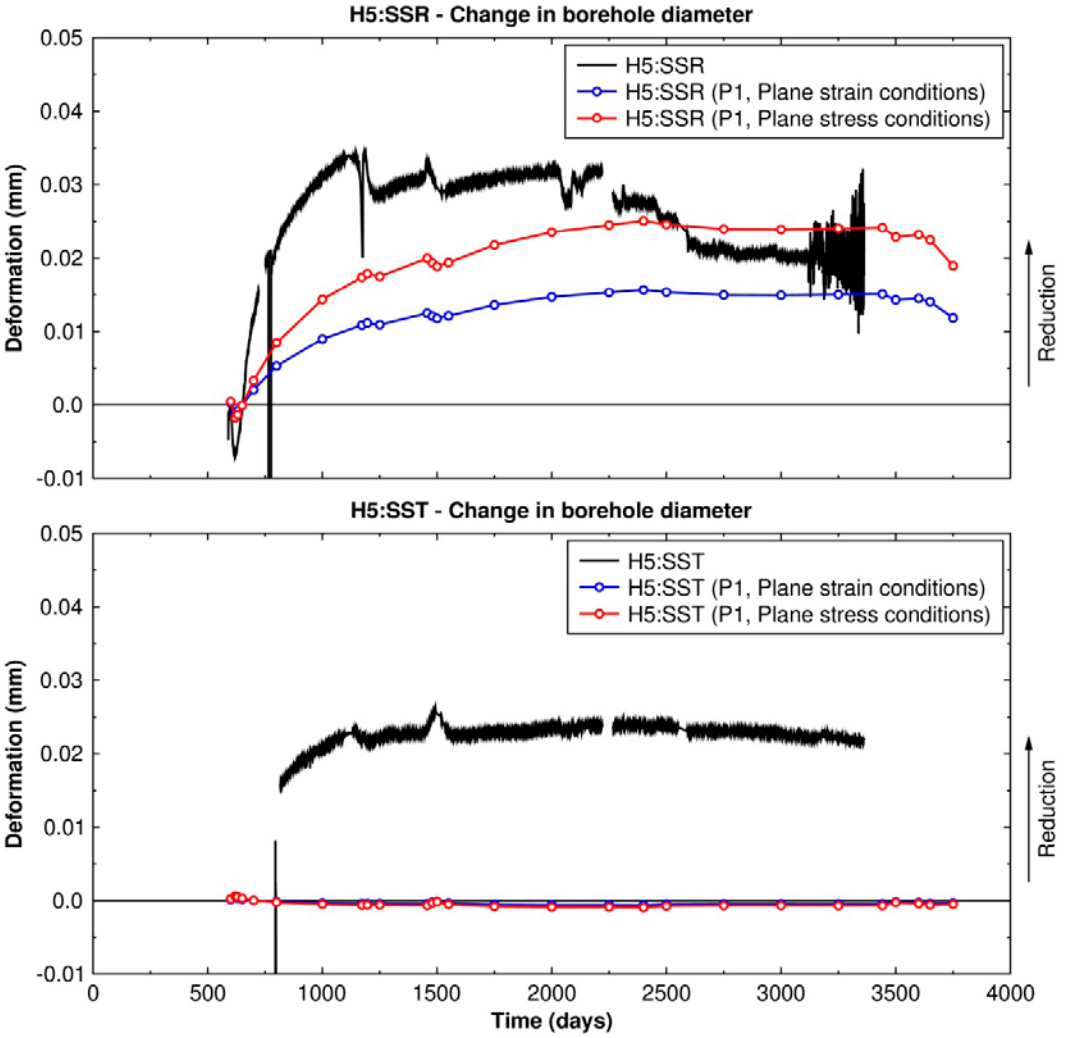

Figure 6-37. *Measured changes in borehole diameter by H5:SSR (top) and H5:SST (bottom). Comparison between measurements and modelling results for plane strain conditions and plane stress conditions. P1 is a 3DEC models with "intact rock" properties.*

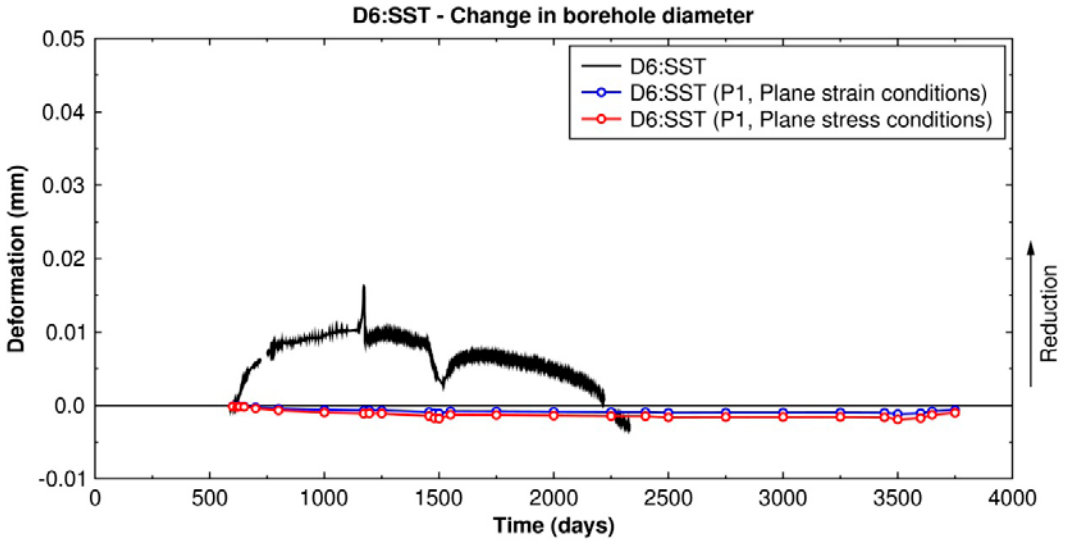

Figure 6-38. *Measured changes in borehole diameter by D6:SST. Comparison between measurements and modelling results for plane strain conditions and plane stress conditions. P1 is a 3DEC models with "intact rock" properties.*

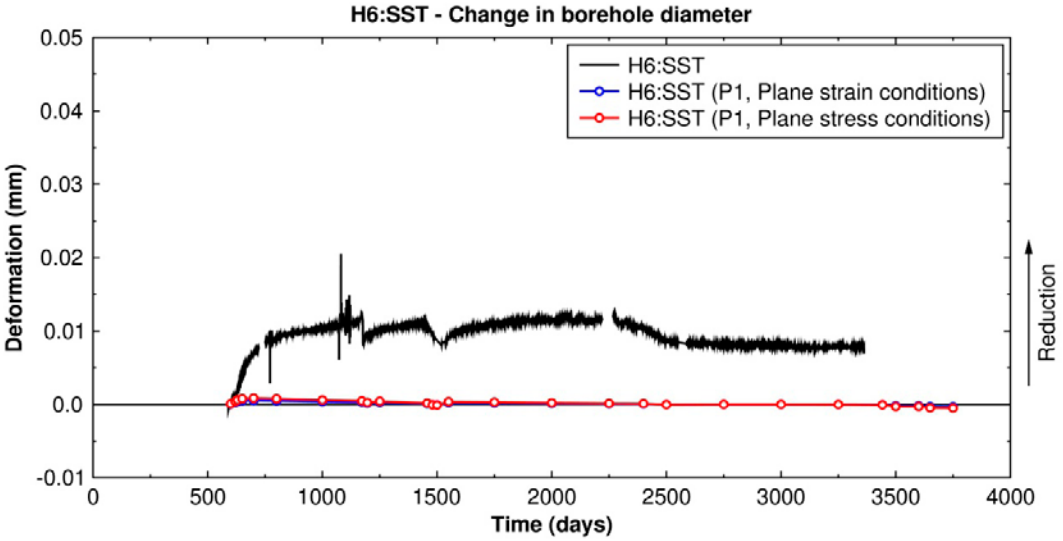

Figure 6-39. *Measured changes in borehole diameter by H6:SST. Comparison between measurements and modelling results for plane strain conditions and plane stress conditions. P1 is a 3DEC models with "intact rock" properties.*

6.6 Deformation meters

6.6.1 Locations of sensors

Vertical deformation meters were installed in two vertical boreholes around Hole 6 and in four vertical boreholes around Hole 5 (see Figure 6-40 for locations) to measure changes in deformation during the drilling of the holes and during the subsequent heated phase. Additional deformation meters specifically aimed at monitoring the response of the rock during the heated phase were installed in four horizontal boreholes drilled from inside each deposition holes (see Figure 6-41).

6.6.2 Excavation

The deformations are significantly influenced by the fluctuations in temperature and no stable final value of the deformation after excavation can be found (see Figure 6-42 and Figure 6-43). Therefore, comparison with modelling results is not meaningful.

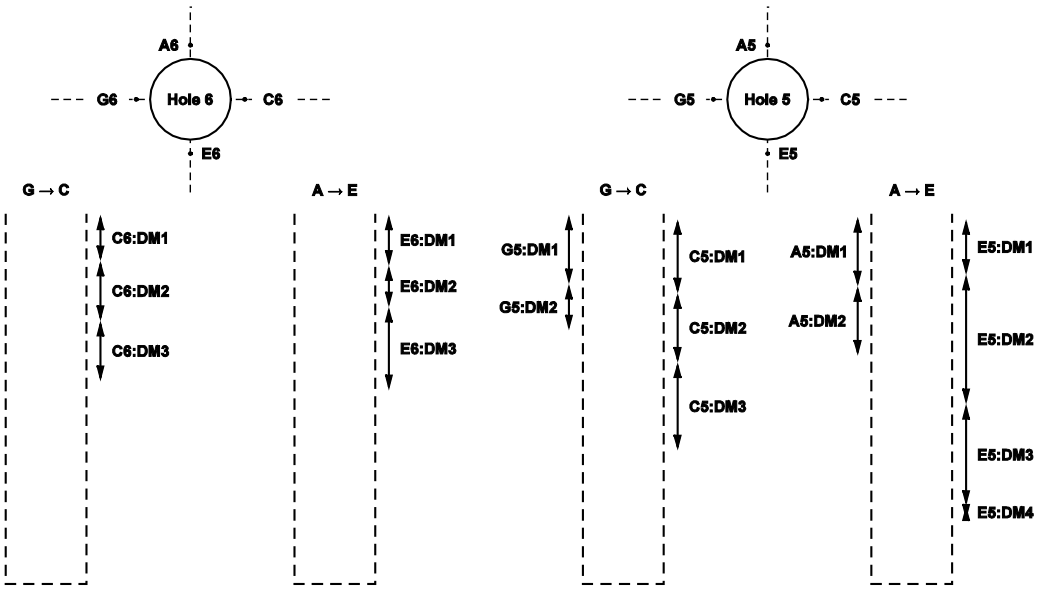

Figure 6-40. *Locations of vertical stress meters.*

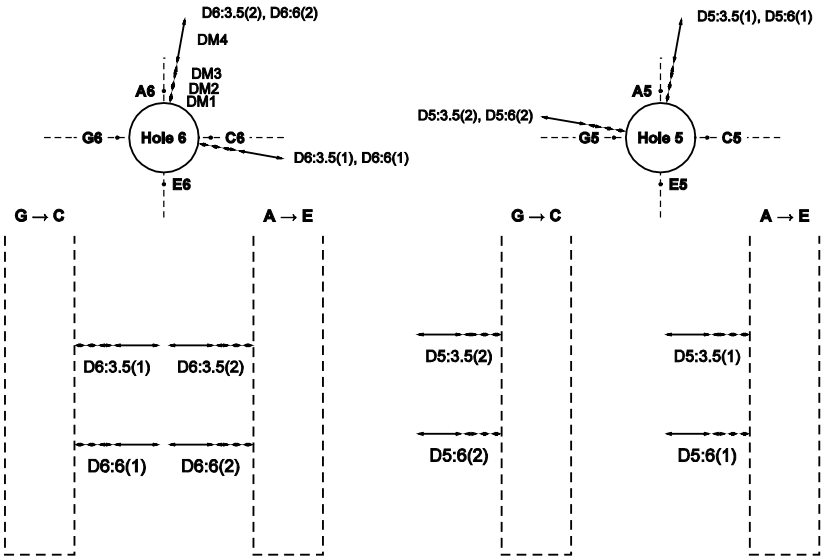

Figure 6-41. *Locations of horizontal stress meters.*

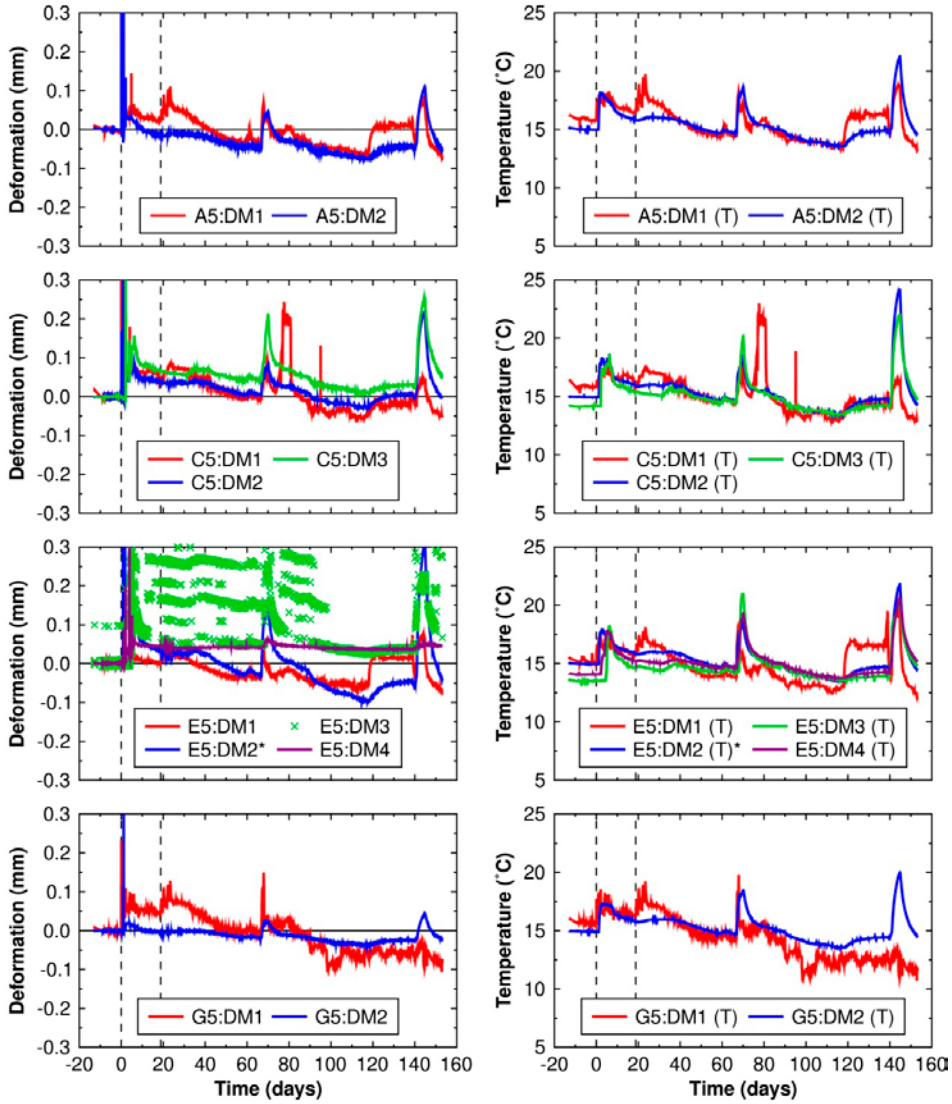

Figure 6-42. *Left column: Measured vertical deformations around Hole 5 as the holes were excavated. Right column: Measured temperature at the corresponding locations. *The temperature sensor in E5:DM2 shows sub-zero temperatures throughout the measurement period. Average values from temperature sensors in A5:DM2, C5:DM2 and G5:DM2 have been used to evaluate the deformation of E5:DM2.*

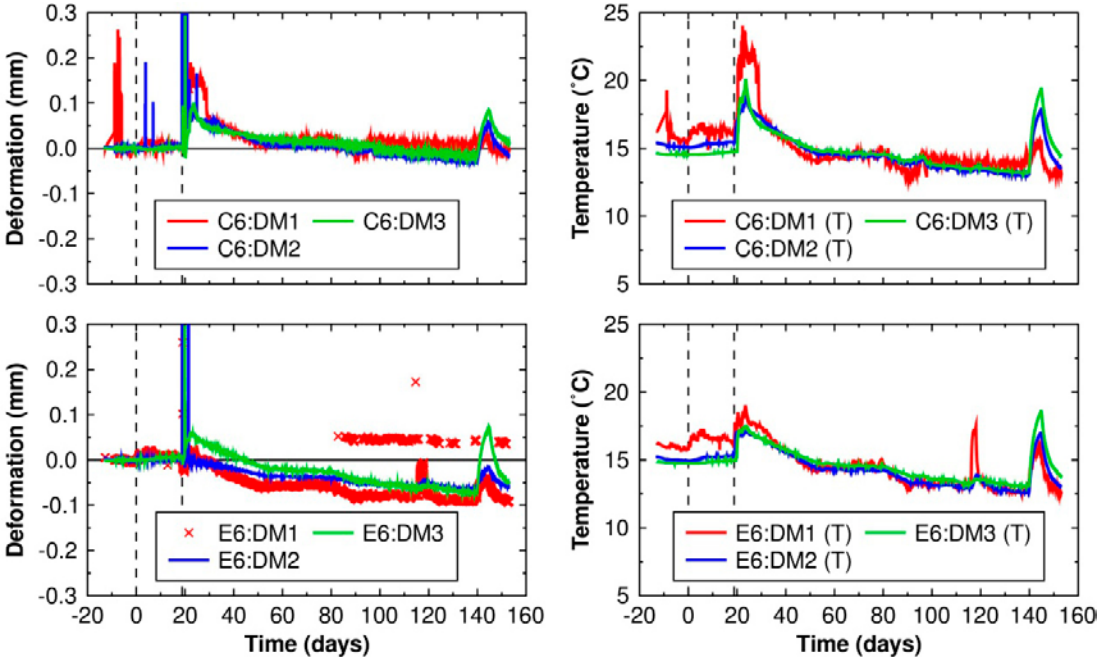

Figure 6-43. *Left column: Measured vertical deformations around Hole 6 as the holes were excavated. Right column: Measured temperature at the corresponding locations.*

6.6.3 Heated phase

During the heated phase, deformation measurements were conducted in both the primary (vertical) boreholes around the deposition holes and in the complementary (horizontal) boreholes drilled from within the deposition holes.

Primary boreholes: Vertical deformation

Figure 6-44 to Figure 6-49 show comparisons between the measured deformations along the vertical boreholes and corresponding deformations as calculated by 3DEC. Data points marked as unreliable in Sicada have been removed in the comparison with 3DEC.

As seen in Figure 6-4, the correction for the thermal expansion of the sensors (particularly for sensors exceeding 0.5 m) is much greater than the corresponding thermal expansion of unconfined rock. This is clearly seen in the comparison between measurements and models: all measurements are significantly greater than the corresponding modelling results.

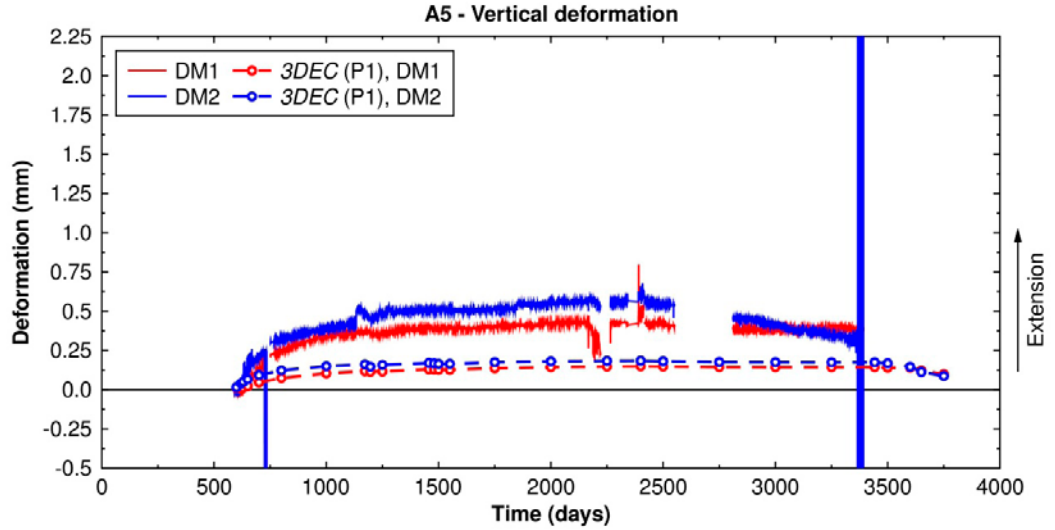

Figure 6-44. *Deformation meters located in borehole A5. Comparison between measurements (DM1 and DM2) and 3DEC.*

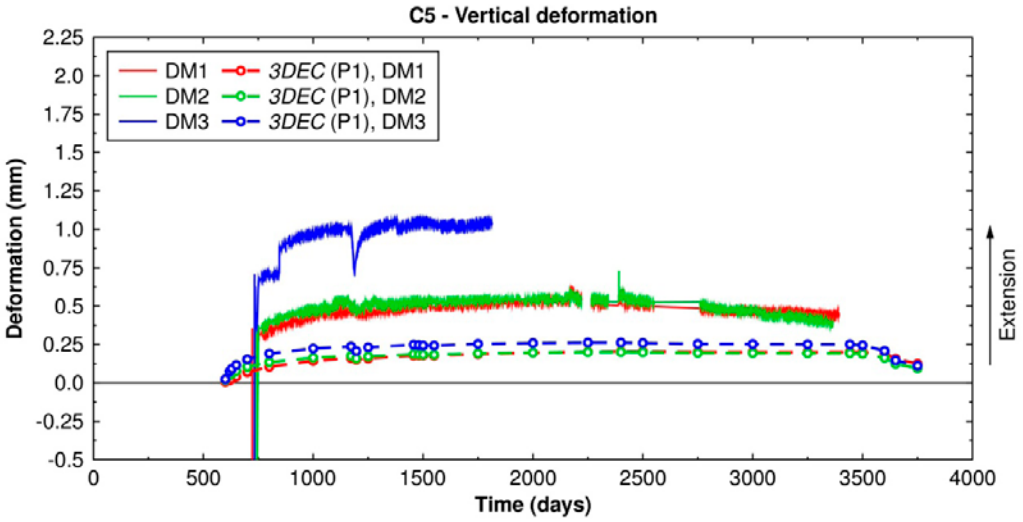

Figure 6-45. *Deformation meters located in borehole C5. Comparison between measurements (DM1, DM2 and DM3) and 3DEC.*

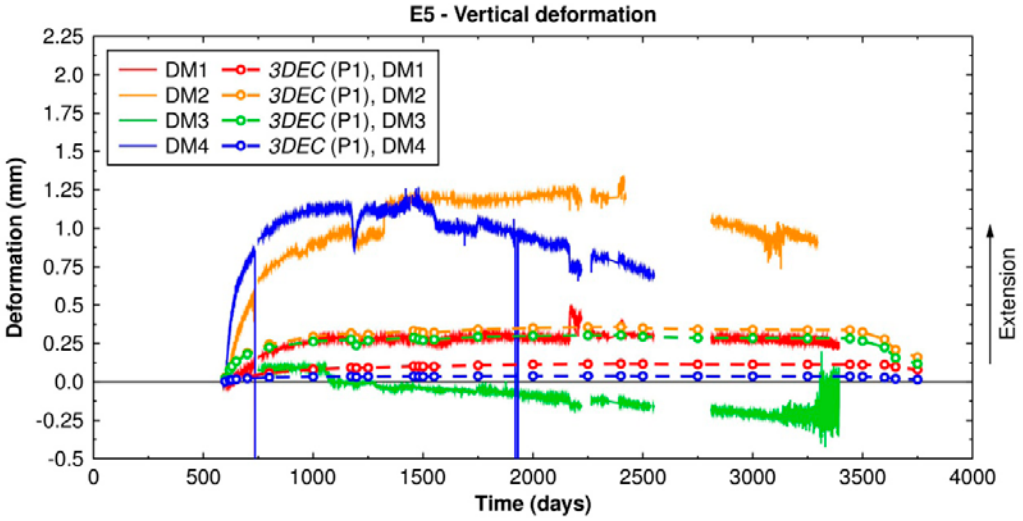

Figure 6-46. *Deformation meters located in borehole E5. Comparison between measurements (DM1, DM2, DM3 and DM4) and 3DEC.*

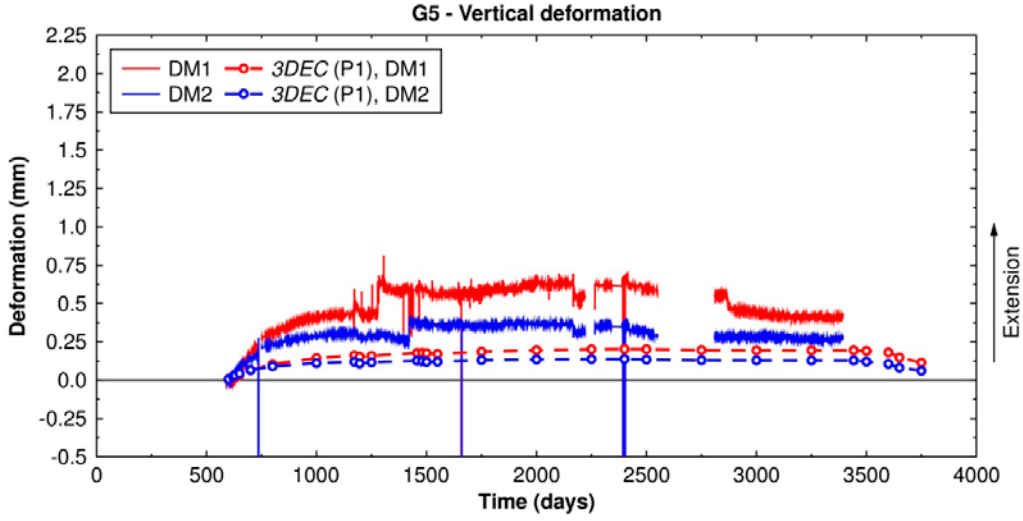

Figure 6-47. *Deformation meters located in borehole G5. Comparison between measurements (DM1 and DM2) and 3DEC.*

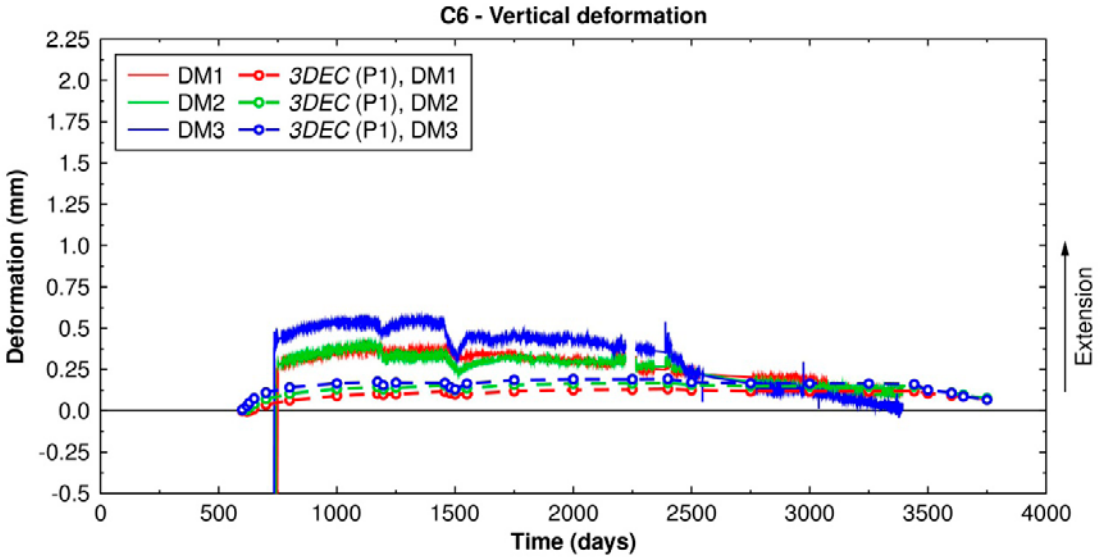

Figure 6-48. *Deformation meters located in borehole C6. Comparison between measurements (DM1, DM2 and DM3) and 3DEC.*

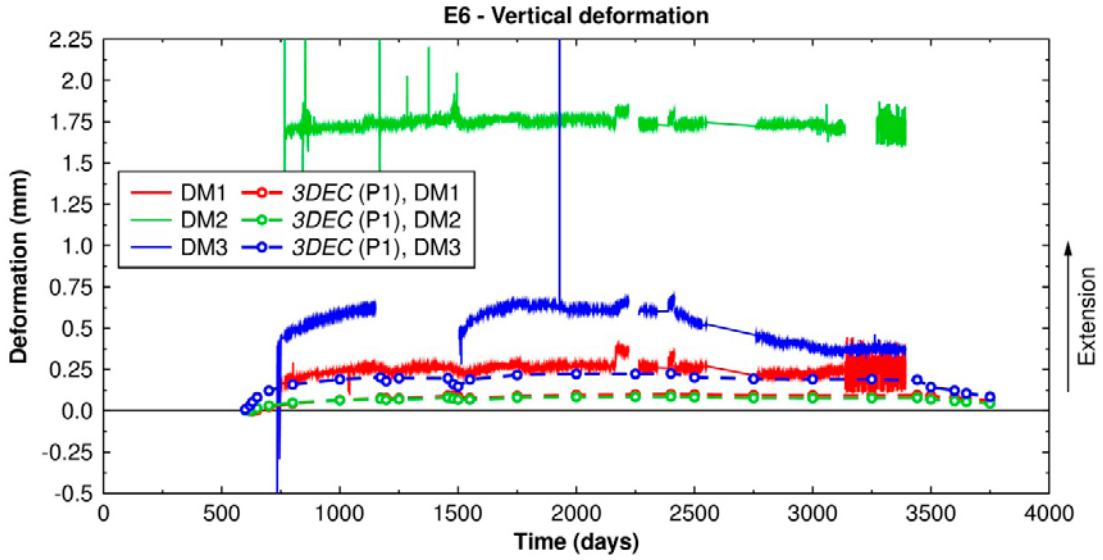

Figure 6-49. *Deformation meters located in borehole E6. Comparison between measurements (DM1, DM2 and DM3) and 3DEC.*

Complementary boreholes: Horizontal deformation

Figure 6-50 to Figure 6-57 show comparisons between the measured deformations along the horizontal boreholes drilled from within the deposition holes and corresponding deformations as calculated by 3DEC. Data points marked as unreliable in Sicada have been removed in the comparison with 3DEC. There are no reliable measurement data from deformation meters D5:3.5(2)_DM1, D6:3.5(1)_DM1, D6:3.5(2)_DM1 and D6:6(1)_DM3. Model results for sensors at these locations are not shown in the figures.

The longest sensor (DM4) in each borehole significantly exceeds the corresponding calculated deformation. This is likely due to the correction for the thermal expansion of the deformation meter (cf. Figure 6-4). For sensors shorter than about 0.5 m (i.e., DM1, 2 and 3) the temperature correction is less than that of unconfined thermal expansion of rock (see Figure 6-4). At later stages of the heated phase, some of the shorter sensors measurements show a decreasing trend, which may be associated with increasing swelling pressure within the deposition holes (cf. Section 6.7).

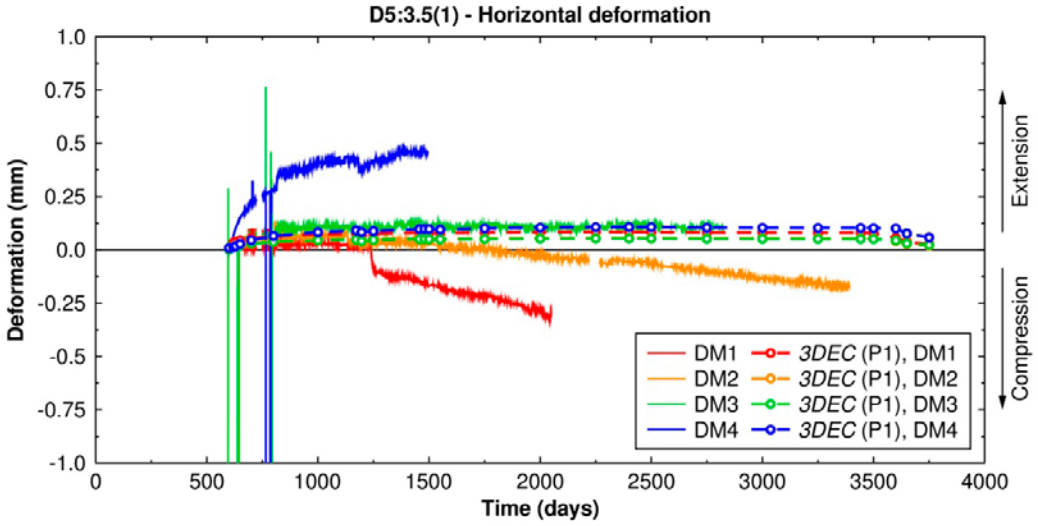

Figure 6-50. *Deformation meters located in borehole D5:3.5(1). Comparison between measurements (DM1, DM2, DM3 and DM4) and 3DEC.*

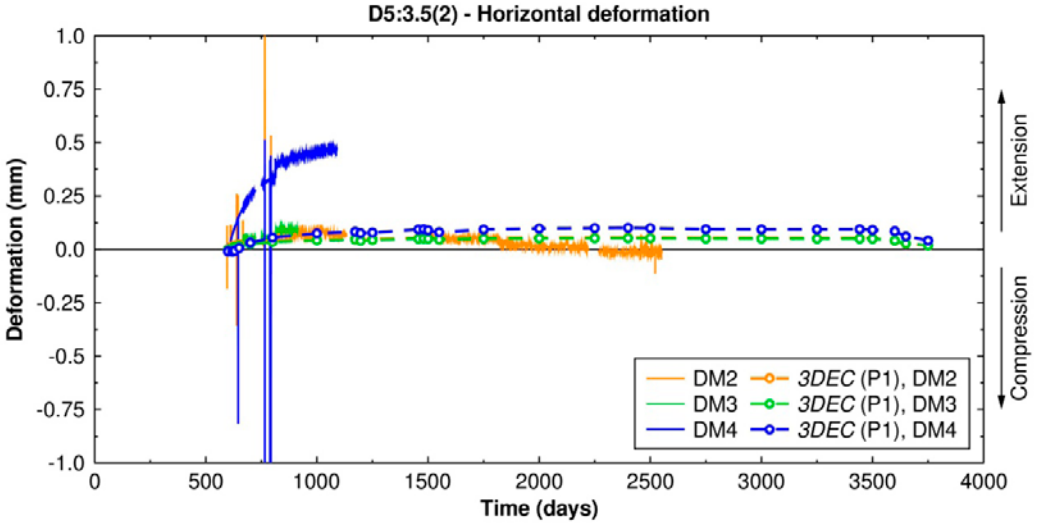

Figure 6-51. *Deformation meters located in borehole D5:3.5(2). Comparison between measurements (DM2, DM3 and DM4) and 3DEC. There are no reliable data from deformation meter DM1.*

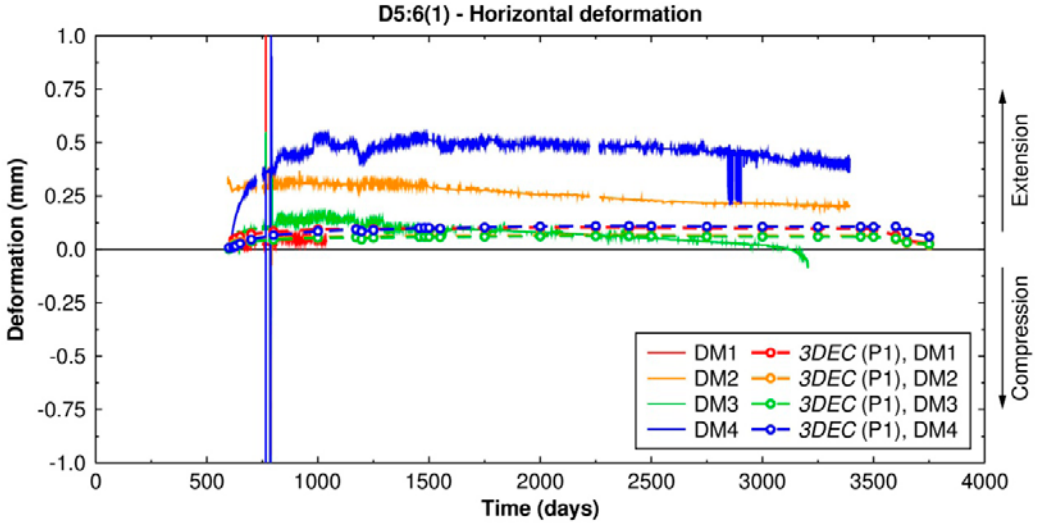

Figure 6-52. *Deformation meters located in borehole D5:6(1). Comparison between measurements (DM1, DM2, DM3 and DM4) and 3DEC.*

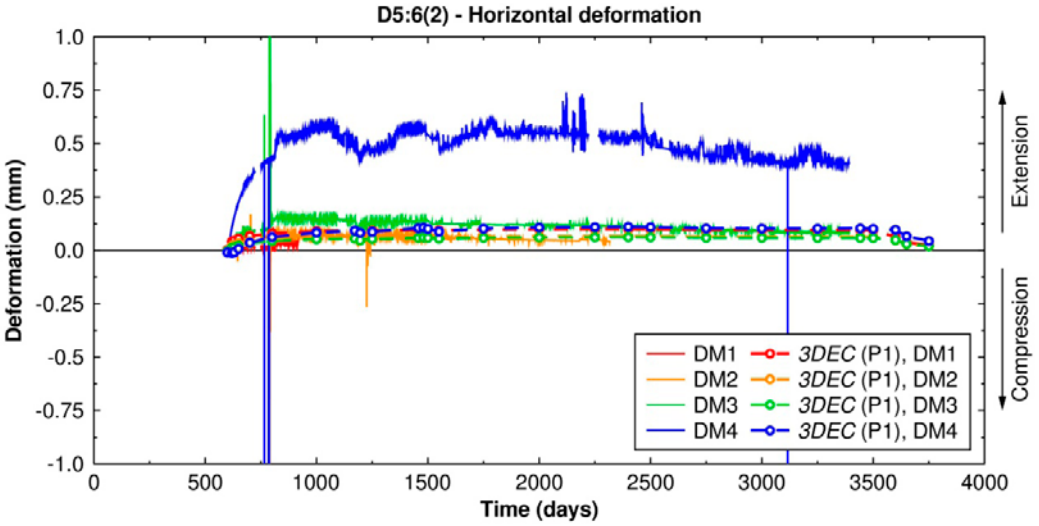

Figure 6-53. *Deformation meters located in borehole D5:6(2). Comparison between measurements (DM1, DM2, DM3 and DM4) and 3DEC.*

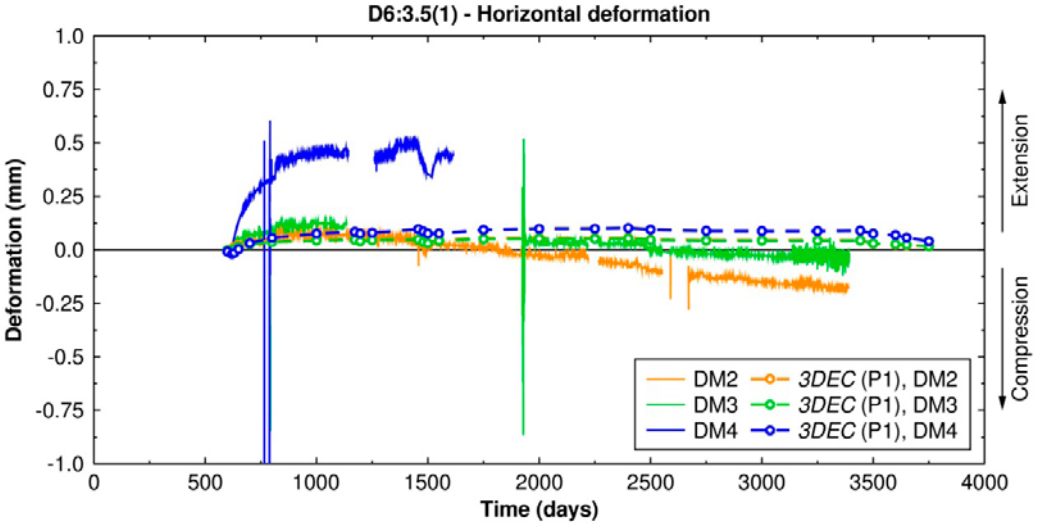

Figure 6-54. *Deformation meters located in borehole D6:3.5(1). Comparison between measurements (DM2, DM3 and DM4) and 3DEC. There are no reliable data from deformation meter DM1.*

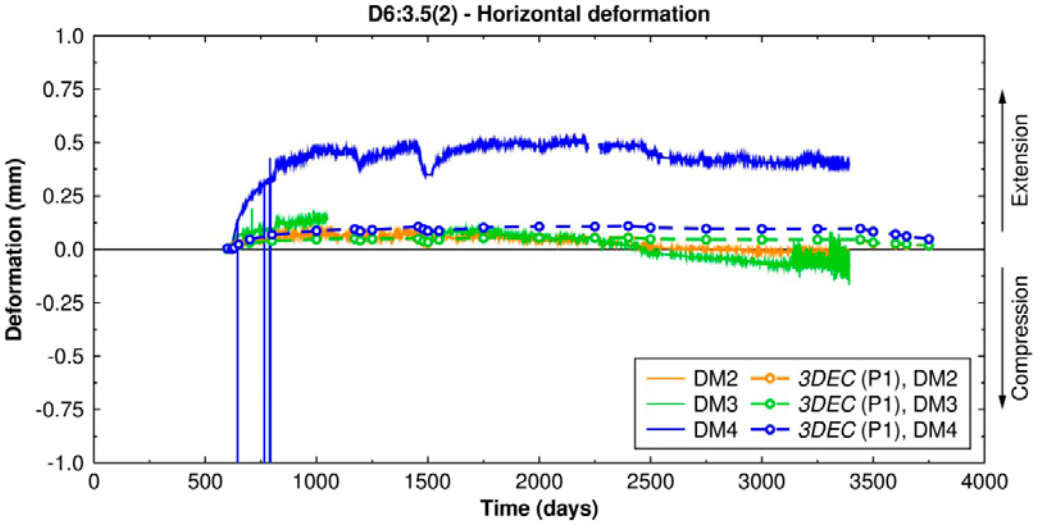

Figure 6-55. *Deformation meters located in borehole D6:3.5(2). Comparison between measurements (DM2, DM3 and DM4) and 3DEC. There are no reliable data from deformation meter DM1.*

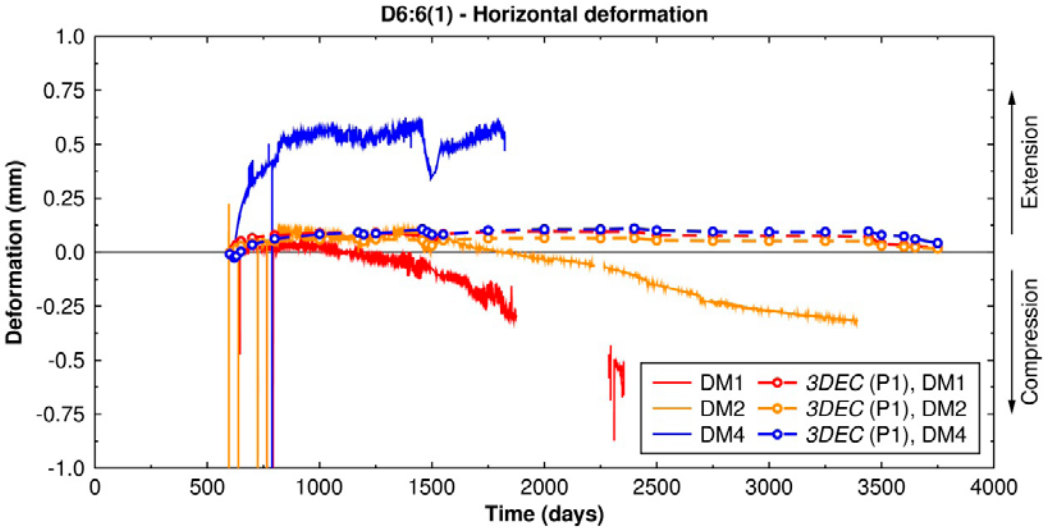

Figure 6-56. *Deformation meters located in borehole D6:6(1). Comparison between measurements (DM1, DM2 and DM4) and 3DEC. There are no reliable data from deformation meter DM3.*

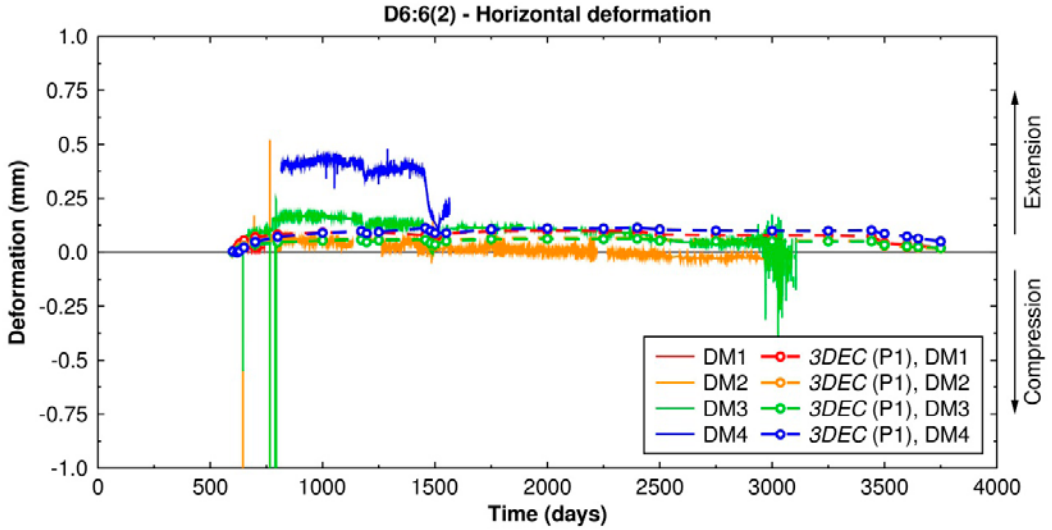

Figure 6-57. *Deformation meters located in borehole D6:6(2). Comparison between measurements (DM1, DM2, DM3 and DM4) and 3DEC.*

6.7 Influence of pressurized tunnel and deposition holes

6.7.1 Expressions for stresses and deformations around a pressurized thick-walled cylinder

In the above analyses, the swelling pressure of the buffer and backfill during the heated phase was not accounted for. Since both the tunnel and the deposition holes have cylindrical geometry, a rough estimate of the impact of the swelling pressure can be obtained by considering the changes in stress and deformation around an infinitely thick hollow cylinder with uniform inner pressure p_i and zero outer pressure.

The expressions for radial stress and tangential stress are given by (Brady and Brown 1993)

$$\sigma_{rr}(r) = p_i \frac{R_i^2}{r^2} \tag{6-9a}$$

$$\sigma_{\theta\theta}(r) = -p_i \frac{R_i^2}{r^2} \tag{6-9b}$$

and for radial displacement under plane strain conditions by (see Appendix D for derivation)

$$u_r(r) = p_i \frac{1}{2G} \frac{R_i^2}{r} \tag{6-10}$$

Here, R_i is the inner radius of the cylinder, r is the radial distance from the hole perimeter and G is the shear modulus of the surrounding rock. In the following, the displacements have been evaluated using "intact rock" properties.

6.7.2 Impact of pressure inside the tunnel

Figure 6-58 (left) shows the tangential stress component around the tunnel normalized to 1 MPa. Below the floor of the tunnel, the tangential stress component corresponds (approximately) to the horizontal stress component across the tunnel. Since the total pressure within the tunnel does not amount to more than 1–1.5 MPa (Goudarzi 2012), it appears that the impact on the stress component across the tunnel can be ignored at the majority of the sensors locations (see Figure 6-58, left). At depths greater than about 3 m below the tunnel floor, the reduction in stress is only about 20% of the swelling pressure. For sensors located above 1 m depth (i.e., the biaxial stressmeters A6:Bi and G6:Bi and all eight soft stress meters), the reduction in stress is between 50 and 100% of the swelling pressure.

The radial deformation component is equivalent to the vertical component. For the vertical deformation meters, the impact is greatest for long sensors with one end point close to the tunnel floor, e.g. C5:DM1 (see Figure 6-45). This particular sensor may experience a reduction in length of about 15 µm per MPa increase in swelling pressure (Figure 6-58, right) or, equivalently, a reduction of about 8%. Shorter sensors will be reduced less depending on position within the boreholes.

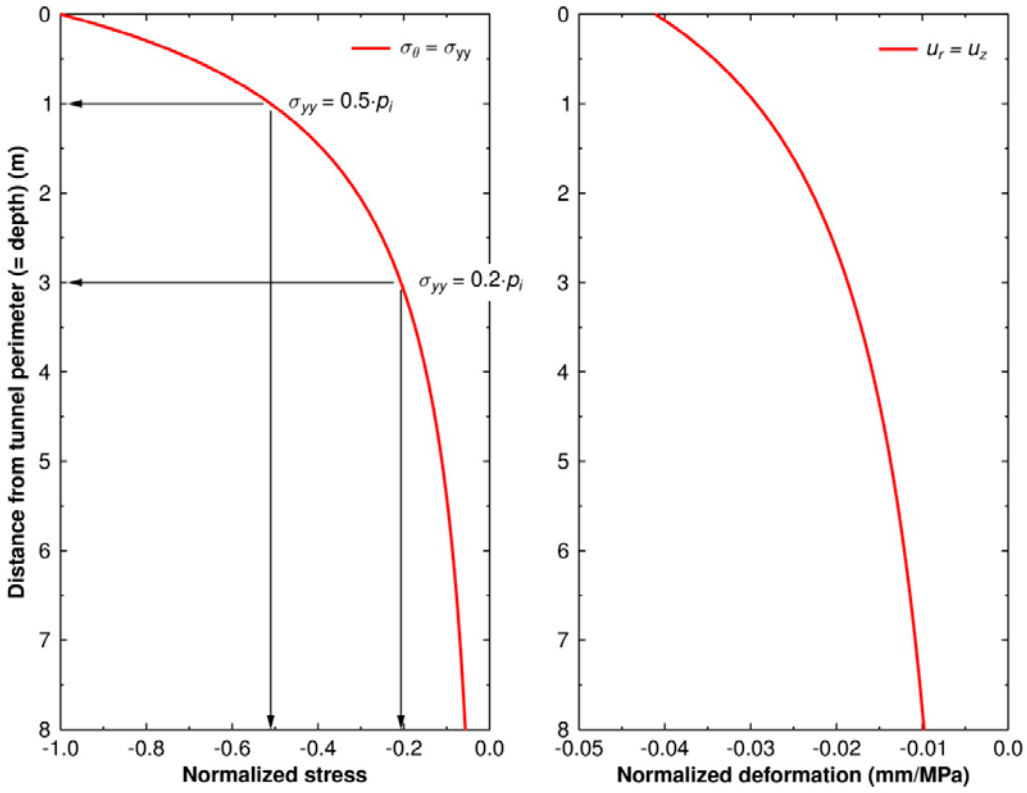

Figure 6-58. *Analytical estimate of impact of pressure within the tunnel on the stress across the tunnel (left) and on the vertical deformation (right).*

6.7.3 Impact of pressure inside the deposition holes

The total pressure within the deposition holes is substantially larger than that inside the tunnel. The maximum pressure reported for the two holes is around 10 MPa (Goudarzi 2014). On average, the pressure is significantly smaller but varies both between the holes as well as within each hole (see Goudarzi 2014 for details).

All biaxial stress meters and soft stress cells are located a distance of 0.3 m from the deposition hole perimeter (Bono and Röshoff 2003). At the positions of these sensors, the radial stress may be increased by about 55% of the swelling pressure and the tangential stress may be reduced by the same amount (see Figure 6-59, top).

Similarly to the vertical deformation meters, the horizontal deformation meters will be compressed as a result of the pressure inside the deposition holes. The reduction in length may be of the order of 2–4 µm per MPa increase in swelling pressure (see Figure 6-59, bottom).

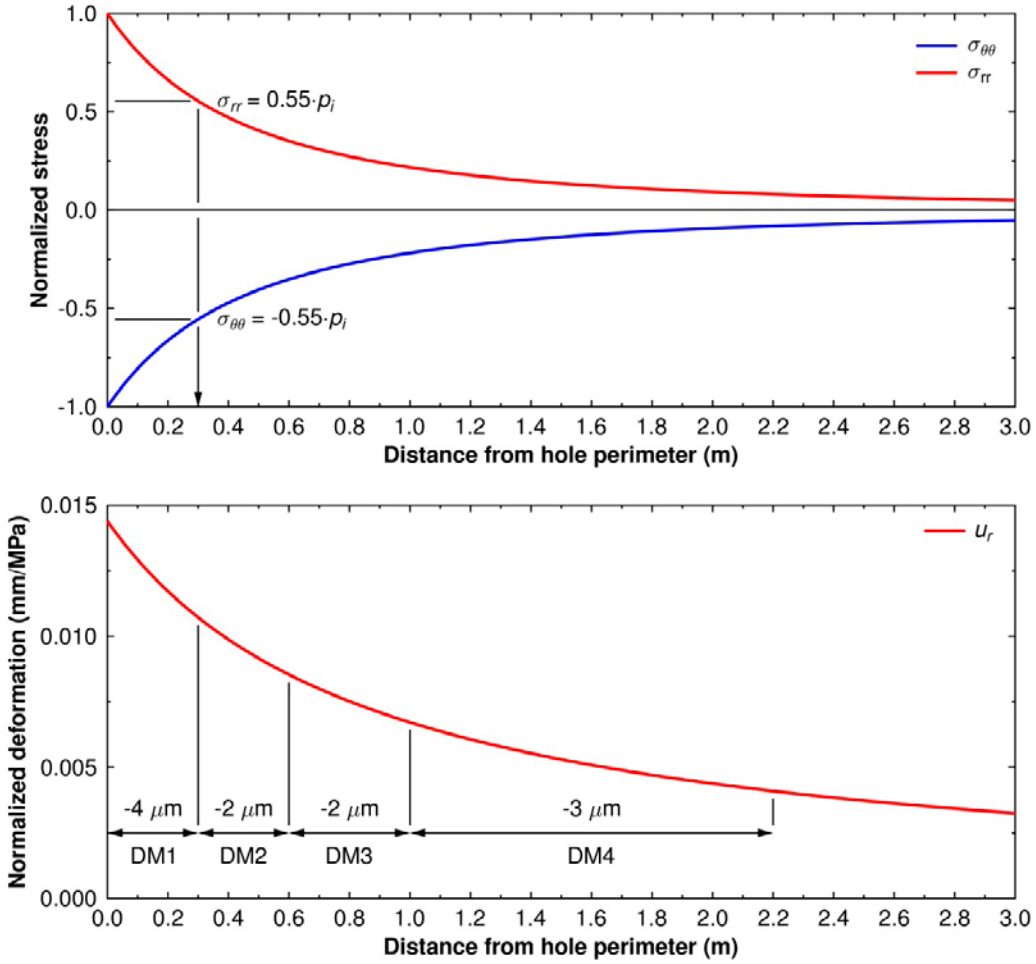

Figure 6-59. *Analytical estimate of impact of pressure within the deposition holes on the radial and tangential stresses (top) and on the radial deformation (bottom).*

6.8 Summary

A summary of the findings is given below:

- The majority of the AE events coincide with the calculated tangential stress maxima for all six tested *in situ* stress models. It can thus be considered verified that the orientations of the horizontal stresses fall within the uncertainty span given in Section 3.3.
- The calculated and measured stress additions caused by the excavation of the holes are qualitatively similar. Reasonable agreements of the stress magnitudes were found at some points, but disagree by about ± 50% at others. The observed anomalies in measurement data could, possibly, be due to a combination of elastic and plastic shear displacements along intersecting fractures or that the instruments are located within inclusions of rock with different mechanical properties (cf. Chapter 8). The majority of the biaxial stressmeters started malfunctioning when the power to all canisters was switched off in December 2004. However, prior to that time, the major horizontal stress can be reproduced reasonable well assuming rock properties consistent with "intact rock". The agreement between the measured and modelled minor horizontal stress component is poor: the modelled stress increases whereas the measured stress is reduced. Taking the effects of the swelling pressure within the deposition holes into account cannot explain the differences in results.
- The change in borehole diameter was evaluated using analytical solutions for the change in diameter of an infinite hollow cylinder subjected to a change in stress under either plane stress conditions or plane strain conditions. Because of the proximity to the tunnel, plane stress conditions are the most relevant approximation. For this approximation, a reasonable, or very good, fit of modelling results to measurements was found for all *in situ* stress assumptions tried here. During the heated phase, the measurements show a reduction of similar magnitude in both the radial and in the tangential directions. As evaluated from the model results, there is an insignificant change in borehole diameter in the radial direction at all measurement positions. The measured reduction in borehole diameter in the tangential direction is more rapid than predicted by the models. Since the thermal stress additions in the uppermost parts of the deposition holes are rather small, the swelling pressure of the buffer and backfill may influence the state of stress at the locations of the soft stress cells.
- The measured vertical deformations were too influenced by fluctuations in temperature during the drilling of the deposition holes for a comparison with modelling results to be meaningful. As seen in Figure 6-4, the correction for the thermal expansion of the sensors (particularly for sensors exceeding 0.5 m) is much greater than the corresponding thermal expansion of unconfined rock. The measured deformations during the heated phase are therefore much greater than the corresponding modelling results.

7 Stresses in deposition hole walls

7.1 Evaluation of spalling

Elastic models have previously been used for predictions of spalling in the walls of deposition holes (e.g. Fälth et al. 2005, Hökmark et al. 2006, 2010, Fälth and Hökmark 2007, Lönnqvist et al. 2008, Glamheden et al. 2010). In the elastic modelling approach, spalling is said to occur when the tangential stress in the wall of a borehole is equal to, or exceeds, the nominal spalling strength. Although, such a model cannot be used to predict the depth or the shape of the spalled region (e.g. Hökmark et al. 2010), it gives an indication of the intervals along the borehole walls where spalling can be expected.

In this chapter, linear elastic 3DEC models are used to assess the potential for spalling in the walls of the two deposition holes in the outer section of the Prototype Repository.

7.2 Observations of spalling in the Prototype Repository

After the dismantling of the outer section of the Prototype Repository, Holes 5 and 6 were inspected with the purpose to make a preliminary documentation of any occurrences of spalling (see Appendix H). With the exception of one location in Hole 6 (see Figure 7-1, right), there were no indications of any stress induced damage to the walls in the two holes. The area in Hole 6 where some potential damage was observed is located approximately at the position marked with the shaded area "9" in Figure 7-1 (left) and coincides with the region where high tangential stresses are expected.

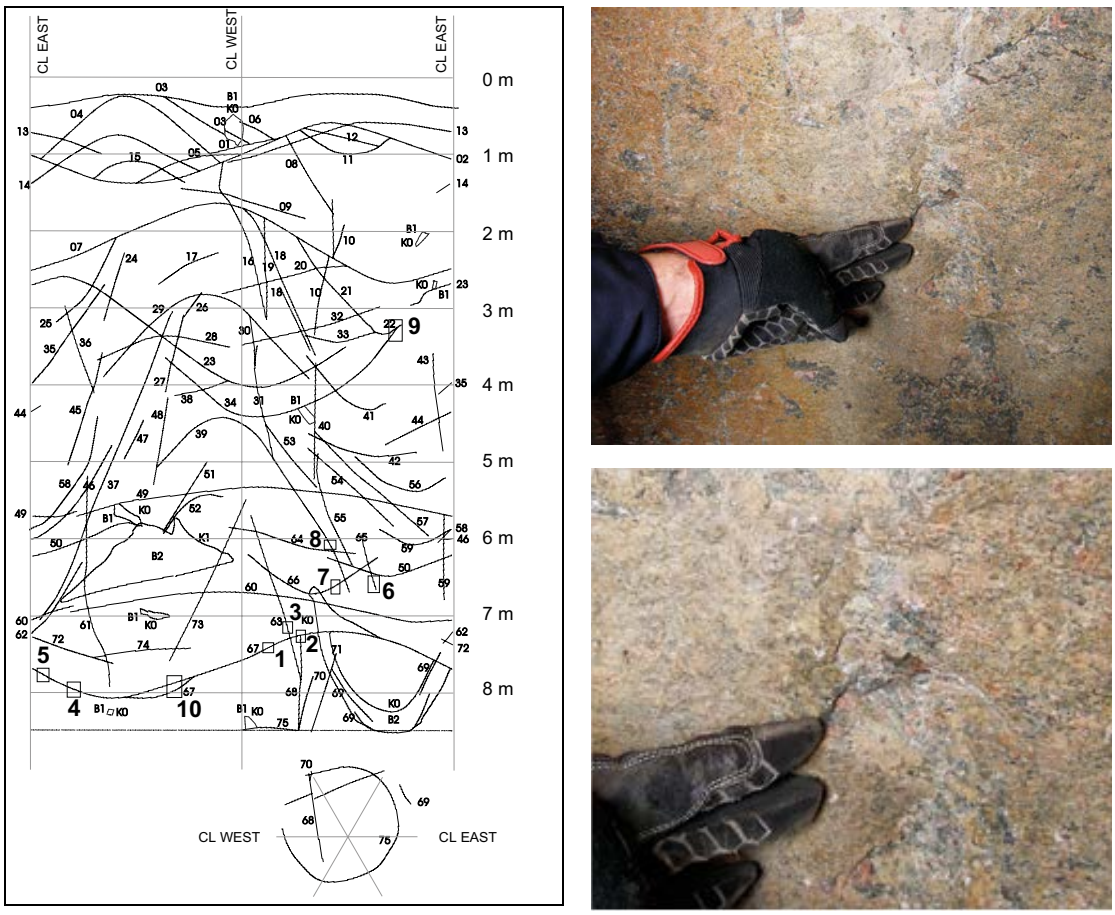

Figure 7-1. *Left: Fracture mapping of Hole 6 (after Rhén and Forsmark 2001). Water bearing features are marked with shaded areas. Top right: Illustration of potential damage to the wall in Hole 6. This area is located approximately at the position marked with the shaded area "9" in the left figure Bottom right: Close-up of the upper right figure.*

7.3 Description of 3DEC models

7.3.1 Geometry

The 3DEC model consists of a 400 m × 400 m × 400 m block of rock in which the tunnel, plug slots and all six deposition holes are explicitly represented (see Figure 7-2). This is the same model that was used for the heated phase in Chapter 6. However, here, this geometry is used for both the excavation phase and for the subsequent heated phase, i.e. no distinction is made between the material properties of the concrete casting at the bottom of the hole and that of the surrounding rock. The depth of all deposition holes is schematically set at 8.1 m.

7.3.2 Input data

Material properties

The thermal, mechanical and thermo-mechanical input parameters to the 3DEC models are listed in Table 7-1. The thermal parameter values are the same as in the Code_Bright model CB 2 (cf. Table 4-1). Parameter values for the mechanical and thermo-mechanical rock properties are chosen from the range established for the APSE test-site (Staub et al. 2004, Andersson 2007). The spalling strength is assumed to be 121 MPa (Staub et al. 2004).

In situ stresses

Five different *in situ* stress models are presented in Table 7-2. The base-case (Case 1) is based on the mean, or average, stress magnitudes and orientations in the stress model given in Section 3.3. Cases 2-5 are bounding estimates based on the ranges of variation in stress magnitudes and orientations given in the stress model (see also Table 6-5). The orientations of the horizontal stress components with respect to the tunnel are also shown in Figure 6-7.

7.3.3 Boundary conditions

The horizontal *in situ* stresses are not aligned with the model axes. Therefore, all vertical boundaries are locked in all directions whereas roller boundaries are applied on the top and bottom boundaries.

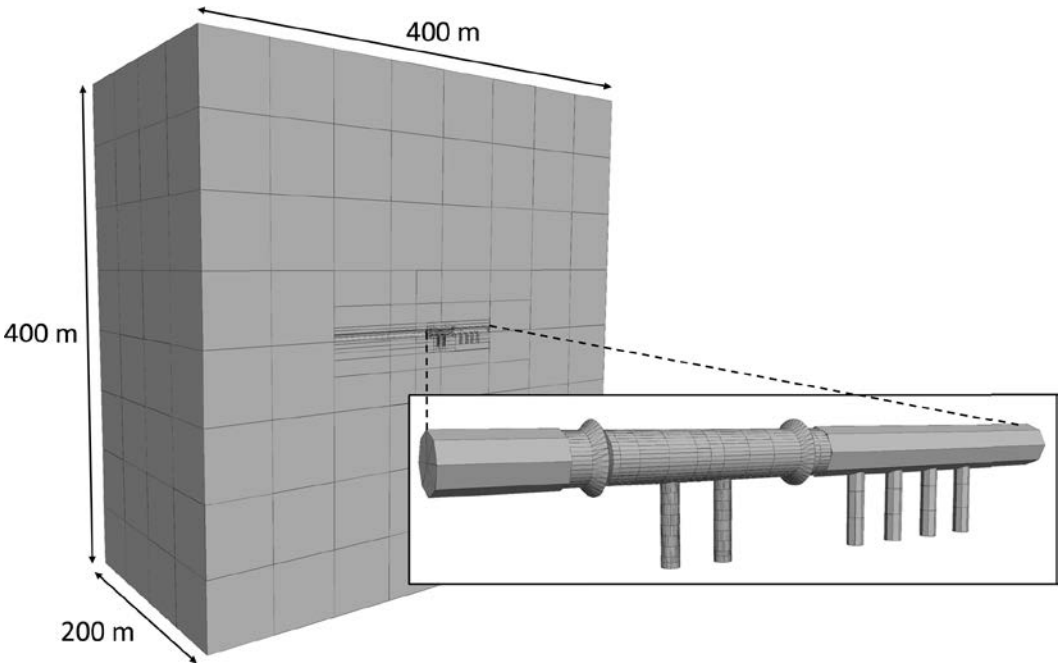

Figure 7-2. *Model geometry in 3DEC. Inset shows the tunnel, deposition holes and plug slots. Note that parts of the model are hidden to expose the tunnel and deposition holes.*

Table 7-1. Thermal, mechanical and thermo-mechanical properties of the rock.

Parameter	Unit	Base-case	Alternative
Thermal conductivity	W/(m·K)	2.72	–
Thermal diffusivity	m^2/s	$1.275 \cdot 10^{-6}$	–
Density	kg/m^3	2,770	–
Young's modulus	GPa	76 (intact rock)	55 (rock mass)
Poisson's ratio	–	0.25	–
Coefficient of thermal expansion	K^{-1}	$7 \cdot 10^{-6}$	$6.2 \cdot 10^{-6}$ (min), $8.3 \cdot 10^{-6}$ (max)

Table 7-2. *In situ* stress models. Magnitudes in MPa; Trend in degrees in the Swedish national RT90 system; Plunge in degrees from horizontal.

Model name	σ1			σ2			σ3		
	Mag.	Trend	Plunge	Mag.	Trend	Plunge	Mag.	Trend	Plunge
Base case (Case 1)	28	304	0	14	214	0	12.8	–	90
Case 2	28	294	0	14	204	0	12.8	–	90
Case 3	28	314	0	14	224	0	12.8	–	90
Case 4	30	304	0	13	214	0	12.8	–	90
Case 5	26	304	0	15	214	0	12.8	–	90

7.3.4 Calculation sequence

The response of the rock mass to changes in mechanical and thermal conditions is assessed in five general steps:

1. A primary equilibrium is established,
2. the tunnel is excavated,
3. the deposition holes are excavated,
4. the plug slots are excavated and
5. the thermal impact is determined.

7.3.5 Model map

A summary of the studied models is provided in Table 7-3.

Table 7-3. Model map.

Model type	Model code	Description
Base-case	P1	Base-case material properties and *in situ* stresses
Variation in Young's modulus	P2	Base-case material properties and *in situ* stresses. Proportions of intact rock and rock mass Young's modulus are varied, cf. Figure 7-8.
	P3	
	P4	
	P5	Same as model P1 but with "rock mass" Young's modulus
Variation in *in situ* stress*	P1-Case2	Base-case material properties and alternative *in situ* stresses Case 2, 3, 4 and 5.
	P1-Case3	
	P1-Case4	
	P1-Case5	
Variation in coefficient of thermal expansion**	P1 ($\alpha = 6.2 \cdot 10^{-6}\ K^{-1}$)	Base-case material properties and *in situ* stresses but with maximum or minimum value of the coefficient of thermal expansion
	P1 ($\alpha = 8.3 \cdot 10^{-6}\ K^{-1}$)	

*Excavation only. Thermal stress additions are added in a post-processing step.

**Thermal stress additions only. Excavation stresses are added in a post-processing step.

7.4 Results

7.4.1 Base-case models

There is always some scatter in stress magnitudes in a 3DEC model due to irregular block sizes and zone sizes. In order to get a representative value for the maximum tangential stress in the walls of a deposition hole, the stresses are averaged over a volume consisting of rock a radial distance of less than 2 cm from the hole perimeter, a vertical distance of ± 10 cm from canister mid-height (–5 m) and at azimuths of ± 10° of the maximum stress.

Excavation

Hökmark et al. (2010) suggested that the more gentle stress path, compared with SKB's spalling experiments APSE (Andersson 2007) or CAPS (Glamheden et al. 2010), that can be expected in a KBS-3 repository may reduce the amount of spalling during the excavation and increase the spalling strength during the subsequent heated phase. Therefore, a more detailed excavation sequence (steps 2–4) was considered in one model with base-case material properties and *in situ* stresses to demonstrate the stress path for the Prototype Repository. The excavation sequence and the evolution of the maximum stress at –0.5 m and at –5 m are shown in Figure 7-4 (middle). Figure 7-4 (bottom) shows the corresponding stress path. Contrary to e.g. APSE, the excavation of one deposition hole does not influence the state of stress in the other one meaning that the stress path is the same in both holes. Furthermore, the excavation of the tunnel has almost no effect on the stresses at the –5 m level.

Heated phase

An example of the stress path in Hole 5 during the excavation and during the subsequent heated phase is shown in Figure 7-5.

The temporal evolution of the major principal stress at 0.5 m and at 5 m below the tunnel in the walls of Holes 5 and 6 is shown in Figure 7-6 and Figure 7-7, respectively. Although the stresses are highest in the uppermost parts of the holes, the stress magnitudes are mainly controlled by stress redistribution effects, i.e., the thermal stress additions are comparatively small. At canister mid-height, the thermal stress addition increases the major principal stress by about 35 MPa (or about 50% of the stress after excavation).

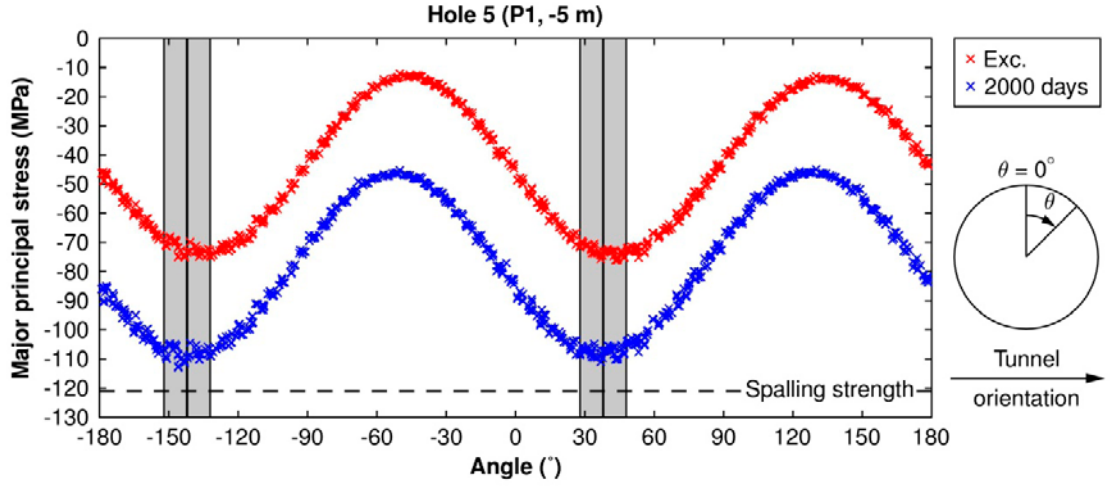

Figure 7-3. *The major principal stress as function of azimuth in Hole 5 at canister mid-height (–5 m) after excavation and after 2,000 days of heating.*

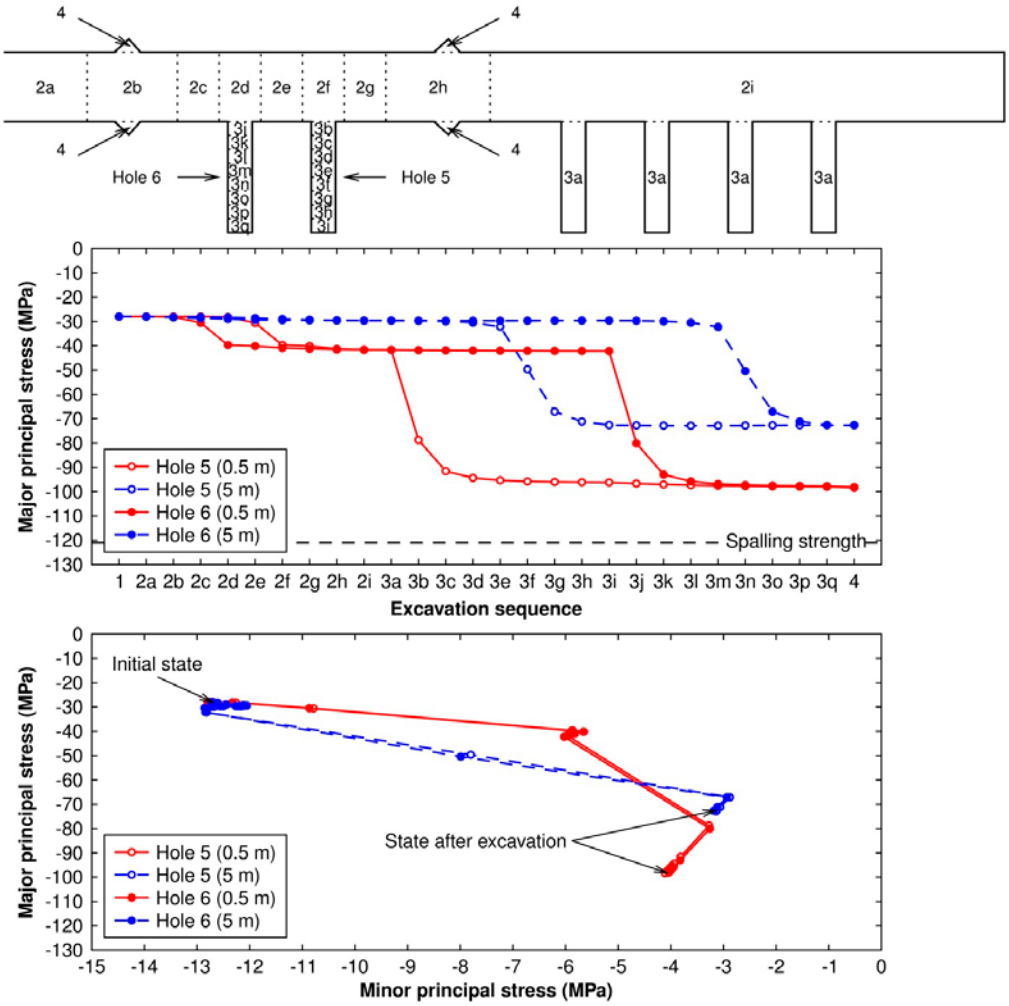

Figure 7-4. *Top: Excavation sequence. Step 1: initial equilibrium. Steps 2a–2i: excavation of the tunnel. The thinnest slices (2c–2g) have a thickness of 3 m. Step 3a: excavation of Holes 1–4 in the inner section simultaneously. Steps 3b–3i: excavation of Hole 5 in slices of 1 m. Steps 3j–3q: excavation of Hole 6 in slices of 1 m. Step 4: excavation of both plug slots simultaneously. Middle: Development of the major principal stress at –0.5 m depth and at canister mid-height (–5 m) during the excavation phase. Bottom: Corresponding stress paths at –0.5 m depth and at canister mid-height.*

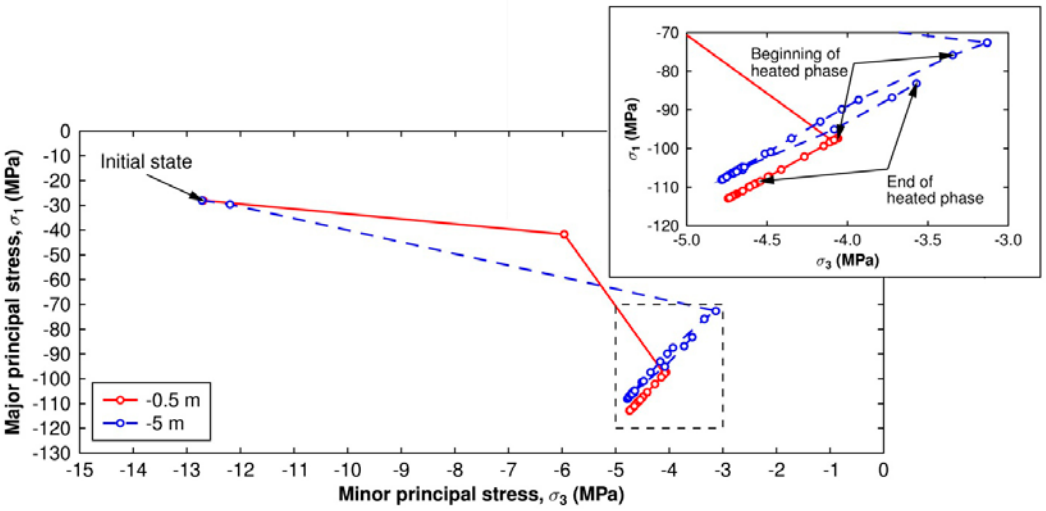

Figure 7-5. *Examples of the stress paths at –0.5 m and at canister mid-height (–5 m) in Hole 5. The inset shows a close-up of the heated phase (region marked with a dashed line). Arrows mark the initial state of stress and the state of stress at the modelled beginning and end, respectively, of the heated phase.*

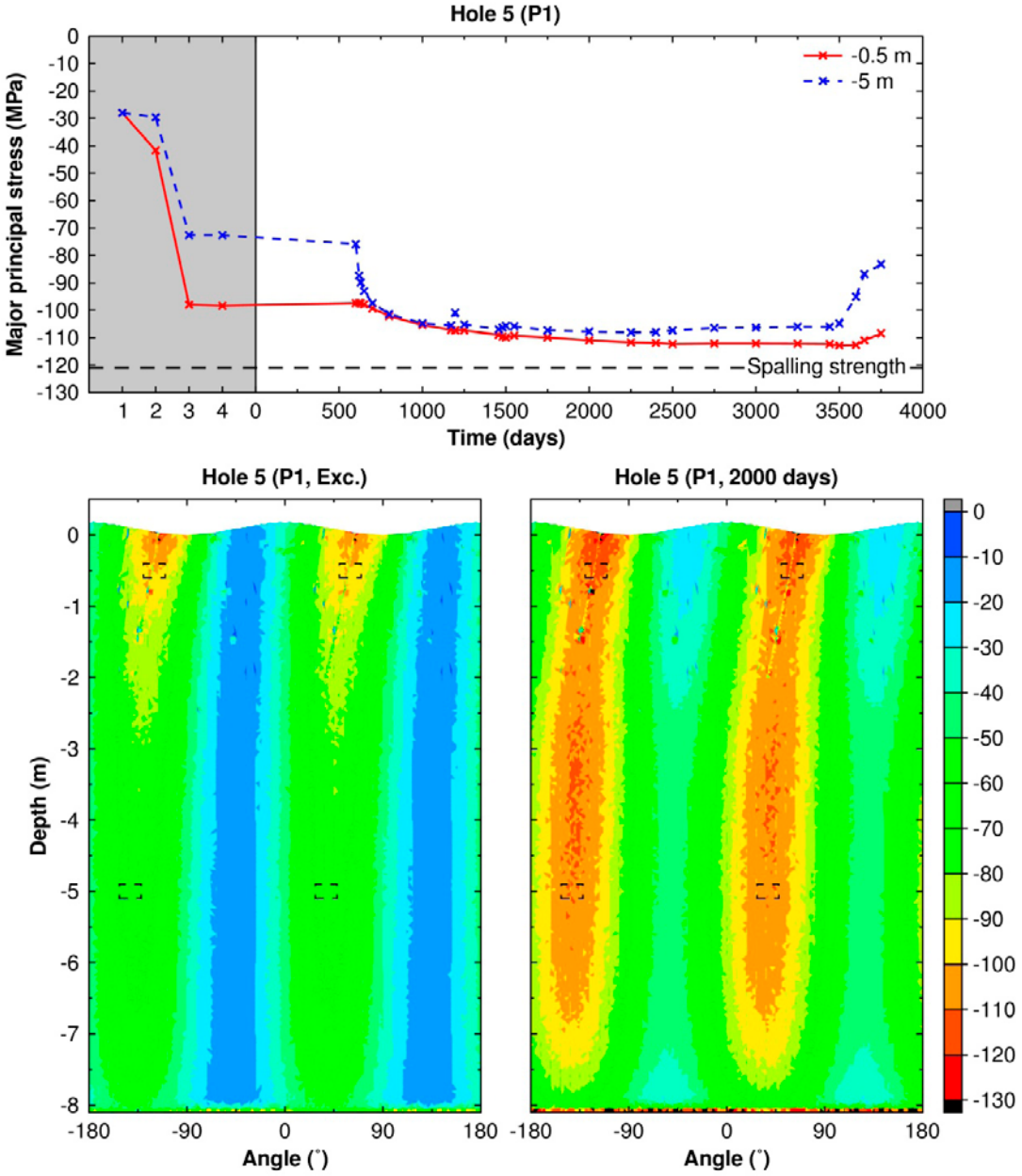

Figure 7-6. *Top: Temporal development of the major principal stress at –0.5 m depth and at canister mid-height (–5 m) in Hole 5. Grey area represents pre thermal time with 1) initial state of stress, 2) excavation of tunnel, 3) excavation of deposition holes and 4) excavation of plug slots. Bottom: Contour plots of the major principal stress after excavation (left) and after 2,000 days of heating (right). Contours in MPa. Dashed rectangles represent the areas used to evaluate the stresses in the upper figure.*

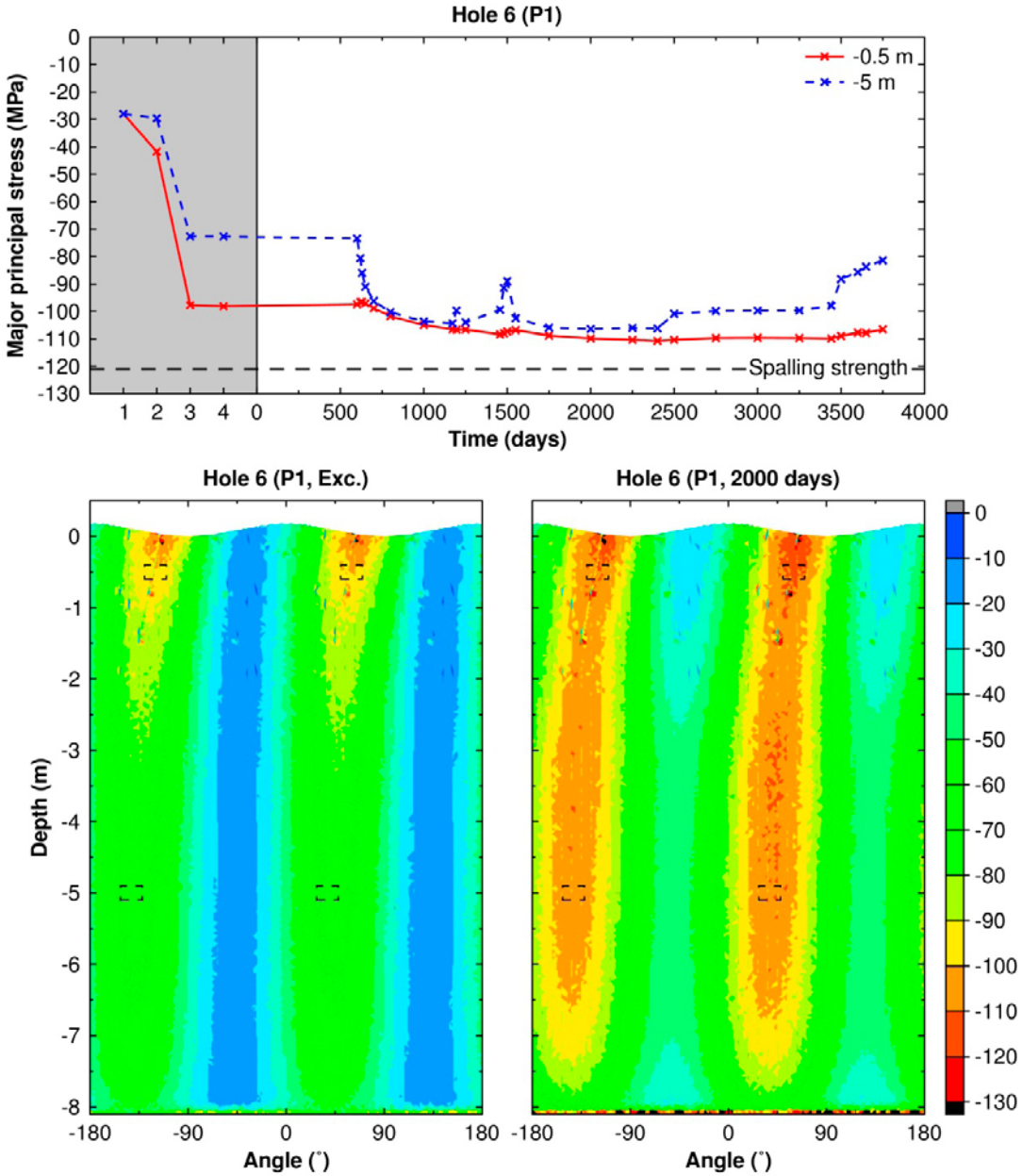

Figure 7-7. *Top: Temporal development of the major principal stress at –0.5 m depth and at canister mid-height (–5 m) in Hole 6. Grey area represents pre thermal time with 1) initial state of stress, 2) excavation of tunnel, 3) excavation of deposition holes and 4) excavation of plug slots. Bottom: Contour plots of the major principal stress after excavation (left) and after 2,000 days of heating (right). Contours in MPa. Dashed rectangles represent the areas used to evaluate the stresses in the upper figure.*

7.4.2 Alternative material properties and *in situ* stresses

In an infinite linear elastic medium with homogeneous properties, the excavation stresses are independent of Young's modulus and the thermal stress additions scale with the product of Young's modulus and the coefficient of linear thermal expansion. For heterogeneous properties, the situation is more complicated. On a large scale, stresses may be represented well by a global "rock mass" value of the rock's elastic properties (e.g. Hakami et al. 2008). However, in the near-field, e.g. around individual deposition holes, local material heterogeneities and individual fractures may play a more important role in determining the magnitude of the stresses.

Variation in Young's modulus

In the present study, five models (labelled P1–P5) with different proportions of "intact rock" and "rock mass" properties (cf. Table 7-1) are considered. Models P1 and P5 have homogeneous elastic properties with the value of Young's modulus set either to that of "intact rock" or "rock mass", respectively. In models P2, P3 and P4 different volumes of rock around the deposition holes in the outer section are assigned "intact rock" properties (see Figure 7-8) whereas the remaining part of the model is assigned "rock mass" properties. It should be noted that none of these correspond to any observed variability in intact rock properties.

The highest stresses occur after approximately 2,000 days of heating (Figure 7-9) with the greatest increase in thermal stress in the walls of Hole 5. Contour plots of the major principal stress in Hole 5 are provided for the state after excavation and after 2,000 days of heating for models P4 (largest overall stresses) and P5 (least overall stresses), see Figure 7-10 and Figure 7-11. If the subdivision of the rock between intact rock and rock mass as in model P4 (Figure 7-10) can be considered representative of the rock in the prototype repository, the major principal stress exceeds the nominal spalling strength in the uppermost 0.5 m of the deposition holes. In the other models, there is no indication of sufficiently high stresses to initiate spalling.

In the models with large volumes of intact rock (P1, P2 and P3), the magnitude of the major principal stress differs only marginally between the models. The model with a small volume of intact rock around the deposition holes (P4) has the overall highest stresses. However, the increase in thermal stress is less than that for the model with intact rock everywhere (P1). The model with rock mass everywhere (P5) has the overall least stresses. For the models with uniform values of Young's modulus (P1 and P5), the stresses after excavation are the same and the thermal stress additions scale linearly with Young's modulus.

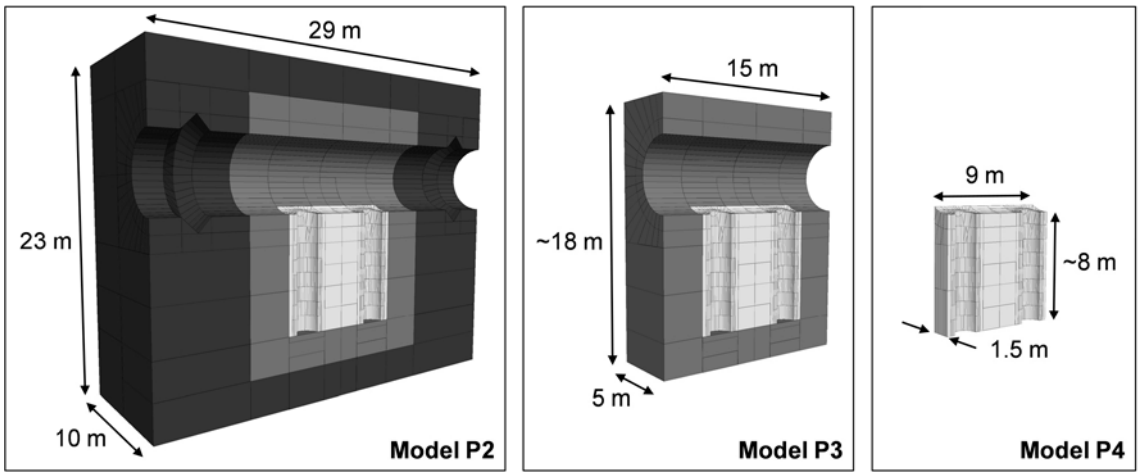

Figure 7-8. *Schematic view of 3DEC models P2, P3 and P4.*

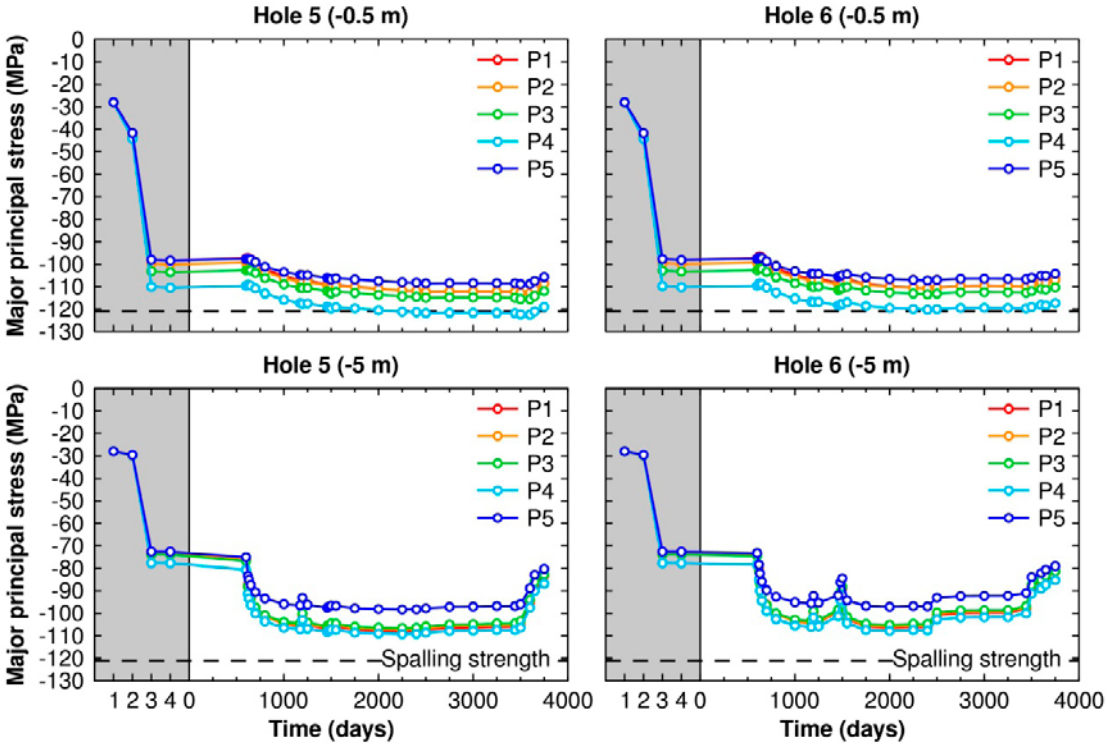

Figure 7-9. *Temporal development of the major principal stress at –0.5 m depth and at canister mid-height (–5 m) in Hole 5 (left column) and in Hole 6 (right column) for models with different proportions of "rock mass" properties and "intact rock" properties. Grey area represents pre thermal time with 1) initial state of stress, 2) excavation of tunnel, 3) excavation of deposition holes and 4) excavation of plug slots.*

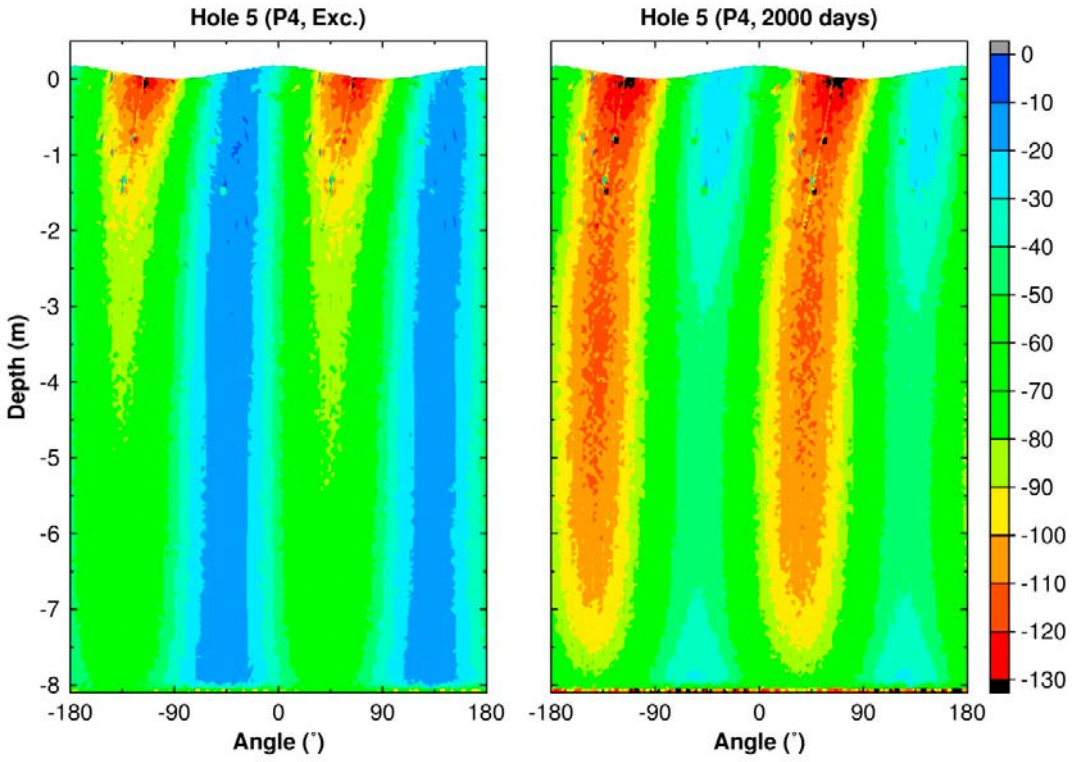

Figure 7-10. *Contour plots of the major principal stress (model P4) around Hole 5 after excavation (left) and after 2,000 days of heating (right).*

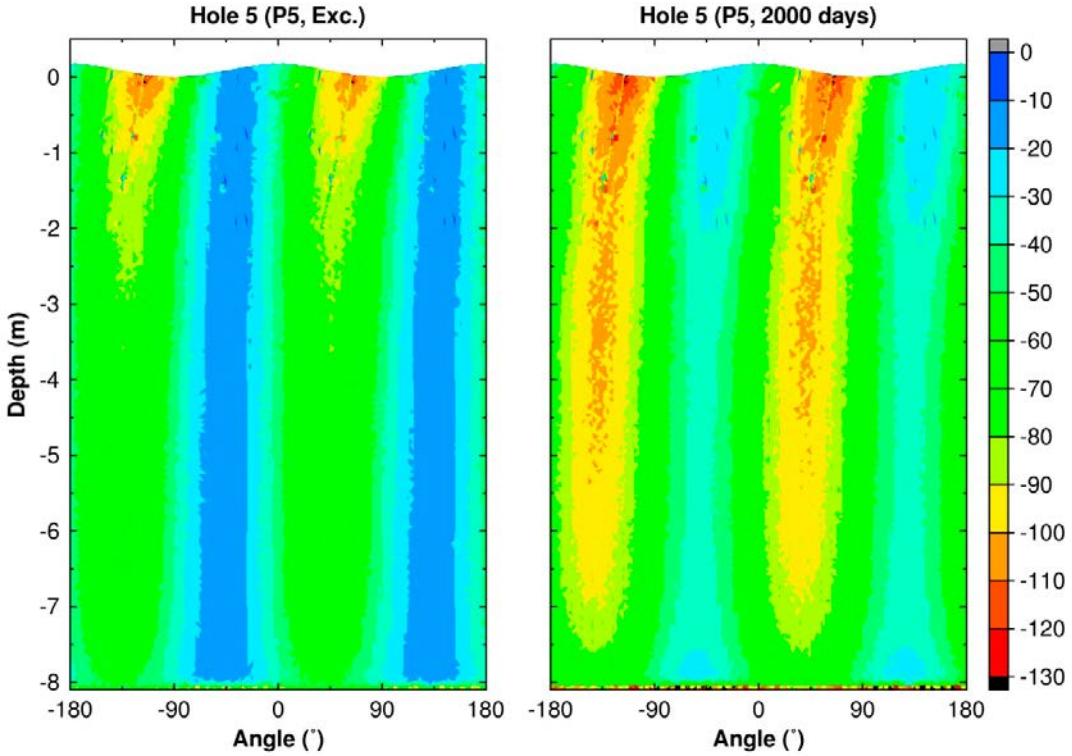

Figure 7-11. *Contour plots of the major principal stress (model P5) around Hole 5 after excavation (left) and after 2,000 days of heating (right).*

Variation in thermal expansion coefficient

For variations of the expansion coefficient in the range $6.2 \cdot 10^{-6}$–$8.3 \cdot 10^{-6}$ K^{-1}, the impact on the major principal stress at the position of maximum stress in the uppermost part of hole is small, see Figure 7-12 (top row). At canister mid-height, the major principal stress obtained for the larger value of the coefficient of thermal expansion is within a few MPa of the spalling strength at the time of stress maximum (Figure 7-12, bottom row). The variations in stress with azimuth and depth along the walls of Hole 5 are shown in Figure 7-13.

Variation in in situ stress

Figure 7-14 shows the temporal evolution of the major principal stress evaluated at the position of maximum stress at –0.5 m and –5 m. Stress contours as functions of depth and azimuth around the deposition hole perimeter of Hole 5 are presented in Figure 7-15 to Figure 7-18. At the –5 m level, there is very little difference between the *in situ* stress models with the same stress magnitudes but different orientations (Case 1, 2 and 3) although the location of maximum stress differs (cf. Figure 7-6, Figure 7-15 and Figure 7-16). The models with the lowest and highest initial horizontal stress anisotropy (Case 4 and 5) have the lowest and highest stresses, respectively. For the stress cases with the major principal *in situ* stress oriented at a large angle with respect to the tunnel or the stress case with the largest horizontal stress anisotropy (Case 3 and Case 4), the nominal spalling strength is reached or exceeded in the uppermost parts of the deposition holes.

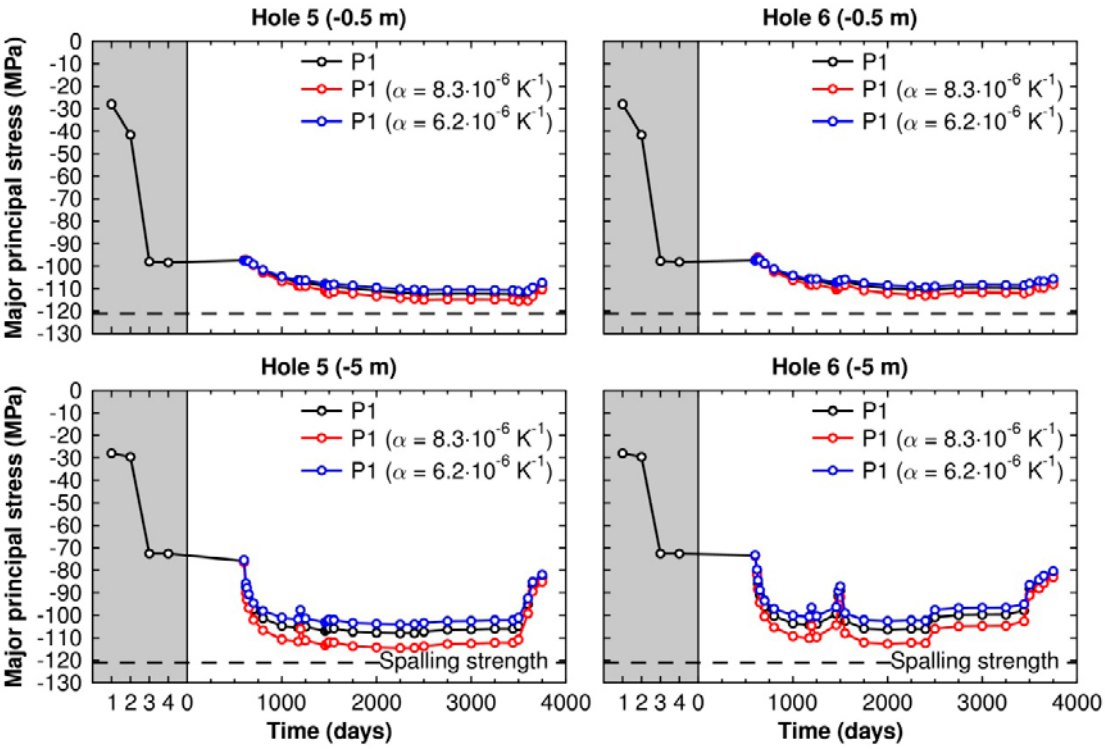

Figure 7-12. *Temporal development of the major principal stress at –0.5 m depth and at canister mid-height (–5 m) in Hole 5 (left column) and in Hole 6 (right column) for different values of the coefficient of thermal expansion. Grey area represents pre thermal time with 1) initial state of stress, 2) excavation of tunnel, 3) excavation of deposition holes and 4) excavation of plug slots.*

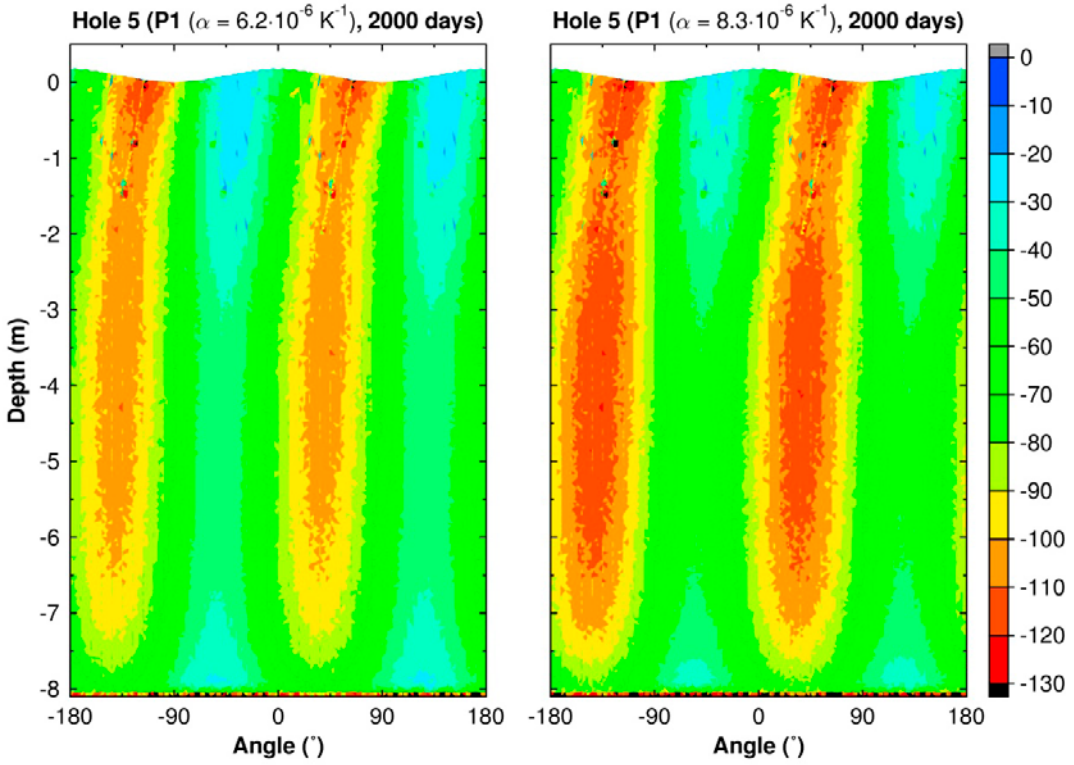

Figure 7-13. *Contour plots of the major principal stress after 2,000 days of heating for a value of the coefficient of thermal expansion of $6.2 \cdot 10^{-6}$ K^{-1} (left) and $8.3 \cdot 10^{-6}$ K^{-1} (right).*

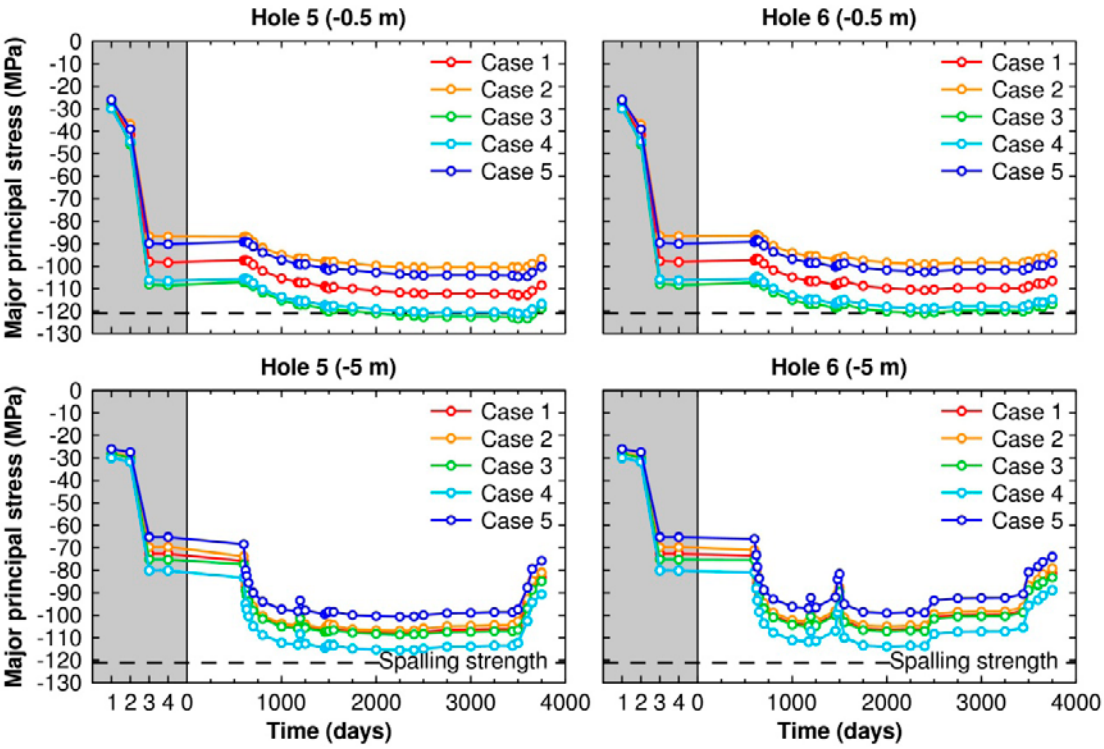

Figure 7-14. *Temporal development of the major principal stress at –0.5 m depth and at canister mid-height (–5 m) in Hole 5 (left column) and in Hole 6 (right column) for base-case material properties but different in situ stress models. Grey area represents pre thermal time with 1) initial state of stress, 2) excavation of tunnel, 3) excavation of deposition holes and 4) excavation of plug slots.*

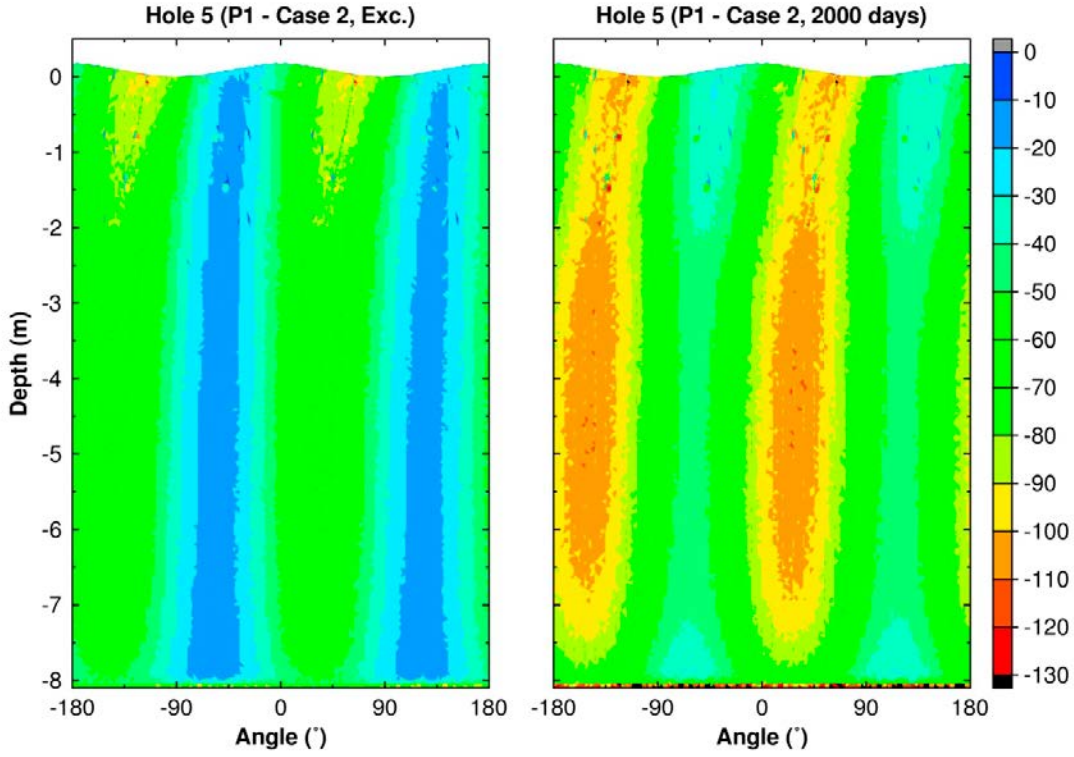

Figure 7-15. *Contour plots of the major principal stress (model P1, Case 2) around Hole 5 after excavation (left) and after 2,000 days of heating (right).*

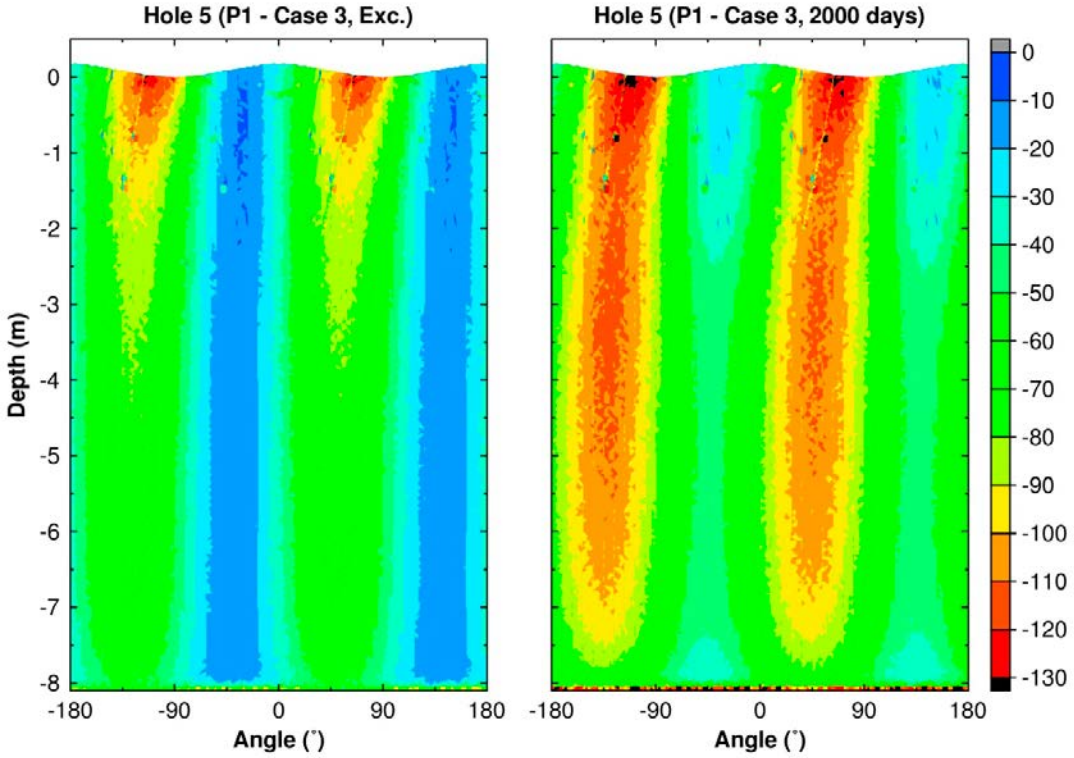

Figure 7-16. *Contour plots of the major principal stress (model P1, Case 3) around Hole 5 after excavation (left) and after 2,000 days of heating (right).*

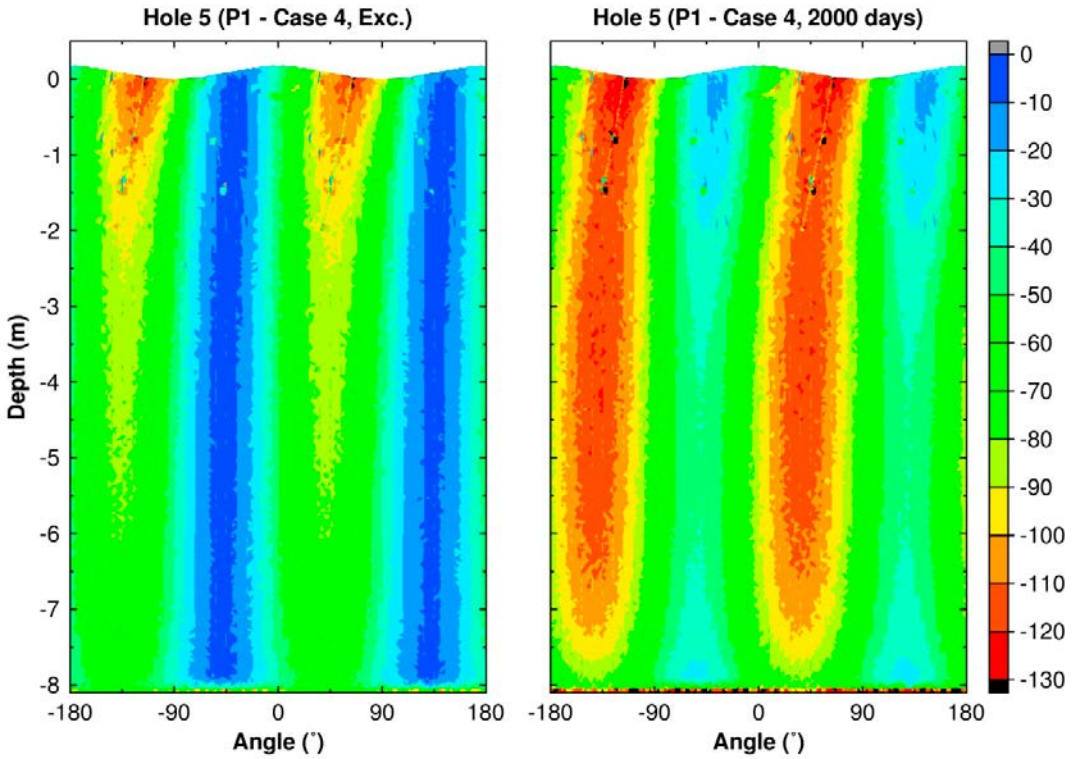

Figure 7-17. *Contour plots of the major principal stress (model P1, Case 4) around Hole 5 after excavation (left) and after 2,000 days of heating (right).*

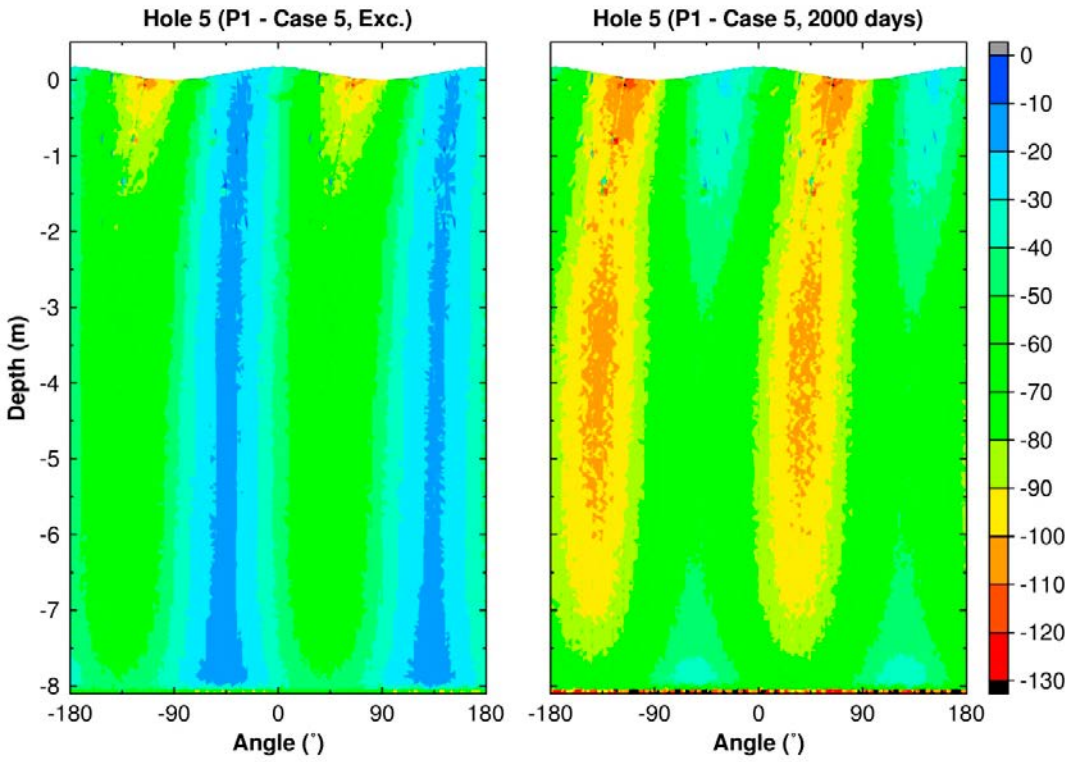

Figure 7-18. *Contour plots of the major principal stress (model P1, Case 5) around Hole 5 after excavation (left) and after 2,000 days of heating (right).*

7.5 Summary

The potential for spalling was assessed assuming the holes were unsupported and that the spalling strength was 121 MPa (corresponding to 57% of the uniaxial compressive strength) (Staub et al. 2004). Given the range of variation in material properties (Staub et al. 2004, Andersson 2007) suggested for the APSE test site and *in situ* stresses considered relevant for the rock mass within the Prototype Repository (cf. Section 3.3), no systematic occurrences of spalling (other than locally at the top of the deposition holes) were predicted by the models. While this is in keeping with the visual observations, i.e., that no spalling had occurred in the walls of the deposition holes, it should be noted that the small support pressure provided by the pellets in the slot between the bentonite blocks and the rock may be sufficient to suppress the initiation of spalling (Glamheden et al. 2010). The absence of spalling is, therefore, an uncertain indication of the magnitudes of the tangential stresses.

8 Influence of near-field fractures

In this chapter, a qualitative assessment is made of the impact of a simplistic fracture network on the stresses in the walls of the around the deposition holes and on the stress addition tensor at the measurement locations. The stability (see also Appendix E) and normal stress variations of selected fracture planes intersecting the repository openings are also assessed.

8.1 Description of 3DEC model

8.1.1 Model geometry

For computational efficiency and for numerical stability, the 3DEC model considered here is smaller and more coarsely meshed than the linear elastic models analysed in Chapters 6 and 7. Here, the model consists of a 60 m × 60 m × 60 m block of rock, centred on Holes 5 and 6 (see Figure 8-1, left), in which the tunnel, plug slots and the two deposition holes in the outer section are explicitly represented (the four holes in the inner section are not modelled explicitly). The outer dimensions of the model are sufficiently large to accommodate the largest fractures in the fracture model with a margin of approximately 50% of the maximum fracture radius (see below). The circular cross-section of the tunnel and deposition holes is approximated by polygons with 16 tangential sections. Similarly to the models in the previous chapters, no distinction is made between the material properties of the concrete casting at the bottom of the hole and that of the surrounding rock. The depth of the two deposition holes is schematically set at 8 m.

8.1.2 Fracture network

Fourteen fractures intersecting the deposition holes or tunnel were selected from the Prototype fracture model (Figure 3-2) for inclusion in the numerical model. The omitted fractures are located either in the inner section or too far from the outer section to be of importance. Centre points, orientations and radii for the selected fractures are listed in Table 8-1. Following the modelling approach made by e.g. Hökmark et al. (2010) all fractures regardless of shape in the fracture model are approximated to be circular, see Figure 8-1 (top right). This is accomplished by assigning actual fracture properties to a circular area of the fracture plane (Figure 8-1, bottom right) and fictitious high-strength/high-stiffness properties to the remaining parts of the plane, see e.g. Fälth et al. (2010, Appendix B) for details.

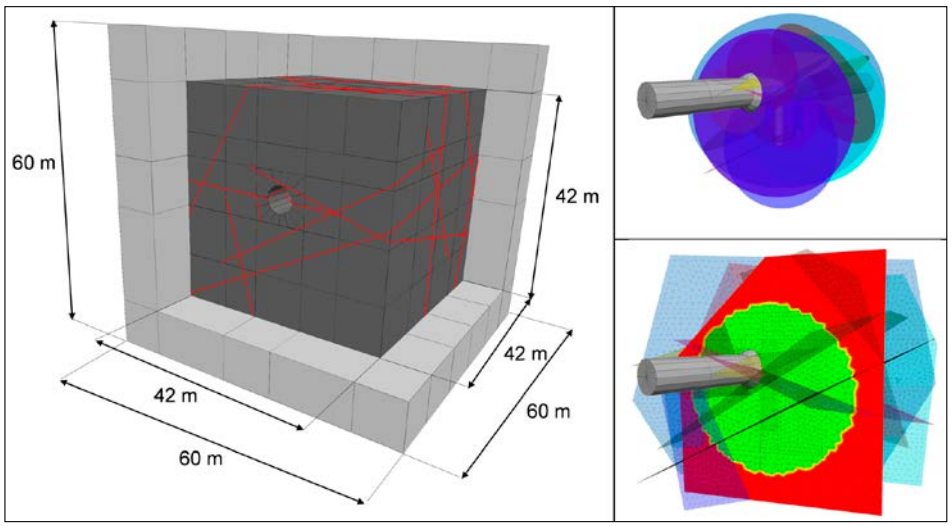

Figure 8-1. *Left: Model geometry in 3DEC. Fracture traces marked in red are real fracture planes with orientations selected from the fracture model. All other traces are construction planes that are mechanically invisible. Top right: Circular fractures intersecting the deposition tunnel and holes. Bottom right: Implementation of circular fractures in 3DEC.*

Table 8-1. Sizes and orientations of the selected fractures from the fracture model (cf. Figure 3-2). Fracture centre points and orientations are given in 3DEC coordinates.

Fracture ID	Fracture ID (3DEC)	Centre point* x (m)	y (m)	z (m)	Dip direction** (°)	Dip (°)	Radius (m)
Mod NW W2	264	–0.3	–0.2	–1.8	44	68	19.2
G W 10	265	0.6	0.8	–0.9	344	32	18.3
G W1	266	0.6	0.8	–6.5	342	28	17.9
NNW Dry 2	267	9.6	2.6	–2.4	248	79	16.4
G Dry 3	268	0.1	0.71	1.1	143	20	14.9
NNW W7	269	–9.6	–3.7	–1.3	66	89	14.5
Mod NNE Dry 1	270	5.1	–3.5	2.8	110	58	14.1
G W11	271	–6.0	0.7	6.4	267	15	12.4
WNW W3	272	–2.4	–0.8	–8.3	208	75	11.6
G Dry 4	273	–1.0	–0.4	3.9	316	31	9.1
WNW W8	274	–7.1	–0.2	6.2	204	77	6.9
WNW W5	275	2.7	0.9	–3.8	19	87	6.4
NW W9	276	–10.6	2.9	–0.3	44	85	5.0
G W4	277	–3.4	0.7	–5.7	215	22	3.8

*Deposition Holes 5 and 6 are located at (3,0,z) and (–3,0,z), respectively, with z = 0 m in the floor of the tunnel.

**Dip direction is measured clockwise from the positive y-axis.

8.1.3 Input data

Material properties

Similarly to the analyses in the previous chapters, the rock mass (between the fractures) is assumed to behave as a linear elastic continuum. Here, one set of mechanical and thermo-mechanical rock properties corresponding to those of intact rock (Staub et al. 2004) is considered. For the fractures, an idealised elasto-plastic material model is chosen with constant normal and shear stiffness, zero tensile strength and a Mohr-Coulomb shear strength criterion. The selected fracture properties values are consistent with average lab-scale values obtained in the Laxemar site-investigation (Hakami et al. 2008). All material property values are listed in Table 8-2. Results for models with other friction angles are presented in Appendix G.

Table 8-2. Base-case material properties.

Component	Property	Unit	Value
Rock	Thermal conductivity	W/(m·K)	2.72
	Thermal diffusivity	m^2/s	$1.275 \cdot 10^{-6}$
	Density	kg/m^3	2,770
	Young's modulus	GPa	76
	Poisson's ratio	–	0.25
	Coefficient of thermal expansion	K^{-1}	$7 \cdot 10^{-6}$
Fractures*	Friction angle	°	35
	Cohesion	MPa	0
	Tensile strength	MPa	0
	Normal stiffness	GPa/m	700
	Shear stiffness	GPa/m	40
Fictitious fractures properties**	Friction angle	°	63
	Cohesion	MPa	500
	Tensile strength	MPa	500
	Normal stiffness	GPa/m	70,000
	Shear stiffness	GPa/m	4,000

*Properties assigned to a circular area of the selected fracture planes.

**Properties assigned to all fracture planes outside the circular areas.

In situ stress

The *in situ* stress model (see Table 8-3) is based on the mean, or average, stress magnitudes and orientations given in the stress model presented in Section 3.3. A Mohr-circle plot of the *in situ* state of stress and stability of the selected fractures is provided in Figure 8-2.

Pore pressure

The pore pressure is set uniformly in all fractures, i.e., no account is made of the variations in pore pressure with proximity to the tunnels or deposition holes. Bounding estimates of the pore pressure are obtained by considering two cases (see Figure 8-3):

1. The pore pressure in all fractures is kept constant at all times at the hydrostatic pressure level relevant for undisturbed *in situ* conditions at the –450 m-level ($\rho \cdot g \cdot z$ = 4.4 MPa).
2. The pore pressure in all fractures is initially kept at hydrostatic pressure level but reduced instantaneously to 0 MPa at the beginning of the excavation phase and subsequently kept constant at 0 MPa.

Table 8-3. *In situ* stress model. Magnitudes in MPa; Trend in degrees in the Swedish national RT90 system; Plunge in degrees from horizontal.

Model name	σ1 Mag.	Trend	Plunge	σ2 Mag.	Trend	Plunge	σ3 Mag.	Trend	Plunge
Base case (Case 1)	28	304	0	14	214	0	12.8	–	90

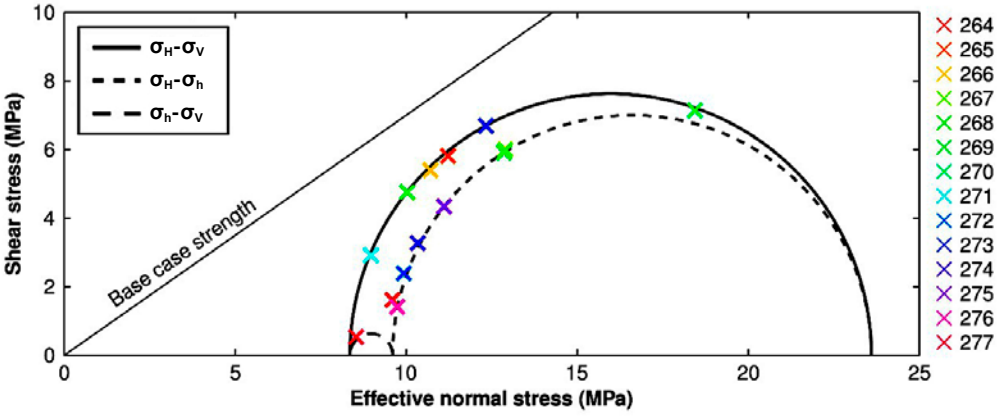

Figure 8-2. *Mohr-circle plot of the in situ state of stress and initial base case shear strength of the selected fractures.*

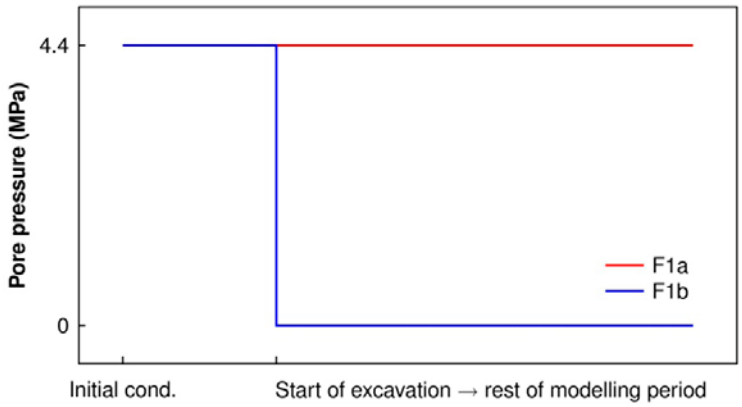

Figure 8-3. *Schematic view of the two pore pressure models: constant hydrostatic pore pressure (model F1a) and reduced pore pressure at the beginning of the excavation phase (model F1b).*

8.1.4 Modelling sequence and boundary conditions

The response of the rock mass and fractures to changes in mechanical and thermal conditions is assessed in five general steps (see Figure 8-4 for details):

1. A primary equilibrium is established,
2. the tunnel is excavated,
3. the deposition holes are excavated,
4. the plug slots are excavated and
5. the thermal impact is determined.

During the initial equilibrium, the excavation of the tunnel, deposition holes and plug slots, the boundaries are locked in all directions. For the subsequent heated phase, the expansion/contraction of the model boundaries as the temperature in the rock mass changes is replicated by importing thermally induced displacements at the boundary locations from the interior of a larger linear-elastic model with the same material properties and heat load (see Appendix F for details).

8.1.5 Model map

Results from three models are presented in this chapter:

- A linear elastic model without fractures (*F1E*).
- Two models with fracture network as given in Table 8-1 and different assumptions regarding the pore pressure (cf. Figure 8-3).
  - Full hydrostatic pore pressure in all fractures throughout the entire modelling period (*F1a*).
  - Reduced pore pressure from the start of the excavation and throughout the entire modelling period (*F1b*).

Models with alternative friction angles are described in Appendix G.

8.2 Modelling results

8.2.1 Stresses in deposition hole walls

There are seven fractures that intersect the two deposition holes in the outer section (cf. Figure 8-5). Out of these, two fractures (#265 and #266) intersect both holes.

As seen in Figure 8-6 and Figure 8-7, the disturbance caused by a combination of elastic and plastic shear displacements along the intersecting fractures is more prominent in the walls of Hole 5 than in Hole 6. This appears to be mainly due to the sub-vertical fracture (#275) that intersects Hole 5.

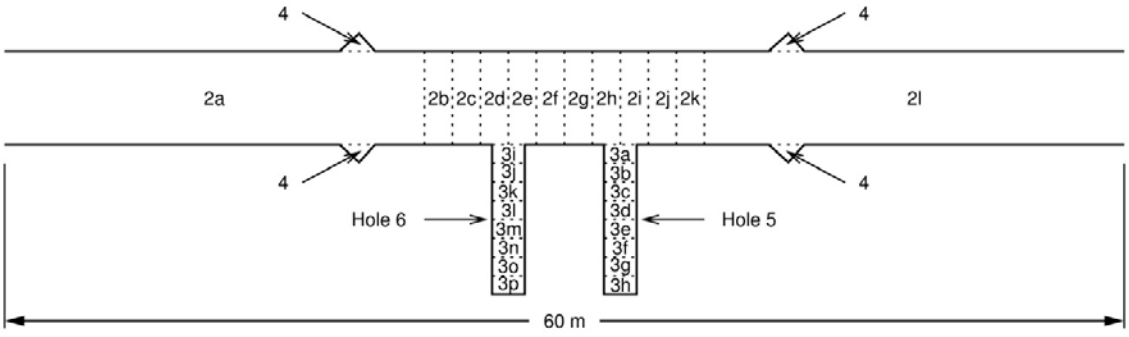

Figure 8-4. *Excavation sequence for base-case models. Steps 2a–2l: excavation of the tunnel. The thinner slices (2b–2k) have a thickness of 1.5 m. Steps 3a–3h: excavation of Hole 5 in slices of 1 m. Steps 3j–3p: excavation of Hole 6 in slices of 1 m. Step 4: excavation of both plug slots simultaneously.*

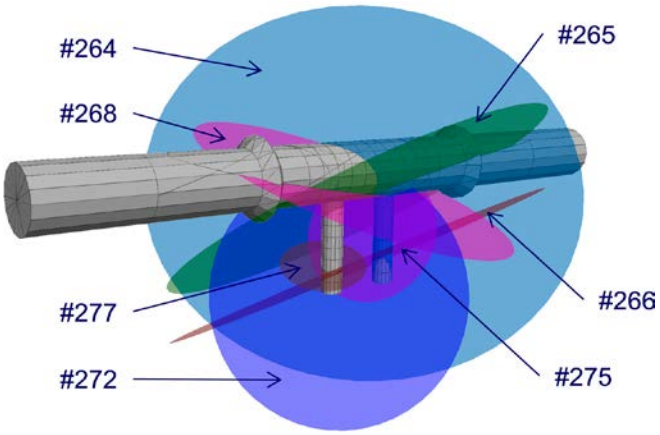

Figure 8-5. *View of fractures that intersect the deposition holes.*

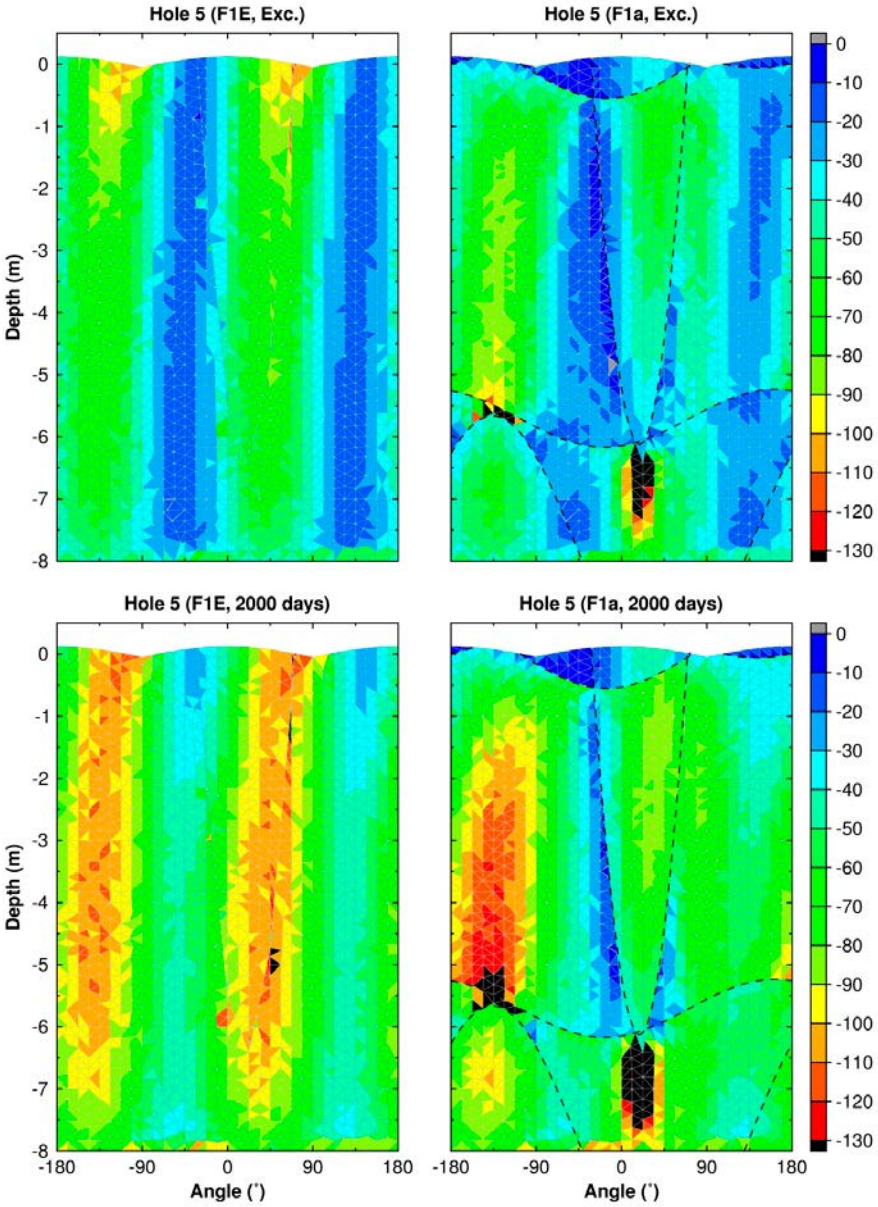

Figure 8-6. *Contour plots of the major principal stresses around Hole 5 after excavation for the linear elastic model (top left) and for the model with fractures, F1a (top right). Bottom row shows corresponding results after 2,000 days of heating. Contours in MPa. Fracture intersections are marked with dashed lines.*

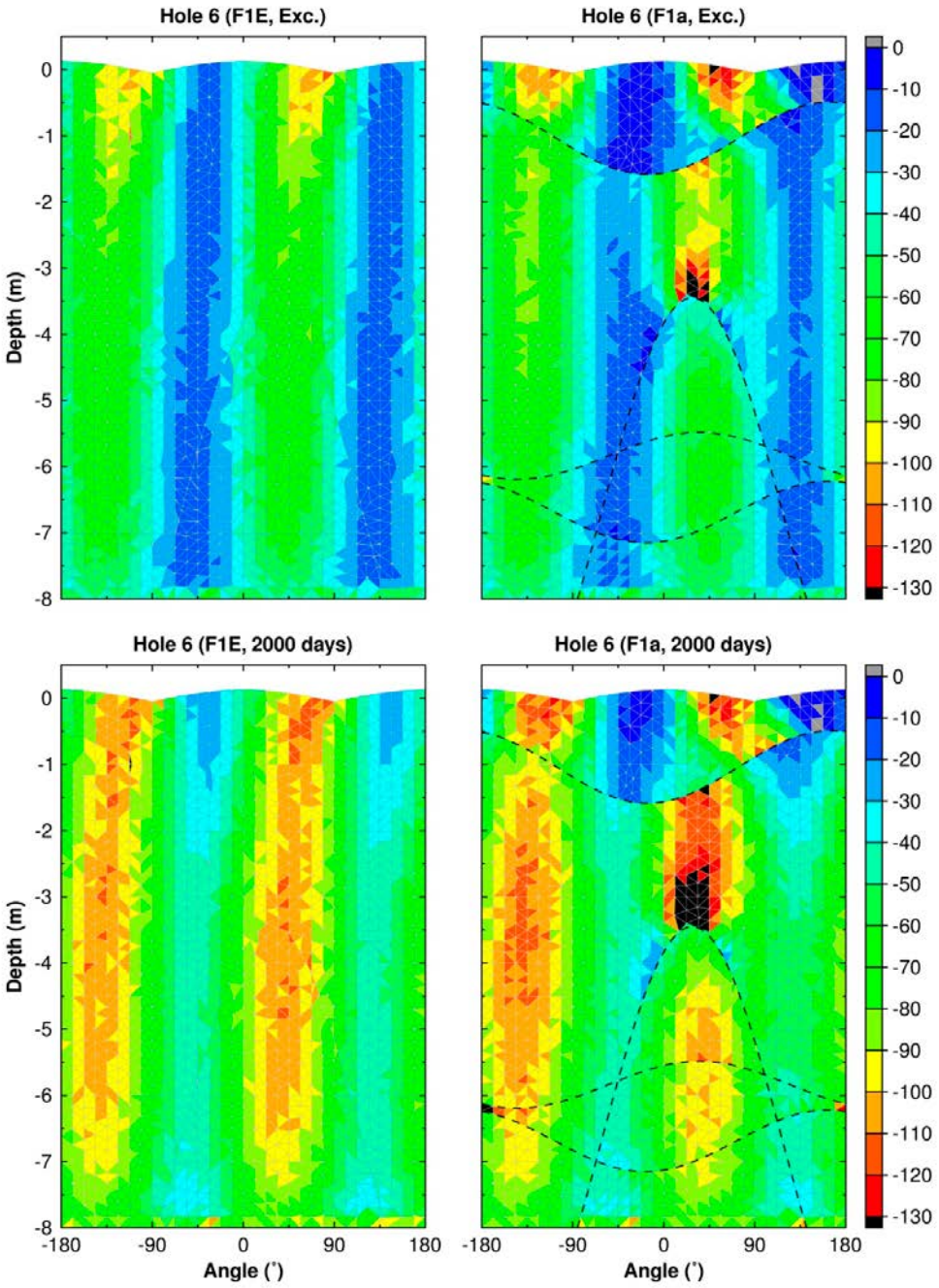

Figure 8-7. *Contour plots of the major principal stresses around Hole 6 after excavation for the linear elastic model (top left) and for the model with fractures, F1a (top right). Bottom row shows corresponding results after 2,000 days of heating. Contours in MPa. Fracture intersections are marked with dashed lines.*

At the tip of the intersections of the steeply dipping fractures in both deposition holes, there are stress concentrations that are above the nominal spalling strength already after excavation. During the heated phase, the stress concentrations at these points increase (cf. bottom sub-figures of Figure 8-6 and Figure 8-7). As expected, increasing the shear strength of the fractures by reduction of the pore pressure such as in model F1b results in less disturbance to the stress-field than in the model with high pore pressure, F1a. In the model with low pore pressure, there is only a local disturbance close to the steeply dipping fracture intersecting Hole 6 whereas the stresses in the walls of Hole 5 are relatively unaffected by the variations in fracture pore pressure (see Figure 8-8).

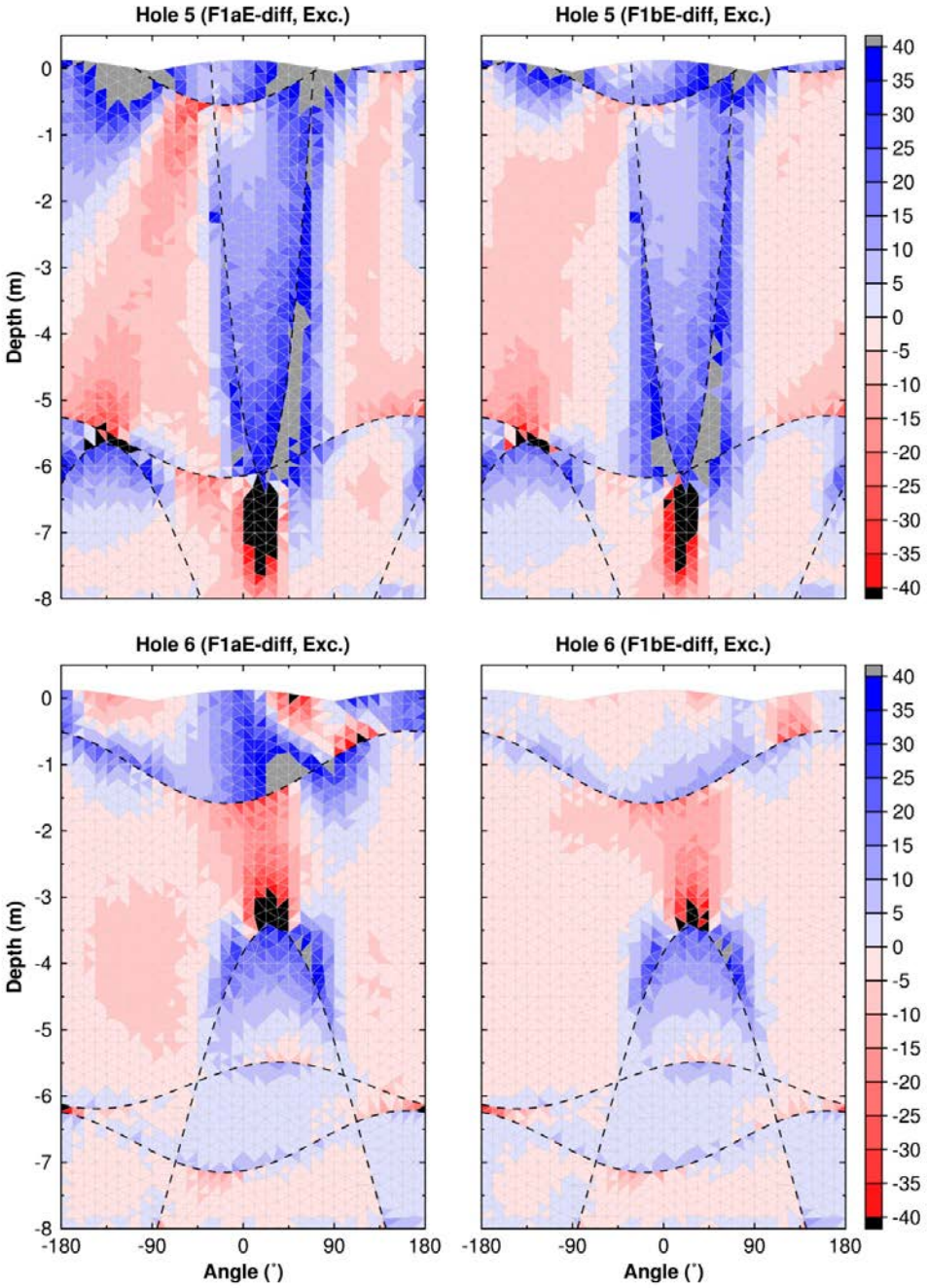

Figure 8-8. *Contour plots of the difference in major principal stress between model F1a and the elastic model (top left) and between model F1b and the elastic model (top right) around Hole 5 after excavation. Bottom row: Corresponding results for Hole 6. Contours in MPa where blue colours represent a reduction in compression and red colours an increase in compression compared with the elastic model. Fracture intersections are marked with dashed lines.*

8.2.2 Stresses at measurement locations

The fractures also disturb the horizontal components of the stress addition tensor at a distance of 0.3 m from the deposition hole perimeter (see Figure 8-9 and Figure 8-10). Similarly to the stresses in the walls of the deposition holes, there is more disturbance to the stress-field in Hole 5 than in Hole 6. The magnitude of the pore pressure influences the results mainly in the uppermost parts of the hole where high pore pressure would de-stabilize rock blocks in the floor of the tunnel (cf. Figure 8-9 and Figure 8-10).

Although the positions for the biaxial stressmeters were selected to avoid rock fractures (Bono and Röshoff 2003), the two figures below show that the stresses could be disturbed by fractures that would not necessarily be visible in any of the small boreholes the stress meters are located in. One clear example in the model is the sub-vertical fracture (#275) that intersects the rock on either side of the measurement position A5:Bi. Stress increases as well as reductions of at maximum 10 MPa are observed in the model. Thus, some of the 5–10 MPa anomalies in the measurement data (cf. Figure 6-19) could very well be attributed to disturbances caused by intersecting fractures. However, the details of the localisations of the disturbances cannot be captured by the simplistic representation of the fracture network.

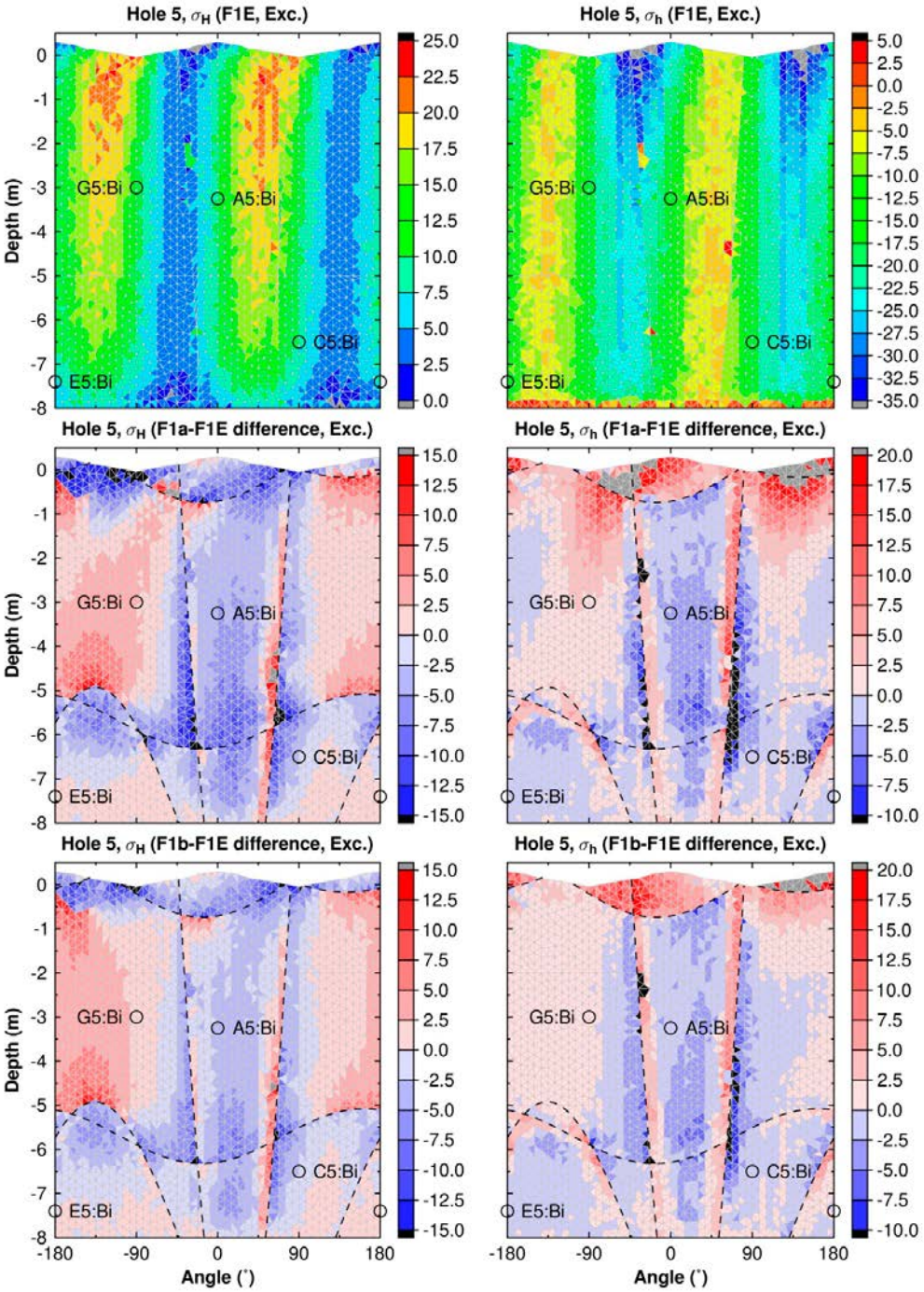

Figure 8-9. *Major (top left) and minor (top right) horizontal component of the stress addition tensor around Hole 5 after excavation for the linear elastic model. Middle: Difference between corresponding stress components in the fracture model (F1a) and the elastic model. Bottom: Corresponding results for model F1b and the elastic model. Contours in MPa. Fracture intersections are marked with dashed lines.*

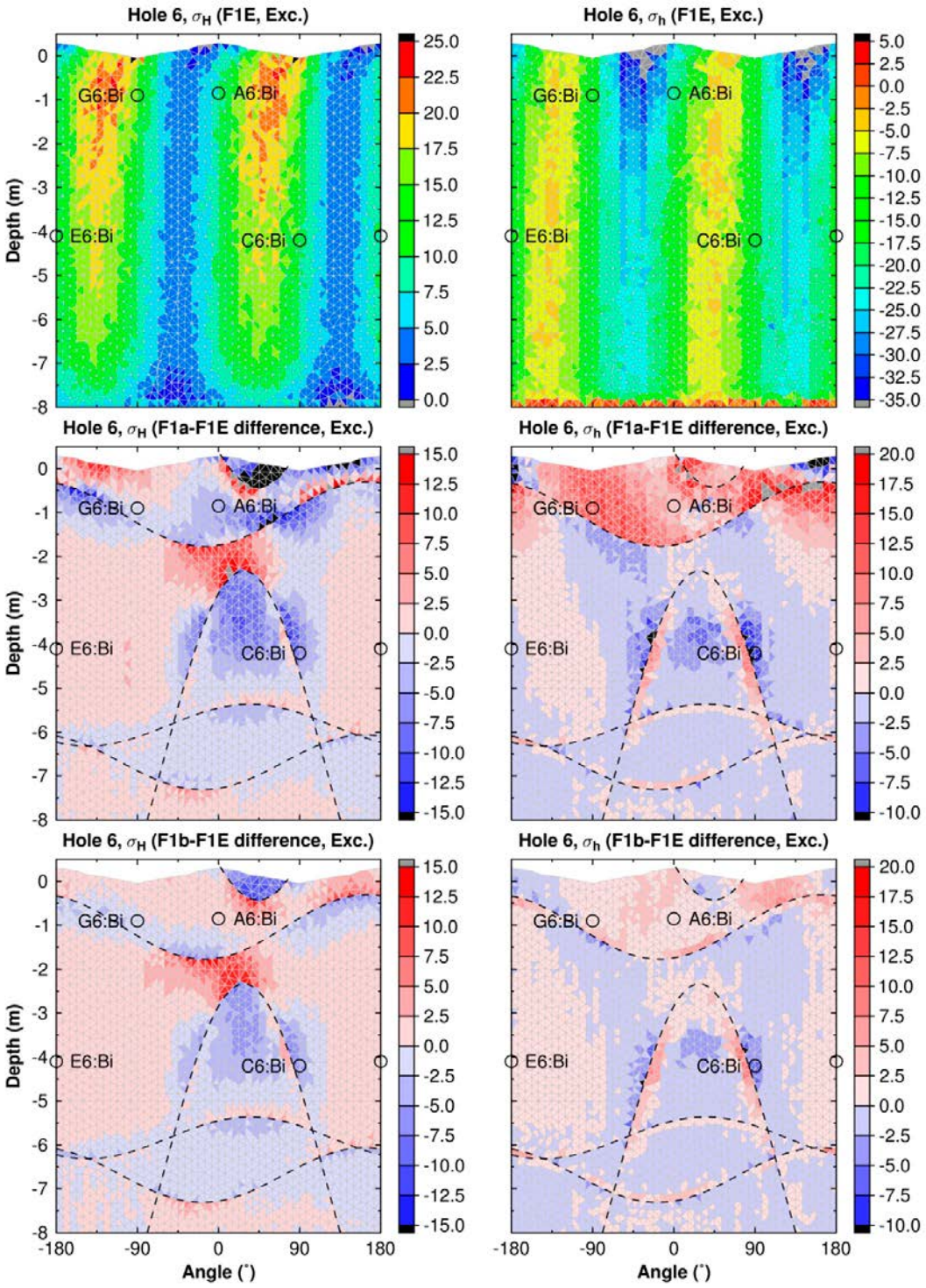

Figure 8-10. *Major (top left) and minor (top right) horizontal component of the stress addition tensor around Hole 6 after excavation for the linear elastic model. Middle: Difference between corresponding stress components in the fracture model (F1a) and the elastic model. Bottom: Corresponding results for model F1b and the elastic model. Contours in MPa. Fracture intersections are marked with dashed lines.*

8.2.3 Wedge displacements

For the simplistic fracture network considered here, wedges with large displacements are formed in the floor of tunnel between the two deposition holes when the pore pressure is kept at the hydrostatic level throughout the modelling period (see Figure 8-11, left column). Accounting for the lower pore pressure close to the tunnel by reducing the pore pressure in all fractures from 4.4 MPa to 0 MPa during excavation stabilises these blocks (Figure 8-11, right column).

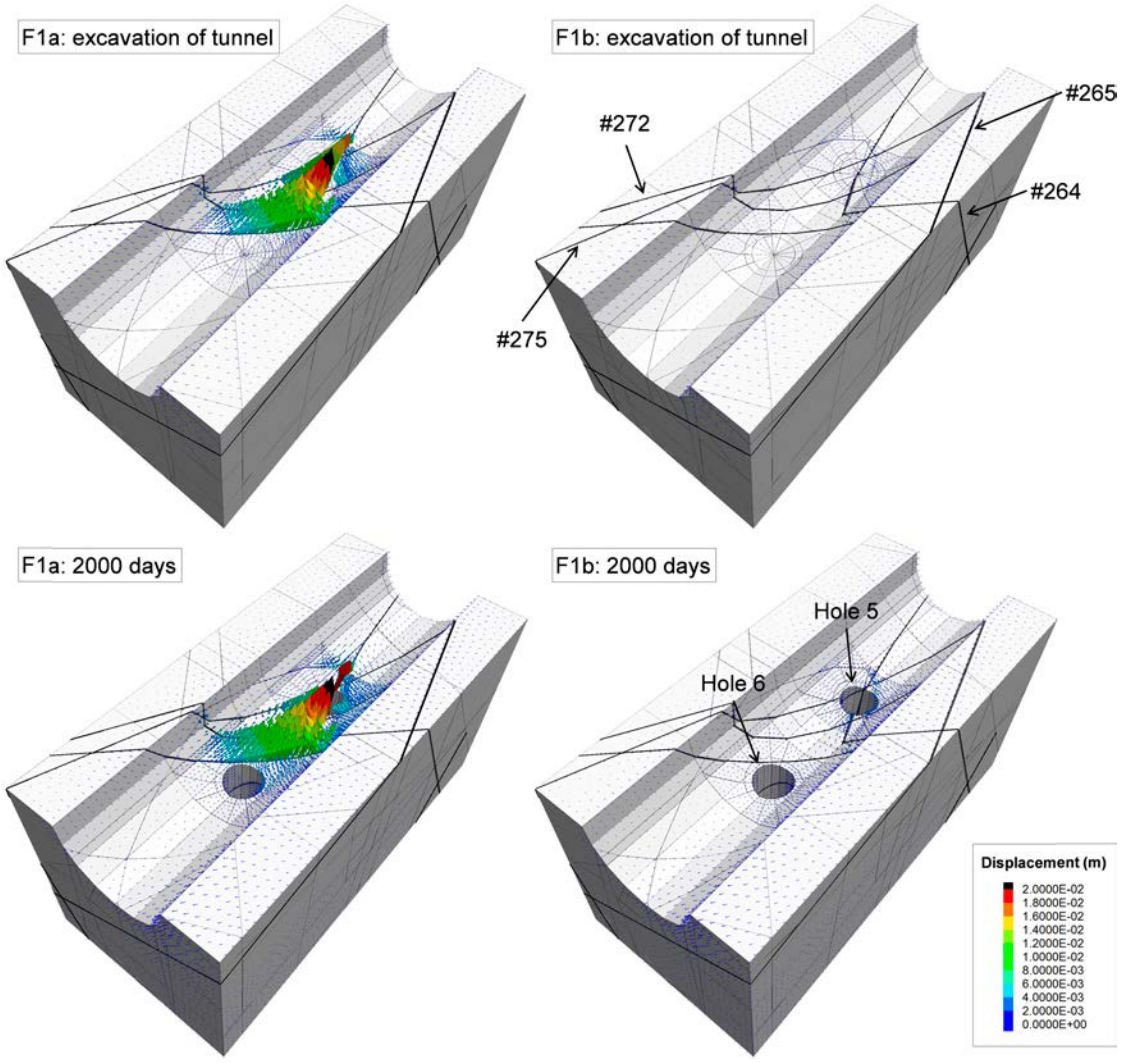

Figure 8-11. *View of displacement vectors in the floor of the tunnel for model F1a (left column) and model F1b (right column).*

8.2.4 Fracture deformations

For the base-case *in situ* stress and shear strength properties of the fractures, all fractures in the fracture model are initially stable and in good compression (see Figure 8-2). When plotting the maximum area with shear displacements equal to, or exceeding, a given value, there are only four fractures (264, 265, 272 and 275) in the fracture model that have shear displacements exceeding a few millimetres over any significant area at any point in time during the excavation phase or during the subsequent heated phase (see Figure 8-12, left). These fractures form the boundaries of the wedges with large displacements located in the tunnel floor (cf. previous subsection). Accounting for the lower pore pressure close to the tunnel by reducing the pore pressure in all fractures from 4.4 MPa to 0 MPa during excavation stabilises these blocks (cf. top row of Figure 8-11) reduces the maximum shear displacements very efficiently (see Figure 8-12, right).

Since fracture 265 has the largest shear displacements for both models, results for this fracture are used as examples. Figure 8-13 shows the cumulative shear displacement after excavation of the tunnel and at the end of the modelling period. Shear displacements exceeding 1 mm are only found in the region close to the tunnel. For the majority of the surface area, the maximum shear displacement is only fractions of a millimetre. It appears that most of the displacements take place during the excavation with very little additional movements during the heated phase (see Figure 8-14, top left. However, even for the lowest friction angle (25°) tried here, large shear displacements exceeding a few millimetres are only found close to the tunnel (see Appendix G).

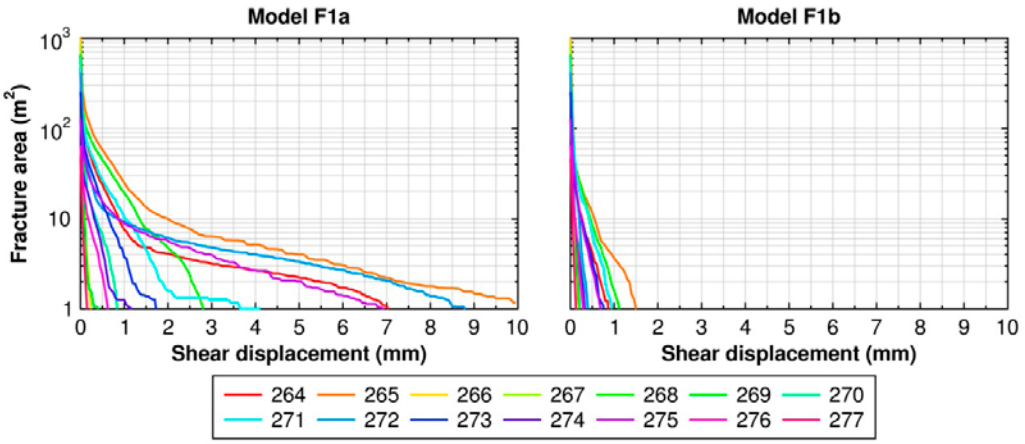

Figure 8-12. *Maximum fracture area with shear displacement equal to, or exceeding, given value for each fracture in the fracture model.*

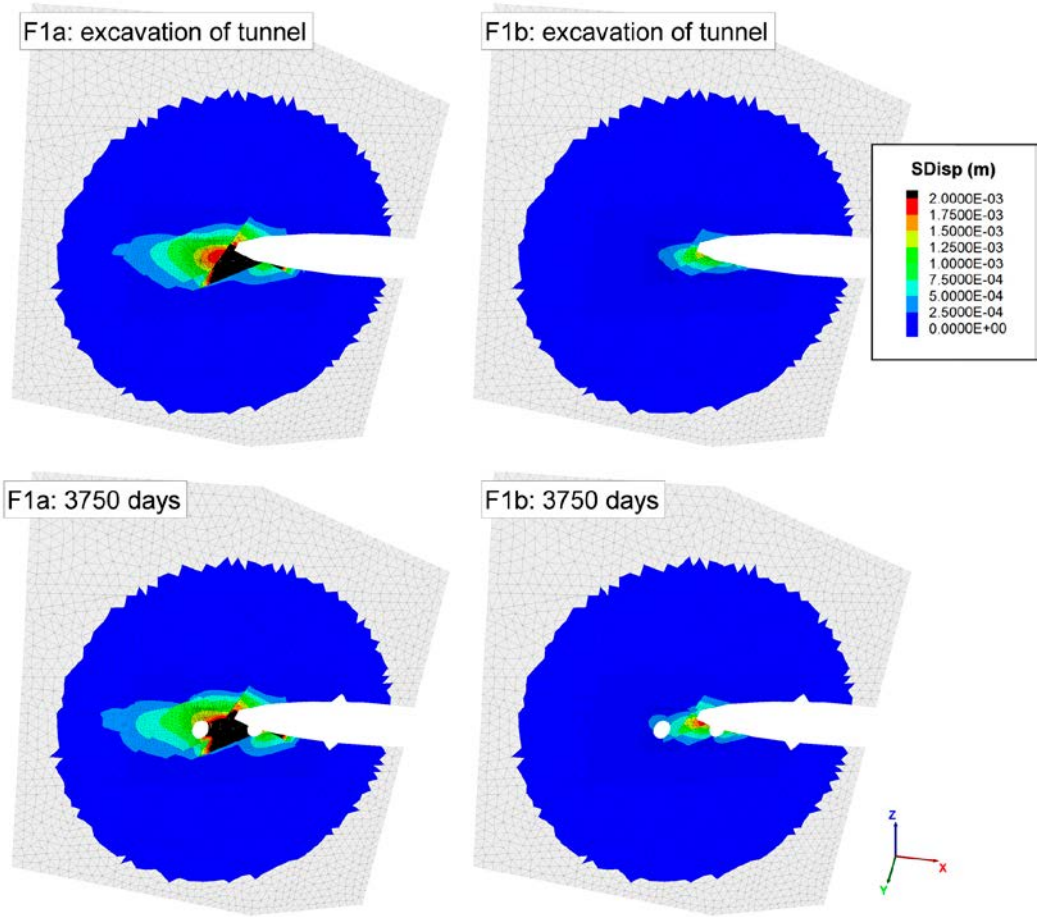

Figure 8-13. *Cumulative shear displacement of fracture 265 after excavation of the tunnel and at the end of the modelling period.*

Regions of low normal stress are found after excavation where the fractures intersect the repository openings or are approximately parallel to them (see Figure 8-15). Given the simplistic fracture network considered here, additional regions of low normal stress are introduced at the boundaries of the wedges with large displacements formed in the floor of the tunnel (cf. top left sub-figures of Figure 8-13 and of Figure 8-15). This is linked to the schematic assignment of pore pressure within the fractures (cf. Figure 8-16, top row). During the heated phase, compression generally increases (see Figure 8-15, bottom row and Figure 8-16, bottom row).

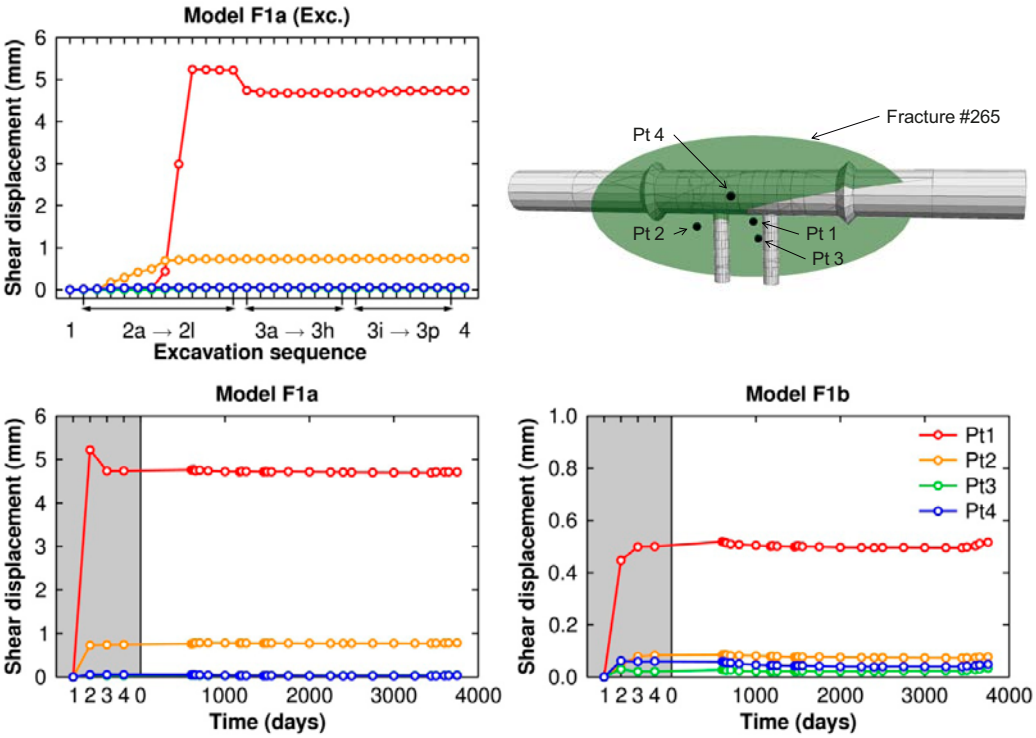

Figure 8-14. *Temporal development of the shear displacement at selected points on Fracture 265 during excavation (top left) and for the subsequent heated phase for Model F1a (bottom left) and for Model F1b (bottom right). Grey area represents pre thermal time with 1) initial state of stress, 2) excavation of tunnel, 3) excavation of deposition holes and 4) excavation of plug slots.*

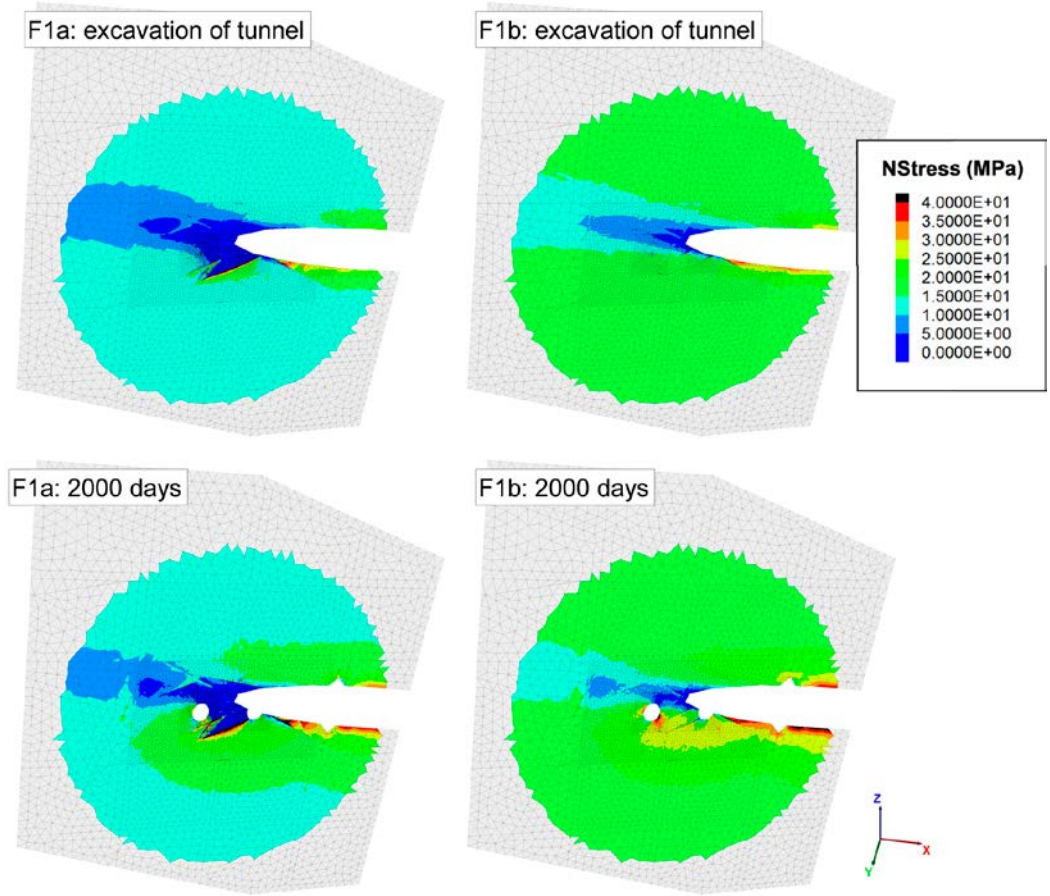

Figure 8-15. *Normal stress variations on fracture 265 after excavation of the tunnel and after 2,000 days of heating.*

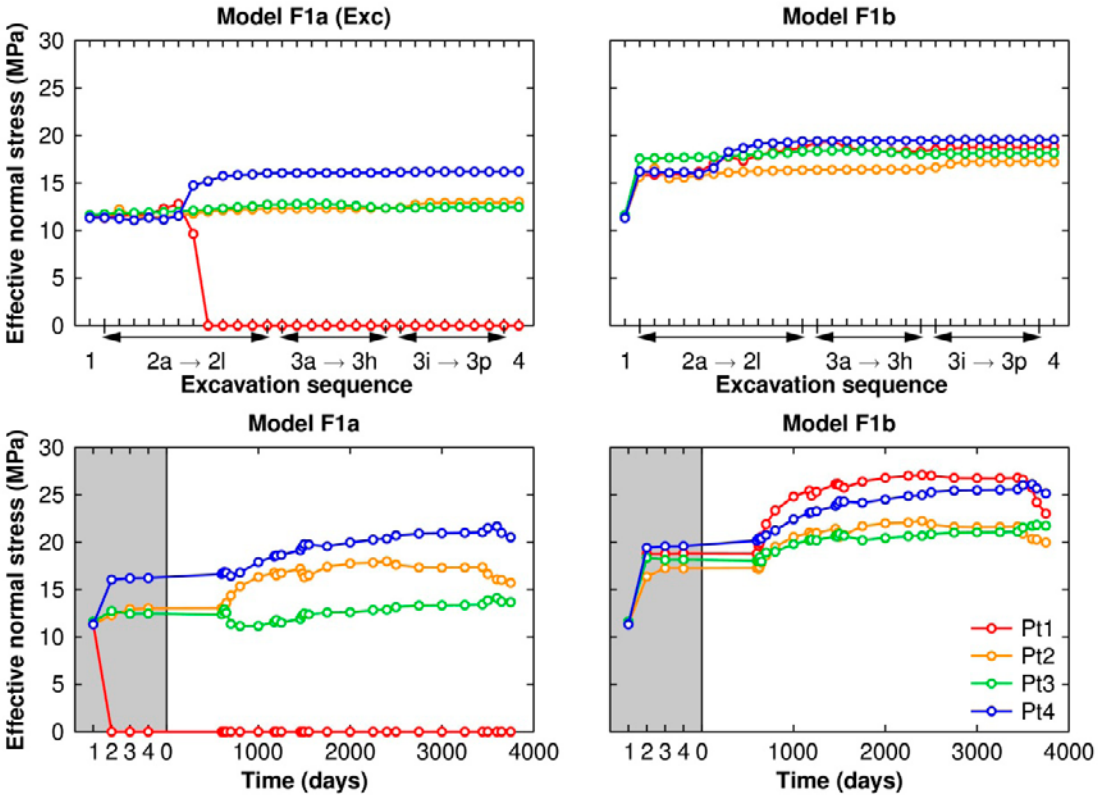

Figure 8-16. *Temporal development of the effective normal stress at selected points on Fracture 265 during excavation (top row) and for the subsequent heated phase (bottom row). Grey area represents pre thermal time with 1) initial state of stress, 2) excavation of tunnel, 3) excavation of deposition holes and 4) excavation of plug slots. For locations of history points, see Figure 8-14 (top right).*

8.3 Summary

The following is concluded:

- There is a significant perturbation of the stresses in the walls of the deposition holes due to the intersecting fractures. At the intersection points of the steeply dipping fractures with the deposition hole walls, there are stress concentrations that are above the nominal spalling strength already after excavation (see Figure 8-6 and Figure 8-7). This is also the case for the model with lower pore pressure and for the models with fracture friction angles as high as 45°. Since no systematic occurrences of spalling were observed in either of the two deposition holes, suggests that the fracture geometry is too schematic.
- Stress concentrations and relaxations due to the intersecting fractures are also observed at the positions of the biaxial stress meters (0.3 m from the deposition hole perimeter). The observed anomalies in the measurement data may, therefore, be partly attributed to disturbances caused by a combination of elastic and plastic shear displacements along intersecting fractures. Differences between the stress additions calculated in the elastic model and those calculated in the models with fractures are of the same order of magnitude as the anomalies indicated in Figure 6-19 but occur at different locations.
- Given the fracture network considered here, wedges with large displacements are formed in the floor of the tunnel between the deposition holes. Accounting for the lower pore pressure close to the tunnel by reducing the pore pressure in all fractures from 4.4 MPa to 0 MPa during excavation stabilises these blocks.
- Shear displacements are typically only a fraction of a millimetre with local larger displacements close to the repository openings or along the boundaries of the wedges formed in the floor of the tunnel. Accounting for the lower pore pressure close to the tunnel by reducing the pore pressure in all fractures to zero during excavation reduces the largest shear displacements significantly.

9 Discussion and summary

9.1 General

The present report is aimed at describing the thermal and thermo-mechanical evolution of the Prototype Repository host rock based on numerical modelling and assessment of sensors data. In the following sections, import results are summarized and discussed.

9.2 Temperature evolution: Comparison with measurements

Temperature measurements in the outer section were reproduced well using the finite element program Code_Bright, assuming a uniform, globally valid, rock mass thermal conductivity. The best-estimate thermal conductivity (2.72 W/(m·K) is higher than that obtained in laboratory tests (Sundberg et al. 2005), which is consistent with some water movements (cf. Goudarzi 2014).

The temperature evolution in the inner section is affected by significant water movements associated with the changes in drainage initiated some 1,000 days after test start and additional changes caused by a broken packer in the rock, meaning that there is no strict verification that the thermal conductivity range established for the outer section is relevant also for the inner section. The water outflow reported for the inner section (cf. Goudarzi 2014) appears to be equivalent to a power loss that would explain the differences between measured and calculated temperatures. It is concluded that the approximation of heat transport exclusively by means of thermal conduction is not fully adequate. Future analyses of the temperature evolution in the inner section would require a different modelling approach that accounts for the large outflow of water.

9.3 Thermal and thermo-mechanical modelling approach using 3DEC

The numerical tool, 3DEC, used for the thermo-mechanical analyses with superimposed line sources calibrated to mimic the heat output of cylindrical canisters reproduced the Code_Bright temperature results in the outer section very satisfactory even though the thermal logic in 3DEC cannot account for variations in thermal properties, e.g. canisters, buffer, backfill, open spaces, etc. Not considering the low-conductivity backfill gave an insignificant temperature underestimate just below the tunnel floor and a corresponding small overestimate just above the tunnel roof. The thermal stresses as calculated by the two codes were generally in good agreement. Differences in results are due to an inadequate mesh density at the rock/buffer interface in the Code_Bright models that overestimates the radial stress.

9.4 Evaluation of rock mass material properties and *in situ* stresses: Comparison with measurements

Having verified that the temperature input to the 3DEC thermo-mechanical analyses is accurate, it remains to assess the relevance of input assumptions that control the response to excavation and heating: magnitudes and orientations of the *in situ* stresses and values of the elastic properties and the coefficient of thermal expansion.

Several types of instruments were installed in the rock surrounding the two deposition holes in the outer section. These included sensors that register micro-seismic events (acoustic emission data), and instruments that monitor stress and deformation within the intact rock and over individual fractures.

9.4.1 AE data

The assumed range in orientations of the horizontal stress components (cf. Section 3.3) appears to be verified by the agreement of locations of AE events with positions of calculated tangential stress maxima (cf. Figure 6-10 to Figure 6-15). Although the registered AE events are mainly concentrated to regions of high compressive stresses, they do not appear to be connected to any observable damage to the rock.

9.4.2 Biaxial stressmeters

The calculated and measured stress additions caused by the excavation of the holes are qualitatively similar. At all points, the major and minor principal components of the stress addition tensor are an increase and a reduction in compression, respectively. The magnitudes of the measured stress additions and corresponding stress additions obtained from the linear elastic models with uniform properties were found to agree reasonably at some points, but disagree by about ± 50% at others (Figure 6-19). The observed anomalies in some of the measurement data could possibly be attributed to disturbances caused by a combination of elastic and plastic shear displacements along fractures intersecting the measurement region. Differences between the stress additions calculated in the elastic model and those calculated in the fractured model are of the same order of magnitude as the anomalies indicated in Figure 6-19 but occur at different locations.

It should be noted that the biaxial stress meters are designed to monitor compressive stresses only (Geokon 2010a) and may give unreliable results when monitoring decreasing compressive stresses (Bono and Röshoff 2003). However, since the calculations and measurements are in reasonable agreement with regard to order of magnitude and the fracture network appears to be a possible explanation for the observed anomalies, no further conclusions regarding the reliability of the sensors during the excavation phase can be drawn from the comparison between measurements and calculations made in this report.

For the heated phase, a reasonable fit of modelling results to measurements of the major horizontal component of thermal stress was obtained during the first approximately 1,200 days. However, the measured minor horizontal thermal stress component differs both qualitatively and quantitatively from the modelled one. Whereas the models show compression in both principal horizontal thermal stress components even without accounting for the influence of the swelling pressure, the measurements systematically show tension in the minor horizontal stress component. As opposed to the possible explanation for the cause of the anomalies observed during excavation, the fracture network is unlikely to have caused the systematic reduction (5–10 MPa) registered in the minor horizontal thermal stress component. The source of the malfunctioning of the sensors is not known. There could for instance be a partial loss of contact between sensors and borehole walls during the three-year-period between excavation and heated phase. The loss of compression in both principal stress directions when the power to all heaters was switched off in December 2004 may have caused some of the sensors to fail completely. There could also be temperature and chemical disturbances, calibration errors etc. Because of the above, the results from the biaxial stress monitoring during the heated phase cannot be used for a meaningful assessment of the modelling approach.

9.4.3 Soft inclusion stress cells

If the rock mass could be considered a homogenous linear elastic continuum, the measured change in borehole diameter at the four measurement positions selected for the soft inclusion stress cells would be identical. Since this is not the case (see Figure 6-36 and Figure 6-37), the measurements are either disturbed by fractures or other inhomogeneities, or by for instance performance or installation errors. Because of the proximity to the stress boundary, i.e. the tunnel, plane stress conditions is the most relevant approximation. For this approximation, a reasonable, or very good, fit of modelling results to measurements was found for intact rock properties for all *in situ* stress assumptions tried here. Therefore, the measurements are likely to be correct and the disturbances probably caused by fractures or other inhomogeneities.

During the heated phase, the measurements show a reduction of similar magnitude in both the radial and in the tangential directions, whereas the model results show an insignificant change in borehole

diameter in the radial direction at all measurement positions. The measured reduction in borehole diameter in the tangential direction is also more rapid than predicted by the models. Since the thermal stress additions in the uppermost parts of the deposition holes are rather small (cf. modelling results in Figure 6-25 and Figure 6-28), the swelling pressure of the buffer and backfill may have an impact on the state of stress at the locations of the soft stress cells (cf. Figure 6-58 and Figure 6-59). However, at present there is no model of the evolution of the swelling pressure that can be used as input to the 3DEC models. It is, therefore, not possible to draw any firm conclusions regarding the reliability of the measurements made by the soft stress cells during the heated phase. Nor is it possible to gain any information regarding the mechanical or thermo-mechanical properties of the rock from these measurements.

9.4.4 Deformation meters

Measurement data from the deformation meters were compensated for changes in temperatures during both the construction phase and the subsequent heated phase. The results are very sensitive to changes in temperature. For both the excavation phase and the subsequent heated phase, the gauge length corrections dominate the measurements. It is concluded that the deformation meters are unsuitable for the type of measurement attempted in the Prototype Repository for the following reasons:

- The axial deformations of the monitoring boreholes resulting from the drilling of the deposition holes are too small to be correctly measured by the deformation meters.
- Since, in some cases, the measured thermally induced rock deformations are much greater than corresponding deformations of unconfined rock, it is concluded that the deformation meters cannot measure thermal expansion of rock properly.

9.4.5 Strain meters

It is judged that there are too many uncertainties associated with the measurement made with the strain meters for a comparison with modelling results to be meaningful:

- A thermal correction factor is applied to account for the thermal expansion of the strain meter (Geokon 2012). Although not as dominating as for the deformation meters, the correction factor corresponds to approximately 50% of the thermal expansion of unconfined rock (cf. Goudarzi 2012).
- The strain meters are installed in grout-filled boreholes (Bono and Röshoff 2003). According to the instruction manual (Geokon 2012), shrinkage and swelling effects of the grout due to changes in water content can result in strain-changes of several hundred microstrain that are not related to any real changes in load.

9.4.6 Summary of instrumentation and instrument performance

As discussed above, the majority of the sensors did not function properly or appear to have been operated outside their intended measurement range. The measurements could, therefore, not be used fully as intended to verify or establish a material model or an *in situ* stress model for the Prototype Repository host rock. An intermediate evaluation of measurement data in connection with the drilling of the deposition holes would therefore have beneficial when deciding on 1) complementary instruments for the heated phase and 2) continued monitoring with existing instruments. While the deformation meters and strain gauges were clearly inappropriate due to their sensitivity to changes in temperature, none of the installed instruments performed well during the heated phase. In future experiments, sensor performance in a variable-temperature environment where thermal expansion of the rock is the primary cause for deformations and for changes in stress needs to be checked prior to installation. A lack of systematics in the positioning of the sensors made it difficult to judge whether the observed differences between measurements and models were the result of measurement errors or indications of genuine stress variations due to e.g. a combination of elastic and plastic shear displacements along fractures intersecting the measurement region.

9.5 Spalling potential

The potential for spalling is assessed assuming the holes are unsupported and that the spalling strength is 121 MPa (Staub et al. 2004), which corresponds to 57% of the uniaxial compressive strength. Given the range of variation in material properties and *in situ* stresses considered relevant for the rock mass within the Prototype Repository (cf. Table 7-1 and Table 7-2), no systematic occurrences of spalling (other than locally at the top of the deposition holes) are predicted by the models.

For the models with base-case *in situ* stresses and material properties, the largest tangential stresses are found just below the tunnel floor. Here this stress is close to the nominal spalling strength in small regions already after excavation, whereas there is a 10–20 MPa margin to that strength in the region of maximum thermal stress at canister mid-height even after 2,000 days of heating. It appears that the magnitudes of the tangential stresses in the walls of the deposition holes are determined by the properties of the local rock volume surrounding the holes, with very little influence of properties assigned to the remaining rock mass. To reduce that uncertainty it would be necessary to establish the pillar scale elastic properties of the pillar region. Assuming intact rock properties, as in models P1 to P4, is likely to overestimate the calculated tangential stresses. Increasing the coefficient of thermal expansion or the *in situ* stress anisotropy would reduce the margin to the spalling strength to about 5 MPa at stress maximum.

Results from the models with fractures show that a combination of elastic and plastic shear displacements along fractures intersecting the deposition holes perturb the stress-field in the walls of the holes quite significantly. Stress concentrations that are above the nominal spalling strength are formed at the tips of the intersections of steeply dipping fractures already after excavation of the holes (cf. Figure 8-6 and Figure 8-7). However, Hökmark et al. (2006) concluded that "small regions of structurally controlled stress concentrations should not be considered relevant for spalling risk estimates, meaning that the elastic approximations should be sufficient". Since there was no evidence of any systematic stress induced damage to the walls of the deposition holes after the dismantling of the outer section (cf. Appendix H), it is likely that the schematic perfectly planar fracture geometry considered here overestimates the impact of the fractures.

9.6 Fracture deformations

9.6.1 Wedge stability

For the simplistic fracture network considered in this study, wedges with large displacements are formed in the floor of tunnel between the two deposition holes when the pore pressure is kept at the hydrostatic level throughout the modelling period. Accounting for the lower pore pressure close to the tunnel by reducing the pore pressure in all fractures from 4.4 MPa to 0 MPa during excavation stabilises these blocks.

Additional analyses specifically aimed at investigating stability of wedges formed in the walls of the deposition holes (see Appendix E), show that the stability predicted by use of a semi-analytical approach based on shear and normal stresses calculated on hypothetical fracture planes in a linear elastic model agrees with corresponding results from models with explicitly represented fractures. Wedges that are stable after excavation of the deposition holes appear to be stable also throughout the heated phase.

9.6.2 Shear displacements

The shear displacements are generally small and located in the most stress-disturbed regions close to the repository openings. It appears that most of the displacements take place during the excavation with very little additional movements during the heated phase.

For the base-case models with full hydrostatic pore pressure throughout the modelling period (model F1a), there are only four fractures in the fracture model that have shear displacements exceeding a few millimetres over any significant area (see Figure 8-12, left). These fractures form the boundaries of the wedges with large displacements located in the tunnel floor. Shear displacements of a few millimetres along the boundaries of these blocks are obtained even if the friction angle is increased

to values as high as 45°. Accounting for the lower pore pressure close to the tunnel by reducing the pore pressure in all fractures from 4.4 MPa to 0 MPa during excavation reduces the maximum shear displacements very efficiently (see Figure 8-12, right). Some distance away from the openings, the shear displacements are small for all considered combinations of pore pressure and friction angles (cf. Appendix G).

9.6.3 Normal stress variations

Similarly to the results obtained in SR-Can and SR-Site (Hökmark et al. 2006, 2010, Fälth and Hökmark 2007), regions of low normal stress are found where the fractures intersect the repository openings or are approximately parallel to them. Given the simplistic fracture network considered here, additional regions of low normal stress are formed at the boundaries of the wedges with large displacements formed in the floor of the tunnel. This is linked to the schematic assignment of pore pressure within the fractures. Accounting for the lower pore pressure close to the tunnel by reducing the pore pressure in all fractures from 4.4 MPa to 0 MPa during excavation stabilises these blocks. During the heated phase, compression generally increases on all fractures.

10 Final remarks

In summary, the thermal and thermo-mechanical evolution of the Prototype Repository could be captured by the relatively simple models analyzed in this report:

- Assuming homogeneous and isotropic thermal properties, with a thermal conductivity that is marginally higher than suggested by results of laboratory tests appears to give a very satisfactory agreement between temperature calculations and temperature measurements conducted in the outer section. Temperature overpredictions in the inner section appear to be well correlated with variations in water flow in that section and are, consequently, concluded to be a result of heat convection. This strengthens the confidence in the laboratory-scale determinations of rock thermal properties and in the thermal modelling approach used in this report and in the assessment of the thermal evolution of the Forsmark repository.
- Looking at the general picture of the AE patterns during the drilling of the deposition holes, the trend of the major horizontal principal stress appears to be reasonably well constrained.
- While the orientation assumed for the *in situ* stresses seems to be verified by the AE observations, the corresponding stress magnitudes are difficult to verify. None of the instruments installed for measurement of stress change, strain or deformation have appeared to be sufficiently reliable to be used to verify the mechanical input with any rigour. Not observing any spalling at any position in the walls of the two deposition holes does, however, indicate that the models did not underpredict the tangential stresses after excavation by any significant amount. In the uppermost parts of the holes, these stresses were close to the nominal spalling strength, meaning that the actual *in situ* stresses cannot have been much higher than the assumed input stresses.
- The registered AE events do not appear to be connected to any observable damage to the rock, although they are mainly concentrated to regions of high compressive stress.
- The model results indicate that stress redistribution effects caused by fracture shear displacements are significant only close to the opening peripheries, and that mainly fractures that are oriented approximately tangentially to the opening peripheries contribute. At some distance from the peripheries, all fractures are in solid compression with considerable stability margins.
- Even close to the opening peripheries, the stress redistribution effects caused by the fracture network are likely to be less pronounced in reality than in the 3DEC models. In models with explicitly modelled fractures, local stress concentrations in the walls of the deposition holes after excavation are sufficiently intense that spalling would be likely to have occurred. Not observing any spalling may indicate that the stress redistribution effects were more modest. Given that 3DEC fractures, with perfectly planar surfaces, are very schematic representations of real fractures, this is a logical conclusion.
- Given that the models with explicitly modelled fractures probably overestimate the impact of the fracture network, it may not be realistic to attribute differences between instrument readings and results from the elastic models entirely to disturbances caused by fractures.

The magnitudes of the tangential stresses obtained from linear elastic and thermo-elastic models are consistent with the observations that no spalling has taken place during the experiment. Although there are no indications of a significant underestimate in modelled stress magnitudes, it should be noted that the small support-pressure provided by the pellets during the heated phase could have been sufficient to suppress the initiation of spalling (Glamheden et al. 2010).

References

SKB's (Svensk Kärnbränslehantering AB) publications can be found at www.skb.se/publications.

Andersson J C, 2007. Äspö Hard Rock Laboratory. Äspö Pillar Stability Experiment, Final report. Rock mass response to coupled mechanical thermal loading. SKB TR-07-01, Svensk Kärnbränslehantering AB.

Ask D, 2003. Evaluation of measurement-related uncertainties in the analysis of overcoring rock stress data from Äspö HRL, Sweden: a case study. International Journal of Rock Mechanics and Mining Sciences 40, 1173–1187.

Bono N, Röshoff K, 2003. Äspö Hard Rock Laboratory. Prototype repository. Instrumentation for stress, strain and displacement measurements in rock. SKB IPR-03-19, Svensk Kärnbränslehantering AB.

Brady B H G, Brown E T, 1993. Rock mechanics for underground mining. 2nd ed. London: Chapman & Hall.

Börgesson L, Gunnarsson D, Johannesson L-E, Sandén T, 2002. Äspö Hard Rock Laboratory. Prototype Repository. Installation of buffer, canisters, backfill and instruments in Section 1. SKB IPR-02-23, Svensk Kärnbränslehantering AB.

Christiansson, R., Jansson T, 2003. A test of different stress measurement methods in two orthogonal bore holes in Äspö Hard Rock Laboratory (HRL), Sweden. International Journal of Rock Mechanics and Mining Sciences 40, 1161–1172.

CIMNE, 2004. Code_Bright. Version 2.2 users guide. Departemento de Ingenieria del Terreno, Cartográfica y Geofísica. Universidad Politécnica de Cataluña, Spain.

Fransson Å, Thörn J, Ericsson L O, Lönnqvist M, Stigsson M, 2012. Hydromechanical characterization of fractures close to a tunnel opening: A case study. In Rock Engineering and Technology for Sustainable Underground Construction. Eurock 2012 – the 2012 ISRM International Symposium, 28–30 May 2012, Stockholm, Sweden.

Fälth B, Hökmark H, 2007. Mechanical and thermo-mechanical discrete fracture near-field analyses based on preliminary data from the Forsmark, Simpevarp and Laxemar sites. SKB R-06-89, Svensk Kärnbränslehantering AB.

Fälth B, Kristensson O, Hökmark H, 2005. Äspö Hard Rock Laboratory. Äspö Pillar Stability Experiment. Thermo-mechanical 3D back analyze of the heating phase. SKB IPR-05-19, Svensk Kärnbränslehantering AB.

Fälth B, Hökmark H, Munier R, 2010. Effects of large earthquakes on a KBS-3 repository. Evaluation of modelling results and their implications for layout and design. SKB TR-08-11, Svensk Kärnbränslehantering AB.

Geokon, 2009. Instruction manual. Model 4360. VW Soft Inclusion Stress Cells. Geokon, Inc.

Geokon, 2010a. Instruction manual. Model 4350BX. Biaxial Stressmeter. Geokon, Inc.

Geokon, 2010b. Instruction manual. Model 4430. VW Deformation Meter. Geokon, Inc.

Geokon, 2012. Instruction manual. Model 4200 Series. Vibrating Wire Strain Gages. Geokon, Inc.

Glamheden R, Fälth B, Jacobsson L, Harrström J, Berglund J, Bergkvist L, 2010. Counterforce applied to prevent spalling. SKB TR-10-37, Svensk Kärnbränslehantering AB.

Goudarzi R, 2012. Prototype Repository – Sensor data report (period 100917–110101). Report no 24. SKB P-12-12, Svensk Kärnbränslehantering AB.

Goudarzi R, 2014. Prototype Repository. Sensor data report (period 2001-09-17 – 2013-01-01). Report No 25. SKB P-13-39, Svensk Kärnbränslehantering AB.

Goudarzi R, Johannesson L-E, 2003. Äspö Hard Rock Laboratory. Prototype repository. Sensors data report (Period 010917–030901). Report No:7. SKB IPR-03-46, Svensk Kärnbränslehantering AB.

Goudarzi R, Johannesson L-E, 2004a. Äspö Hard Rock Laboratory. Prototype repository. Sensors data report (Period 010917–031201). Report No:8. SKB IPR-04-04, Svensk Kärnbränslehantering AB.

Goudarzi R, Johannesson L-E, 2004b. Äspö Hard Rock Laboratory. Prototype repository. Sensors data report (Period 010917–040301). Report No:9. SKB IPR-04-24, Svensk Kärnbränslehantering AB.

Goudarzi R, Johannesson L-E, 2004c. Äspö Hard Rock Laboratory. Prototype repository. Sensors data report (Period 010917–040601). Report No:10. SKB IPR-04-36, Svensk Kärnbränslehantering AB (SKB), Stockholm, Sweden.

Goudarzi R, Johannesson L-E, 2004d. Äspö Hard Rock Laboratory. Prototype Repository. Sensors data report (Period 010917–040901). Report No:11. SKB IPR-04-48, Svensk Kärnbränslehantering AB.

Goudarzi R, Johannesson L-E, 2004e. Äspö Hard Rock Laboratory. Prototype Repository. Sensors data report (Period 010917–041201). Report No:12. SKB IPR-05-13, Svensk Kärnbränslehantering AB.

Goudarzi R, Johannesson L-E, 2005a. Äspö Hard Rock Laboratory. Prototype Repository. Sensors data report (Period 010917–050601). Report No:13. SKB IPR-05-28, Svensk Kärnbränslehantering AB.

Goudarzi R, Johannesson L-E, 2005b. Äspö Hard Rock Laboratory. Prototype Repository. Sensors data report (Period 010917–051201). Report No:14. SKB IPR-06-08, Svensk Kärnbränslehantering AB.

Goudarzi R, Johannesson L-E, 2006a. Äspö Hard Rock Laboratory. Prototype Repository. Sensors data report (Period 010917–060601). Report no:15. SKB IPR-06-26, Svensk Kärnbränslehantering AB.

Goudarzi R, Johannesson L-E, 2006b. Äspö Hard Rock Laboratory. Prototype Repository. Sensors data report (Period 010917–061201). Report No:16. SKB IPR-07-05, Svensk Kärnbränslehantering AB.

Goudarzi R, Johannesson L-E, 2007a. Äspö Hard Rock Laboratory. Prototype Repository. Sensors data report (Period 010917–070601). Report No:17. SKB IPR-07-19, Svensk Kärnbränslehantering AB.

Goudarzi R, Johannesson L-E, 2007b. Äspö Hard Rock Laboratory. Prototype Repository. Sensors data report (Period 010917–071201). Report No:18. SKB IPR-08-15, Svensk Kärnbränslehantering AB.

Goudarzi R, Johannesson L-E, 2008. Äspö Hard Rock Laboratory. Prototype Repository. Sensors data report (Period 010917–080601). Report No:19. SKB IPR-08-21, Svensk Kärnbränslehantering AB.

Goudarzi R, Johannesson L-E, 2009a. Äspö Hard Rock Laboratory. Prototype Repository. Sensors data report (Period 010917–081201). Report No: 20. SKB IPR-09-09, Svensk Kärnbränslehantering AB.

Goudarzi R, Johannesson L-E, 2009b. Äspö Hard Rock Laboratory. Prototype Repository. Sensors data report (Period 010917-090601). Report No: 21. SKB IPR-09-17, Svensk Kärnbränslehantering AB.

Goudarzi R, Johannesson L-E, 2009c. Äspö Hard Rock Laboratory. Prototype Repository. Sensors data report (Period 010917–091201). Report No: 22. SKB IPR-10-05, Svensk Kärnbränslehantering AB.

Goudarzi R, Johannesson L-E, 2010. Äspö Hard Rock Laboratory. Sensors Data Report No 23. SKB IPR-10-18, Svensk Kärnbränslehantering AB.

Hakala M, Siren T, Kemppainen K, Christiansson R, Martin C D, 2013. In situ stress measurement with the new LVDT-cell – Method Description and Verification. Posiva Report 2012-43, Posiva Oy, Finland.

Hakami E, Fredriksson A, Lanaro F, Wrafter J, 2008. Rock mechanics Laxemar. Site descriptive modelling, SDM-Site Laxemar. SKB R-08-57, Svensk Kärnbränslehantering AB.

Hakami H, 2003. Äspö Hard Rock Laboratory. Update of the rock mechanical model 2002. SKB IPR-03-37, Svensk Kärnbränslehantering AB.

Hökmark H, Fälth B, 2003. Thermal dimensioning of the deep repository. Influence of canister spacing, canister power, rock thermal properties and nearfield design on the maximum canister surface temperature. SKB TR-03-09, Svensk Kärnbränslehantering AB.

Hökmark H, Fälth B, Wallroth T, 2006. T-H-M couplings in rock. Overview of results of importance to the SR-Can safety assessment. SKB R-06-88, Svensk Kärnbränslehantering AB.

Hökmark H, Lönnqvist M, Kristensson O, Sundberg J, Hellström G, 2009. Strategy for thermal dimensioning of the final repository for spent nuclear fuel. SKB R-09-04, Svensk Kärnbränslehantering AB.

Hökmark H, Lönnqvist M, Fälth B, 2010. THM-issues in repository rock. Thermal, mechanical, thermo-mechanical and hydro-mechanical evolution of the rock at the Forsmark and Laxemar sites. SKB TR-10-23, Svensk Kärnbränslehantering AB.

Itasca, 2007. 3DEC – 3-dimensional distinct element code. User's guide. Minneapolis, MN: Itasca Consulting Group, Inc.

Johannesson L-E, Gunnarsson D, Sandén T, Börgesson L, Karlzén R, 2004. Äspö Hard Rock Laboratory. Prototype repository. Installation of buffer, canisters, backfill, plug and instruments in Section II. SKB IPR-04-13, Svensk Kärnbränslehantering AB.

Kristensson O, Hökmark H, 2007. Prototype Repository. Thermal 3D modelling of Äspö Prototype Repository. SKB IPR-07-01, Svensk Kärnbränslehantering AB.

Lönnqvist M, Kristensson O, Hökmark H, 2008. Äspö Hard Rock Laboratory. CAPS - Confining Application to Prevent Spalling. Scoping calculations – Field test at Äspö HRL. SKB IPR-08-08, Svensk Kärnbränslehantering AB.

Patel S, Dahlström L-O, Stenberg L, 1997. Äspö Hard Rock Laboratory. Characterisation of the rock mass in the Prototype Repository at Äspö HRL. Stage 1. SKB HRL Progress Report HRL-97-24, Svensk Kärnbränslehantering AB.

Pettitt W, Baker C, Young R P, 1999. Äspö Hard Rock Laboratory. Prototype Repository. Acoustic emission and ultrasonic monitoring during the excavation of deposition holes in the Prototype Repository. SKB IPR-01-01, Svensk Kärnbränslehantering AB.

Pettitt W, Baker C, Young R P, 2000. Äspö Hard Rock Laboratory. Analysis of the in-situ principal stress field at the HRL using acoustic emission data. SKB IPR-01-09, Svensk Kärnbränslehantering AB.

Pusch R, Andersson C, 2004. Äspö Hard Rock Laboratory. Prototype Repository. Preparation of deposition holes prior to emplacement of buffer and canisters in Section II. SKB IPR-04-21, Svensk Kärnbränslehantering AB.

Rhén I, Forsmark T, 2001. Äspö Hard Rock Laboratory. Prototype Repository. Hydrogeology. Summary report of investigations before the operation phase. SKB IPR-01-65, Svensk Kärnbränslehantering AB.

Rhén I (ed), Gustafson G, Stanfors R, Wikberg P, 1997. Äspö HRL – Geoscientific evaluation 1997/5. Models based on site characterization 1986–1995. SKB TR 97-06, Svensk Kärnbränslehantering AB.

Schneider P J, Eberly D H, 2003. Geometric tools for computer graphics. San Francisco: Morgan Kaufmann.

Staub I, Andersson J C, Magnor B, 2004. Äspö Pillar Stability Experiment. Geology and mechanical properties of the rock in TASQ. SKB R-04-01, Svensk Kärnbränslehantering AB.

Sundberg J, 2003. Thermal properties at Äspö HRL. Analysis of distribution and scale factors. SKB R-03-17, Svensk Kärnbränslehantering AB.

Sundberg J, Back P-E, Hellström G, 2005. Scale dependence and estimation of rock thermal conductivity. Analysis of upscaling, inverse thermal modelling and value of information with the Äspö HRL prototype repository as an example. SKB R-05-82, Svensk Kärnbränslehantering AB.

Sundström B, 1988. Allmänna tillstånd och dimensioneringskriteria. 4th ed. Stockholm: Kungliga Tekniska Högskolan. (In Swedish.)

Vince J, 2010. Mathematics for computer graphics. 3rd ed. London: Springer.

Appendix A

Thermal evolution: Complementary analyses

In this appendix, results for the inner section as well as complementary analyses for the outer section are presented.

A.1 Results for the inner section

Comparisons between calculated and measured temperatures in the inner section are provided in Figure A-1 to Figure A-8. The calculated temperatures overestimate the measured temperatures, even for the highest thermal conductivity values tried here. The temperature overestimate is, however, significant only after a little more than 1,000 days, i.e., the overestimate appears to coincide with changes to the drainage of the inner section (cf. Goudarzi 2014).

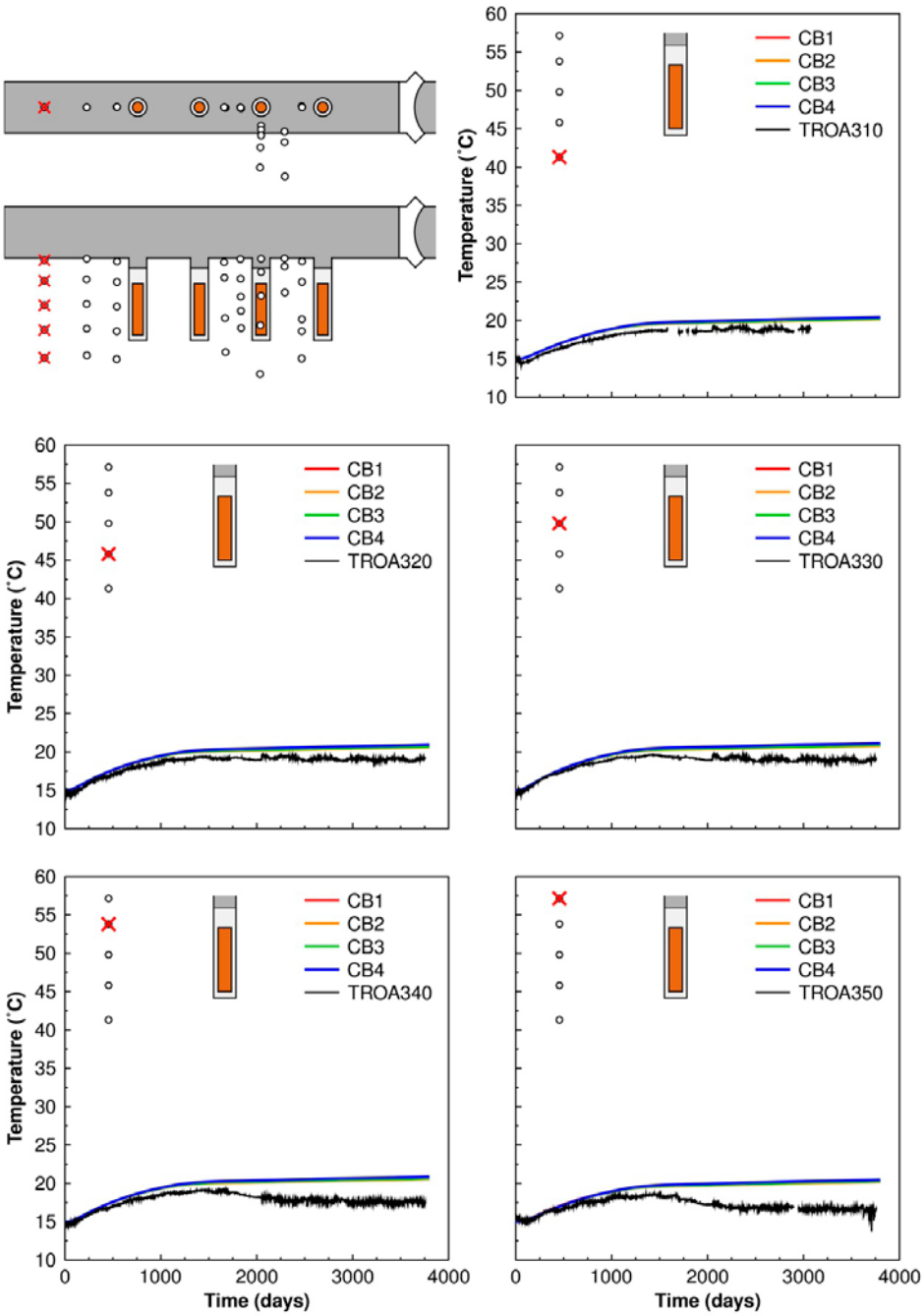

Figure A-1. *Sensors located around Hole 1. Comparison between measurements (black curves) and models.*

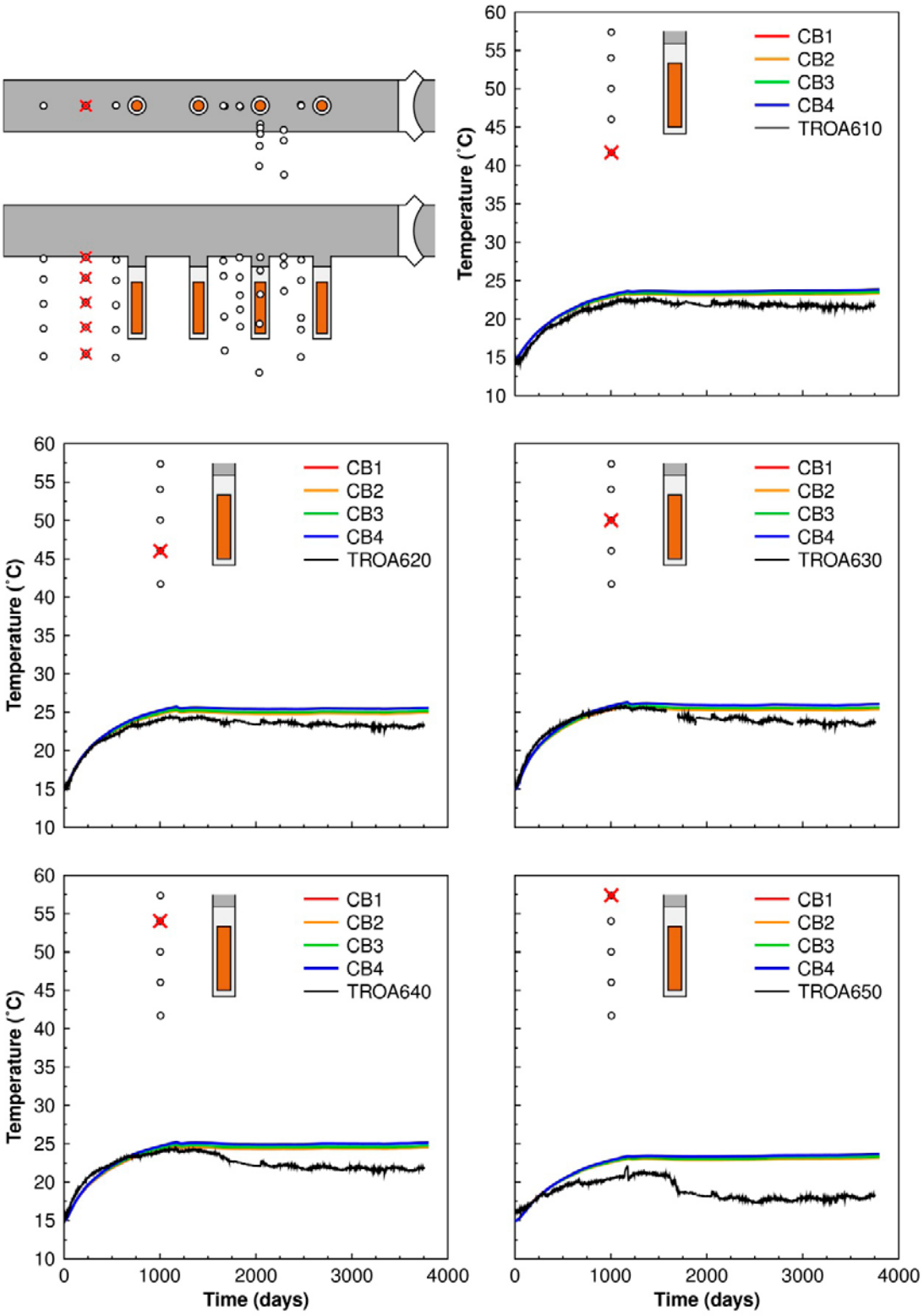

Figure A-2. *Sensors located around Hole 1 (Contd). Comparison between measurements (black curves) and models.*

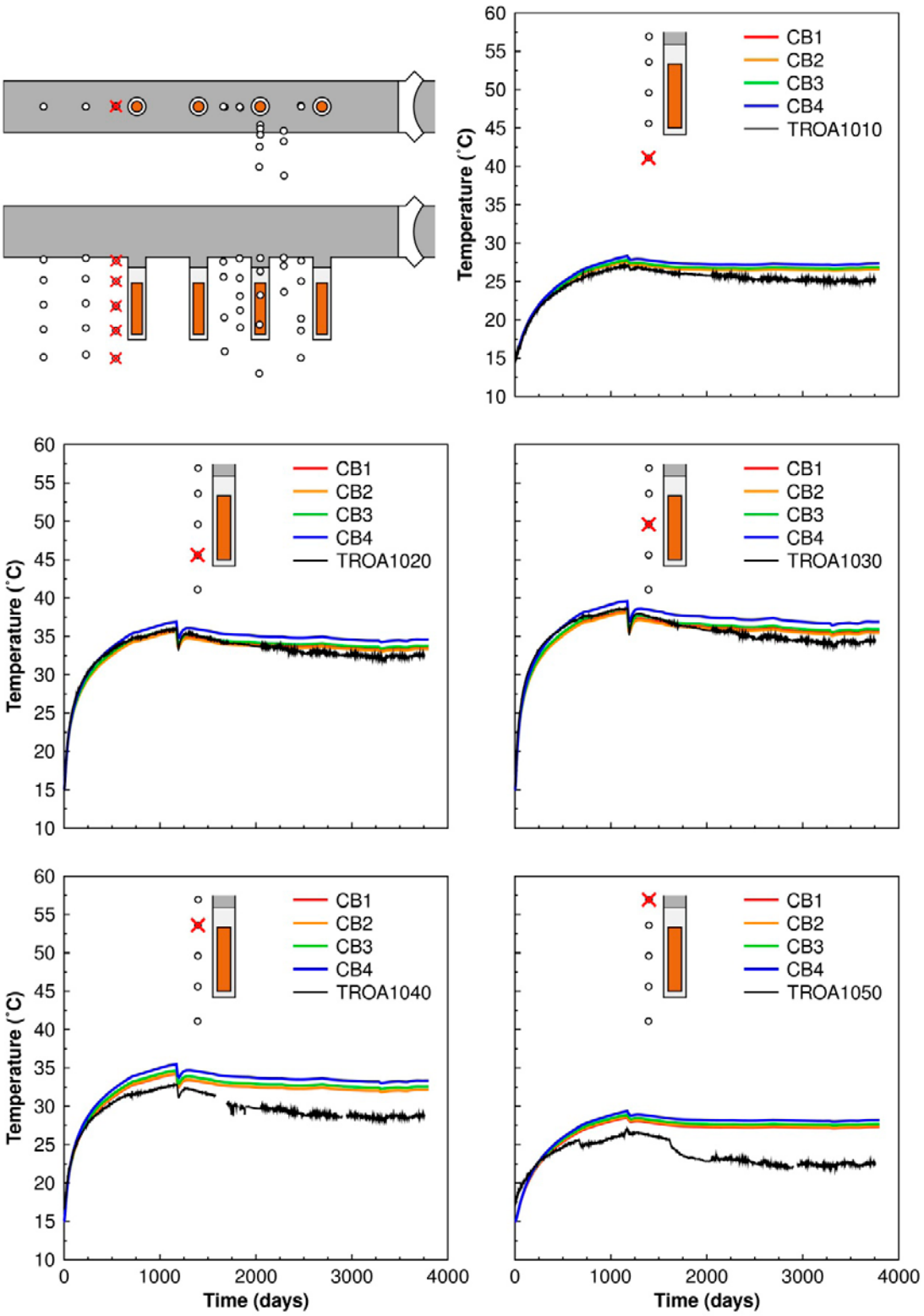

Figure A-3. *Sensors located around Hole 1 (Contd). Comparison between measurements (black curves) and models.*

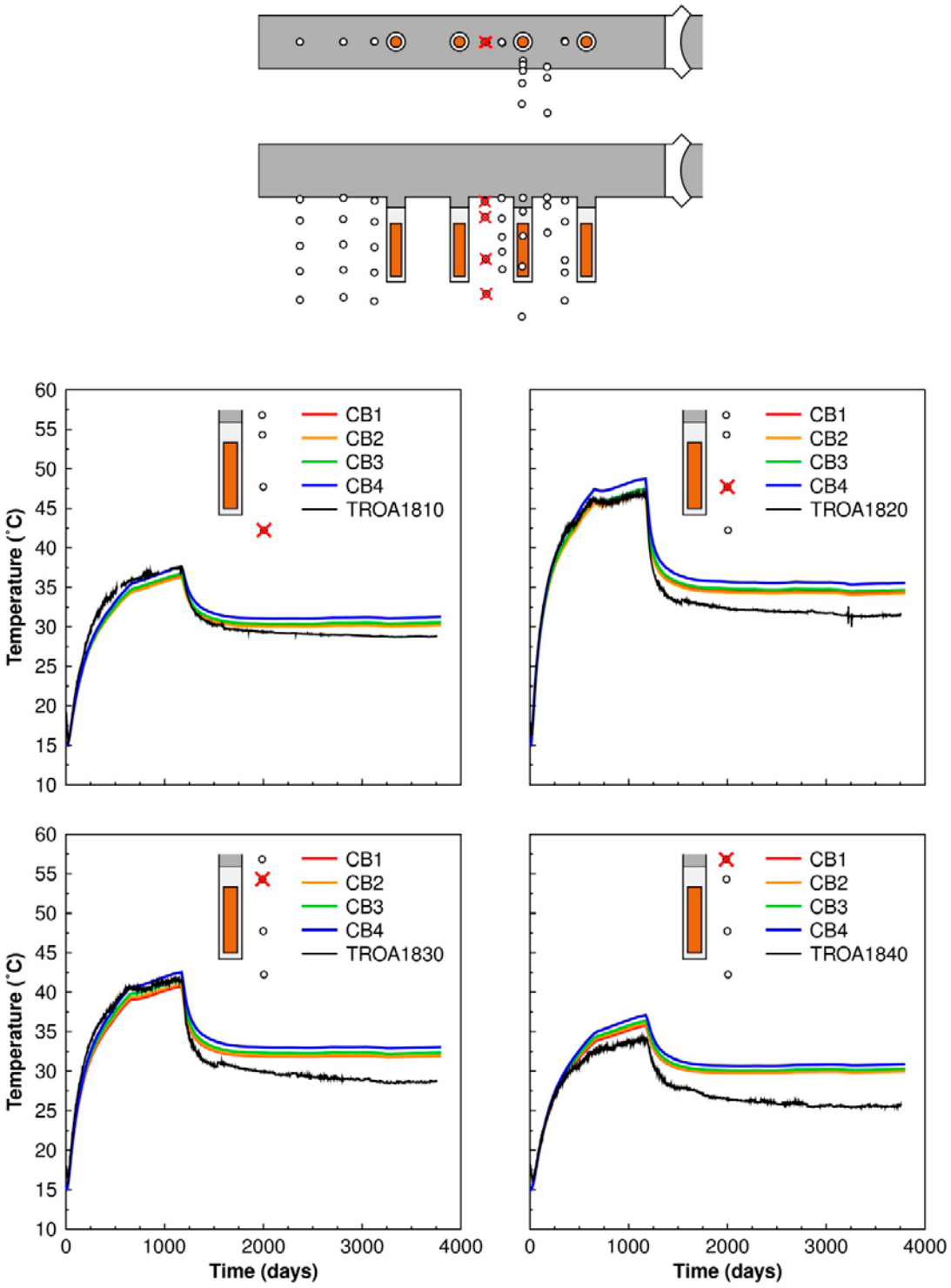

Figure A-4. *Sensors located around Hole 2. Comparison between measurements (black curves) and models.*

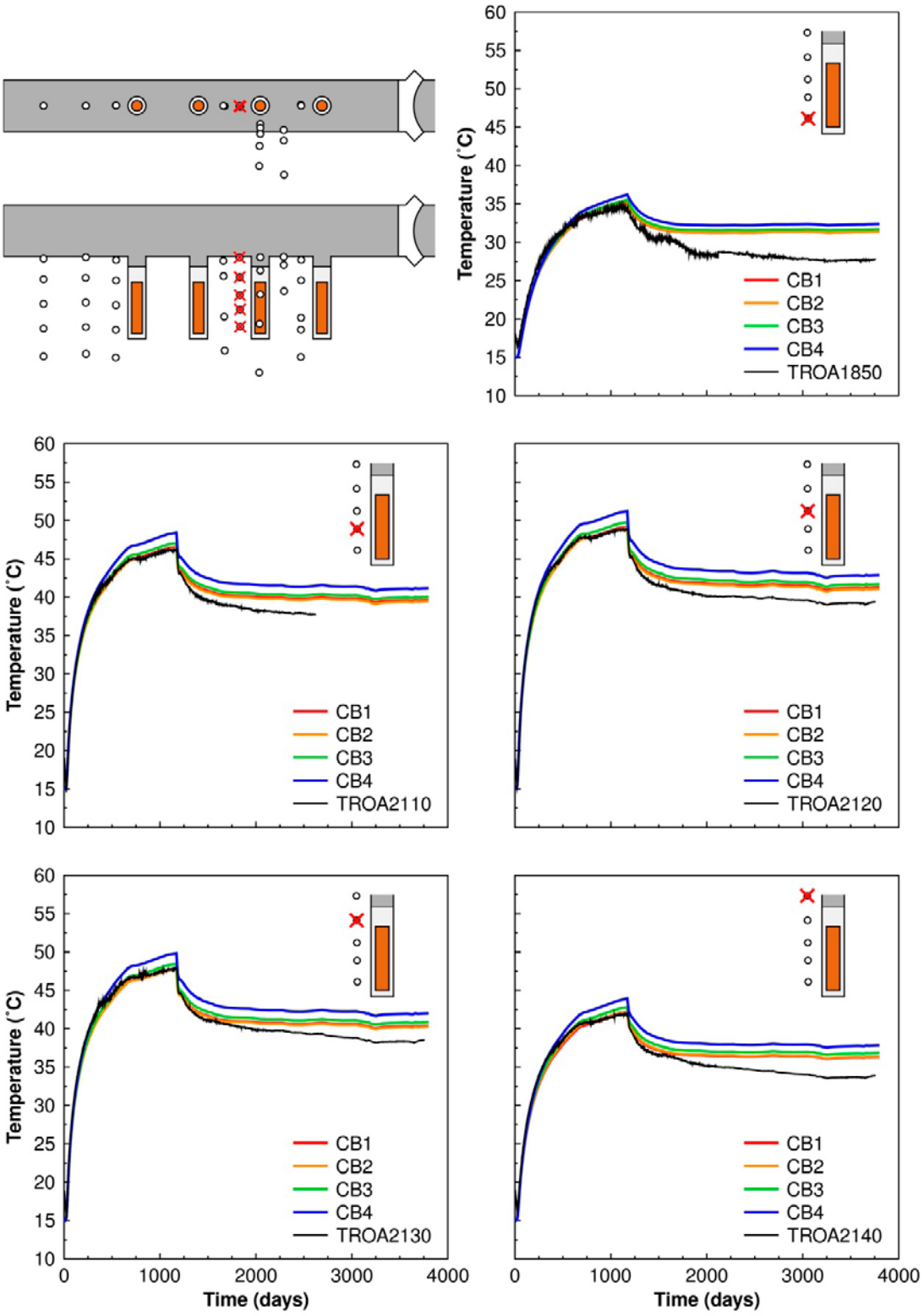

Figure A-5. *Sensors located around Hole 3. Comparison between measurements (black curves) and models.*

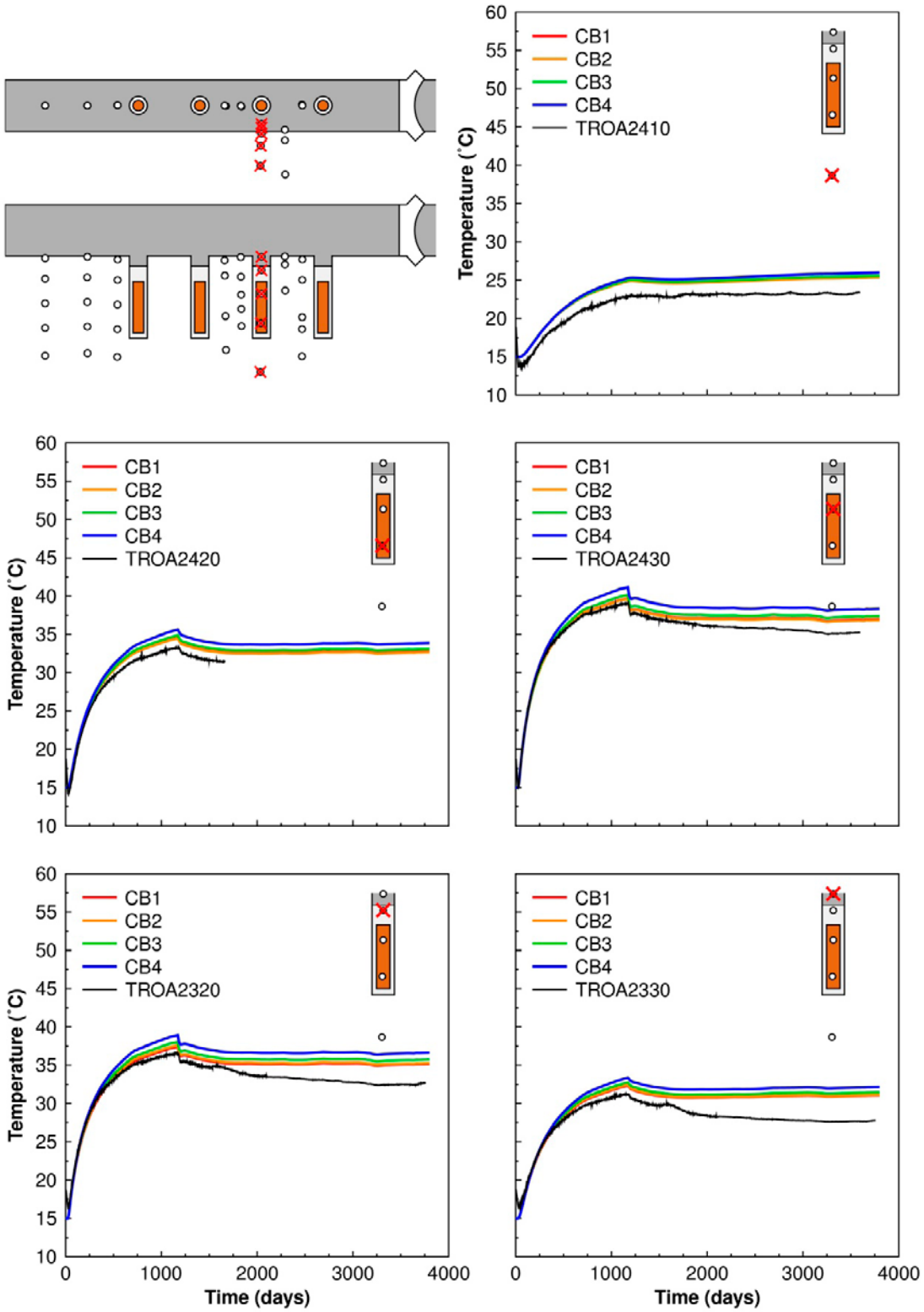

Figure A-6. *Sensors located around Hole 3 (Contd). Comparison between measurements (black curves) and models.*

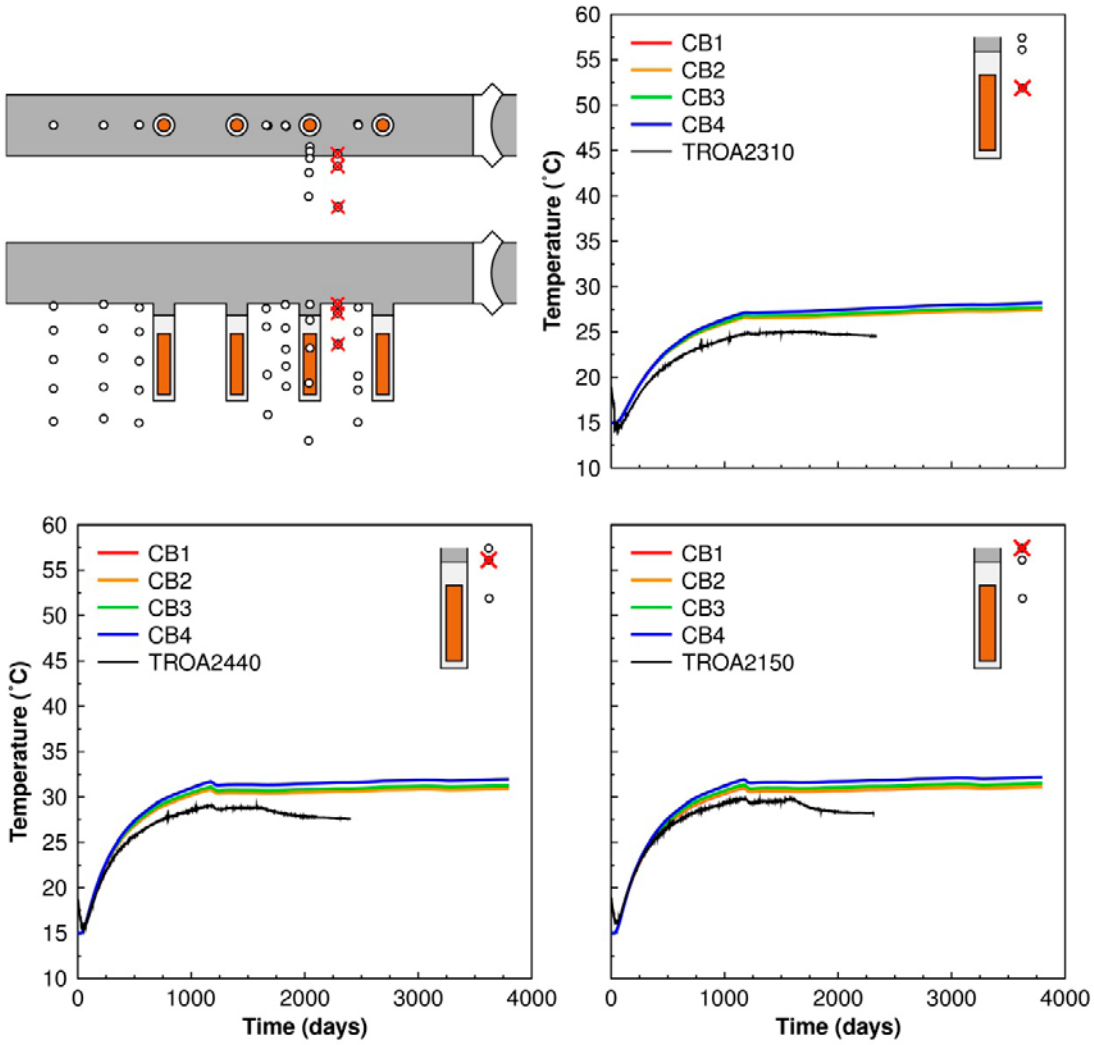

Figure A-7. *Sensors located around Hole 3 (Contd). Comparison between measurements (black curves) and models.*

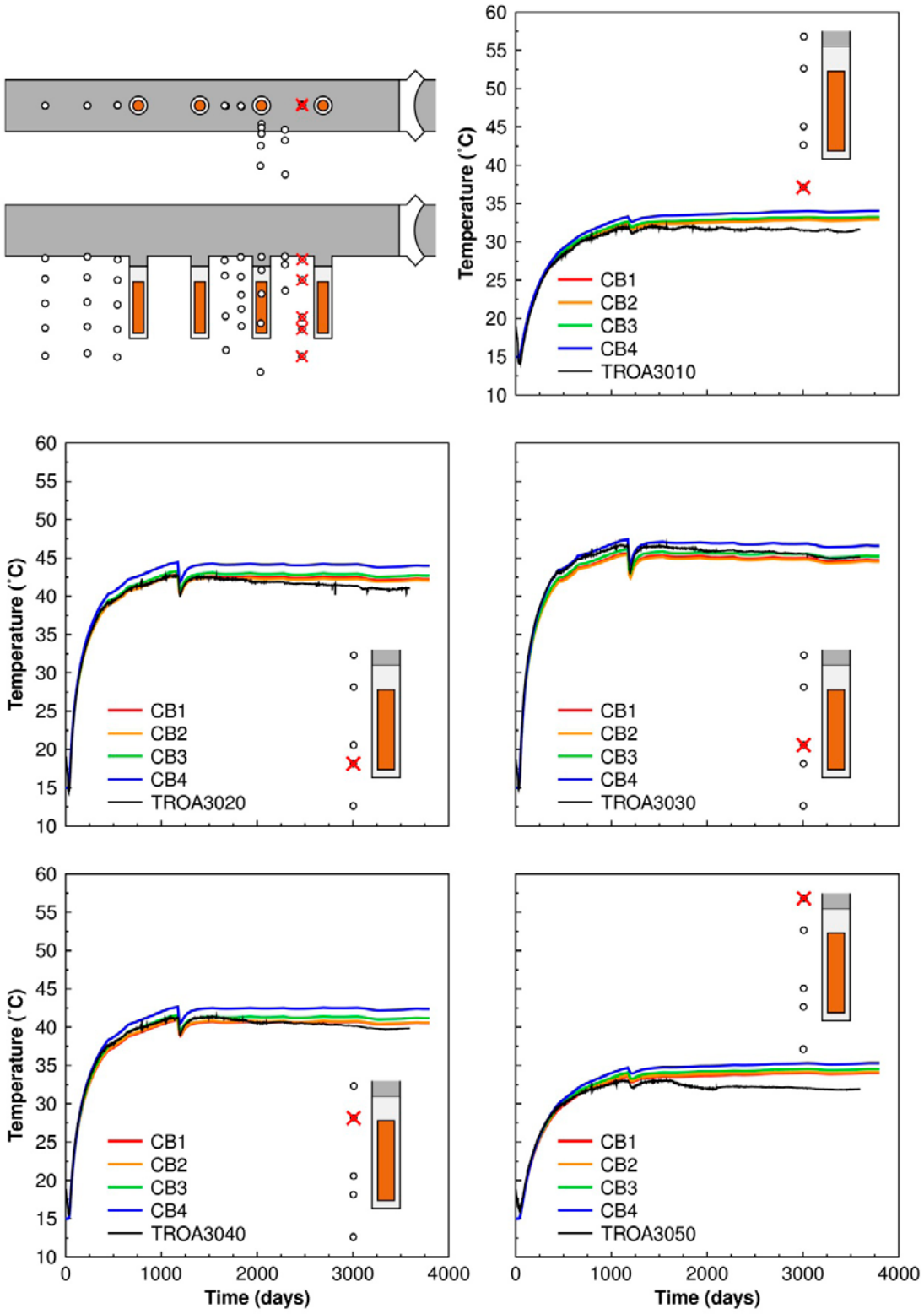

Figure A-8. *Sensors located around Hole 4. Comparison between measurements (black curves) and models.*

A.2 Complementary results for the outer section

Typical variations in heat capacity for the APSE test site and for Äspö in general are 2.05–2.29 MJ/(m^3·K) (Andersson 2007) and 1.93–2.34 MJ/(m^3·K) (Sundberg 2003), respectively. Here, values of the heat capacity in the range 2.0–2.3 MJ/(m^3·K) are tested. For the parameter range given in Table A-1, only an insignificant variation in temperature is observed (see Figure A-9 and Figure A-10).

Table A-1. Model map and data used in the complementary analyses.

Parameter	Unit	Rock mass and plugs			Backfill	Buffer	Canister
		CB4	CB4a	CB4b			
Thermal conductivity	W/(m·K)	2.52	2.52	2.52	1.5	1.0	390
Specific heat	J/(kg·K)	770	720	830	780	800	390
Density	kg/m^3	2,770	2,770	2,770	2,500	2,780	8,930

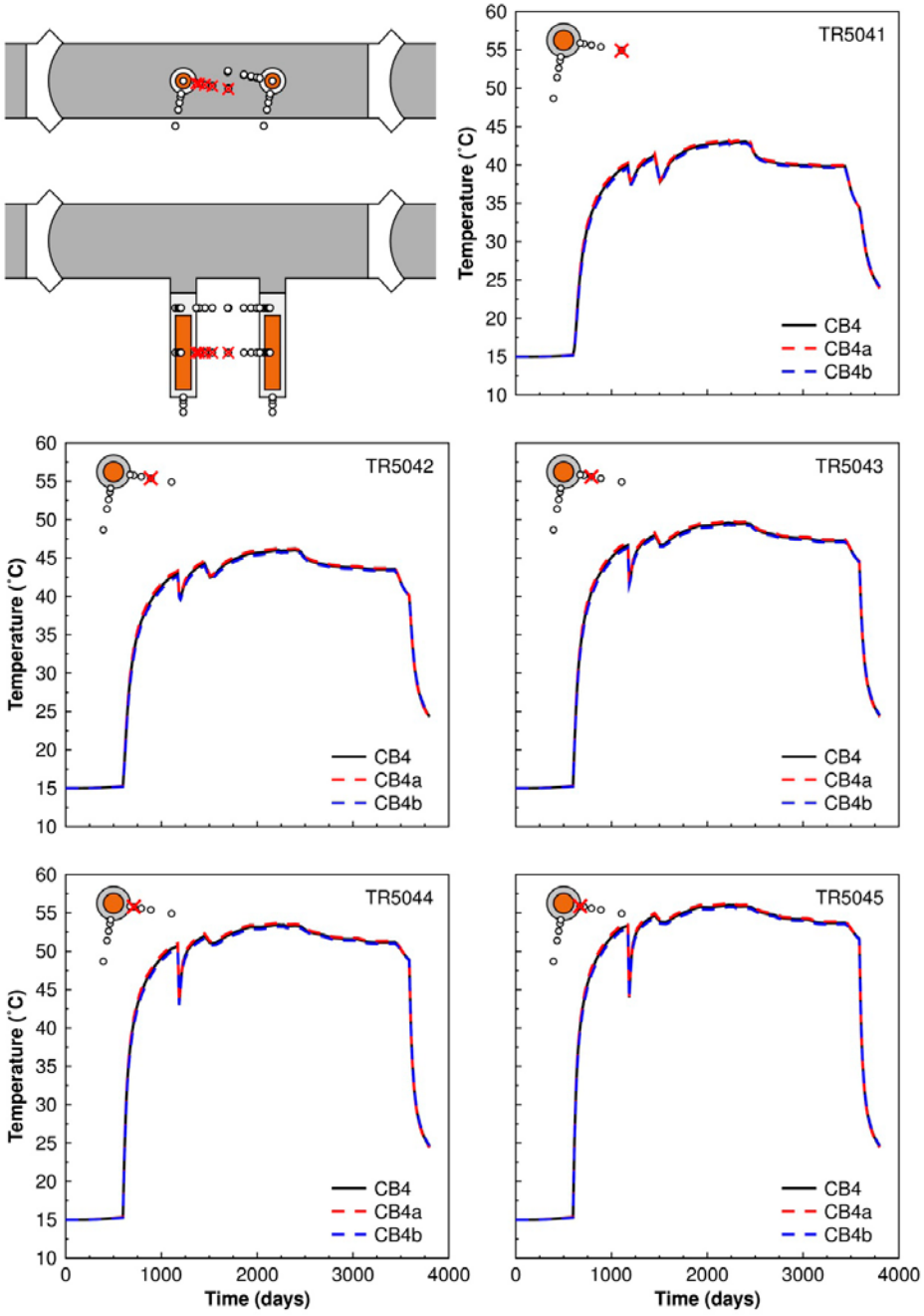

Figure A-9. *Sensors located in the pillar between Holes 5 and 6 at 5 m below the tunnel floor. Impact of variations in rock mass heat capacity, cf. Table A-1.*

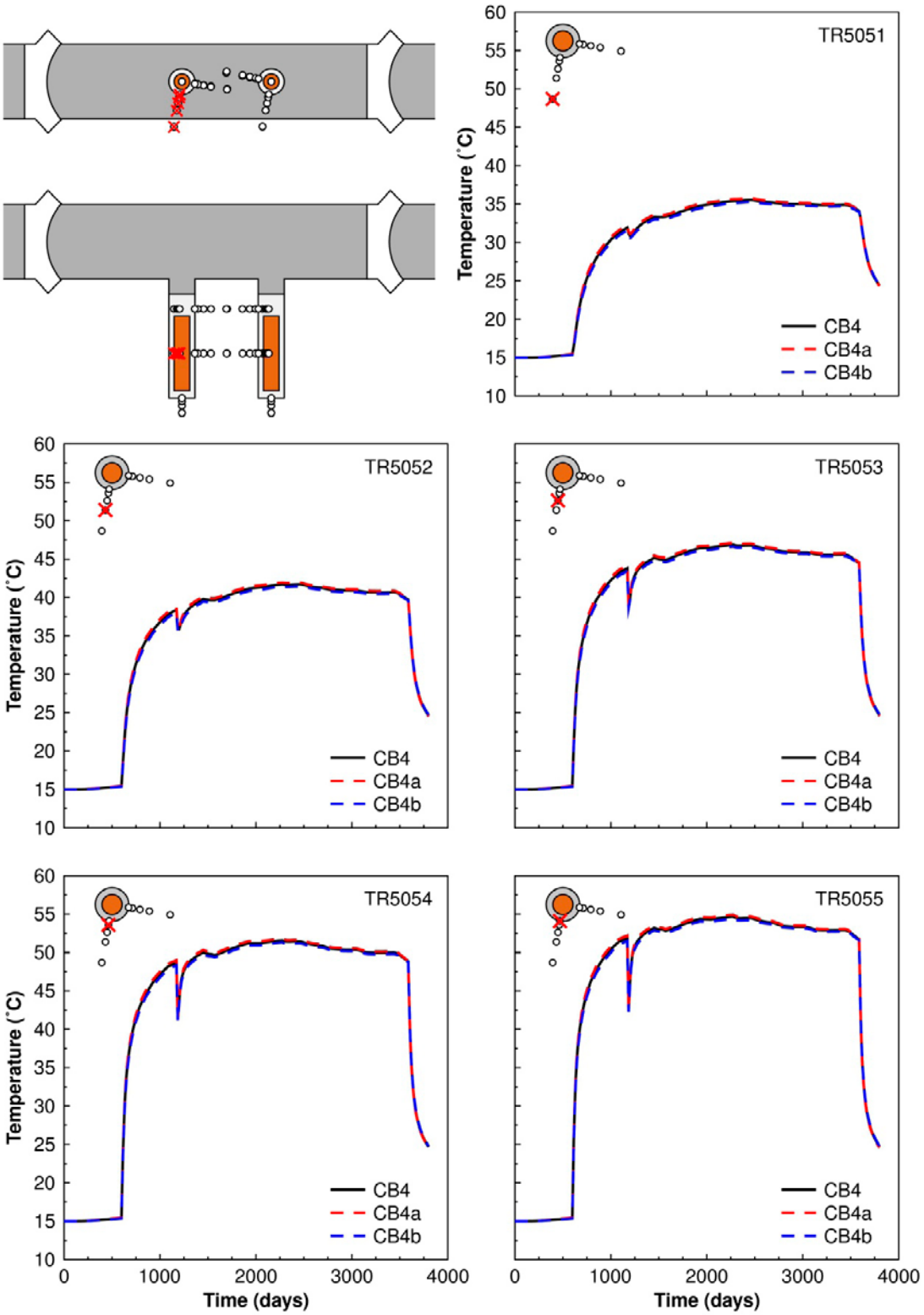

Figure A-10. *Sensors located approximately perpendicular to the tunnel axis at 5 m below the tunnel floor. Impact of variations in rock mass heat capacity, cf. Table A-1.*

Appendix B

Locations of rock mechanical instruments

The labelling of instruments and instrumentation boreholes used by Bono and Röshoff (2003) have also been used in this report. For completeness, the corresponding labelling used by SKB and coordinates (RT90-RHB70) for each instrument are provided in this appendix (see Table B-1).

B.1 Locations of primary instruments

Biaxial stress meters, soft inclusion stress cells and deformation meters, aimed at monitoring the response of the rock mass during the drilling of the deposition holes and during the subsequent heated phase, were installed in vertical boreholes drilled 0.3 m from the periphery of each deposition hole in the outer section, see Figure 6-1, Figure 6-16, Figure 6-29 and Figure 6-40. Labels and coordinates for each biaxial stress meter, soft inclusion stress cell and deformation meter are presented in Table B-2, Table B-3 and Table B-4, respectively.

In total, seven strain gauges were also installed in the vertical boreholes (Bono and Röshoff 2003). Data from these instruments have not been analyzed in this report (see Table 6-1 and Chapter 9). Therefore, instrument labels and coordinates are not presented here.

Table B-1. Sources for SKB's labelling of instruments and boreholes and coordinates for instruments.

Type of instrument	Instrument labels and coordinates	Borehole ID
Biaxial stress meters	Sicada_11_066	Sicada_12_104_1
Soft inclusion stress cells	Sicada_11_066	Sicada_13_057
Deformation meters	Sicada_11_066	Sicada_12_104_1

Table B-2. Labels and coordinates for each biaxial stress meter.

Labelling used in this report			Labelling used by SKB				
Sensor ID	Borehole ID	Depth in borehole (m)	Sensor ID	Borehole ID	Northing (m)	Easting (m)	Elevation (m.a.s.l.)
A5:Bi	A5	3.25	PXPA5BIAX	KA3551G03	6367759.55	1551212.65	–451.88
C5:Bi	C5	6.50	PXPC5BIAX	KA3552G03	6367760.63	1551211.44	–455.40
E5:Bi	E5	7.40	PXPE5BIAX	KA3551G04	6367761.82	1551212.34	–456.00
G5:Bi	G5	3.00	PXPG5BIAX	KA3550G03	6367760.73	1551213.75	–451.89
A6:Bi	A6	0.85	PXPA6BIAX	KA3545G03	6367759.92	1551218.78	–449.61
C6:Bi	C6	4.20	PXPC6BIAX	KA3546G03	6367761.01	1551217.41	–453.27
E6:Bi	E6	4.10	PXPE6BIAX	KA3545G04	6367762.24	1551218.48	–452.86
G6:Bi	G6	0.90	PXPG6BIAX	KA3544G03	6367761.15	1551219.74	–449.98

Table B-3. Labels and coordinates for each soft inclusion stress cell.

Labelling used in this report			Labelling used by SKB				
Sensor ID	Borehole ID	Depth in borehole (m)	Sensor ID	Borehole ID	Northing (m)	Easting (m)	Elevation (m.a.s.l.)
D5:SST	D5	0.8	PXPD5SOF1	KA3552G02	6367761.45	1551211.71	–449.54
D5:SSR	D5	0.6	PXPD5SOF2	KA3552G02	6367761.46	1551211.71	–449.34
H5:SST	H5	0.3	PXPH5SOF1	KA3550G02	6367759.91	1551213.47	–449.06
H5:SSR	H5	0.2	PXPH5SOF2	KA3550G02	6367759.91	1551213.47	–448.96
D6:SST	D6	0.4	PXPD6SOF1	KA3546G02	6367761.84	1551217.71	–449.28
D6:SSR	D6	0.3	PXPD6SOF2	KA3546G02	6367761.84	1551217.71	–449.18
H6:SST	H6	0.4	PXPH6SOF1	KA3544G02	6367760.30	1551219.45	–449.33
H6:SSR	H6	0.3	PXPH6SOF2	KA3544G02	6367760.30	1551219.45	–449.23

Table B-4. Labels and coordinates for each deformation meter.

Labelling used in this report			Labelling used by SKB				
Sensor ID	Borehole ID	Installation section (depth) in borehole (m)	Sensor ID	Borehole ID	Northing (m)	Easting (m)	Elevation (m.a.s.l)
A5:DM1	A5	0.05–1.55	PXPA5DEF1	KA3551G03	6367759.53	1551212.66	–448.68
A5:DM2	A5	1.55–3.05	PXPA5DEF2	KA3551G03	6367759.54	1551212.65	–450.18
C5:DM1	C5	0.10–1.70	PXPC5DEF1	KA3552G03	6367760.63	1551211.41	–449.00
C5:DM2	C5	1.70–3.20	PXPC5DEF2	KA3552G03	6367760.63	1551211.41	–450.60
C5:DM3	C5	3.20–5.10	PXPC5DEF3	KA3552G03	6367760.63	1551211.42	–452.10
E5:DM1	E5	0.10–1.30	PXPE5DEF1	KA3551G04	6367761.85	1551212.36	–448.70
E5:DM2	E5	1.30–4.10	PXPE5DEF2	KA3551G04	6367761.84	1551212.36	–449.90
E5:DM3	E5	4.10–6.30	PXPE5DEF3	KA3551G04	6367761.83	1551212.35	–452.70
E5:DM4*	E5	6.30–6.60	PXPE5DEF4	KA3551G04	6367761.82	1551212.35	–454.70
G5:DM1	G5	0.00–1.50	PXPG5DEF1	KA3550G03	6367760.73	1551213.74	–448.89
G5:DM2	G5	1.50–2.50	PXPG5DEF2	KA3550G03	6367760.73	1551213.75	–450.39
C6:DM1	C6	0.00–1.00	PXPC6DEF1	KA3546G03	6367761.02	1551217.39	–449.07
C6:DM2	C6	1.00–2.30	PXPC6DEF2	KA3546G03	6367761.02	1551217.40	–450.07
C6:DM3	C6	2.30–3.60	PXPC6DEF3	KA3546G03	6367761.01	1551217.40	–451.37
E6:DM1	E6	0.00–1.10	PXPE6DEF1	KA3545G04	6367762.24	1551218.49	–448.76
E6:DM2	E6	1.10–2.00	PXPE6DEF2	KA3545G04	6367762.24	1551218.49	–449.86
E6:DM3	E6	2.00–3.80	PXPE6DEF3	KA3545G04	6367762.24	1551218.49	–450.76

*Note that an incorrect upper coordinate is given for deformation meter E5:DM4 in Bono and Röshoff (2003). The correct coordinate is 6.30 m (Ann Bäckström, ÅF, personal communication).

B.2 Complementary instruments

Complementary deformation meters, specifically aimed at monitoring the response of the rock mass during the heated phase, were installed in horizontal boreholes drilled from the inside of the deposition holes in the outer section, see Figure 6-2 and Figure 6-41. Labels and coordinates for each complementary deformation meter are presented in Table B-5.

In addition, four strain gauges were installed in a vertical borehole drilled from the bottom of each deposition hole in the outer section (Bono and Röshoff 2003). Data from these instruments have not been analyzed in this report (see Table 6-1 and Chapter 9). Therefore, instrument labels and coordinates are not presented here.

Table B-5. Labels and coordinates for each complementary deformation meter.

Labelling used in this report				Labelling used by SKB				
Sensor ID	Borehole ID	Gauge length (m)	Borehole depth (m)*	Sensor ID	Borehole ID	Northing (m)	Easting (m)	Elevation (m.a.s.l.)
DM1	D5:3.5(1)	0.3	2.46	PXPD53D11	KA3551G08	6367759.67	1551212.47	–451.27
DM2	D5:3.5(1)	0.3	2.46	PXPD53D12	KA3551G08	6367759.38	1551212.44	–451.29
DM3	D5:3.5(1)	0.4	2.46	PXPD53D13	KA3551G08	6367759.03	1551212.40	–451.31
DM4	D5:3.5(1)	1.2	2.46	PXPD53D14	KA3551G08	6367758.24	1551212.32	–451.37
DM1	D5:3.5(2)	0.3	2.46	PXPD53D21	KA3551G06	6367760.58	1551213.60	–451.26
DM2	D5:3.5(2)	0.3	2.46	PXPD53D22	KA3551G06	6367760.55	1551213.90	–451.28
DM3	D5:3.5(2)	0.4	2.46	PXPD53D23	KA3551G06	6367760.51	1551214.25	–451.31
DM4	D5:3.5(2)	1.2	2.46	PXPD53D24	KA3551G06	6367760.43	1551215.04	–451.37
DM1	D5:6(1)	0.3	4.96	PXPD56D11	KA3551G09	6367759.67	1551212.48	–453.75
DM2	D5:6(1)	0.3	4.96	PXPD56D12	KA3551G09	6367759.38	1551212.45	–453.77
DM3	D5:6(1)	0.4	4.96	PXPD56D13	KA3551G09	6367759.03	1551212.41	–453.79
DM4	D5:6(1)	1.2	4.96	PXPD56D14	KA3551G09	6367758.24	1551212.33	–453.84
DM1	D5:6(2)	0.3	4.96	PXPD56D21	KA3551G07	6367760.60	1551213.60	–453.76
DM2	D5:6(2)	0.3	4.96	PXPD56D22	KA3551G07	6367760.57	1551213.90	–453.79
DM3	D5:6(2)	0.4	4.96	PXPD56D23	KA3551G07	6367760.54	1551214.25	–453.82
DM4	D5:6(2)	1.2	4.96	PXPD56D24	KA3551G07	6367760.46	1551215.04	–453.89
DM1	D6:3.5(1)	0.3	2.73	PXPD63D11	KA3545G05	6367761.21	1551217.55	–451.38
DM2	D6:3.5(1)	0.3	2.73	PXPD63D12	KA3545G05	6367761.24	1551217.25	–451.41
DM3	D6:3.5(1)	0.4	2.73	PXPD63D13	KA3545G05	6367761.29	1551216.90	–451.43
DM4	D6:3.5(1)	1.2	2.73	PXPD63D14	KA3545G05	6367761.39	1551216.11	–451.49
DM1	D6:3.5(2)	0.3	2.73	PXPD63D21	KA3545G07	6367760.07	1551218.43	–451.38
DM2	D6:3.5(2)	0.3	2.73	PXPD63D22	KA3545G07	6367759.77	1551218.39	–451.40
DM3	D6:3.5(2)	0.4	2.73	PXPD63D23	KA3545G07	6367759.43	1551218.35	–451.42
DM4	D6:3.5(2)	1.2	2.73	PXPD63D24	KA3545G07	6367758.64	1551218.24	–451.47
DM1	D6:6(1)	0.3	5.23	PXPD66D11	KA3545G06	6367761.24	1551217.55	–453.89
DM2	D6:6(1)	0.3	5.23	PXPD66D12	KA3545G06	6367761.28	1551217.26	–453.92
DM3	D6:6(1)	0.4	5.23	PXPD66D13	KA3545G06	6367761.34	1551216.91	–453.96
DM4	D6:6(1)	1.2	5.23	PXPD66D14	KA3545G06	6367761.46	1551216.12	–454.04
DM1	D6:6(2)	0.3	5.23	PXPD66D21	KA3545G08	6367760.08	1551218.41	–453.87
DM2	D6:6(2)	0.3	5.23	PXPD66D22	KA3545G08	6367759.78	1551218.38	–453.89
DM3	D6:6(2)	0.4	5.23	PXPD66D23	KA3545G08	6367759.43	1551218.34	–453.91
DM4	D6:6(2)	1.2	5.23	PXPD66D24	KA3545G08	6367758.64	1551218.24	–453.96

* The depth of horizontal borehole is measured from the deposition hole perimeter.

Appendix C

Influence of tunnel plugs

In this appendix, the thermo-mechanical impact of the two tunnel plugs on the stresses in the outer section is assessed.

C.1 Description of 3DEC model

C.1.1 Geometry

The 3DEC model has the same geometry as the models in Chapters 5, 6 (heated phase) and 7, see e.g. Figure 5-7. Although the plugs were not included in the mechanical calculations in these Chapters, the plug geometry has been incorporated into the models considered here. Figure C-1 shows a close-up view of the outer section with the plug geometry.

C.1.2 Calculation sequence

The response of the rock mass to changes in mechanical and thermal conditions is assessed in five general steps:

1. A primary equilibrium is established,
2. the tunnel is excavated,
3. the deposition holes are excavated,
4. the plug slots are excavated,

(4b. in the model with plugs, the volumes corresponding to the plugs are reinstated and assigned suitable material properties, see below)

5. the thermal impact is determined.

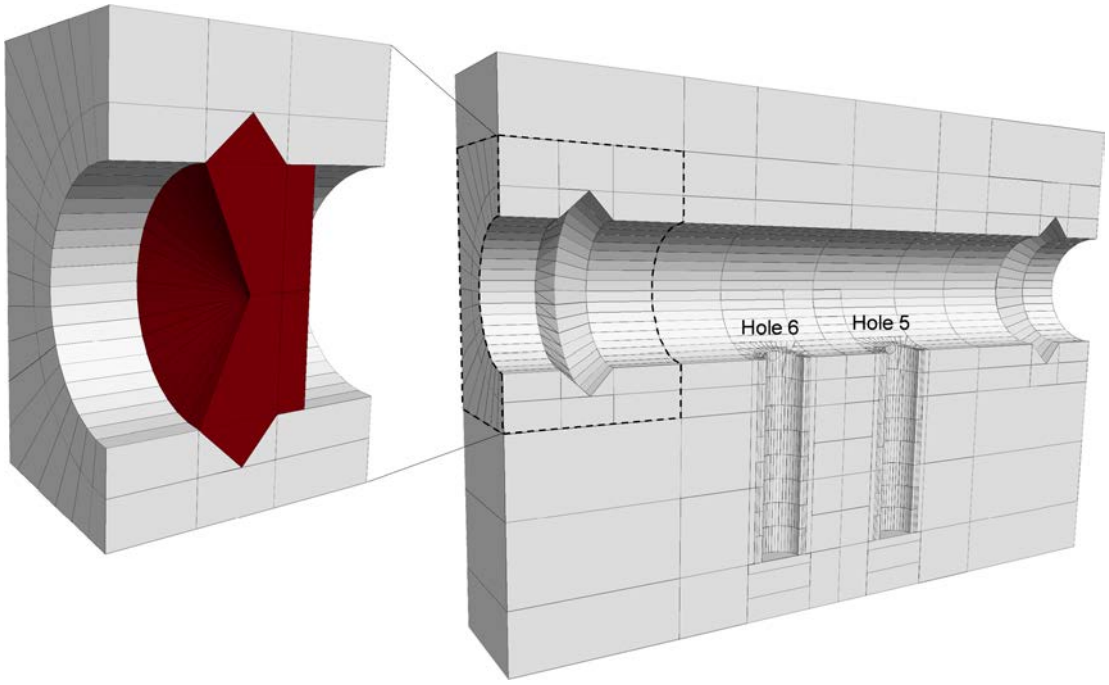

Figure C-1. *Close-up of outer section of Prototype 3DEC model.*

C.1.3 Input data

The mechanical and thermo-mechanical properties of the rock are taken from Staub et al. (2004), see Table C-1. The thermal properties and Poisson's ratio of the concrete plugs are taken to be the same as for the rock, whereas the coefficient of linear thermal expansion and Young's modulus of the plugs are based on standard textbook data for concrete, see Table C-1. The interfaces between the rock and the plugs are given fictitious high-strength/high-stiffness properties, see Table C-2.

Table C-1. Input data for thermo-mechanical 3DEC models.

Material property	Unit	Rock	Plugs
Thermal conductivity	W/(m·K)	2.72	2.72
Heat capacity	MJ/(m^3·K)	2.13	2.13
Density	kg/m^3	2,770	2,770
Young's modulus	GPa	76	30
Poisson's ratio	–	0.25	0.25
Coefficient of linear thermal expansion	K^{-1}	$7 \cdot 10^{-6}$	$1.2 \cdot 10^{-5}$

Table C-2. Fictitious fracture material for intersection between excavated/backfilled materials and rock.

Material property	Unit	Value
Fracture normal stiffness	GPa/m	20,000
Fracture shear stiffness	GPa/m	20,000
Cohesion	MPa	500
Friction angle	°	45
Tensile strength	MPa	500

The *in situ* stress model is based on the mean, or average, stress magnitudes and orientations given in the stress model in Section 3.3, see Table C-3.

Table C-3. In situ stress model. Magnitudes in MPa; Trend in degrees in the Swedish national RT90 system; Plunge in degrees from horizontal.

Model name	σ1			σ2			σ3		
	Mag.	Trend	Plunge	Mag.	Trend	Plunge	Mag.	Trend	Plunge
Base case (Case 1)	28	304	0	14	214	0	12.8	–	90

C.2 Results

Figure C-2 shows the evolution of stresses within the rock at nine points around the deposition holes and around the plug slots. At close proximity to the tunnel plugs, there is some influence on the stresses (see Pts. 8 and 9). However, at positions close to the deposition holes, the plugs have no influence on the stresses (e.g. Pt. 1, 2 and 3).

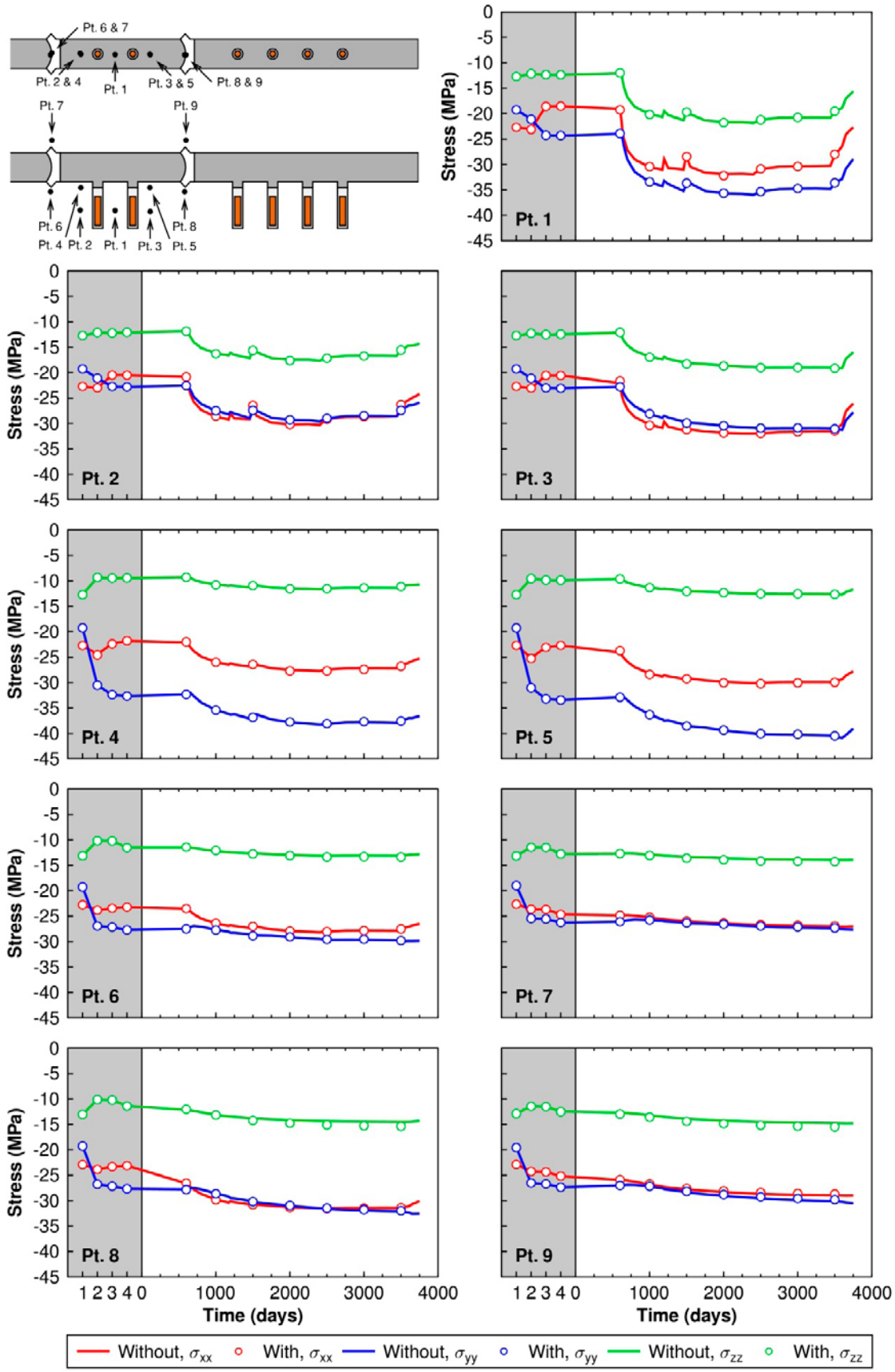

Figure C-2. *Comparison between stresses in the rock above and below the plugs.*

Appendix D

Derivation of radial deformation around a pressurized thick-walled cylinder

An expression for the radial deformation (u_r) around a thick-walled cylinder (see Figure D-1) with inner radius R_i and inner pressure p_i, and outer radius R_o and outer pressure p_o, under plane stress conditions is given by e.g. Sundström (1988). The corresponding expression for plane strain conditions is derived here.

In cylindrical polar coordinates, axisymmetric geometry and no body forces, the equilibrium equation is given by (Brady and Brown 1993)

$$\frac{d\sigma_{rr}}{dr} + \frac{(\sigma_{rr} - \sigma_{\theta\theta})}{r} = 0 \tag{D-1}$$

where σ_{rr} and $\sigma_{\theta\theta}$ are the radial and tangential stress components, respectively. Adopting the common sign convention that compressive stresses are positive, the corresponding strain components for plane strain conditions are given by (Brady and Brown 1993)

$$\varepsilon_{rr} = -\frac{\partial u_r}{\partial r},$$

$$\varepsilon_{\theta\theta} = -\frac{u_r}{r} \text{ and} \tag{D-2}$$

$$\varepsilon_{zz} = 0$$

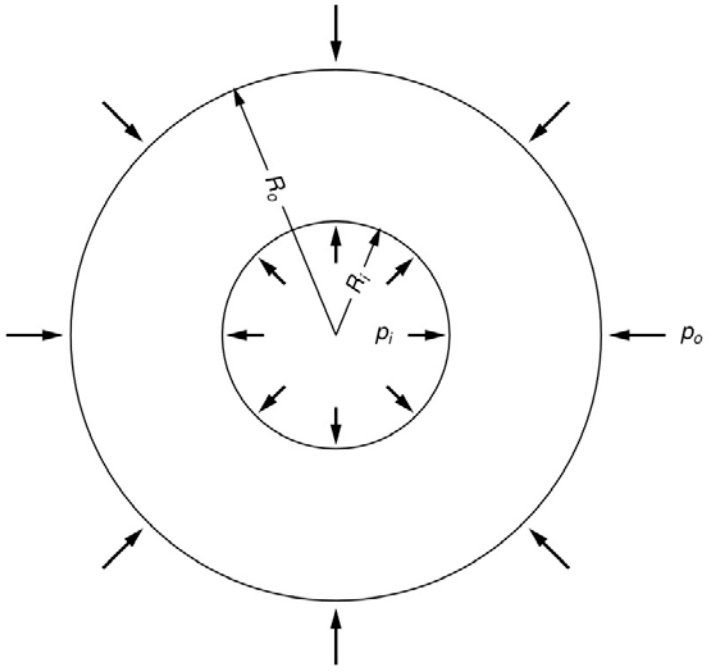

Figure D-1. *Cross-section of a thick-walled cylinder with inner radius R_i and inner pressure p_i and with outer radius R_o and outer pressure p_o.*

Assuming isotropic elasticity, Hooke's law gives the following stress-strain relations (Brady and Brown 1993)

$$\varepsilon_{rr} = \frac{1}{E}\left(\sigma_{rr} - \nu\left[\sigma_{\theta\theta} + \sigma_{zz}\right]\right),$$
$$\varepsilon_{\theta\theta} = \frac{1}{E}\left(\sigma_{\theta\theta} - \nu\left[\sigma_{rr} + \sigma_{zz}\right]\right) \quad \text{(D-3)}$$

with

$$\sigma_{zz} = \nu\left(\sigma_{rr} + \sigma_{\theta\theta}\right)$$

where E is Young's modulus and v is Poisson's ratio.

Combining equations (D-2) and (D-3) and expressing them in terms of stresses and radial displacement gives

$$\sigma_{rr} = -\frac{E'}{1-\nu'^2}\left(\frac{\partial u_r}{\partial r} + \nu'\frac{u_r}{r}\right)$$
$$\sigma_{\theta\theta} = -\frac{E'}{1-\nu'^2}\left(\frac{u_r}{r} + \nu'\frac{\partial u_r}{\partial r}\right) \quad \text{(D-4)}$$

where $E' = E/(1–\nu^2)$ and $\nu' = \nu/(1–\nu)$.

Inserting the expressions given by Equation (D-4) into Equation (D-1) and simplifying yields an expression for the radial displacement identical to the case for plane stress (Sundström 1988)

$$\frac{d^2u_r}{dr^2} + \frac{1}{r}\frac{du_r}{dr} - \frac{u_r}{r^2} = \frac{d}{dr}\left[\frac{1}{r}\frac{d}{dr}\left(ru_r\right)\right] = 0$$

with solution

$$u_r(r) = C_1 r + \frac{C_2}{r} \quad \text{(D-5)}$$

The expressions for the radial and tangential stress components are given by (Brady and Brown 1993)

$$\sigma_{rr} = \frac{R_i^2\left(p_i - p_o\right)}{1 - R_i^2/R_o^2}\frac{1}{r^2} + \frac{p_o - p_i R_i^2/R_o^2}{1 - R_i^2/R_o^2}$$
$$\sigma_{\theta\theta} = -\frac{R_i^2\left(p_i - p_o\right)}{1 - R_i^2/R_o^2}\frac{1}{r^2} + \frac{p_o - p_i R_i^2/R_o^2}{1 - R_i^2/R_o^2} \quad \text{(D-6)}$$

Where R_i and R_o are the inner and outer radii of the cylinder, respectively.

Thus, combining equations (D-2), (D-3) and (D-6) yields values for the constants of integration C_1 and C_2:

$$C_1 = -\frac{p_o - p_i R_i^2 / R_o^2}{1 - R_i^2 / R_o^2} \frac{1-\nu'}{E'}$$

$$C_2 = \frac{R_i^2 \left(p_i - p_o \right)}{1 - R_i^2 / R_o^2} \frac{1+\nu'}{E'}$$

The expression for an infinitely thick cylinder with inner pressure p_i and outer pressure $p_o = 0$ is obtained by letting $R_o \rightarrow \infty$

$$u_r(r) = p_i \frac{1}{2G} \frac{R_i^2}{r} \tag{D-7}$$

Appendix E

Wedge stability

E.1 General

In this appendix, we investigate whether wedges formed between two steeply dipping fractures and one gently dipping fracture may become unstable during the heated phase. Rather than basing the analyses on the actually observed fractures that intersect the two deposition holes (cf. Figure E-1), a more generic approach is taken. For base-case material properties and *in situ* stresses, the stress magnitudes are highest in the uppermost parts of the holes and overall higher in Hole 5 than in Hole 6 (cf. Figure 7-6 and Figure 7-7). Therefore, it is assumed that wedges are located in the region of high compressive stress perpendicular to the major principal stress in Hole 5.

E.2 Modelling approach

The wedge stability analyses are based on two independent approaches using 3DEC version 4.10:

1. A semi-analytical approach where stability of the fracture planes forming the wedge is quantified in terms of the Coulomb Failure Stress (*CFS*). The state of stress is obtained from a large linear elastic model with a detailed representation of deposition holes and tunnel geometry.
2. Stability analyses based on 3DEC models with explicitly modelled wedges.

Conclusions regarding stability are drawn based on consistency between the two approaches.

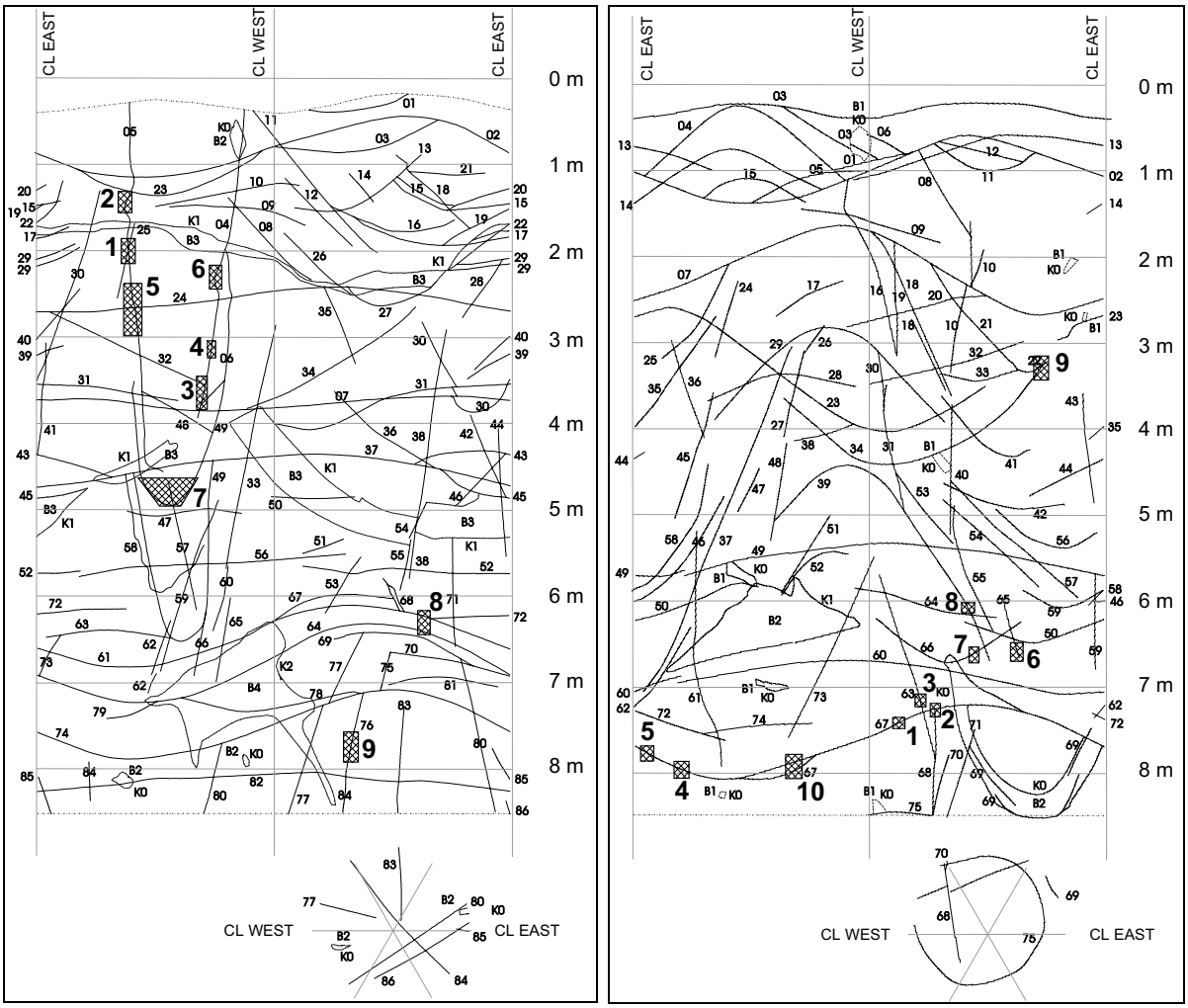

Figure E-1. *Fracture mapping of the two deposition holes in the outer section left: Hole 5 and right: Hole 6 (from Rhén and Forsmark 2001).*

E.2.1 Semi-analytical approach

The state of stress ($\boldsymbol{\sigma}$) on the fracture planes forming the wedge is represented by that at a number of discrete points sampled from the continuum at positions close to the fracture planes. The state of stress at any given point is represented by the six stress components

$$\boldsymbol{\sigma} = \begin{pmatrix} \sigma_{xx} & \sigma_{xy} & \sigma_{xz} \\ \sigma_{xy} & \sigma_{yy} & \sigma_{yz} \\ \sigma_{xz} & \sigma_{yz} & \sigma_{zz} \end{pmatrix} \tag{E-1}$$

where σ_{xx} is the stress component along the tunnel, σ_{yy} across the tunnel, σ_{zz} vertical and σ_{xy}, σ_{xz} and σ_{yz} are shear stresses. The normal (σ_N) and shear (τ) stresses on a plane with unit normal vector $\underline{\hat{n}}$ are obtained from the stress matrix (Eq. (E-1)) using the following expressions:

$$\begin{aligned} \underline{t} &= \boldsymbol{\sigma} \cdot \underline{\hat{n}}, \\ \sigma_N &= \underline{t} \cdot \underline{\hat{n}}, \\ \tau &= \sqrt{\left|\underline{t}\right|^2 - {\sigma_N}^2}. \end{aligned} \tag{E-2}$$

The stability of the fracture plane is subsequently quantified in terms of the Coulomb Failure Stress (*CFS*), which is defined as

$$CFS = \tau - \left(c + \sigma_N \tan\left(\phi\right)\right), \tag{E-3}$$

where c is cohesion (MPa) and ϕ is the friction angle (°). Parameter values for the cohesion and friction angle are consistent with data obtained in the Laxemar site-investigation (Hakami et al. 2008), cf. Table E-1.

Table E-1. Fracture strength properties.

Parameter	Unit	Value
Friction angle (ϕ)	°	35.7
Cohesion (c)	MPa	0

E.2.2 Description of 3DEC models

Geometry

The linear elastic model consists of a 200 m × 200m × 200 m block of rock in which the tunnel, plug slots and all six deposition holes are explicitly represented (see Figure E-2). Roller boundaries are applied on the top and bottom boundaries whereas all outer boundaries are locked in the horizontal directions

For the purpose of this study, the 3DEC models with wedges are reduced in size to 24 m (along the tunnel), 20 m (across the tunnel) and 30 m (vertically), cf. Figure E-3 (upper left) and only include the rock around the deposition holes in the outer section of the Prototype Repository. However, the temperature contribution from the canisters in the inner section is accounted for. Figure E-3 shows the displacement field along the linear elastic model's coordinate axes after 2,000 days of heating. The positions of the smaller "wedge-model's" boundaries are outlined in black. Locking the boundary movements at these positions is likely to overestimate the stresses by about 2–3 MPa.

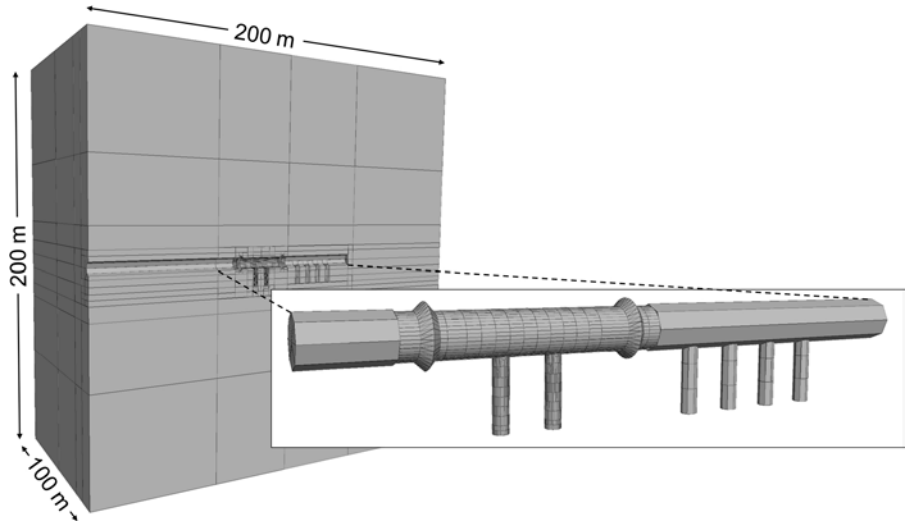

Figure E-2. *Outline of the linear elastic 3DEC model. Note that parts of the model are hidden to expose the tunnel and deposition holes. Inset shows the geometry of the tunnel, plug slots and deposition holes.*

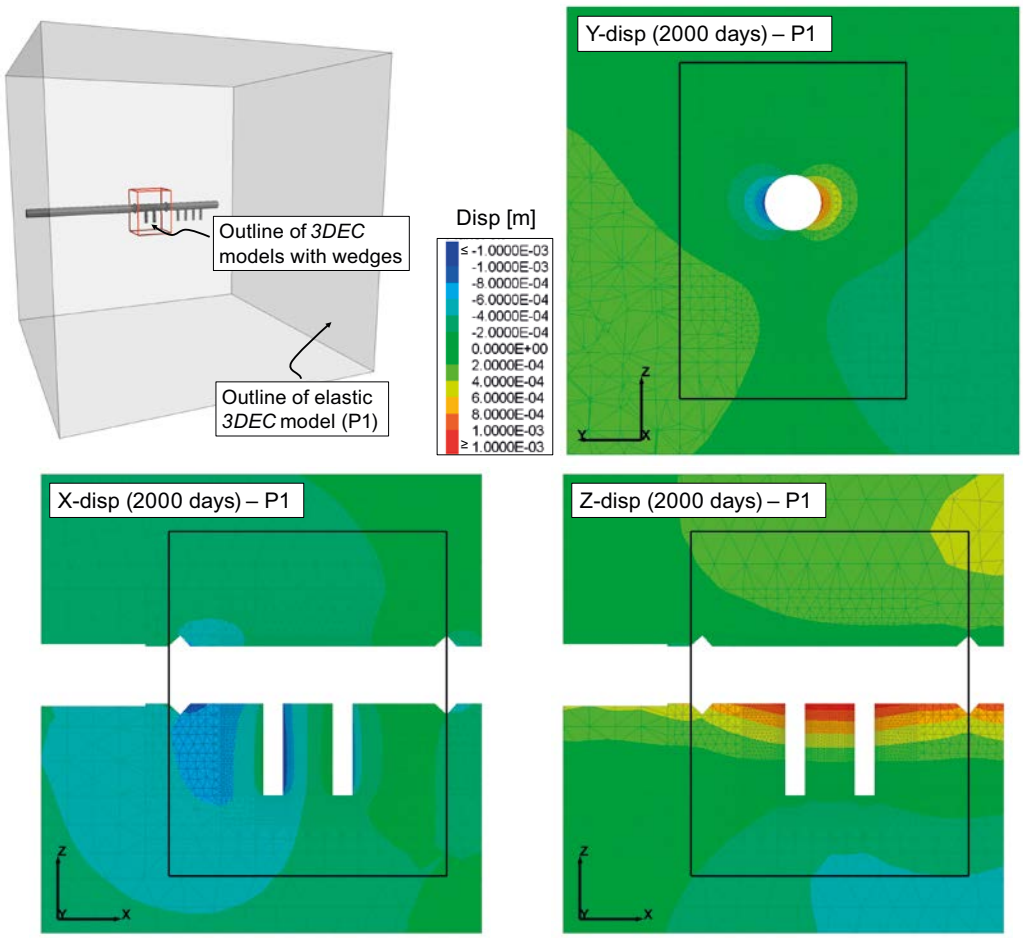

Figure E-3. *Top left: Schematic drawing of difference in size between the linear elastic model and smaller models with wedges. Top right and lower row: Displacement magnitudes after 2,000 days of heating along the model's coordinate axes as calculated by the linear elastic model P1. The boundaries of the 3DEC models with wedges are outlined in black.*

The circular cross-section of the tunnel and deposition holes is approximated by polygons with ten tangential sections. For practical purposes, *i.e.* to avoid forming very small blocks, the wedges are symmetrically positioned with respect to the deposition hole geometry. This means that the dip direction of the gently dipping fracture deviates by about 2° from the most likely orientation of the minor horizontal *in situ* stress.

Two wedges are considered with separate geometries for each wedge and mesh sizes adjusted to suit each model. Orientations of the fracture planes forming the wedge are given in terms of dip and dip direction. In 3DEC, dip direction is measured clockwise from the positive *y*-axis.

- **Wedge 1 (Figure E-4, left):** Wedge formed between fractures with orientation (dip/dip direction) – 30/216, 64.9/329.3, 64.9/102.7
- **Wedge 2 (Figure E-4, right):** Wedge formed between fractures with orientation (dip/dip direction) – 30/216, 68.5/345.2, 68.5/86.8

Input data

Input data for the thermal, mechanical and thermo-mechanical properties are given in Table E-2. The thermal parameter values are the same as in the Code_Bright model CB 2 (cf. Table 4-1). Parameter values for the mechanical and thermo-mechanical rock properties are chosen from the range established for the APSE test-site (Staub et al. 2004).

Table E-2. Thermal, mechanical and thermo-mechanical properties of the rock.

Parameter	Unit	Value
Thermal conductivity	W/(m·K)	2.72
Thermal diffusivity	m^2/s	$1.275 \cdot 10^{-6}$
Density	kg/m^3	2,770
Young's modulus	GPa	76
Poisson's ratio	–	0.25
Coefficient of thermal expansion	K^{-1}	$7 \cdot 10^{-6}$

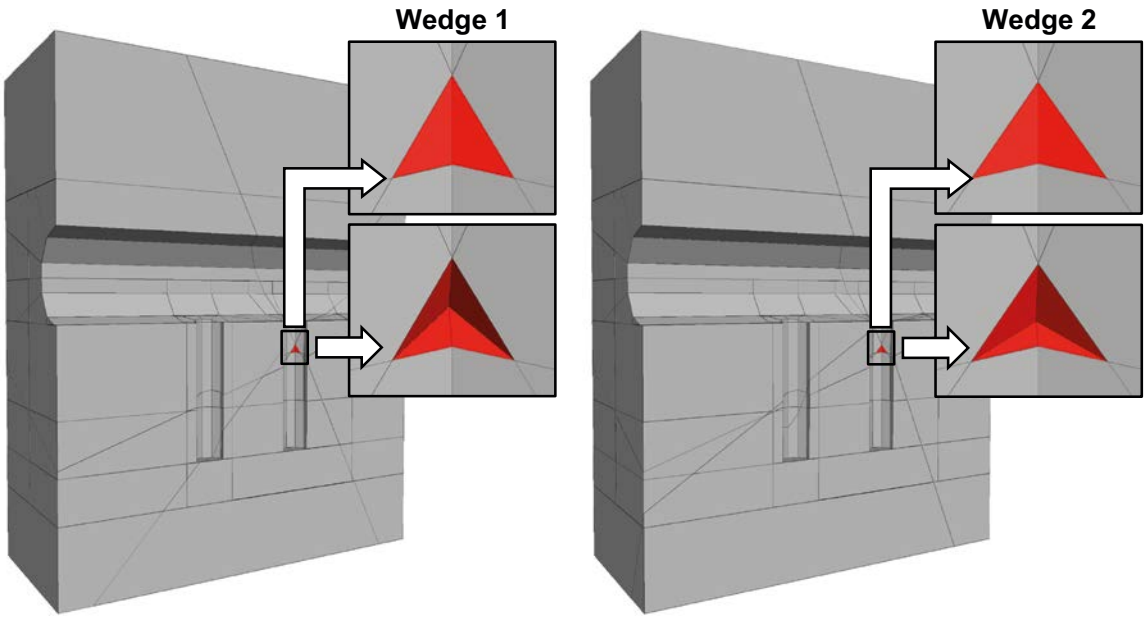

Figure E-4. *Outlines of models with wedges: Wedge 1 (left) and Wedge 2 (right). Top insets show a close-up of deposition hole with the wedge shown in red. Bottom insets show the void formed when removing the wedge. Note that parts of the model are hidden to expose the tunnel and deposition holes.*

The *in situ* stress model is based on the mean, or average, stress magnitudes and orientations given in the stress model in Section 3.3, see Table E-3.

Table E-3. *In situ* stress models. Magnitudes in MPa; Trend in degrees in the Swedish national RT90 system; Plunge in degrees from horizontal.

σ1			σ2			σ3		
Mag.	Trend	Plunge	Mag.	Trend	Plunge	Mag.	Trend	Plunge
28	304	0	14	214	0	12.8	–	90

Fracture deformation and strength properties are based on data from the Laxemar site description (Hakami et al. 2008), cf. Table E-4.

Table E-4. Fracture deformation and strength properties, based on data from Laxemar (Hakami et al. 2008).

Parameter	Unit	Value
Normal stiffness (jkn)	GPa/m	721
Shear stiffness (jks)	GPa/m	39
Friction angle (ϕ)	°	35.7
Cohesion (c)	MPa	0.6 (0 after slip)

E.3 Results

Figure E-5 shows that all three fracture planes forming Wedge 1 are stable after excavation and during the subsequent heated phase. With the exception of parts of the steeply dipping fractures close to the deposition hole opening (Point 2 in the bottom sub-figure), the stability margin increases during heating.

In the numerical model with an explicitly modelled wedge, the displacements inside the wedge are of the same magnitude as in the surrounding parts of the rock (Figure E-6). This confirms the result from the semi-analytical analyses in Figure E-5 that Wedge 1 is stable.

Figure E-7 (top) shows that, similarly to Wedge 1, the gently dipping fracture is stable at all points in time. The two steeply dipping fractures (middle and lower sub-figures) are unstable from the point of excavation of the holes and through the subsequent heated phase. Possible exceptions from this are parts of the fractures planes located far away from the hole opening. For the parts of the fracture planes that were stable (or bordering on instability) after excavation of the deposition holes, the stability margin increases during the heated phase. For the parts of the fractures planes that were instable already after excavation of the holes, the instability increases during the heated phase.

In the numerical model with an explicitly modelled wedge, the displacement magnitudes inside the wedge are greater than in the surrounding parts of the rock (Figure E-8). This confirms the result from the semi-analytical analyses in Figure E-7 that Wedge 2 is unstable.

E.4 Summary

For the wedge examples considered here, the stability predicted by use of a semi-analytical approach based on shear and normal stresses calculated on hypothetical fracture planes in a linear elastic model, agreed with corresponding results from inelastic models with explicitly modelled fractures. The deep Wedge 1 was found to be stable whereas the shallow Wedge 2 detached from the rock wall.

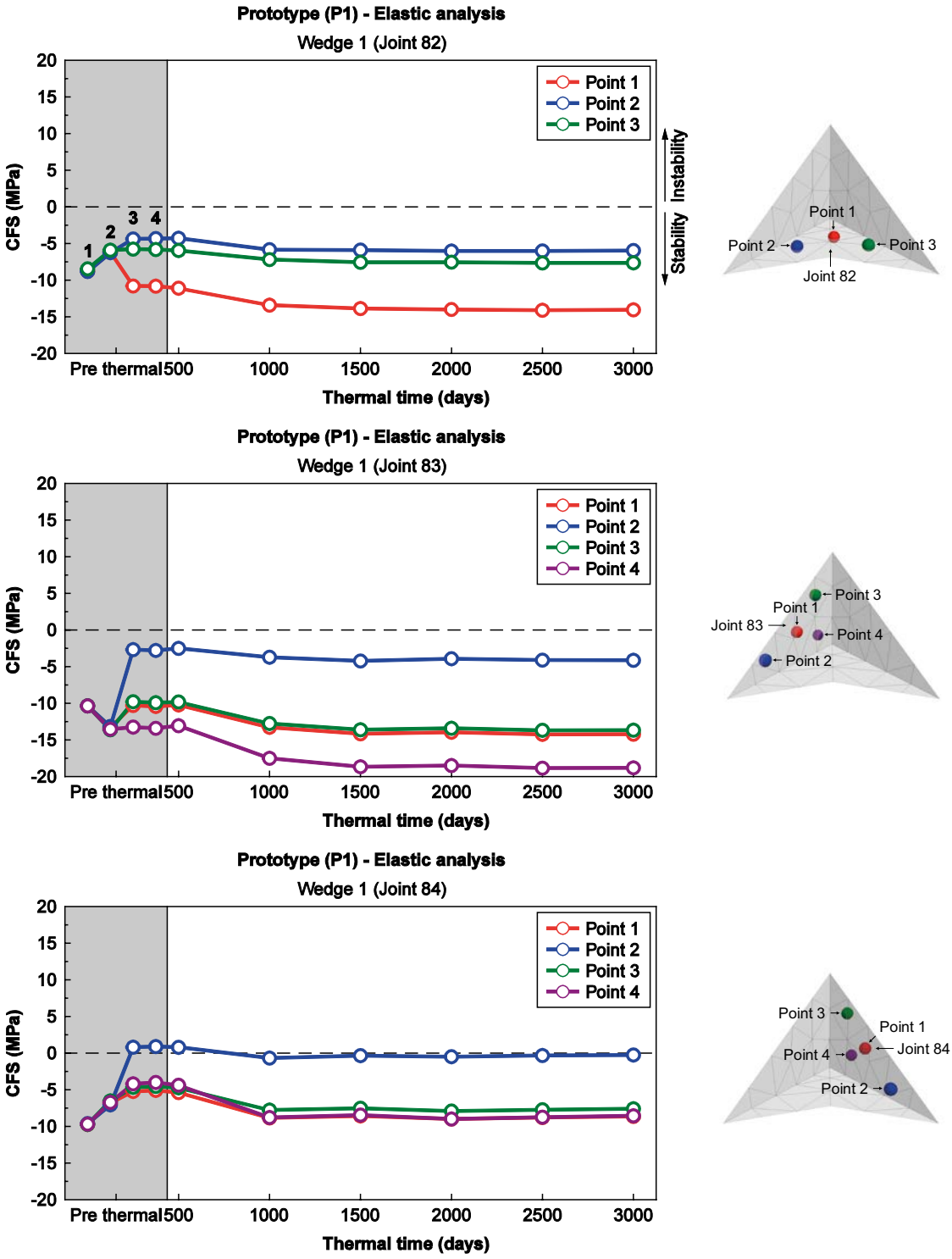

Figure E-5. *Stability analysis of fracture planes surrounding Wedge 1 based on state of stress as calculated by the linear elastic model. Pre thermal time (marked in grey) represents 1) initial state of stress, 2) excavation of the tunnel, 3) excavation of the deposition holes and 4) excavation of the plug slots.*

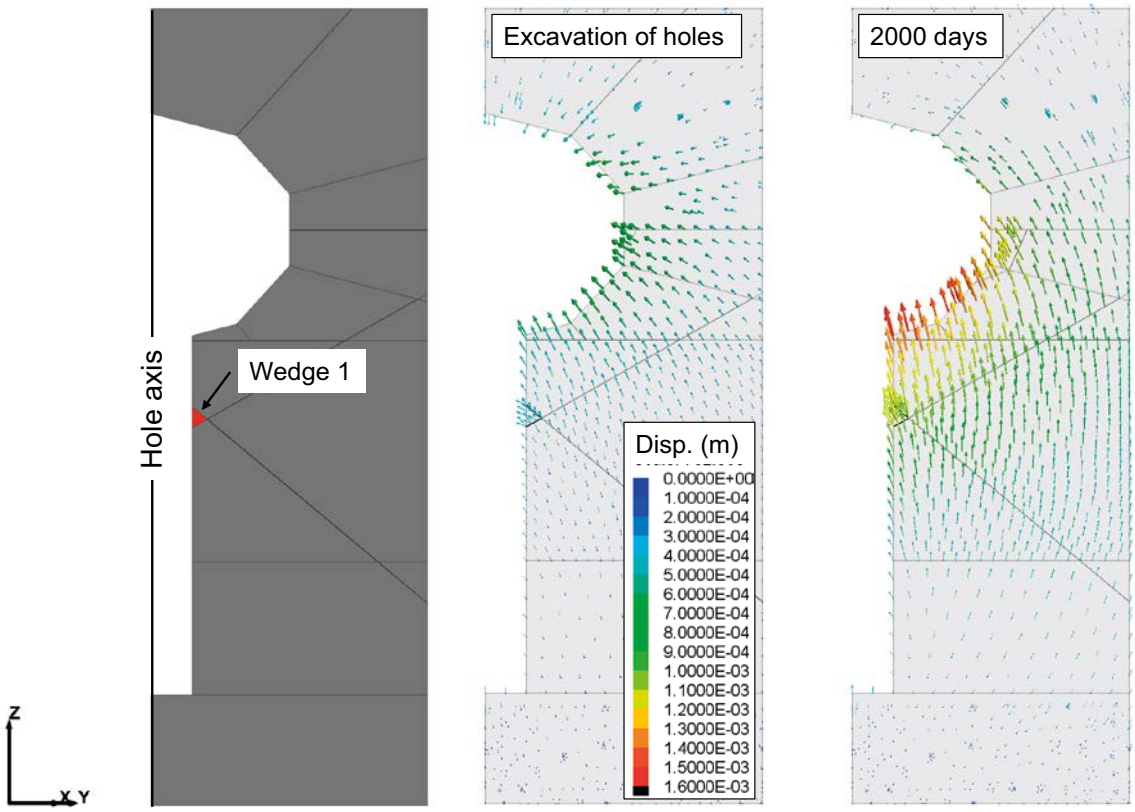

Figure E-6. *Displacement vectors in a vertical cross-section through the centre of Wedge 1 after excavation (middle) and after 2,000 days of heating (right).*

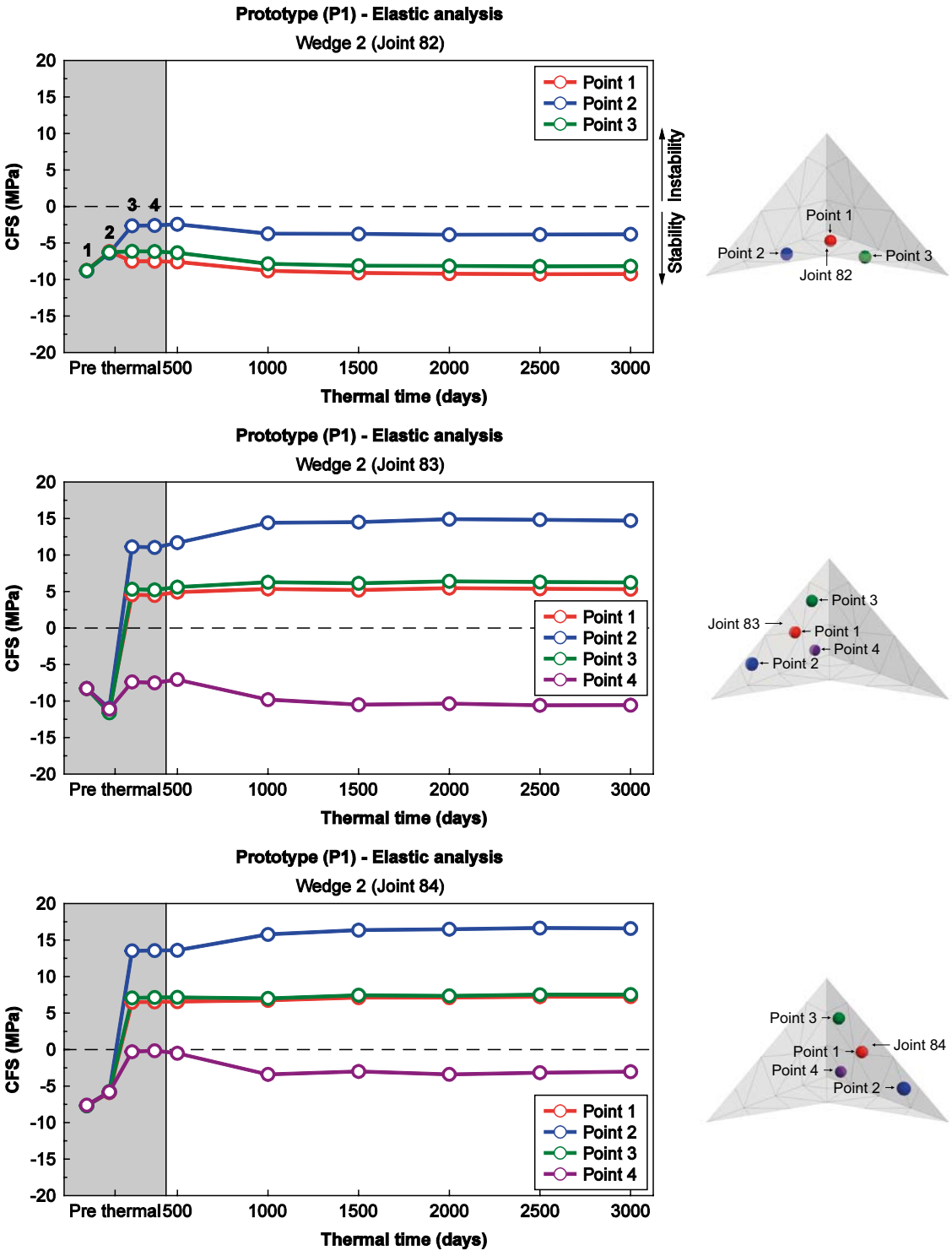

Figure E-7. *Stability analysis of fracture planes surrounding Wedge 2 based on state of stress as calculated by the linear elastic model. Pre thermal time (marked in grey) represents 1) initial state of stress, 2) excavation of the tunnel, 3) excavation of the deposition holes and 4) excavation of the plug slots.*

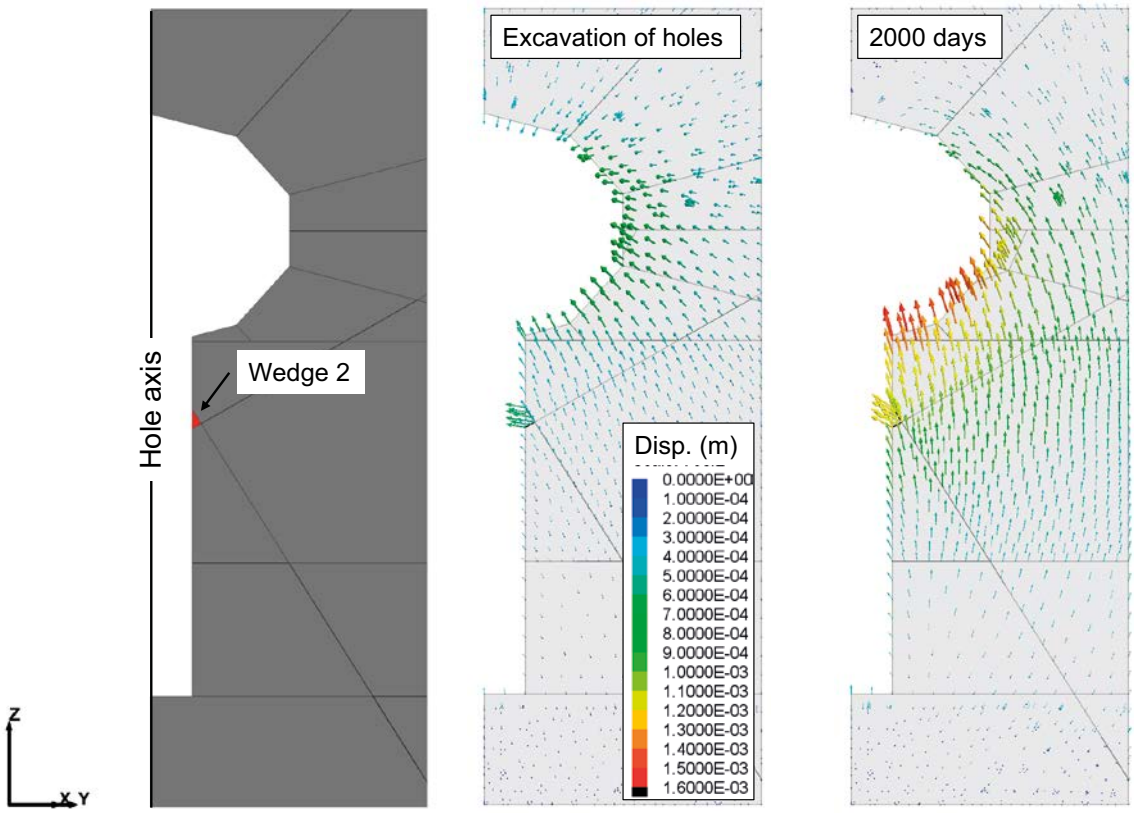

Figure E-8. *Displacement vectors in a vertical cross-section through the centre of Wedge 2 after excavation (middle) and after 2,000 days of heating (right).*

Appendix F

FISH-functions for export and import of boundary conditions

F.1 Description of method to assign boundary conditions

A method is set up to assign displacement-type boundary conditions to a small 3DEC model using data from the interior of a larger model. First, position vectors and displacement vectors are transferred from the large model to a text file for import into the smaller model (see Table F-1). Second, the data are imported into the smaller model and an interpolation scheme is set up to approximate the displacements on the boundaries (see Table F-2).

The interpolation scheme is based on linear interpolation of the displacement vectors at the four gridpoints of an imported tetrahedral zone using barycentric coordinates (see e.g. Vince 2010, Chapter 11). If a boundary gridpoint at location $\boldsymbol{r}$ is inside or on the boundary of an imported tetrahedral zone, the interpolated displacement vector ($\boldsymbol{u}_I$) at that gridpoint is given by

$$\boldsymbol{u}_I(\boldsymbol{r}) = \sum_{i=1}^{4} \alpha_i \boldsymbol{u}(\boldsymbol{r}_i) \tag{F-1}$$

where $\boldsymbol{u}(\boldsymbol{r}_i)$ the imported displacement vector at each of the four nodes of the tetrahedral zone and α_i is the barycentric coordinate of $\boldsymbol{r}$ relative to $\boldsymbol{r}_i$. The barycentric coordinates are defined as (Schneider and Eberly 2003)

$$\alpha_1 = \frac{\boldsymbol{n}_1 \cdot (\boldsymbol{r} - \boldsymbol{r}_4)}{\boldsymbol{n}_1 \cdot (\boldsymbol{r}_1 - \boldsymbol{r}_4)};\ \alpha_2 = \frac{\boldsymbol{n}_2 \cdot (\boldsymbol{r} - \boldsymbol{r}_3)}{\boldsymbol{n}_2 \cdot (\boldsymbol{r}_2 - \boldsymbol{r}_3)};\ \alpha_3 = \frac{\boldsymbol{n}_3 \cdot (\boldsymbol{r} - \boldsymbol{r}_2)}{\boldsymbol{n}_3 \cdot (\boldsymbol{r}_3 - \boldsymbol{r}_2)};\ \alpha_4 = \frac{\boldsymbol{n}_4 \cdot (\boldsymbol{r} - \boldsymbol{r}_1)}{\boldsymbol{n}_4 \cdot (\boldsymbol{r}_4 - \boldsymbol{r}_1)} \tag{F-2}$$

where each $\boldsymbol{n}_i$ is the outwards-pointing normal vector to the face that is located opposite $\boldsymbol{r}_i$ and contains $\boldsymbol{r}_{4-i}$. Note that a boundary gridpoint can be located on the boundary of several imported tetrahedral zones. However, to speed up the calculation, the FISH code (see Table F-2) is written such that only the first tetrahedral zone in the imported list that has the given boundary gridpoint in its interior or on its boundary is used for interpolation. The code can easily be adapted to average the displacement at a boundary gridpoint over all tetrahedral zones that fit the criterion of having the given boundary gridpoint in their interior or on their boundaries.

If a boundary gridpoint is not inside or on the boundary of any imported tetrahedral zone, for example on the tunnel boundary, the displacement vector at that point is set equal to that of the nearest imported gridpoint.

F.2 FISH-functions

The FISH codes used for export and import of data are provided in Table F-1 and Table F-2, respectively.

Table F-1. FISH code for exporting displacement boundary conditions.

```
;--- export displacement boundary conditions to file filename ---
;--- needs: two concentric 'boxes' (name range) bigBox and smallBox that enclose the boundary of the smaller
;--- model with a suitable margin
;--- needs: a suitable block region bregion that enclose bigBox and smallBox to speed up export

def write_bc(bigBox,smallBox,bregion,filename)

;--- defines new index to list of blocks in bregion
  bhead = null                                          ; index to list of blocks in bregion
  bi = block_head                                       ; index to list of blocks

  loop while bi # 0                                     ; loop over all blocks

    if b_region(bi) # bregion                           ; block not inside bregion

      bi = b_next(bi)                                   ; next block

    else

      bd = get_mem(2)                                   ; new index
      mem(bd) = bhead
      bhead = bd
      mem(bd+1) = bi                                    ; returns block index

      bi = b_next(bi)                                   ; next block

    endif

  endloop

;--- defines new index to list of zones in bregion
  znum = 0                                              ; counter of number of zones in bregion
  zhead = null                                          ; index to list of blocks in bregion
  bd = bhead

  loop while bd # null                                  ; loop over all blocks in bregion

    bi = mem(bd+1)                                      ; block index
    zi = b_zone(bi)                                     ; index to list of zones in block

    loop while zi # 0                                   ; loop over all zones in block

    ; check if zone intersects boundary region
      section

        j1 = in_range(string(smallBox),gp_pos(z_gp(zi,1)))   ; checks if zone gp 1,2,3
        j2 = in_range(string(smallBox),gp_pos(z_gp(zi,2)))   ; and 4 are inside (returns
        j3 = in_range(string(smallBox),gp_pos(z_gp(zi,3)))   ; 1) or outside (returns
        j4 = in_range(string(smallBox),gp_pos(z_gp(zi,4)))   ; 0) of the range smallBox
        j = j1+j2+j3+j4

        if j = 4                                        ; all four gp inside smallBox
          exit section
        endif

        j1 = in_range(string(bigBox),gp_pos(z_gp(zi,1)))   ; checks if zone gp 1,2,3 and
        j2 = in_range(string(bigBox),gp_pos(z_gp(zi,2)))   ; 4 are inside (returns 1) or
        j3 = in_range(string(bigBox),gp_pos(z_gp(zi,3)))   ; outside (returns 0) of the
        j4 = in_range(string(bigBox),gp_pos(z_gp(zi,4)))   ; range bigBox
        j = j1+j2+j3+j4
```

```
        if j = 0                                        ; all four gp outside bigBox
          znum = znum                                   ; does not count to zones around boundary
          exit section


        else

          znum = znum + 1                               ; intersects boundary region

          zd = get_mem(2)                               ; new index
          mem(zd) = zhead
          zhead = zd
          mem(zd+1) = zi                                ; returns zone index

        endif

      endsection

      zi = z_next(zi)                                   ; next zone in block

    end_loop

    bd = mem(bd)                                        ; next block in bregion

  end_loop

;--- create array of positions and displacements and print to file ---

  myarray = get_array(znum+1)                           ; create array
  myarray(1) = znum                                     ; put number of zones znum at top of array

  count = 2
  zd = zhead

  loop while zd # null

    zi = mem(zd+1)
    pos1 = string(gp_pos(z_gp(zi,1)))                   ; position vector of gp 1
    dis1 = string(gp_dis(z_gp(zi,1)))                   ; displacement vector of gp 1
    pos2 = string(gp_pos(z_gp(zi,2)))                   ; position vector of gp 2
    dis2 = string(gp_dis(z_gp(zi,2)))                   ; displacement vector of gp 2
    pos3 = string(gp_pos(z_gp(zi,3)))                   ; position vector of gp 3
    dis3 = string(gp_dis(z_gp(zi,3)))                   ; displacement vector of gp 3
    pos4 = string(gp_pos(z_gp(zi,4)))                   ; position vector of gp 4
    dis4 = string(gp_dis(z_gp(zi,4)))                   ; displacement vector of gp 4

    mystring =              pos1+' '+dis1               ; write gp position
    mystring = mystring+' '+pos2+' '+dis2               ; and displacements
    mystring = mystring+' '+pos3+' '+dis3               ; as a
    mystring = mystring+' '+pos4+' '+dis4               ; string

    myarray(count) = mystring                           ; put string into array
    count = count + 1
    zd = mem(zd)

  end_loop

  o_status=open(string(filename),1,1)                   ; write myarray
  r_status=write(myarray,znum+1)                        ; to
  c_status=close                                        ; file filename

end
```

Table F-2. FISH code for importing and interpolating displacement boundary conditions.

```
;---import boundary conditions from file filename, assign number of cycles mycycles to calculate boundary gp
velocity---
def read_bc(filename,mycycles)

;--- read number of zones on the boundary in the larger model into variable znum ---
   znumarray = get_array(1)

   o_status=open(string(filename),0,1)
   r_status=read(znumarray,1)
   c_status=close

   znum = parse(znumarray(1),1)

;--- for each tetrahedral zone, read string of positions and displacements of each node into array temp, NOTE THAT
znum IS ON LINE 1!!! ---
   temp = get_array(znum+1)

   o_status=open(string(filename),0,1)
   r_status=read(temp,znum+1)
   c_status=close

;--- assign memory for arrays ---
   p1 = get_array(znum)
   p2 = get_array(znum)
   p3 = get_array(znum)
   p4 = get_array(znum)

   d1 = get_array(znum)
   d2 = get_array(znum)
   d3 = get_array(znum)
   d4 = get_array(znum)

   n1 = get_array(znum)
   n2 = get_array(znum)
   n3 = get_array(znum)
   n4 = get_array(znum)

;--- for each tetrahedral zone, read string-array temp into separate arrays for position (px) and displacement (dx) --
-
   n = 2
   loop while n <= znum+1

     k = n-1

   ;--- arrays of node positions ---
     p1(k) = vector(parse(temp(n),1),parse(temp(n),2),parse(temp(n),3))
     ; position of node p1
     p2(k) = vector(parse(temp(n),7),parse(temp(n),8),parse(temp(n),9))
     ; position of node p2
     p3(k) = vector(parse(temp(n),13),parse(temp(n),14),parse(temp(n),15))
     ; position of node p3
     p4(k) = vector(parse(temp(n),19),parse(temp(n),20),parse(temp(n),21))
     ; position of node p4


 ;--- arrays of displacements ---
     d1(k) = vector(parse(temp(n),4),parse(temp(n),5),parse(temp(n),6))
     ; displacements of node p1
     d2(k) = vector(parse(temp(n),10),parse(temp(n),11),parse(temp(n),12))
     ; displacements of node p2
     d3(k) = vector(parse(temp(n),16),parse(temp(n),17),parse(temp(n),18))
     ; displacements of node p3
     d4(k) = vector(parse(temp(n),22),parse(temp(n),23),parse(temp(n),24))
     ; displacements of node p4
```

```
 ;--- arrays of normal vectors ---
    n1(k) = cross(p2(k)-p4(k),p3(k)-p4(k))
    n2(k) = cross(p1(k)-p3(k),p4(k)-p3(k))
    n3(k) = cross(p4(k)-p2(k),p1(k)-p2(k))
    n4(k) = cross(p3(k)-p1(k),p2(k)-p1(k))

    n = n + 1                          ; next element of array

  endloop


;--- interpolate imported boundary displacements ---
  bh = bou_head                        ; index to list of boundary corners
  mycount = 0
  loop while bh # 0                    ; loop over all boundary gridpoints

    gp = bou_gp(bh)                    ; index of boundary gridpoint

    n = 1
    count = 0                          ; number of tetrahedral zones intersected by boundary gp
    sumdispP = vector(0,0,0)           ; sum of displacement vectors

    loop while n <= znum               ; loop over all imported tetrahedral zones

      posP = gp_pos(gp)                ; position of boundary gp

    ;--- test whether point P is inside tetrahedron ---
      section

        if dot(n1(n),posP-p1(n))>0.0
        ; boundary gp not inside or on boundary of tetrahedral zone

          exit section

        else

          if dot(n2(n),posP-p2(n))>0.0
          ; boundary gp not inside or on boundary of tetrahedral zone

            exit section

          else

            if dot(n3(n),posP-p3(n))>0.0
            ; boundary gp not inside or on boundary of tetrahedral zone

              exit section

            else

              if dot(n4(n),posP-p4(n))>0.0
              ; boundary gp not inside or on boundary of tetrahedral zone

                exit section

              else
              ; boundary gp is inside or on boundary of tetrahedral zone
      ; --- interpolated displacement vector
                sumdispP = (dot(n1(n),posP-p4(n))/dot(n1(n),p1(n)-
p4(n)))*d1(n)+(dot(n2(n),posP-p3(n))/dot(n2(n),p2(n)-
p3(n)))*d2(n)+(dot(n3(n),posP-p2(n))/dot(n3(n),p3(n)-
p2(n)))*d3(n)+(dot(n4(n),posP-p1(n))/dot(n4(n),p4(n)-p1(n)))*d4(n)
                count = count + 1              ; count # of tetrahedral zones
                exit loop

              endif
```

```
          endif

        endif

      endif

    end_section

    n = n + 1                                          ; next element of array

  endloop

;--- check if all boundary gps are located in or on the boundary of at least one tetrahedral zone ---
  section

    if count # 0        ; boundary gp is inside or on the boundary of at least one tetrahedral zone

      exit section

    else                ; boundary gp not inside or on boundary of any tetrahedral zone

  ;--- put boundary displacement to that of the nearest neighbour node
      n = 1
      mindist = sqrt(dot(gp_pos(gp)-(p1(n)+p4(n)),gp_pos(gp)-(p1(n)+p4(n))))
      sumdispP = d1(n)
      count = 1

      n = 2
      loop while n <= znum          ; finds nearest neighbour among node p1 positions
        dist = sqrt(dot(gp_pos(gp)-(p1(n)+p4(n)),gp_pos(gp)-(p1(n)+p4(n))))
        if dist >= mindist
          n = n + 1
        else
          mindist = dist
          sumdispP = d1(n)
          n = n + 1
        endif
      endloop

      n = 1
      loop while n <= znum          ; checks if nearest neighbour is in node p2 list
        dist = sqrt(dot(gp_pos(gp)-(p2(n)+p4(n)),gp_pos(gp)-(p2(n)+p4(n))))
        if dist >= mindist
          n = n + 1
        else
          mindist = dist
          sumdispP = d2(n)
          n = n + 1
        endif
      endloop

      n = 1
      loop while n <= znum          ; checks if nearest neighbour is in node p3 list
        dist = sqrt(dot(gp_pos(gp)-(p3(n)+p4(n)),gp_pos(gp)-(p3(n)+p4(n))))
        if dist >= mindist
          n = n + 1
        else
          mindist = dist
          sumdispP = d3(n)
          n = n + 1
        endif
      endloop

      n = 1                         ; checks if nearest neighbour is in node p4 list
      loop while n <= znum
        dist = sqrt(dot(gp_pos(gp)-p4(n),gp_pos(gp)-p4(n)))
```

```
          if dist >= mindist
            n = n + 1
          else
            mindist = dist
            sumdispP = d4(n)
            n = n + 1
          endif
        endloop

      endif

    end_section

  ;--- calculate the average displacement of boundary gp
    averdispP = sumdispP/float(count)

  ;--- assign boundary gp velocity
    bou_vel(bh) = (averdispP-gp_dis(gp))/(tdel*float(mycycles))

    bh = bou_next(bh)                                    ; repeat for next boundary gridpoint

  endloop

end
```

F.3 Description of model used for extracting boundary conditions

F.3.1 Model specifications

The large model used to extract boundary conditions for the near-field models with fractures (see Chapter 8) consists of a 400 m × 400 m × 400 m linear elastic block of rock in which only the tunnel is explicitly represented, see Figure F-1. Input data to the model with regards to heat load, intact rock properties and *in situ* stresses are as specified in Chapter 8. The vertical boundaries are locked in all directions and roller boundaries are applied on the top and bottom boundaries.

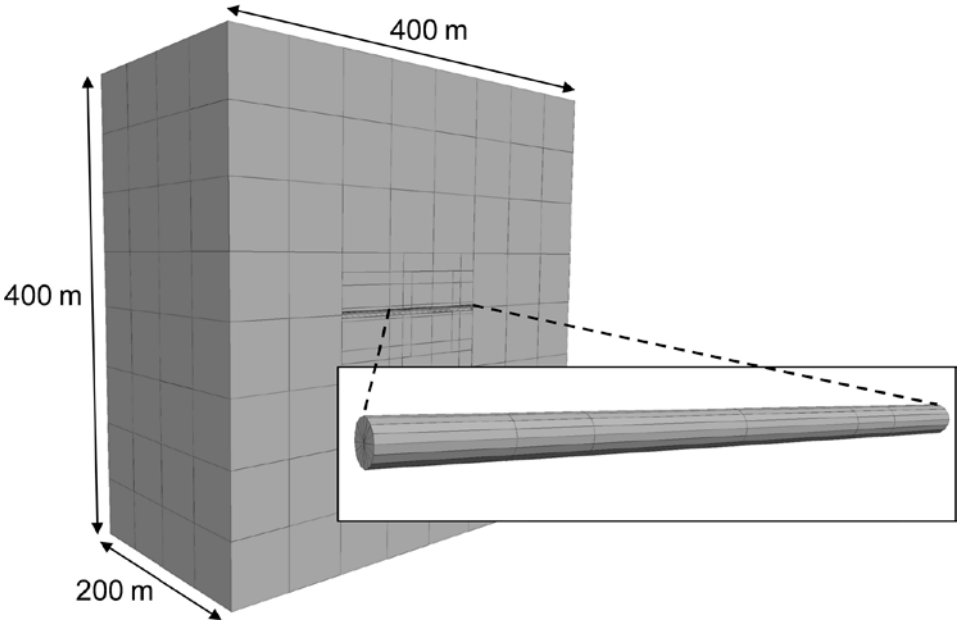

Figure F-1. *Model geometry for the large model used for extracting boundary conditions for the fracture models. Note that parts of the model are hidden to expose the tunnel.*

F.3.2 Output

The model is analyzed in three general steps: 1) a primary equilibrium is established, 2) the tunnel is excavated and 3) the thermal impact is determined. Position vectors and displacement vectors are extracted from steps 2 and 3 and saved to text files using the FISH code described in Table F-1. For the problem considered here (and in Chapter 8), the sidelengths of the "big box" and "small box" (cf. the export FISH code above), enclosing the boundaries of the smaller model, are 20 cm larger and smaller, respectively, than the boundary sidelength of the smaller model. Note that data from step 2 are only used in the verification example presented below. In the fracture models analyzed in Chapter 8, the boundaries are locked in all directions during the initial equilibrium and during the excavation of the tunnel, deposition holes and plug slots.

F.4 Verification example

In order to verify that a small model with imported and interpolated boundary conditions can reproduce the stresses as calculated by a large-scale model, two linear elastic models with the same input data as the model in the previous section are analyzed.

First, a small 3DEC model is analyzed (see Figure F-2, left) with boundary conditions extracted from the model described in the previous section. Second, a large model is analyzed (see Figure F-2, right). The large model has the same level of detail with regard to geometry and mesh density in the region corresponding to the small model. The vertical boundaries are locked in all directions and roller boundaries are applied on the top and bottom boundaries.

A comparison of the stresses as calculated by the two models at five points around the deposition holes and tunnel are presented in Figure F-3. As seen in the figure, there is an excellent agreement between the results from the large model and from the small model with imported and interpolated boundary conditions.

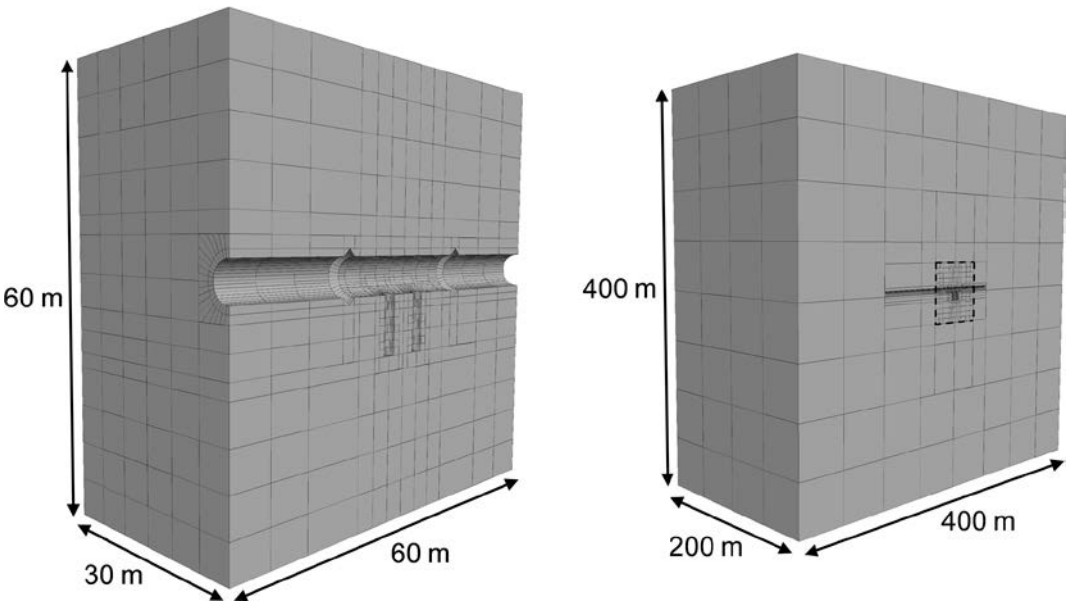

Figure F-2. *Left: View of the small 3DEC model. Right: View of the large model. The region mark with a dashed line corresponds to the boundaries of the small model. In both sub-figures, parts of the model have been hidden to expose the tunnel and deposition holes.*

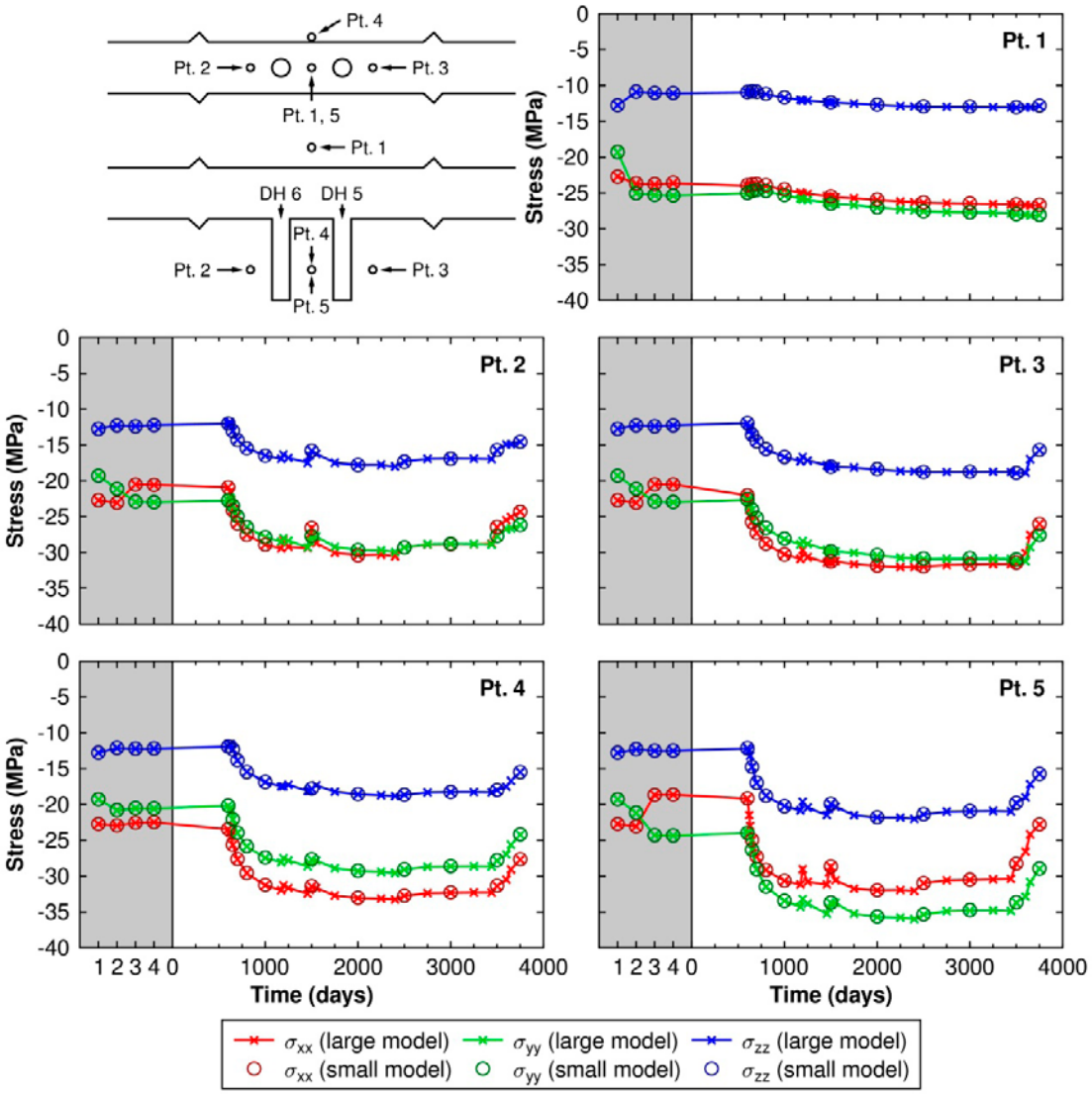

Figure F-3. *Comparison between the stress component along the tunnel (σ_{xx}),the stress component across the tunnel (σ_{yy}) and the vertical stress (σ_{zz}) as calculated by the small model with imported and interpolated boundary conditions and by the large model.*

Appendix G

Influence of near-field fractures: Complementary analyses

In this appendix, complementary analyses are made of the impact of the simplistic fracture network described in Chapter 8 on the stresses in the walls of the around the deposition holes and on the major and minor horizontal components of the stress addition tensor at the measurement locations. The stability (see also Appendix E) and normal stress variations of selected fracture planes intersecting the repository openings are also assessed.

G.1 Description of numerical models

The 3DEC models considered in this appendix are identical to model F1a (described in Chapter 8) with regard to geometry, heat load, boundary conditions, intact rock properties, fictitious fracture properties, *in situ* stresses and pore pressure. The differences lie in the excavation sequence and in the fracture material properties.

The response of the rock mass to changes in mechanical and thermal conditions is assessed in five general steps: 1) a primary equilibrium is established, 2) the tunnel is excavated, 3) the deposition holes are excavated, 4) the plug slots are excavated and 5) the thermal impact is determined. Instead of excavating the tunnel and deposition hole in thin slices as shown in Figure 8-4, a simplified excavation sequence (steps 2–3) is considered here in which the tunnel is excavated in one step and the two deposition holes are excavated simultaneously in another step, see Figure G-1.

Four complementary fracture models with different fracture properties are analyzed (see Table G-1 for parameter values):

- One model in which the friction angle is set at 25°.
- One model in which the friction angle is set at 35°. This model has the same parameter values as model F1a in Chapter 8.
- One model in which the friction angle is set at 45°.
- One model with an elastic fracture material model.

Table G-1. Fracture properties.

Property	Unit	Value
Friction angle*	°	25
		35
		45
Cohesion*	MPa	0
Tensile strength*	MPa	0
Normal stiffness	GPa/m	700
Shear stiffness	GPa/m	40

*Not used in the elastic fracture model.

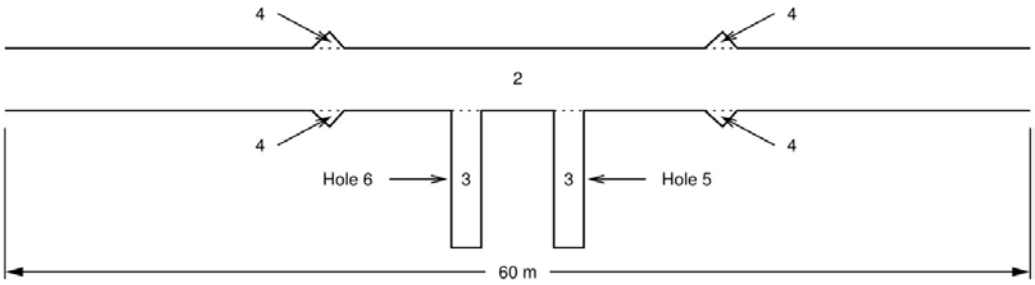

Figure G-1. *Schematic view of the excavation sequence for the complementary models. Step 2: excavation of the tunnel. Step 3: excavation of both deposition holes simultaneously. Step 4: excavation of both plug slots simultaneously.*

G.2 Modelling results

G.2.1 Fracture deformations

Stability and fracture shear displacements

A Mohr-circle plot of the *in situ* state of stress and stability of the selected fractures is provided in Figure G-2. The majority of the fractures are initially stable for all three models with a Mohr-Coulomb shear strength criterion. Only for the lowest considered friction angle (25°) would the most unfavourably oriented fractures be unstable initially.

Figure G-3 shows the maximum area with shear displacements equal to, or exceeding, a given value at any point in time during the excavation phase or during the subsequent heated phase. Similarly to the analyses presented in Chapter 8, the largest displacements occur along the boundaries of the wedges formed in the floor. In the model with the elastic fracture model there are no shear displacements exceeding 0.5 mm over an area of more than 1 m^2.

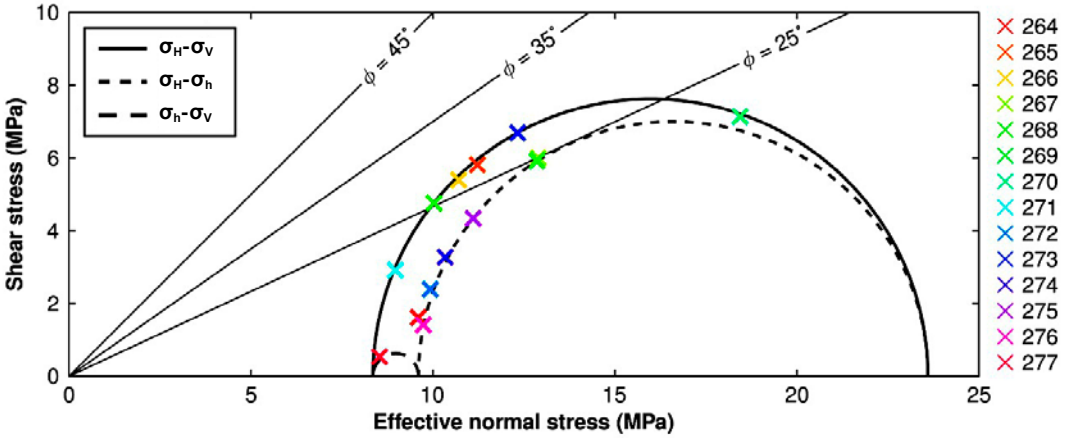

Figure G-2. *Mohr-circle plot of the in situ state of stress and shear strength of the selected fractures.*

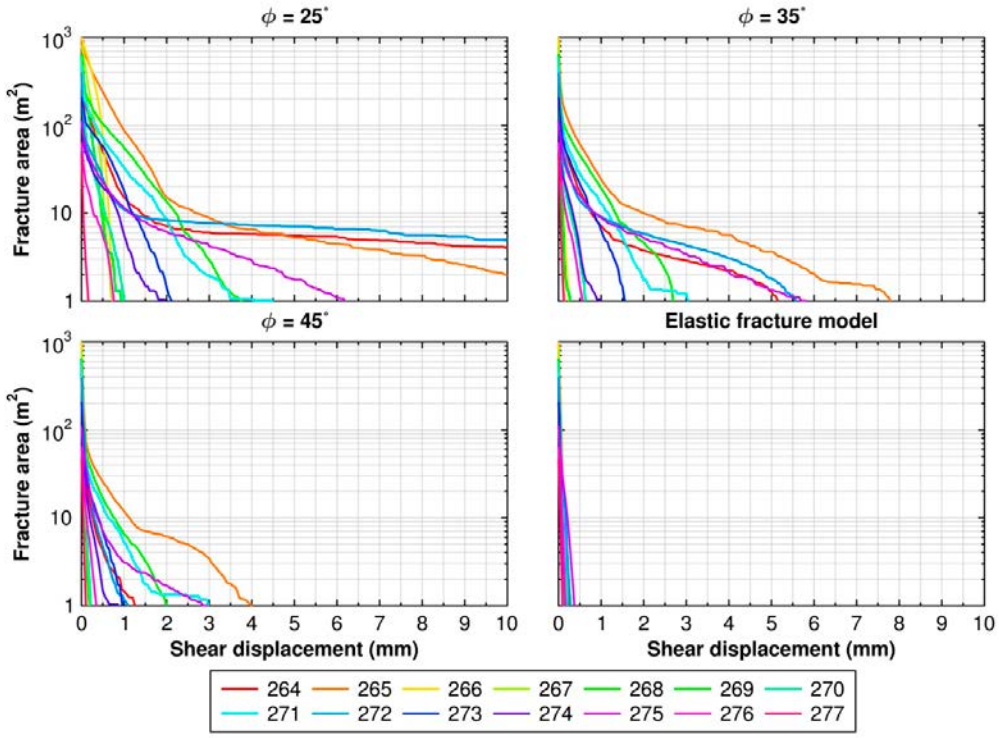

Figure G-3. *Maximum fracture area with shear displacement equal to, or exceeding, given value for each fracture in the fracture model.*

Contour plots of the shear displacement on fracture #265 after excavation of the tunnel and of the cumulative shear displacement of the same fracture at the end of the modelling period are presented in Figure G-4. In the model with the linear elastic fracture model, the shear displacements are too small to be visible in the contour plot. Results from this model are, therefore, not shown in the figure. An example of the temporal evolution of the shear displacement at a point at which the shear displacement is not directly associated with the movements along the boundaries of the wedges with large displacements is presented in Figure G-5. For all four tested models, most of the displacements appear to take place during the excavation of the tunnel with little additional movements during the heated phase.

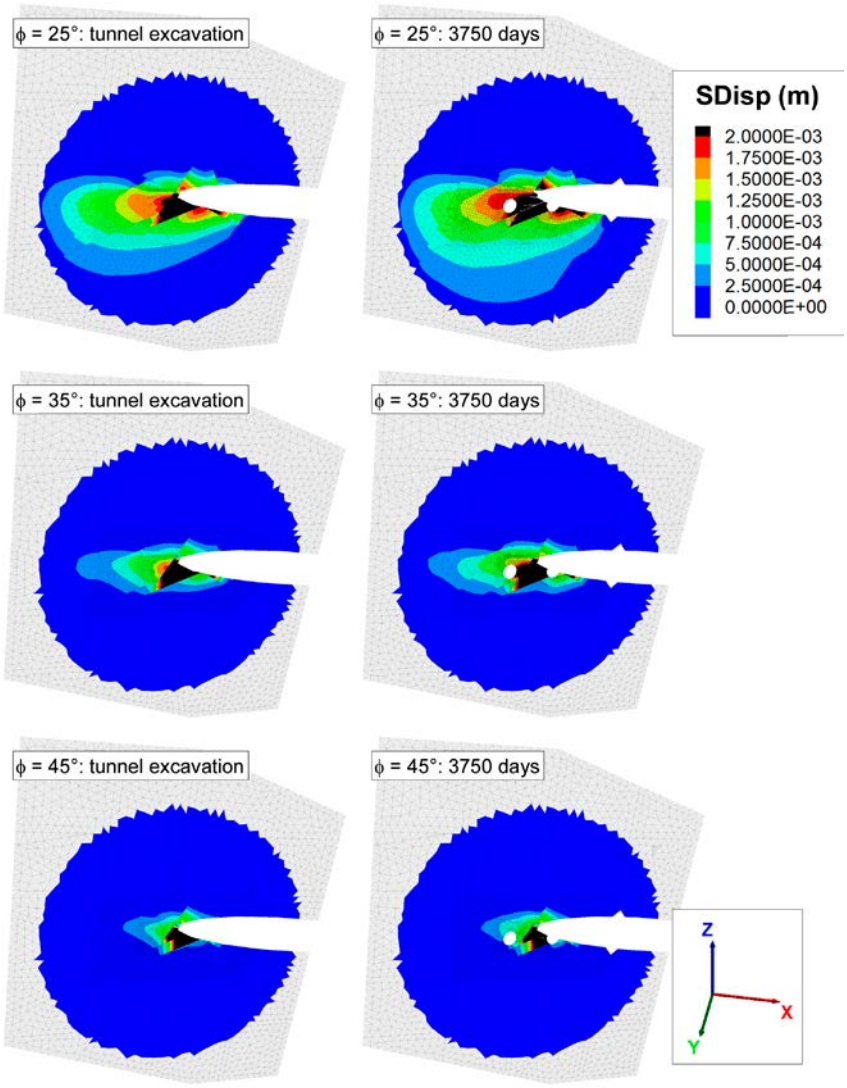

Figure G-4. *Cumulative shear displacement of fracture 265 after excavation of the tunnel and at the end of the modelling period.*

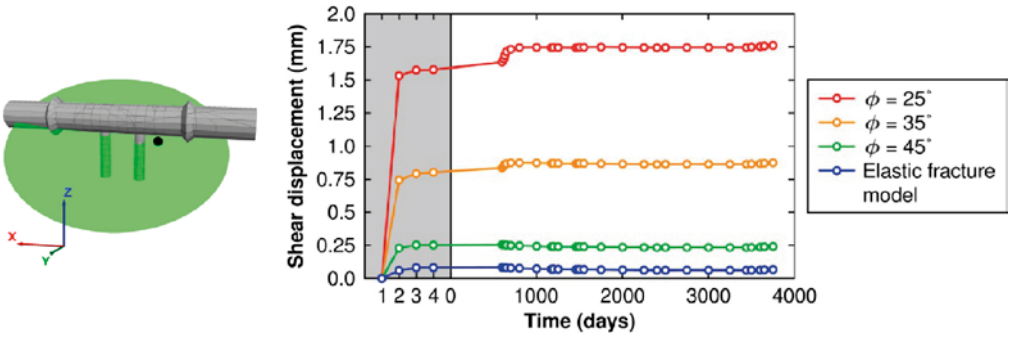

Figure G-5. *Temporal development of the shear displacement at the location shown in the left part of the figure.*

Normal stress variations

As seen in Chapter 8, regions of low normal stress are found after excavation where the fractures intersect the repository openings or are approximately parallel to them. Additional regions of low normal stress are introduced at the boundaries of the wedges with large displacements formed in the floor of the tunnel. Figure G-6 shows contour plots of the effective normal stress on fracture #265 after excavation of the tunnel and after 2,000 days of heating. An example of the temporal evolution of the effective normal stress is shown in Figure G-7. For all four models, compression generally increases during the heated phase.

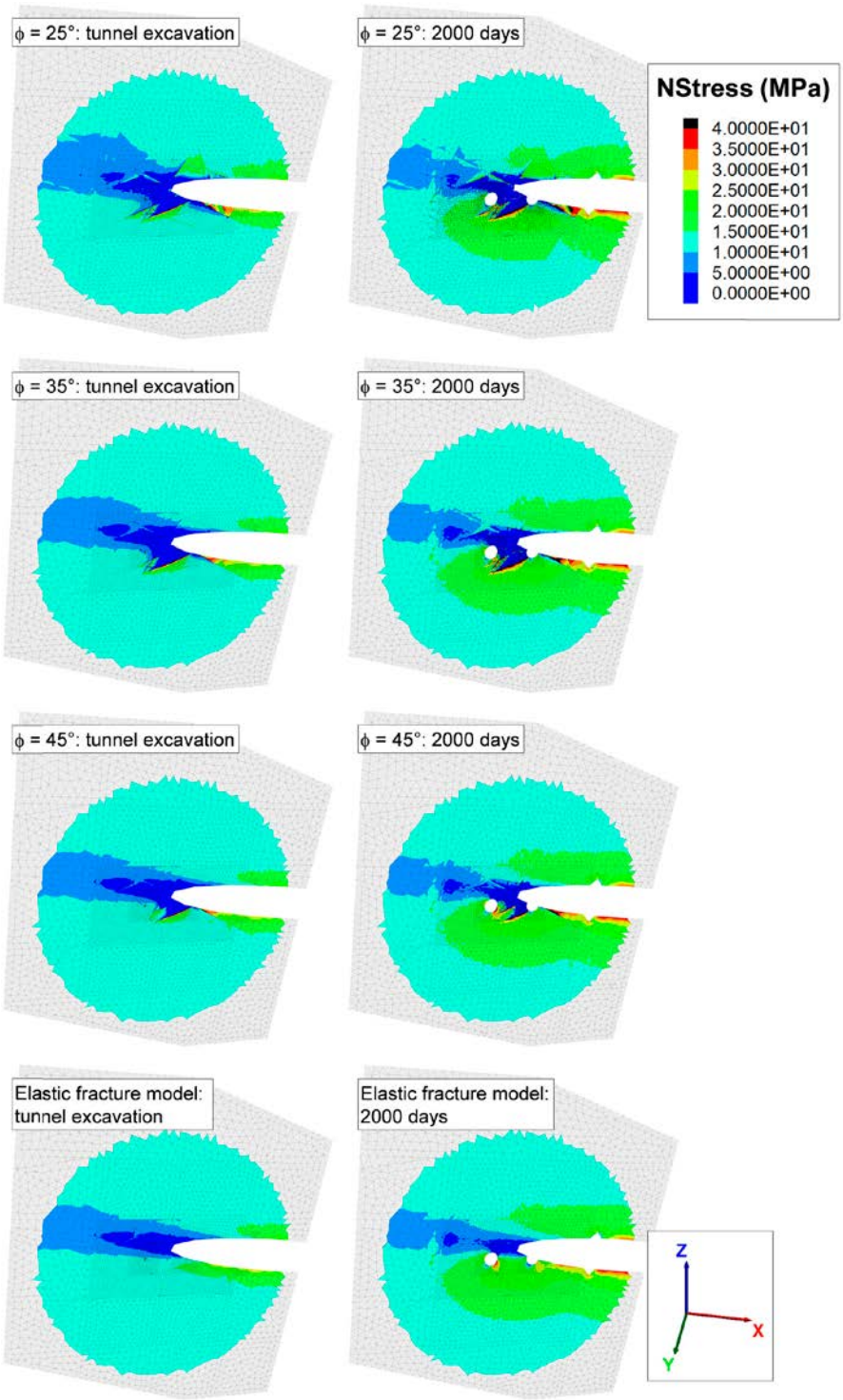

Figure G-6. *Normal stress variations on fracture 265 after excavation of the tunnel and after 2,000 days of heating.*

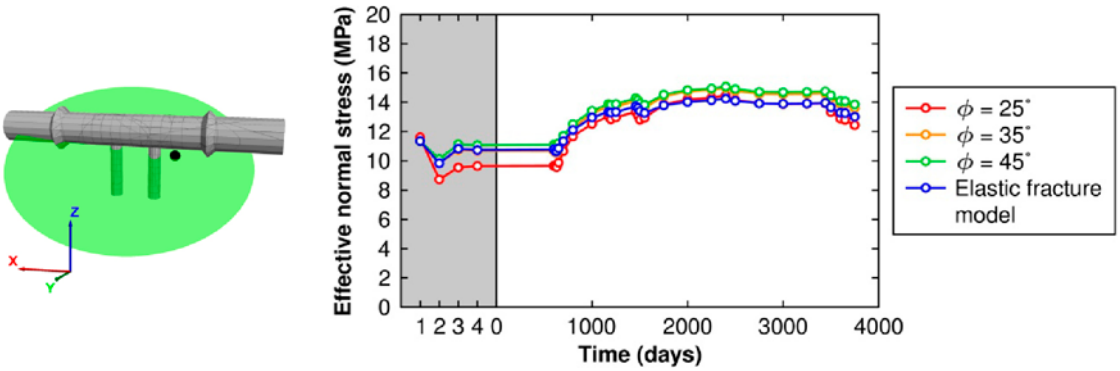

Figure G-7. *Temporal development of the effective normal stress at the location shown in the left part of the figure.*

G.2.2 Stresses in deposition hole walls

Figure G-8 and Figure G-9 shows contour plots of the major principal stress around Hole 5 and Hole 6, respectively, after excavation of the holes. For each hole, the impact of the fracture network is also presented. As expected, increasing the shear strength of the fractures decreases the disturbance caused by shear displacements along the fractures. However, also for the elastic fracture model some disturbances are observed. Similarly to the analyses conducted in Chapter 8, the disturbances are most prominent in Hole 5 and appear to be mainly associated with shear displacements along the steeply dipping fracture (cf. Figure G-8).

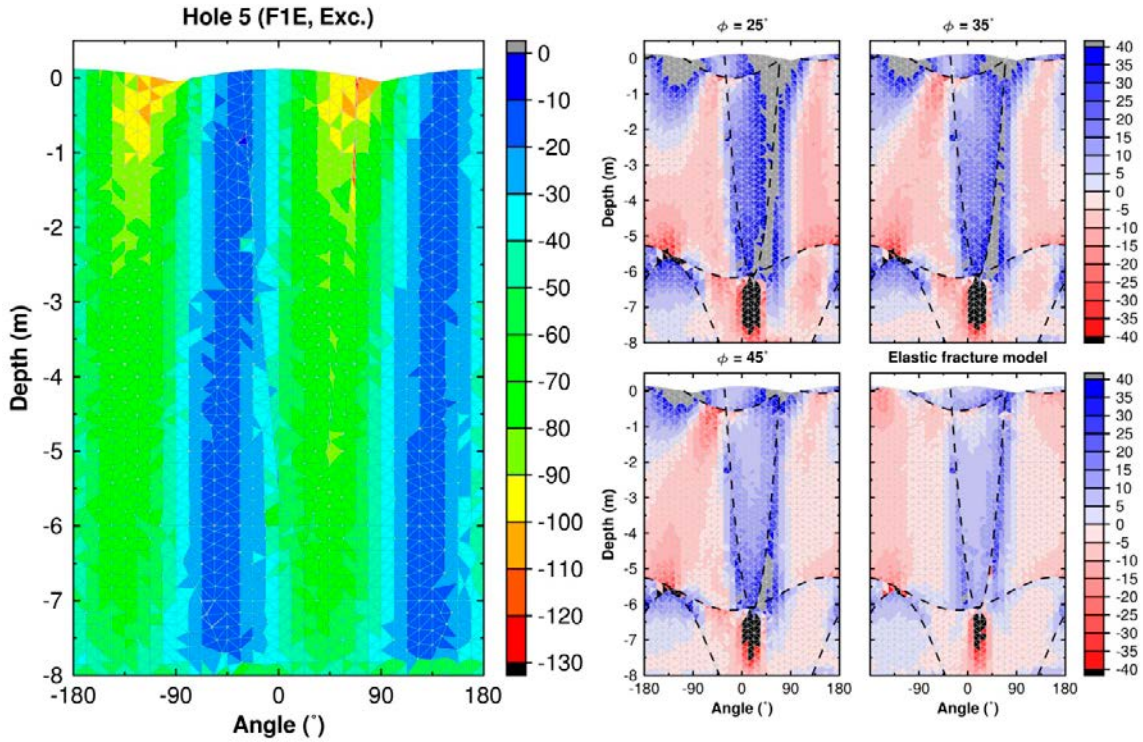

Figure G-8. *Left: Contour plot of the major principal stress around Hole 5 after excavation in the elastic model. Contours in MPa. Right sub-figures: Contour plots of the difference in the major principal stress for each of the complementary fracture models compared with the elastic model. Contours in MPa where blue colours represent a reduction in compression and red colours an increase in compression compared with the elastic model. Fracture intersections are marked with dashed lines.*

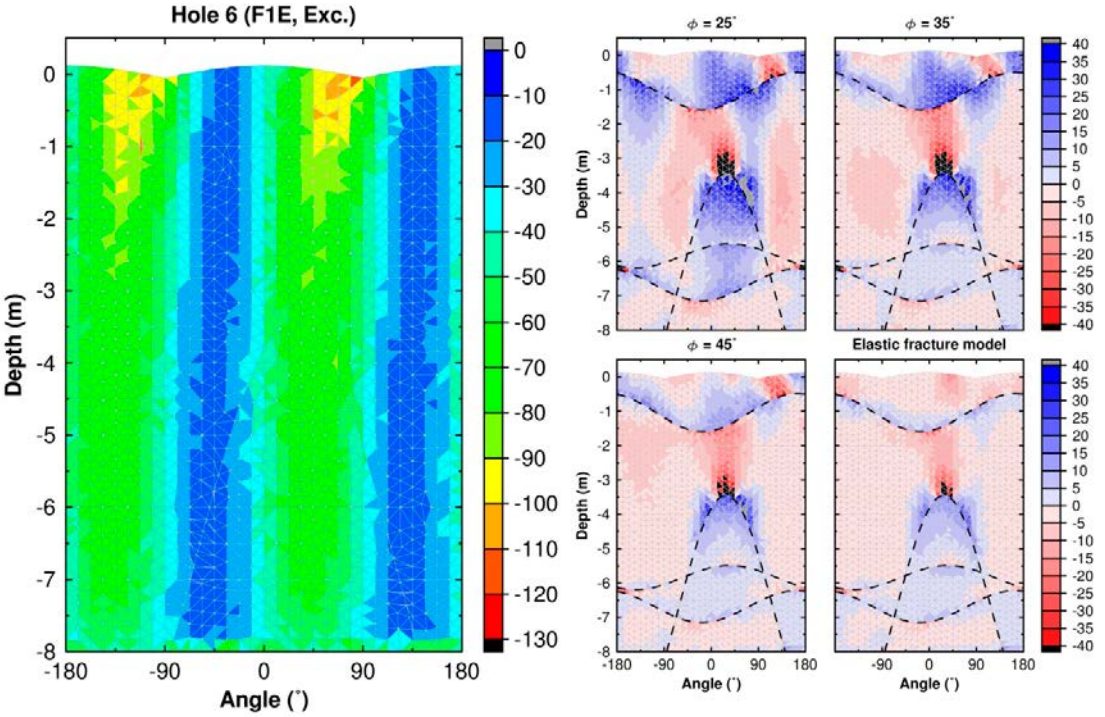

Figure G-9. *Left: Contour plot of the major principal stress around Hole 6 after excavation in the elastic model. Contours in MPa. Right sub-figures: Contour plots of the difference in the major principal stress for each of the complementary fracture models compared with the elastic model. Contours in MPa where blue colours represent a reduction in compression and red colours an increase in compression compared with the elastic model. Fracture intersections are marked with dashed lines.*

G.2.3 Stresses at measurement locations

For completeness, the impact of the fracture network, with different shear strength, on the major and minor components of the stress addition tensor is shown in Figure G-10, Figure G-11, Figure G-12 and Figure G-13. Similarly to the stresses in the deposition hole walls, the disturbances caused by displacements along the intersecting fractures decrease with increasing fracture shear strength.

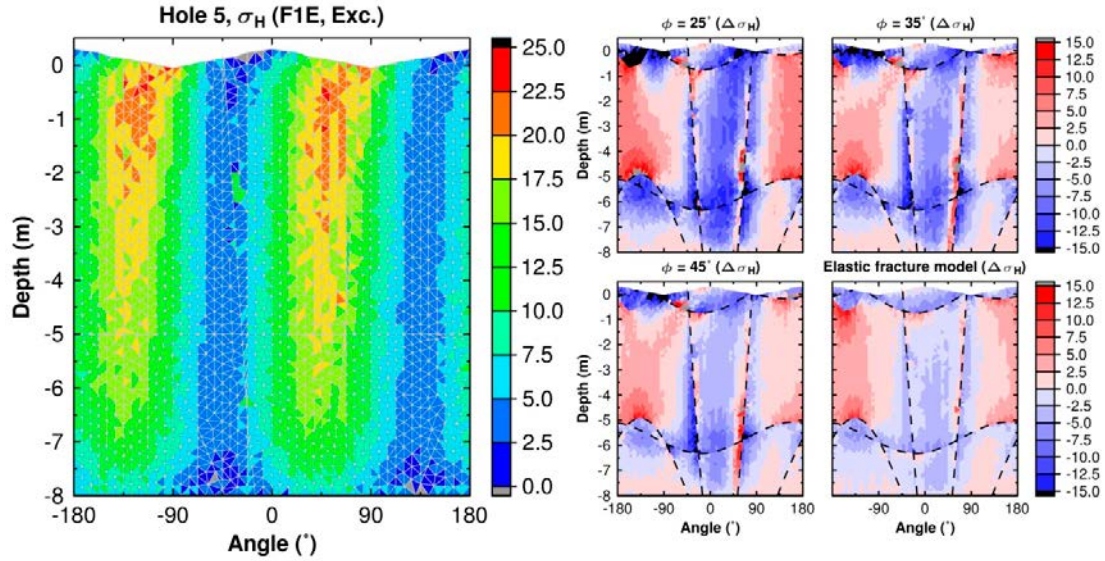

Figure G-10. *Left: Major horizontal component of the stress addition tensor around Hole 5 after excavation in the linear elastic model. Right sub-figures: Difference between the major stress components in each complementary fracture model and the elastic model. Contours in MPa. Fracture intersections are marked with dashed lines.*

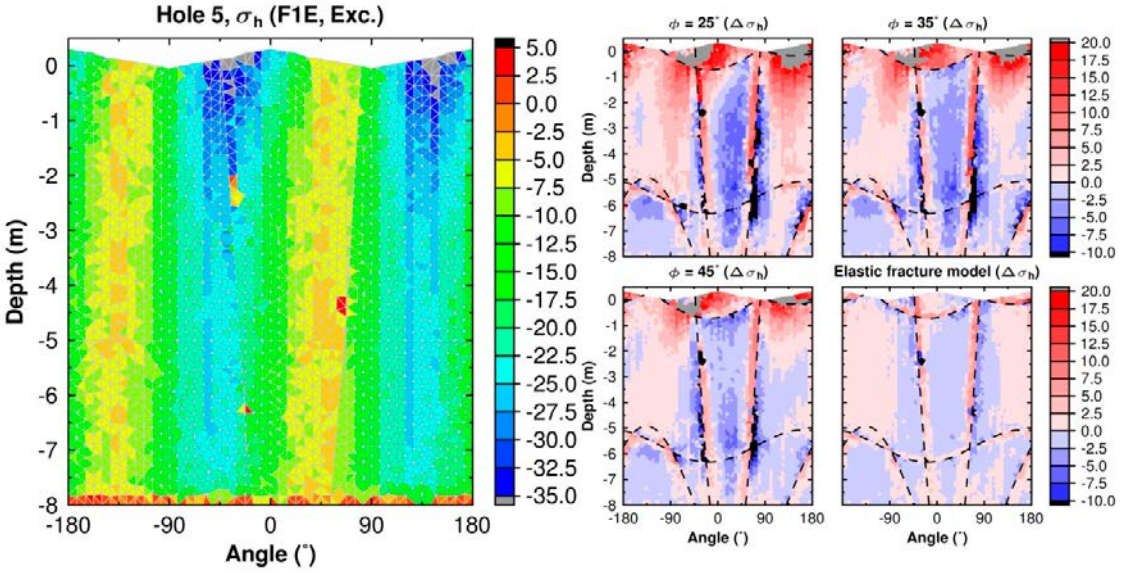

Figure G-11. *Left: Minor horizontal component of the stress addition tensor around Hole 5 after excavation in the linear elastic model. Right sub-figures: Difference between the minor stress components in each complementary fracture model and the elastic model. Contours in MPa. Fracture intersections are marked with dashed lines.*

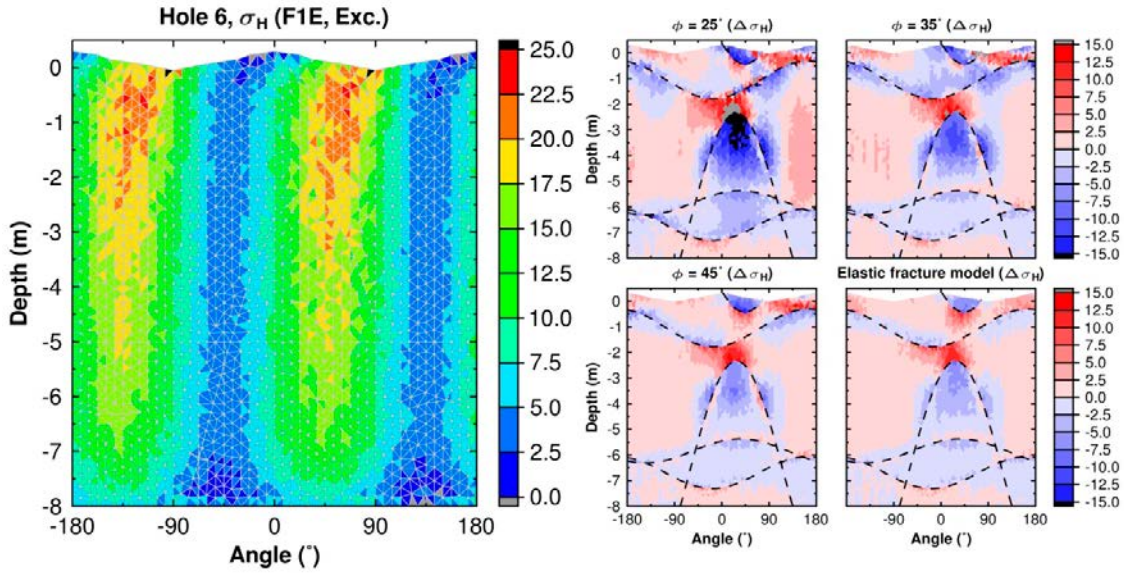

Figure G-12. *Left: Major horizontal component of the stress addition tensor around Hole 6 after excavation in the linear elastic model. Right sub-figures: Difference between the major stress components in each complementary fracture model and the elastic model. Contours in MPa. Fracture intersections are marked with dashed lines.*

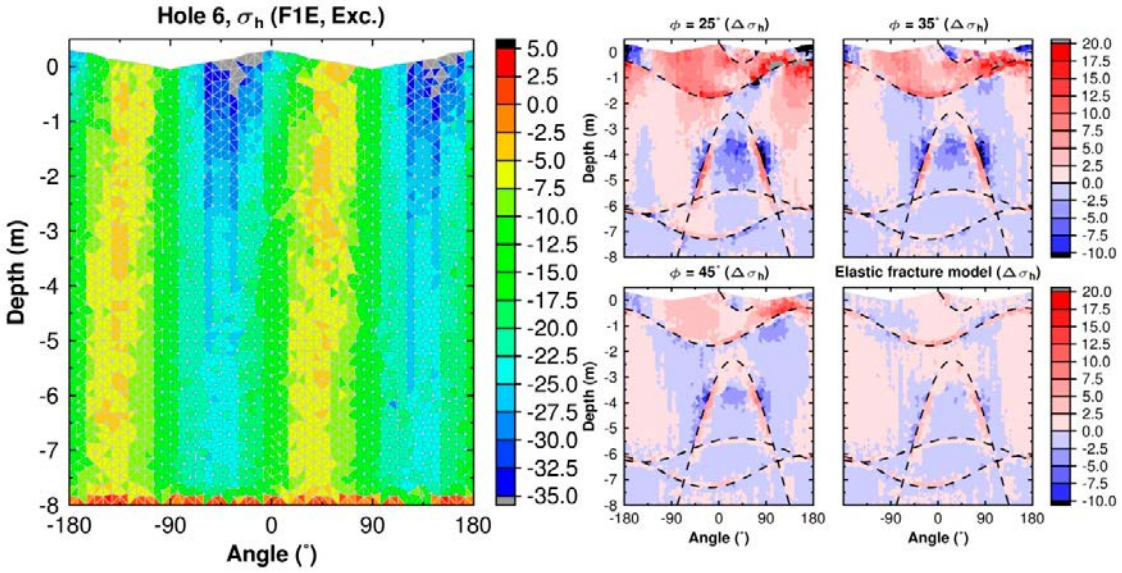

Figure G-13. *Left: Minor horizontal component of the stress addition tensor around Hole 6 after excavation in the linear elastic model. Right sub-figures: Difference between the minor stress components in each complementary fracture model and the elastic model. Contours in MPa. Fracture intersections are marked with dashed lines.*

Appendix H

Inspection of deposition holes in the Prototype Repository

H.1 Introduction

The two holes in the outer section of the Prototype Repository, DA3551G01 (Hole 5) and DA3545G01 (Hole 6), were inspected on February 23 2012 with the purpose to make a preliminary documentation of any occurrences of spalling in the walls of these holes and to determine whether or not a more detailed survey of the holes would be required.

H.2 Method

The inspection was carried out by Derek Martin (University of Alberta) and Margareta Lönnqvist (Clay Technology AB) from a cage lowered into each hole. Occurrences of spalling were assessed by means of visual inspection and by tapping on the walls with a hammer. Particular attention was paid to areas of the walls expected to be most highly stressed, i.e. at azimuths perpendicular to the orientation of the major horizontal *in situ* stress (the most likely orientation of σ_H is 304° ± 10° with respect to North, RT90, see Section 3.3). Fracture mappings of the holes (Figure H-1) were used as a guide to document the findings.

H.3 Results

There was no evidence of any damage to the walls in Hole 5. With the exception of one location (see Figure H-2) in Hole 6, there were no indications of any stress induced damage to the walls in that hole. The area in Hole 6 where some potential damage was observed is located approximately at the position marked with the shaded area "9" in Figure H-1 (right) and coincides with the region where high tangential stresses are expected.

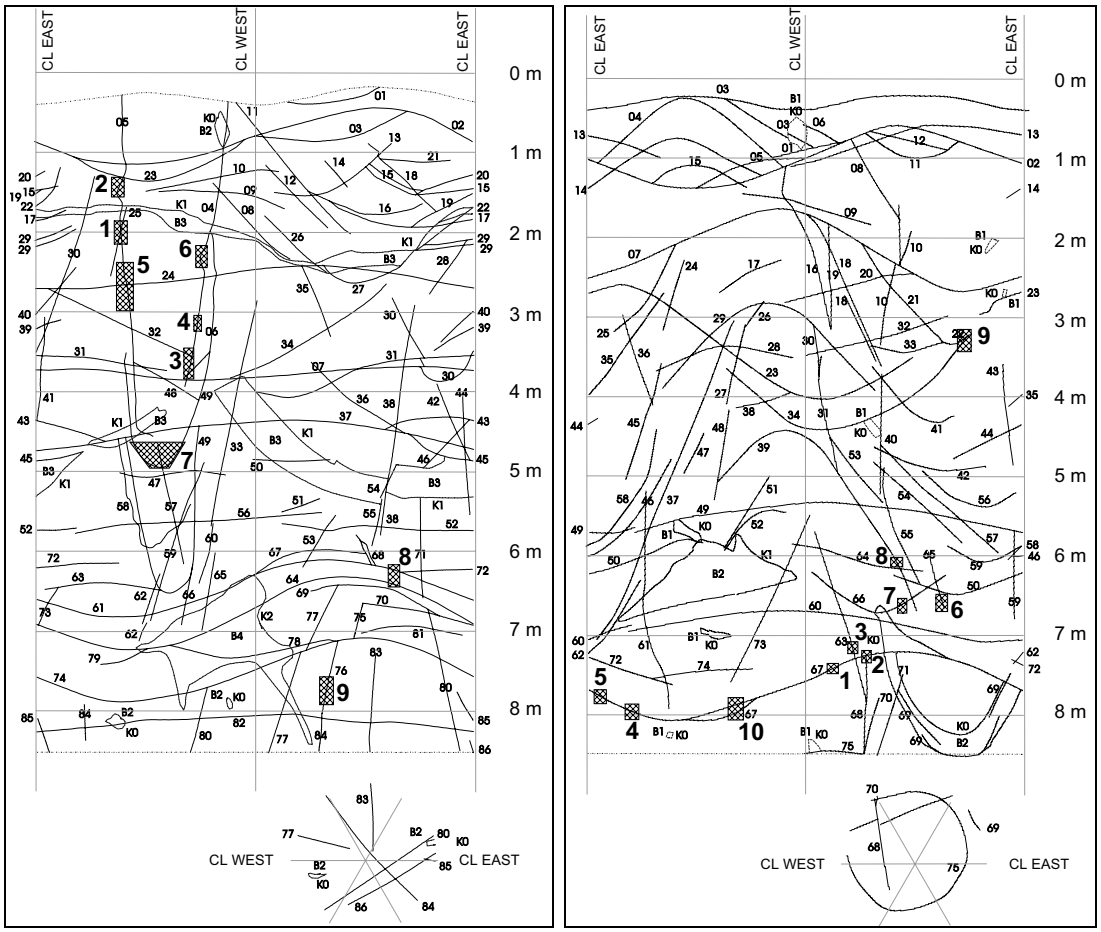

Figure H-1. *Fracture mapping of Hole 5 (left) and Hole 6 (right). Water bearing features are marked with shaded areas. Both figures from Rhén and Forsmark (2001).*

Figure H-2. *Illustration of potential damage to the wall in Hole 6. This area is located approximately at the position marked with the shaded area "9" in Figure H-1 (right). Right: Close-up of left figure.*

H.4 Conclusions

Since only very little or no damage to the walls of Holes 5 and 6 was observed, it was concluded, on site, that no further surveys of these holes are necessary.

Appendix I

Background to *in situ* stress model

The following text that gives a background to and justification for the *in situ* stress model used in this report has been provided by Rolf Christiansson, Svensk Kärnbränslehantering AB.

Determination of the state of stress at the Äspö HRL has been carried out in different campaigns and with different methods for *in situ* measurements over the years. Summary of measuring results in boreholes and interpretation of these measurements has been published by various authors. Ask (2003) concluded significant differences in results from different measuring methods and re-evaluated the data using a proposed strategy for Integrated Stress Determination Method (ISDM). The proposed stress magnitudes at the 450-m level were (interpreted from diagrams in Ask (2003, Figure 7)):

$\sigma_H \approx 30$ MPa

$\sigma_h \approx 12$ MPa

$\sigma_v \approx 14$ MPa

The orientation of σ_H was determined to approximately 108º (in the coordinate system RT90) from north with the ISDM approach. However, Ask (2003) also concluded that there is indication for two stress domains at Äspö HRL, controlled by the minor deformation zone NE-2 (Rhén et al. 1997). The Prototype repository is located in the NW stress domain were stress magnitude was interpreted to be higher, compared to the SE block. The relevance in two stress domains at the 420–450 m depth was also indicated by Hakami (2003) using 3DEC for stress modelling. Figure I-1 shows a plan view through his 3DEC model at the 455-m level and the scan line with calculated stress distribution due to influence of minor deformation zones within the Prototype area. Hakami (2003) also concluded that the main variation of stress tensor occurs in the σ_2–σ_3-plane, where the rotation of the two principal stresses can be so high that σ_2 and σ_3 replace each other within a certain depth interval. Hakami (2003) presents the principal stresses, but the plunge is rather small for the σ_1 and σ_2 components. The modelling results indicate for the rock mass around the Prototype Repository:

$\sigma_1 \approx \sigma_H \approx 30$–$32$ MPa

$\sigma_2 \approx \sigma_h \approx 16$–$18$ MPa

$\sigma_3 \approx \sigma_v \approx 12$–$13$ MPa

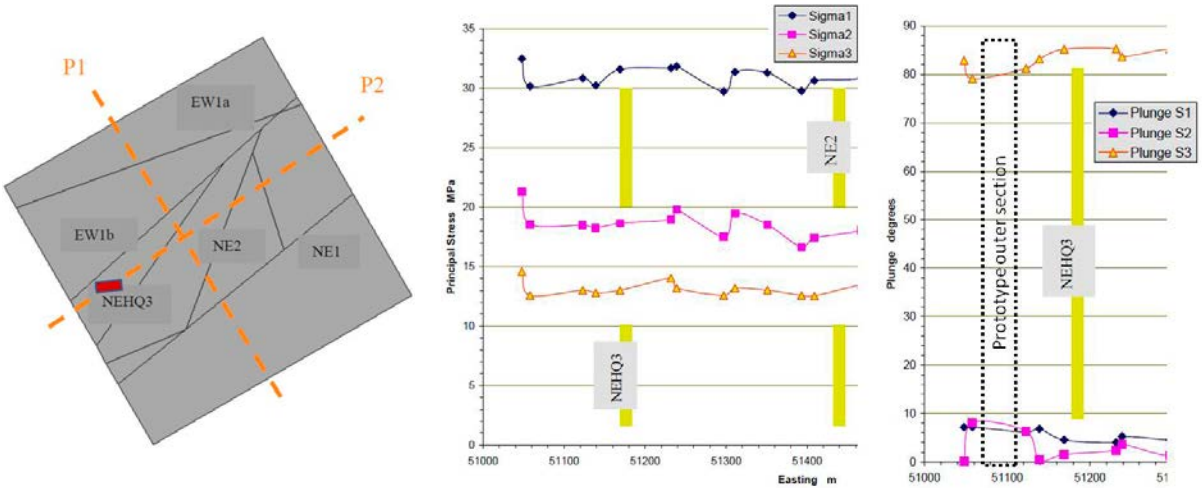

Figure I-1. *Left: plan view of the 455-m level with deformation zones used in the 3DEC modelling marked. The approximate location of the Prototype Repository is marked with a red square. Central: estimated variability of principal stresses. Right: estimated variability of plunge of the principal stresses. Based on Hakami (2003).*

Christiansson and Jansson (2003) compared different stress measurement methods in two orthogonal boreholes at the 450-m level. The test location is about 150 m NE of the Prototype repository, see left part of Figure I-1 and Figure I-2. They concluded the following stress state at the target volume at about 455 m-level:

$\sigma_H \approx 24 \pm 5$ MPa, most likely within the upper range

$\sigma_h \approx 10–13$ MPa

$\sigma_v \approx 15–20$ MPa, most probably only is a local value due to the presence of a nearby fracture.

Christiansson and Jansson (2003) also noticed local disturbance of the stress field in the rock mass, due to discontinuities. They concluded that if the rock behaves reasonably elastically, the overcoring methods provide stress magnitudes with an uncertainty of 15–20% and that in the area with significant anisotropic stress conditions all the tested methods were able to determine the orientation of the principal major horizontal stress within ± 10º.

Staub et al. (2004) carried out convergence measurements and back analyses of the stress from the Q-tunnel purposely developed for the Äspö Pillar Stability Experiment (APSE). The tunnel was aligned perpendicular to the previously estimated orientation of the major horizontal stress (298º in the coordinate system RT90). They concluded:

$\sigma_1 = \sigma_H = 30$ MPa

$\sigma_2 = \sigma_v = 15$ MPa

$\sigma_3 = \sigma_h = 10$ MPa

Recently, Hakala et al. (2013) conducted measurements with a newly developed device for *in situ* stress measurements based on LVDT gauges. The cell was installed in different location along the perimeter of the TBM tunnel and a drill&blast tunnel (the S-tunnel), see Figure I-2.

The results from Hakala et al. (2013) are given in Table I-1 and Table I-2. This includes a combined solution using the deep TASS and all TBM measurements.

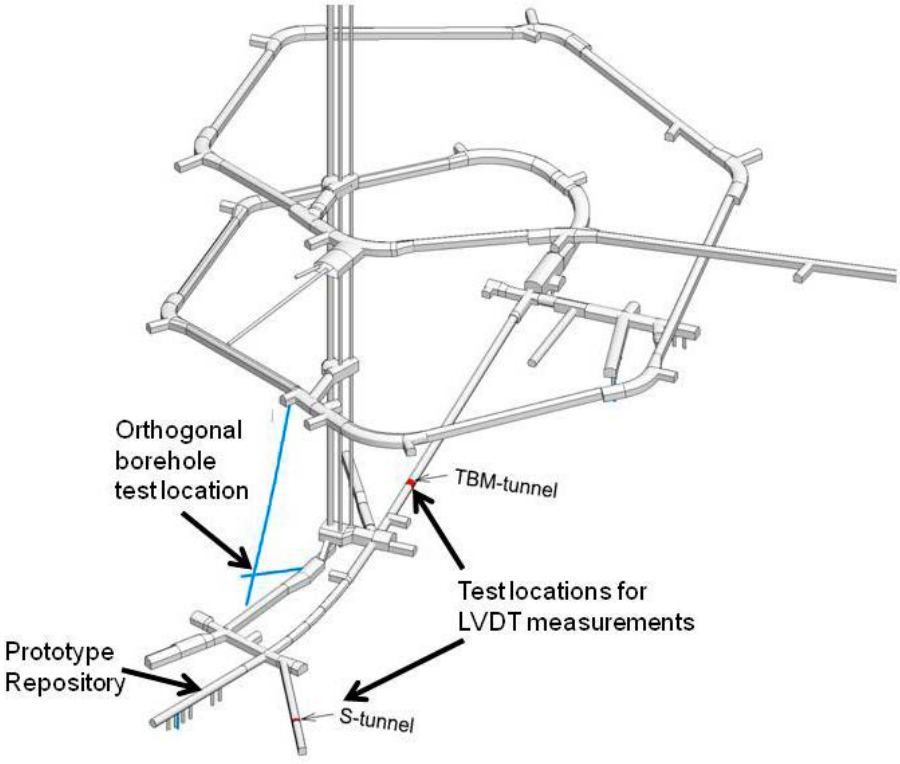

Figure I-2. *Location for the measurements with the newly developed LVDT cell for stress measurements (Hakala et al. 2013).*

Table I-1. Best fit solution for *in situ* principal stresses based on the Äspö TBM tunnel and TASS tunnel deep LVDT-measurements. The stress magnitudes are in MPa and trends are in the co-ordinate system RT90.

Solution	σ_1	trend,°	plunge,°	σ_2	trend,°	plunge,°	σ_3	trend,°	plunge,°
TBM & TASS	24.9	131	23	19.1	20	40	12.9	243	41
TBM All	25.5	140	18	22.5	34	39	13.9	249	46
TASS Deep	24.6	134	7	13.6	40	28	9.2	238	60

Table I-2. Best fit solution for horizontal and vertical *in situ* stress components based on the Äspö TBM tunnel and TASS tunnel deep LVDT-measurements. The stress magnitudes are in MPa and the trends are in the co-ordinate system RT90.

Solution	σ_H	trend,°	σ_h	trend,°	σ_v
TBM & TASS	23.7	140	15.8	230	17.3
TBM All	25.0	152	18.5	242	18.4
TASS Deep	24.3	136	12.6	226	10.5

In summary, over time there has been carried out significant efforts to determine the state of stress at the lower level of the Äspö HRL with different methods. The results show variability in magnitude and orientation, but are roughly within the ranges of the estimated uncertainties discussed by Christiansson and Jansson (2003). It is therefore assessed that there is not a unique state of stress within the rock mass of the analysed section of the Prototype Repository. In this study, the principal *in situ* stress components are assumed to lie in the horizontal-vertical planes with the major principal stress ($\sigma_1 = \sigma_H$) equal to 26–30 MPa and oriented 304° ± 10° (in the coordinate system RT90), the intermediate principal stress ($\sigma_2 = \sigma_h$) equal to 13–15 MPa and the minor principal (vertical) stress ($\sigma_3 = \sigma_v$) equal to 12.5–13 MPa. This is in close agreements with the results by Christiansson and Jansson (2003) as well as Staub et al. (2004), but the vertical stress is adjusted to the gravitorial stress.